Characterizing the Cellular Role of PHF6

Matthew Andrew Melville Todd

Thesis submitted to the Faculty of Graduate and Postdoctoral Studies
in partial fulfillment of the requirements for the degree of

Doctorate in Philosophy
in Biochemistry
with specialization in Human and Molecular Genetics

Department of Biochemistry, Microbiology, and Immunology
Faculty of Medicine
University of Ottawa, Ontario, Canada

Abstract

Defective chromatin remodeling proteins are associated with both germline and acquired human disease. PHF6 is encoded by an X-linked gene that is predominantly expressed in the brain and thymus. Structurally, PHF6 contains nuclear and nucleolar localization sequences as well as two ZaP domains, which bind dsDNA. Germline mutations in PHF6 are the cause of BFLS, an XLID, while somatic PHF6 mutations have been identified in T-ALL, AML, and CML. Indeed, screening of a pediatric cohort of nine T-ALL patients revealed a novel H329Q mutation. In a further clinical analysis, T-ALL onset occurred in a 9-year old male BFLS patient with an R342X mutation, suggesting that BFLS might be a cancer predisposition syndrome. To better understand its protein function, recombinant PHF6 was co-immunoprecipitated for a mass spectrometry based proteomic screen. Notably, PHF6 co-purified with multiple constituents of the NuRD complex, an important transcriptional regulator during embryogenesis and lineage commitment with particularly well characterized responsibilities during lymphogenesis. PHF6-NuRD localization was restricted to the nucleoplasm, however PHF6 also co-purified with several ribosomal and splicing proteins. When examined further, PHF6 was found to be recruited to the nucleolus by an RNA-mediated interaction and co-localized within the subnucleolar FC and DFC compartments. ChIP-qPCR revealed that PHF6 binds to transcribed regions of rDNA, resulting in the repression of rRNA. These data thus present a model of PHF6 acting as a tumour suppressor by mediating both nucleoplasmic and nucleolar transcriptional events.

Acknowledgements

I would like to foremost thank my supervisor Dr. David Picketts for the mentorship, training, and opportunities from which I have benefitted during my graduate studies. David has guided me with both the personal and professional values that I will always strive to emulate in my future career. I would also like to acknowledge the critical support and feedback provided by the members of my thesis advisory committee: Dr. Rashmi Kothary, Dr. Robin Parks, and Dr. Laura Trinkle-Mulcahy; as well as staff at the Ottawa Hospital Research Institute and the University of Ottawa for the necessary resources and facilities to support my graduate research and degree requirements.

Throughout my time in the Picketts lab, I have formed important friendships and collaborations that will persist beyond my training. While too numerous to recount in their entirety, I offer my particular thanks to Dr. Michael Huh, Dr. Darren Yip, Lemuel Racacho, Dr. Dennis Bulman, as well as all members of the Picketts lab, past and present, that I have had the pleasure of working alongside: Dr. Pamela Lagali, Keqin Yan, Danton Ivanochko, Dr. Matias Alvarez-Saavedra, Emile Hashem, Maureen Curtin, Steve Rennick, Chelsea McGregor, Marilyne Delorme, Emma Goodall, Tina Price O'Dea, Chantal Medina, Yusuf Ahmad, Olivia Zhang, Mélissa Geoffroy, and Khalid Al-Zahrani.

Finally, I thank all of my family and friends. You are the support system that instills within me the resolve and passion to pursue a career where I endeavour to answer the basic questions of life itself, and I am immensely grateful.

Contents

Appendices

List of Abbreviations

5mC	5-methylcytosine
5hmC	5-hydroxymethylcytosine
ActD	actinomycin D
ADD	ATRX-DNMT3-DNMT3L
ADP	adenosine diphosphate
AML	acute myeloid leukemia
ARID	AT-rich interaction domain
ARF	ADP ribosylation factor
ASE	nuclease (buffer)
ATM	ataxia telangiectasia mutated kinase
ATMDS	alpha-thalassemia-myelodysplastic syndrome
ATP	adenosine triphosphate
ATRX	alpha thalassemia/mental retardation syndrome X-linked
BCL11B	B-cell chronic lymphocytic leukemia/lymphoma protein 11B
BCOR	BCL-6 corepressor
BFLS	Börjeson-Forssman-Lehman syndrome
bHLH	basic helix-loop-helix transcription factor
BrdU	bromodeoxyuridine
BPTF	bromodomain PHD finger transcription factor
BRG1	brahma-related gene 1
BRPF	bromodomain and PHD finger-containing transcription factor
BSA	bovine serum albumin
CBP	CREB-binding protein
CD	cluster of differentiation protein
CDK	cyclin-dependent kinase
cDNA	complementary DNA
CGH	comparative genomic hybridization
CHD	chromodomain helicase DNA binding protein
ChIP	chromatin immunoprecipitation
ChIP-Seq	ChIP with massively parallel DNA sequencing
CML	chronic myeloid leukemia
CMV	cytomegalovirus
CNS	central nervous system
CpG	CG dinucleotide (cytosine-phosphate-guanine)
CREBBP	CREB-binding protein
CSB	Cockayne syndrome B protein
CSK	cytoskeleton (buffer)
Ct	threshold cycle
CTAP	C-terminal TAP tag
CTCF	CCCTC-binding factor
DAPI	4',6-diamidino-2-phenylindole
DFC	dense fibrillar component
DMEM	Dulbecco's modified Eagle medium
DN	double positive ($CD4^-CD8^-$) thymocyte

DNA	deoxyribonucleic acid
DNMT	DNA methyltransferase
DP	double positive ($CD4^+CD8^+$) thymocyte
dPC	*Drosophila* Polycomb
DRB	5,6-dichloro-β-D-ribofuranosylbenzimadole
dsDNA	double-stranded DNA
EDTA	ethylene diamine tetraacetic acid
ESI	electrospray ionization
ETP	early thymic progenitor
ETS	external transcribed spacer
EZH2	enhancer of zeste homolog 2
FBRL	fibrillarin
FBXL	F-box protein
FC	fibrillar centre
FOG-1	friend of GATA protein 1
G_1 phase	gap/growth 1 phase
G_2 phase	gap/growth 2 phase
G2E3	G2/M-phase specific E3 ubiquitin protein ligase
GADD45A	growth arrest and DNA-damage-inducible, 45 alpha
GAPDH	glyceraldyde-3-phosphate dehydrogenase
GATA1	GATA-binding protein 1
GC	granular component
GFP	green fluorescent protein
γH2AX	histone H2AX, phosphorylated on serine 139
HEEBO	human exonic evidence based oligonucleotide
HEK 293T	human embryonic kidney 293 cells, transformed with SV40 T antigen
HRP	horseradish peroxidase
ICF	immunodeficiency, centromere instability, and facial anomalies
IgG	immunoglobulin G
IGS	intergenic spacer
ISWI	imitation switch ATP-dependent chromatin remodeling protein
JARID	jumonji/ARID domain-containing protein
JmjC	jumonji C histone lysine demethylation domain
JMJD	jumonji domain-containing protein
HAT	histone acetyltransferase
HDAC	histone deacetylase
HPLC	high performance liquid chromatography
HSP70	heat shock protein 70
ITS	internal transcribed spacer
IP	immunoprecipitation
IP-MS/MS	immunoprecipitation followed by tandem mass spectrometry
KDM	histone lysine demethylase
KMT	histone lysine methyltransferase
L3MBTL1	lethal (3) malignant brain tumor-like protein 1
LC-MS/MS	liquid chromatography with tandem mass spectrometry
LMO	LIM (Lin-1, Isl-1, Mec-3) domain only protein

lncRNA	long non-coding RNA
LSD1	lysine-specific demethylase 1
M phase	mitosis
MBD	methyl-CpG-binding domain
MBT	malignant brain tumour domain
MDM2	mouse double minute 2 protein homolog
MECP2	methyl CpG binding protein 2
meCpG	methyl CpG
MIM	Mendelian inheritance in man
miR(NA)	microRNA
MLL	mixed-lineage leukemia protein
mRNA	messenger RNA
MS/MS	tandem mass spectrometry
MTA	metastasis-associated protein
NCL	nucleolin
NGC/CSPG5	neuroglycan C/chrondroitin sulfate proteoglycan 5
NGS	next-generation sequencing
NLS	nuclear localization sequence
NoLS	nucleolar localization sequence
NoDP	nucleolar detention pathway
NOR	nucleolar organizing region
NoRC	nucleolar remodeling complex
NSD1	nuclear receptor binding SET domain protein 1
NTAP	N-terminal TAP tag
NuRD	nucleosome remodeling and deacetylation (complex)
ORF	open reading frame
PAF	RNA polymerase associated factor
PARP	poly ADP ribose polymerase
PBS	phosphate buffered saline
PCAF	P300/CBP-associated factor
PCR	polymerase chain reaction
PHD	plant homeodomain
PHF6	PHD finger protein 6
PIC	pre-initiation complex
PLK1	polo-like kinase 1
PML	promyelocytic leukemia protein
PP1/2A	protein phosphatase 1/2A
pRB	retinoblastoma protein
PRC2	Polycomb repressor complex 2
PRDM	PR domain zinc finger protein
pre-rRNA	precursor rRNA
pRNA	promoter associated ribonucleic acid
PTM	post-translational modification
PVDF	polyvinylidene difluoride
PZP	PHD followed by a zinc knuckle with an atypical PHD
qPCR	quantitative PCR

RT	reverse transcription
rDNA	ribosomal DNA
RBBP	retinoblastoma binding protein
RIPA	radioimmunoprecipitation assay (buffer)
RNA	ribonucleic acid
RNA Pol	RNA polymerase
rRNA	ribosomal RNA
RPS6KA3	ribosomal protein S6 kinase, 90kDa, polypeptide 3
RUNX	runt-related transcription factor
S phase	DNA synthesis phase
SALL1	spalt-like transcription factor 1
SANT	SWI3, ADA2, N-CoR and TFIIIB DNA-binding domain
SDS-PAGE	sodium dodecyl sulfate-polyacrylamide gel electrophoresis
SET	Su(var)3-9, Enhancer of zeste, Trithorax
SETDB	SET domain, bifurcated
shRNA	short hairpin RNA
siRNA	small interfering RNA
SIN3	suppressor interacting 3
SIRT	sirtuin
SL1	selectivity factor 1
SNF2	sucrose non-fermenting 2
SNF2H	SNF2 homolog
snoRNA	small nucleolar RNA
SP	single positive ($CD4^+CD8^-$ or $CD4^-CD8^+$) thymocyte
SPARC	secreted protein, acidic, rich in cysteine
SRCAP	SNF2-related CREBBP activator protein
SWI/SNF	switch/sucrose non-fermenting
T-ALL	T-cell acute lymphoblastic leukemia
TAL1	T-cell acute lymphocytic leukemia protein 1
TAP	tandem affinity purification
TBP	TATA-binding protein
TBST	Tris-buffered saline with Tween 20
TCR	T-cell receptor
TDG	thymine DNA glycosylase
TET	ten-eleven translocation methylcytosine dioxygenase
TF	transcription factor
TIP5	TTF-I-interacting protein 5
TLX	T-cell leukemia homeobox
TSS	transcription start site
TTF-I	transcription termination factor I
UBF	upstream binding factor
UTR	untranslated region
VHL	von Hippel-Lindau protein
XLID	X-linked intellectual disability
XLMR	X-linked mental retardation
ZaP	zinc knuckle with atypical PHD

List of Figures

List of Tables

CHAPTER 1

General Introduction

1.1 CHROMATIN REMODELING MECHANISMS

Epigenetic mechanisms are responsible for regulating the structural composition of DNA to influence the means by which genetic information is, or is not, replicated or expressed in the form of RNA and protein. In eukaryotes, epigenetic factors are required to accommodate the compaction of all chromosomes within the nucleus, yet also to allow accessibility to DNA for transcription, replication, recombination, and repair. Moreover, epigenetics is responsible for the expression of different sets of genes not only between different tissues, but also throughout different time points during human development. To accomplish these levels of regulation, DNA is organized with RNA and protein into a macromolecular complex known as chromatin. The basic unit of chromatin is a nucleosome, consisting of a pair of each of the four histone proteins (H2A, H2B, H3, and H4), around which 147 bp of DNA is wrapped (Kornberg, 1974; Richmond and Davey, 2003). Both DNA and histones are covalently modified to designate transcriptionally inaccessible and accessible regions, known respectively as heterochromatin and euchromatin (Campos and Reinberg, 2009). The deposition of these activating and silencing marks provides binding sites for additional chromatin modifiers that can re-localize nucleosomes through ATP hydrolysis (Hargreaves and Crabtree, 2011). The faithful orchestration of these enzymatic mechanisms is essential during development, and when dysregulated, they contribute to developmental disease and the onset of cancer.

1.1.1 DNA methylation

DNA methylation refers to the covalent addition of a methyl group to cytosine at the carbon-5 position (5mC). Most commonly associated with transcriptional silencing, the 5mC mark is abundant throughout heterochromatin and can also be deposited in CpG

islands, which are present in about 70-80% of human gene promoters (Goll and Bestor, 2005). CpG islands contain a high amount of cytosine-guanine dinucleotides, with the cytosine being methylated on both the sense and antisense DNA strand. *De novo* DNA methyltransferases (DNMT3A, DNMT3B, DNMT3L) deposit the 5mC mark on unmethylated DNA templates, while DNMT1, which primarily methylates hemimethylated templates, is considered a maintenance DNMT (Liang et al., 2002; Okano et al., 1998; Ooi et al., 2007; Yoder et al., 1997). Without a maintenance DNMT, 5mC would otherwise be passively removed upon successive rounds of DNA replication.

Recently, a mechanism has emerged for the active erasure of 5mC as well, in particular with respect to the widespread demethylation that occurs in the zygotic paternal genome, after fertilization, and the primordial germ cells, during embryogenesis (Kohli and Zhang, 2013). Ten-eleven translocation methylcytosine dioxygenases (TETs) were reported to successively catalyze the oxidation of 5mC into 5-hydroxymethylcytosine (5hmC), 5-formylcytosine, and 5-carboxycytosine (Ito et al., 2011; Tahiliani et al., 2009). The oxidized 5mC marks are then proposed to be removed through base or nucleotide excision repair processes (He et al., 2011; Kohli and Zhang, 2013).

DNA methylation induces silencing both by preventing transcription factors from recognizing their nucleic acid target sequences, and also through the recruitment of proteins containing methyl-CpG binding domains (MBDs) (Klose and Bird, 2006; Watt and Molloy, 1988). MBD proteins, in turn, may either recruit repressive chromatin remodeling complexes (e.g. MBD1-SETDB1, NuRD) or induce chromatin condensation (e.g. MECP2) themselves (Georgel et al., 2003; Sarraf and Stancheva, 2004; Zhang et al., 1999). Interestingly, the mutually exclusive MBD2 and MBD3 have differential targeting

and developmental effects within the NuRD (nucleosome remodeling and deacetylation) complex. Unlike MBD2, MBD3 does not bind 5mC, but a recent study suggests that it may instead bind 5hmC (Saito and Ishikawa, 2002; Yildirim et al., 2011).

Defects in the deposition, removal, and recognition of genomic DNA methylation contribute to both germline and acquired human disease. Developmental diseases are associated with mutations in both DNMT3B (ICF syndrome) and MECP2 (Rett syndrome) genes (Amir et al., 1999; Ehrlich et al., 2001). Moreover, the loss both of 5mC and 5hmC, due to DNMT and TET mutations respectively, are hallmarks of cancer, and the resultant decondensation of repetitive heterochromatin leads to an increase in genomic instability (Plass et al., 2013). Additionally, defective DNA methylation often contributes to the hypermethylation of CpG islands in the promoters of tumour suppressors, causing them to be silenced through the inappropriate recruitment of MBD proteins (Lai and Wade, 2011; McCabe et al., 2009).

1.1.2 Covalent histone modifications

Within the nucleosome, histones contain globular domains around which DNA wraps, and tail domains to mediate interactions with both chromatin remodeling proteins and DNA (Alberts et al., 2002). Histones carry a net positive charge due to an abundance of lysine and arginine residues which facilitate their interaction with the negatively charged phosphodiester backbone of DNA. Tail domains interact with the minor groove of DNA but are subject to covalent modifications such as acetylation and methylation which reduce the electrostatic interactions with DNA and act as a platform for other protein-protein interactions (Bannister and Kouzarides, 2011). Moreover, the collection and location of these modifications on histones and within DNA are critical for

hierarchical regulation, constituting the histone code (Strahl and Allis, 2000). Indeed genome-wide chromatin immunoprecipitation (ChIP) screens with massively parallel sequencing (ChIP-Seq) indicates that the presence of specific histone PTMs can distinguish transcriptionally accessible and inaccessible regions of the genome, such as promoters (H3K4me2/3), elongated gene regions (H3K36me3), active regulatory elements (H3K9ac, H3K27ac), constitutive heterochromatin (H3K9me3), and silenced genes (H3K27me3) (Encode Project, 2012). Additional modifications (e.g. ADP ribosylation, phosphorylation, ubiquitylation, sumoylation, deimination, histone tail clipping), as well as the incorporation of histone variants and non-coding RNA, also contribute to chromatin regulation (Bannister and Kouzarides, 2011; Moran et al., 2012; Talbert and Henikoff, 2010). In the following paragraphs, I focus the discussion on the proteins that write, read, and erase the histone acetylation and methylation marks.

Histone lysine residues are acetylated by histone acetyltransferase (HAT) enzymes (e.g. P300, PCAF, TIP60, HBO1), using acetyl-CoA as a cofactor, and the removal of this mark is catalyzed by histone deacetylases (HDACs) (e.g. HDAC1/2, SIRT2) (Kouzarides, 2007). Each nucleosomal histone subunit is capable of being acetylated and the deposition of this PTM contributes to the decondensation of chromatin by removing positive charges from lysine residues, which correlates with the reduced association of histone tails with linker DNA, fewer internucleosomal contacts, and a reduction in the higher order packaging of chromatin (Shahbazian and Grunstein, 2007). HDACs, on the other hand, are generally considered to contribute to the spread of heterochromatin silencing (Shahbazian and Grunstein, 2007). However, histone deacetylation is also necessary in advance of the deposition of additional PTMs at lysine

residues, such as histone methylation, which may themselves be active or repressive. In embryonic stem cells, for instance, NuRD is recruited to deacetylate H3K27 (via HDAC1/2), in advance of Polycomb Repressor 2 (PRC2)-mediated H3K27 methylation (via EZH2) (Reynolds et al., 2012b).

Histone lysine methyltransferases (KMTs) achieve their enzymatic activity using SET (Su(var)3-9, Enhancer of zeste, Trithorax) domains to catalyze the addition of methyl groups derived from S-adenosylmethionine to the ε-amino group of lysine (Bannister and Kouzarides, 2011). Collectively, KMTs permit four binding states: unmethylated, monomethylated, dimethylated, and trimethylated lysine. SET proteins include KMTs such as MLL1-4 (modification: H3K4me1/2/3), SUV39H1 (H3K9me2/3), G9A (H3K9me1/2), SETDB1 (H3K9me1/2/3), EZH1/2 (H3K27me2/3), SETD2 (H3K36me1/2/3), NSD1 (H3K36me1/2), and SUV420H1/2 (H4K20me2/3) (Greer and Shi, 2012). DOT1L is also a non-SET KMT that methylates H3K79 following H2BK123 mono-ubiquitylation (McGinty et al., 2008; Min et al., 2003a). Conversely, histone lysine demethylation (KDM) is achieved by LSD1 (substrates: H3K4me1/2, H3K9me2) and by a family of proteins containing the Jumonji C (JmjC) domain (Shi et al., 2004; Tsukada et al., 2006). Among the JmjC demethylases, and demethylated substrates, that have been identified include JARID (H3K4me2/3), JMJD1 (H3K9me1/2/3), JMJD2 (H3K9me2/3, H3K36me2/3), JMJD3 (H3K27me2/3), UTX (H3K27me2/3), FBXL (H3K361/2), PHF8 (H3K9me1/2, H4K20me1), and PHF2 (H3K9me2, H4K20me3) (Baba et al., 2011; Greer and Shi, 2012; Lee et al., 2007; Stender et al., 2012).

Several interaction domains have been identified for the recognition of post-translational histone modifications (see Table 1-1). Bromodomains are the only known

Table 1-1. Chromatin remodeling recognition domains for binding to chromatin that has been covalently modified by DNA methylation, histone acetylation, or histone methylation.[1]

	Domain	Modification	Writer	Eraser
DNA methylation	MBD	5-methylcytosine	DNMT1, DNMT3A/B/L	TET1-3
		5-hydroxymethylcytosine[2]	TET1-3	TDG, GADD45A (?)
Histone acetylation	Bromo	H2Aac, H2Bac H3ac, H4ac	P300, PCAF, TIP60, HBO1	HDAC1-11, SIRT1-7
Histone methylation	PHD	H3K4me3 (BPTF, ING2, RAG2)	MLL1-4, SETD1, ASH1L, SMYD3, PRMD9	JARID
		H3K4me2 (PYGO2) H3K4me0 (PHF21A)	MLL1-4, SETD1, SMYD3	LSD1
		H3K4me0/H3K9me3 (CHD4)[3]	SUV39H, SETDB1, PRDM2	JMJD1, JMJD2
	ADD[4]	H3K4me0/H3K9me3 (ATRX, DNMT3B, DNMT3L)	SUV39H, SETDB1, PRDM2	JMJD1, JMJD2
	CHD[5]	H3K9me3 (HP1, Cbx7)	SUV39H, SETDB1, PRDM2	JMJD1, JMJD2
		H3K27me3 (dPC, Cbx7)	EZH1, EZH2	JMJD3, UTX
	TUDOR	H3K4me3 (JMJD2A)	MLL1-4, SETD1, ASH1L, SMYD3, PRMD9	JARID
		H4K20me1/2 (JMJD2, 53BP1)	SETD8, PR-SET7	PHF8
	WD40 β-propeller	H3K27me3 (EED)[6]	EZH1, EZH2	JMJD3, UTX
	PWWP[7]	H3K36me3 (DNMT3A)	SETD2	JMJD2
		H4K20me3 (Pdp1)	SUV420H1, SUV420H2	PHF2
	MBT	H4K20me1/2 (L3MBTL1)	SETD8, PR-SET7	PHF8

[1] Table adapted from (Adams-Cioaba and Min, 2009; Greer and Shi, 2012; Kohli and Zhang, 2013; Kouzarides, 2007)
[2] (Yildirim et al., 2011)
[3] (Mansfield et al., 2011)
[4] (Eustermann et al., 2011; Iwase et al., 2011; Zhang et al., 2010a)
[5] (Bernstein et al., 2006; Min et al., 2003b)
[6] (Xu et al., 2010a)
[7] (Dhayalan et al., 2010; Qiu et al., 2012)

structure that binds acetylated lysine residues (Dhalluin et al., 1999). Histone methylation can be recognized by zinc finger domains, such as the PHD domain and the ADD domain. The structure of the PHD domain (C_4HC_3 zinc finger) is variable among proteins as several binding substrates have been identified among different proteins including ING2 and BPTF (binds: H3K4me3), PYGO (H3K4me2), PHF21A (H3K4me0), and CHD4 (H3K4me0/H3K9me3) (Adams-Cioaba and Min, 2009; Mansfield et al., 2011; Shi et al., 2006). Another set of domains that recognize histone methylation include members of Royal Family, such as Tudor domains, chromodomains, WD40 β-propeller domains, PWWP domains, MBT domains (Adams-Cioaba and Min, 2009; Qin and Min, 2014; Xu et al., 2010a). Variation among the binding substrates are observed in this group as well, including recognition of methylated H3K9 by the chromodomain of heterochromatin protein 1 (HP1), the binding of JMJD2A to H3K4me3 and H4K20me3 through its Tudor domain, and the binding of L3MBTL1 to H4K20me1/2 through its MBT domain (Adams-Cioaba and Min, 2009; Jacobs and Khorasanizadeh, 2002).

Any given nucleosome is likely to have multiple PTMs, and this crosstalk can influence the binding of chromatin regulators. For instance, the ATRX ADD domain requires both H3K4me0 and H3K9me3 (Eustermann et al., 2011; Iwase et al., 2011). In addition, many chromatin remodelers have binding domains for multiple substrates, such as P300, which contains both a Bromodomain and a PHD domain (Ragvin et al., 2004). Moreover, histone PTMs work in concert with multiple interactions to initiate further modifications. The NuRD complex, for example, binds 5mC through MBD2, H3K4me0/H3K9me3 through the PHD domain of CHD4, and DNA sequences through MTA transcription factor subunits (Lai and Wade, 2011; Mansfield et al., 2011). NuRD

subsequently catalyzes histone demethylation with LSD1, histone acetylation with HDAC1/2, and ATP-dependent nucleosome remodeling with CHD4. Thus, through the recruitment, coordination, and feedback with activating or silencing catalytic processes, accessible or inaccessible chromatin can be specified through histone PTMs.

1.3 Chromatin remodeling complexes in human disease

With DNA methylation and histone PTMs establishing activating and silencing signatures, active changes in nucleosome distribution are still required for localized processes such as transcription and also to induce changes in higher order chromatin structure. Enzymes known as ATP-dependent nucleosome remodelers accomplish this task through the use of their DEAD/H box helicase domain which hydrolyzes ATP, yielding the necessary energy to disrupt nucleosome-DNA interactions and redistribute the nucleosomes via sliding, removal, or exchange mechanisms (Hargreaves and Crabtree, 2011). In humans, 27 ATP-dependent nucleosome remodelers are known and subdivided into four major families: SWI/SNF (e.g. BRG1, ATRX), ISWI (e.g. SNF2H), CHD (e.g. CHD4), and INO80/SWR1 (e.g. SRCAP), with the majority incorporated into multiprotein complexes (e.g. NuRD) (Hargreaves and Crabtree, 2011). Like other enzymatic regulators of chromatin, most ATP-dependent chromatin remodelers have at least one binding domain (e.g. SANT, Bromodomain, PHD), which allows for an interaction with DNA and/or nucleosomes (Hargreaves and Crabtree, 2011).

Mutations in the chromatin remodeling marks responsible for depositing histone PTMs, as well as interactions with PTMs and the relocalization of nucleosomes, have long been associated in the etiologies of human developmental disease (van Bokhoven, 2011). More recently, the high-throughput screening of various cancer genomes using

next-generation screening technologies (e.g. Roche/454, Illumina/Solexa), has yielded mutations in many of these same epigenetic regulators (see Table 1-2) (Baylin and Jones, 2011; Metzker, 2010; Plass et al., 2013). These mutations target ATP-dependent nucleosome remodelers (ATRX), KMTs (EZH2, JARID1C, MLL2, NSD1), KDMs (ARID1B, JARID1C), HATs (CBP), histone kinases (RPS6KA3), DNMTs (DNMT3A/B), and proteins that interface with chromatin (BCOR, MECP2, PHF6). In some instances, the cancerous mutations are identical to germline mutations (e.g. EZH2) (Brookes and Shi, 2014). In others, (e.g. ATRX), developmental mutations appear to be hypomorphic, while cancer mutations are more frequently truncating (Jiao et al., 2011).

The dysregulation of epigenetic mechanisms is an early event in the onset of tumorigenesis (Baylin and Jones, 2011; Feinberg et al., 2006; Plass et al., 2013; Suva et al., 2013; You and Jones, 2012). These defects are somatically inherited and contribute toward widespread genomic instability that can accelerate the occurrence of additional mutagenic events (Baylin and Jones, 2011). Indeed, the global deregulation of DNA methylation is an early event in almost all tumours, including those that are benign (Feinberg et al., 2006; Suva et al., 2013). Moreover, PRC2 is commonly hyperactivated in cancer, leading to upregulation of the H3K27me3 silencing mark (Baylin and Jones, 2011). Thus, the epigenetic reprogramming that occurs during tumorigenesis takes advantage of the enzymes mediating both DNA methylation and covalent histone modification. However, some of the proteins in Table 1-2, including PHF6, lack the catalytic domains necessary for establishing such modifications, yet are still predicted to interact with chromatin through conserved binding domains. To better understand the role of such proteins in disease, additional functional characterization is required.

Table 1-2. Chromatin remodeling proteins that are both germline mutated in developmental disease and somatically mutated in cancer.

Gene	Function	Developmental disease	Type of tumour	Reference
ARID1B	Histone lysine demethylase	Coffin-Siris syndrome	Breast	(Stephens et al., 2012; Wieczorek et al., 2013)
ATRX	SNF2 chromatin remodeling protein	ATR-X syndrome	Glioblastoma, Pancreatic, Myelodysplasia	(Gibbons et al., 1995; Gibbons et al., 2008; Jiao et al., 2011; Schwartzentruber et al., 2012)
BCOR	Histone binding	Oculofaciocardiodental syndrome	AML	(Grossmann et al., 2011; Ng et al., 2004)
CREBBP	Histone acetyltransferase	Rubinstein-Taybi syndrome	AML	(Borrow et al., 1996; Petrij et al., 1995)
DNMT3	DNA methyltransferase	ICF syndrome	AML	(Cancer Genome Atlas Research, 2013; Ehrlich et al., 2001)
EZH2	Histone lysine methyltransferase	Weaver syndrome	Lymphoma	(Gibson et al., 2012; Morin et al., 2010)
JARID1C	Histone lysine demethylase	Syndromic XLID	Renal	(Dalgliesh et al., 2010; Jensen et al., 2005)
MECP2	Binds methylated DNA	Rett syndrome	Multiple cancers	(Amir et al., 1999; Plass et al., 2013)
MLL2	Histone lysine methyltransferase	Kabuki syndrome	Medulloblastoma	(Ng et al., 2010; Parsons et al., 2011)
NSD1	Histone lysine methyltransferase	Sotos syndrome	AML	(Jaju et al., 2001; Kurotaki et al., 2002)
PHF6	PHD-like domains	Börjeson-Forssman-Lehman syndrome	AML, T-ALL	(Borjeson et al., 1962; Van Vlierberghe et al., 2010; Van Vlierberghe et al., 2011)
RPS6KA3	Serine/threonine histone kinase	Coffin-Lowry syndrome	Prostate	(Clark et al., 2005; Trivier et al., 1996)

1.2 THE MOLECULAR GENETICS OF *PHF6*

Mutations in genes that encode chromatin remodeling proteins (e.g. *ATRX*, *JARID1C*, *MECP2*, *RPS6KA3*) are an underlying cause of many X-linked intellectual disability (XLID) syndromes (Amir et al., 1999; Chiurazzi et al., 2008; Gibbons et al., 1995; Jensen et al., 2005; Picketts et al., 1996; Trivier et al., 1996). While cognitive impairments are a defining phenotype of XLID, many of these syndromes also feature developmental abnormalities in other tissues (Stevenson et al., 2013). One such XLID is Börjeson-Forssman-Lehman syndrome (BFLS, MIM #301900), which has primarily been described in males (Gecz et al., 2006). The BFLS phenotype was first reported a half century ago (Borjeson et al., 1962) and in 1996, the responsible gene was mapped to the Xq26-27 chromosomal region (Gedeon et al., 1996; Mathews et al., 1989; Turner et al., 1989). In 2002, *PHD finger protein 6* (*PHF6*) mutations were identified as the cause of BFLS (Lower et al., 2002). More recently, *PHF6* mutations have also been identified in T-cell acute lymphoblastic leukemia (T-ALL) and acute myeloid leukemia (AML) patients (Van Vlierberghe et al., 2010; Van Vlierberghe et al., 2011). In order to better understand the contribution of *PHF6* mutations to the respective etiologies of BFLS, T-ALL, and AML, the structural and functional features of PHF6 will first be reviewed.

1.2.1 PHF6 structural features and functional studies in animal models

PHF6 (Gene ID: 84295) consists of 11 exons and is transcribed into a 4.5 kb mRNA (see Figure 1-1A). Exons 2-10 encode a 365 amino acid (41 kDa) protein (Uniprot: Q8IWS0) (see Figure 1-1B), while exons 1 and 11 comprise the 5’ and 3’ UTRs respectively. Two mRNA isoforms exist in humans, with the second incorporating

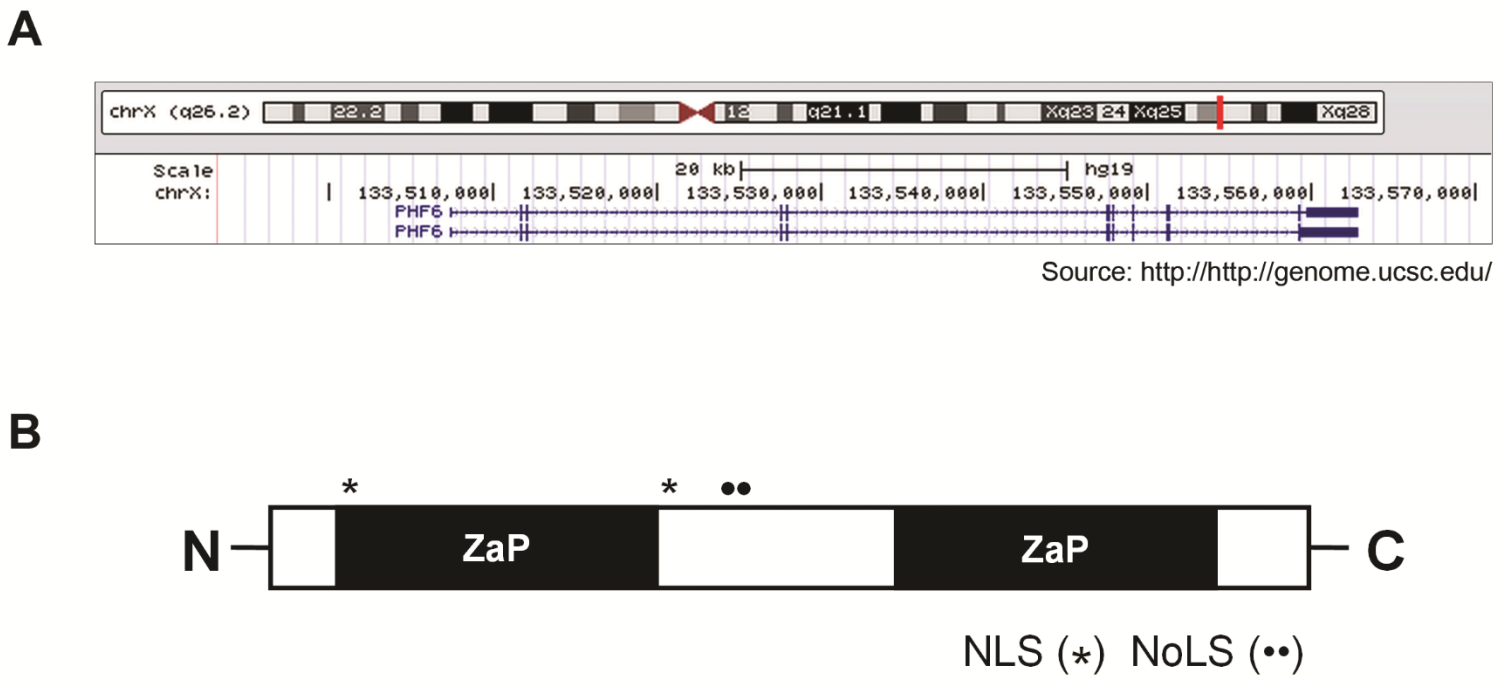

Figure 1-1. Schematic of the human *PHF6* gene structure and its protein product.
(A) The human *PHF6* gene (Gene ID: 84295) is situated at Xq26.2 (133.51 to 133.56 Mb of the human GRCh37/hg19 assembly, February 2009). Two alternative transcripts have been identified and are shown, consisting of 11 or 10 exons respectively, indicated by the blue lines. In the first transcript (above), the 5' and 3' UTRs are encoded by exons 1 and 11 respectively. In the second transcript (below), exon 10 incorporates intron 10 and exon 11 from the first transcript, with the 3' UTR sequence remaining unchanged. Screen shot generated using the UCSC Genome Browser (Kent et al., 2002).
(B) PHF6 is a 365 amino acid protein (Uniprot: Q8IWS0). The locations of the ZaP domains (Zn knuckle followed by an atypical PHD), as well as the nuclear (NLS) and nucleolar (NoLS) localization sequences, are indicated.

intron 10 to increase the size of the 3' UTR (Lower et al., 2002). A third isoform is predicted to encode a truncated 312 amino acid version of the PHF6 protein, but its existence has not been confirmed experimentally (Gerhard et al., 2004).

The PHF6 protein is highly conserved among vertebrates, with 97.5% amino acid identity between humans and mice. Invertebrates do not have a *PHF6* homolog. Structural features of PHF6 include two nuclear localization sequences (NLSs), a nucleolar localization sequence (NoLS), and two zinc finger domains (Figure 1-1B). The localization of PHF6 to the nucleus and nucleolus has been confirmed by immunocytochemistry in NIH 3T3 cells, immunofluorescence of GFP-tagged PHF6 in HeLa cells, and by mass spectrometry profiles of the protein content within different subcellular compartments (Ahmad et al., 2009; Boisvert et al., 2012; Landais et al., 2005; Lower et al., 2002; Vallee et al., 2004). In mice, the loss of both NLSs and the NoLS results in the nuclear, but not nucleolar, localization of PHF6, suggesting the presence of additional interactions that recruit PHF6 to the nucleoplasm (Landais et al., 2005).

Structurally, the most prominent features of PHF6 are its two nearly identical zinc finger domains that are derived from a PZP motif (Perry, 2006). PZP motifs consist of PHD domain, followed by a zinc knuckle, followed by an atypical PHD domain However, each zinc finger domain of PHF6 is a degenerate version of this structure as they consist only of the zinc knuckle and the atypical PHD (ZaP) (Todd and Picketts, 2012). In humans, ZaP domains are primarily found in proteins that regulate chromatin (e.g. MLL, BRPF, JMJD2) and are further discussed in Chapter 3 (see Figure 3-1).

To date, no *Phf6* animal knockout models have been published and only one study records its gene expression patterns during embryonic and postnatal mouse development.

In these mice, *Phf6* was observed to be ubiquitous, with particularly high expression in the brain and CNS throughout embryonic development, and more moderately during post-natal development and in adult tissue (Voss et al., 2007). *Phf6* was highly expressed in other embryonic tissues also, including the anterior pituitary at E12.5, nasal processes at E9.5 to E12.5, pharyngeal arches at E9.5, and limb buds at E12.5. In humans, *PHF6* is highly expressed in adult B- and T-lymphoid cells (Van Vlierberghe et al., 2011). Indeed, another study identified high *Phf6* expression levels in murine T-cell lymphoma (Landais et al., 2005). Thus collectively, these expression studies seem to indicate a greater requirement for Phf6 in proliferating cells than in post-mitotic cells.

While mapping *Phf6* gene expression patterns is informative, the underlying etiology of BFLS cannot be fully understood without functionally characterizing the molecular pathways within which Phf6 participates. Towards this end, PHF6 interaction studies were performed (see Chapter 3), describing its interaction with the NuRD complex, a chromatin remodeling regulator that contributes to lineage commitment (Reynolds et al., 2012a; Todd and Picketts, 2012). More recently, Phf6 was also found to interact with the Paf1 transcriptional elongation complex and be responsible for mediating neurogenesis in mice (Zhang et al., 2013). In this study, *Phf6* and *Paf1* shRNA was electroporated into mouse cerebral cortices, resulting in impaired neuronal migration between E14 and E19. Using gene expression arrays, the authors identified *Neuroglycan C/Chrondroitin Sulfate Proteoglycan 5* (*NGC/CSPG5*) as a commonly regulated target gene, and when the *NGC/CSPG5* transcript was electroporated into cortical tissue alongside *Phf6* shRNA, the neuronal migration phenotype was rescued (Zhang et al., 2013). Taken together, the results reported by Zhang et al. are consistent with the high

Phf6 expression observed by Voss et al. in the embryonic brain, and the contribution of PHF6 towards neuronal migration during neurogenesis may partially account for the intellectual disability phenotype in BFLS patients.

1.2.2 PHF6 mutations in Börjeson-Forssman-Lehmann syndrome

The majority of BFLS cases described in the literature occur in males who display developmental delay within their first year after birth, with mild to severe intellectual disability becoming apparent during childhood and adolescence (Gecz et al., 2006; Turner et al., 2004). Additional features of the BFLS phenotype include large ears, coarse facial features (e.g. deep set eyes), long tapered fingers, syndactyly and shortening of the toes, gynaecomastia, truncal obesity, hypogonadism, hypotonia, and feeding problems during infancy. Some features are present at birth (e.g. hypogonadism), however other aspects of the phenotype present themselves during childhood and adolescence (e.g. coarse facial features, truncal obesity). Gynaecomastia in particular emerges during adolescence, although it is unclear if it is caused by breast tissue hyperplasia or lipomastia (Carter et al., 2009). Less common features of BFLS include microcephaly/macrocephaly, short stature, epilepsy, cleft lip and palate, hearing impairment, and hypopituitarism (Gecz et al., 2006). Two independent probands have also been diagnosed with bone marrow cancers, including Hodgkin's lymphoma and T-ALL (see Chapter 2) (Carter et al., 2009; Chao et al., 2010).

PHF6 mutations that cause BFLS include missense mutations, nonsense mutations, and deletions (see Table 1-3). To date, no other mutations are known to cause BFLS, however not all BFLS patients have an identified *PHF6* mutation. In one cohort, for instance, *PHF6* mutations were only identified in 5/25 patients, indicating that there

Table 1-3. PHF6 mutations associated with developmental intellectual disability.

Gender	Nucleotide change	Amino acid change	Type of mutation	Location of mutation	Cancer	Isolated[3]/ *De novo*	Reference
M	c.2T>C	p.M1T	Missense	Exon 2			(Lower et al., 2002)
M	c.2T>C	p.M1T	Missense	Exon 2			(Crawford et al., 2006)
M	c.134G>A	p.C45Y	Missense	Exon 2			(Lower et al., 2002)
M	c.134G>A	p.C45Y	Missense	Exon 2		Isolated	(Lower et al., 2002)
M	c.266G>T	p.G89V	Missense	Exon 4			(Mangelsdorf et al., 2009)
M	c.296G>T	p.C99F	Missense	Exon 4		Isolated	(Lower et al., 2002)
M, F	c.686A>G	p.H229R	Missense	Exon 7			(Lower et al., 2002)
M	c.700A>G	p.K234E	Missense	Exon 7			(Lower et al., 2002)
M	c.769A>G	p.R257G	Missense	Exon 8			(Lower et al., 2002)
M	c.769A>G	p.R257G	Missense	Exon 8	Yes[2]	Isolated	(Vallee et al., 2004)
M	c.940A>G	p.I314V	Missense	Exon 9			(Crawford et al., 2006)
M	c.22A>T	p.K8*	Nonsense	Exon 2			(Lower et al., 2002)
F	c.955C>T	p.R319*	Nonsense	Exon 9		De novo	(Zweier et al., 2013)
M	c.1024C>T	p.R342*	Nonsense	Exon 10		De novo	(Borjeson et al., 1962; Gecz et al., 2006)
M	c.1024C>T	p.R342*	Nonsense	Exon 10			(Lower et al., 2002)
M	c.1024C>T	p.R342*	Nonsense	Exon 10			(Lower et al., 2002)
M	c.1024C>T	p.R342*	Nonsense	Exon 10			(Lower et al., 2002)
M	c.1024C>T	p.R342*	Nonsense	Exon 10	Yes[3]		(Chao et al., 2010)
F	c.27dupA	p.G10fs*21	Frameshift	Exon 2		De novo	(Crawford et al., 2006)
M	IVS2-8A>G	M46fsΔexon3	Frameshift	Exon 3			(Vallee et al., 2004)
F	c.677delG	p.G226fsE*53	Frameshift	Exon 7		De novo	(Wieczorek et al., 2013)
F	c.914G>T	p.C305F	Frameshift	Exon 9		De novo	(Wieczorek et al., 2013)
F			Duplication	Exons 4-5		De novo	(Zweier et al., 2013)
F			Duplication	Exons 4-5		De novo	(Zweier et al., 2013)
F	6 kb deletion		Deletion	Exons 4-5		De novo	(Zweier et al., 2013)
F	100 kb deletion		Deletion	Exons 6-10		De novo	(Di Donato et al., 2014)
F	15 kb deletion		Deletion	Exons 9-11		De novo	(Berland et al., 2011)
M	c.999-1001 delTGA	p.D333del	Deletion	Exon 10			(Baumstark et al., 2003)
M	c.999-1001 delTGA	p.D333del	Deletion	Exon 10			(Borjeson et al., 1962; Gecz et al., 2006)
F	Entire gene deleted		Deletion	Whole gene		De novo	(Zweier et al., 2013)
F	270 kb deletion		Deletion	Whole gene		Isolated	(Di Donato et al., 2014)

[1] Isolated refers to instances where the parents have not been screened for *PHF6* mutations.
[2] Hodgkin's lymphoma
[3] T-cell acute lymphoblastic leukemia

could be additional BFLS loci, or more likely, that the clinical diagnosis of BFLS overlaps with other syndromes (Crawford et al., 2006).

BFLS with mild intellectual disability caused by a *de novo PHF6* mutation was described in one female patient (Crawford et al., 2006). In other BFLS families, female carriers were described as having mild to no intellectual disability. However, recent studies have identified *PHF6* mutations in female patients who exhibit more severe intellectual disability and a distinctive phenotype in comparison to classical BFLS features (Berland et al., 2011; Di Donato et al., 2014; Wieczorek et al., 2013; Zweier et al., 2013; Zweier et al., 2014). Features of this "female BFLS" phenotype overlap with Coffin-Siris syndrome and include sparse hair, deep set eyes, hypoplasia of the fifth digit, linear skin hyperpigmentation, and dental abnormalities (Di Donato et al., 2014). The female BFLS phenotype can be distinguished from male BFLS by the absence of truncal obesity and syndactyly occurring between the third and fifth toes, rather than between the second and third toes (Di Donato et al., 2014; Zweier et al., 2013).

In Table 1-3, *de novo* mutations associated with the female BFLS phenotype are mostly deletions, whereas male BFLS patients more commonly have point mutations. Moreover, female carriers that lack linear skin hyperpigmentation still exhibit a phenotype that more closely resembles male BFLS than the novel female BFLS phenotype (Zweier et al., 2014). The linear skin hyperpigmentation is also a distinguishing feature between female BFLS and Coffin-Siris syndrome, and Zweier et al. argue that its presence is indicative of functional mosaicism in establishing the female BFLS phenotype (Zweier et al., 2014). In support of this claim, Zweier et al. report that

the rates of X-chromosome inactivation are variable between different tissues in patients expressing the female BFLS phenotype.

1.2.3 PHF6 mutations in T-cell acute lymphoblastic leukemia

Somatic *PHF6* mutations have also been recently identified in T-ALL (see Chapter 2) (Chao et al., 2010; Van Vlierberghe et al., 2010). Van Vlierberghe and colleagues reported *PHF6* mutations in 16% of pediatric and 38% of adult subjects. These mutations overwhelmingly consisted of deletions, frameshifts, nonsense mutations, or missense mutations that target zinc ion stabilizing residues in the second ZaP domain. In four additional studies, other groups have identified T-ALL-related *PHF6* mutation frequencies varying from 5% to 40% within each cohort (Grossmann et al., 2013; Huh et al., 2013; Wang et al., 2011; Yoo et al., 2012). While Van Vlierberghe et al. reported a significantly higher incidence of PHF6 mutations among males, significant gender differences were not observed in these later studies.

T-ALL arises in immature T-cells of the lymphoid lineage (see Figure 1-2A). During normal development (reviewed in Janeway, 2005), immature thymocytes are derived from hematopoietic progenitors migrating from bone marrow to the thymus, where they develop into immature CD4/CD8 double negative (DN), double positive (DP), and single positive (SP) thymocytes (Figure 1-2B). DN stages 1-4 can be distinguished from one another by quantifying the expression of cell surface markers (e.g. CD25, CD44, CD117) through immunophenotyping (Maecker et al., 2012). Thymocyte maturation proceeds through selection events that follow VDJ recombination of the β and α T-cell receptors (TCRs). Failure to proceed past these checkpoints (i.e. β selection, -/+ selection) results in apoptosis, with the surviving cells undergoing extensive proliferation.

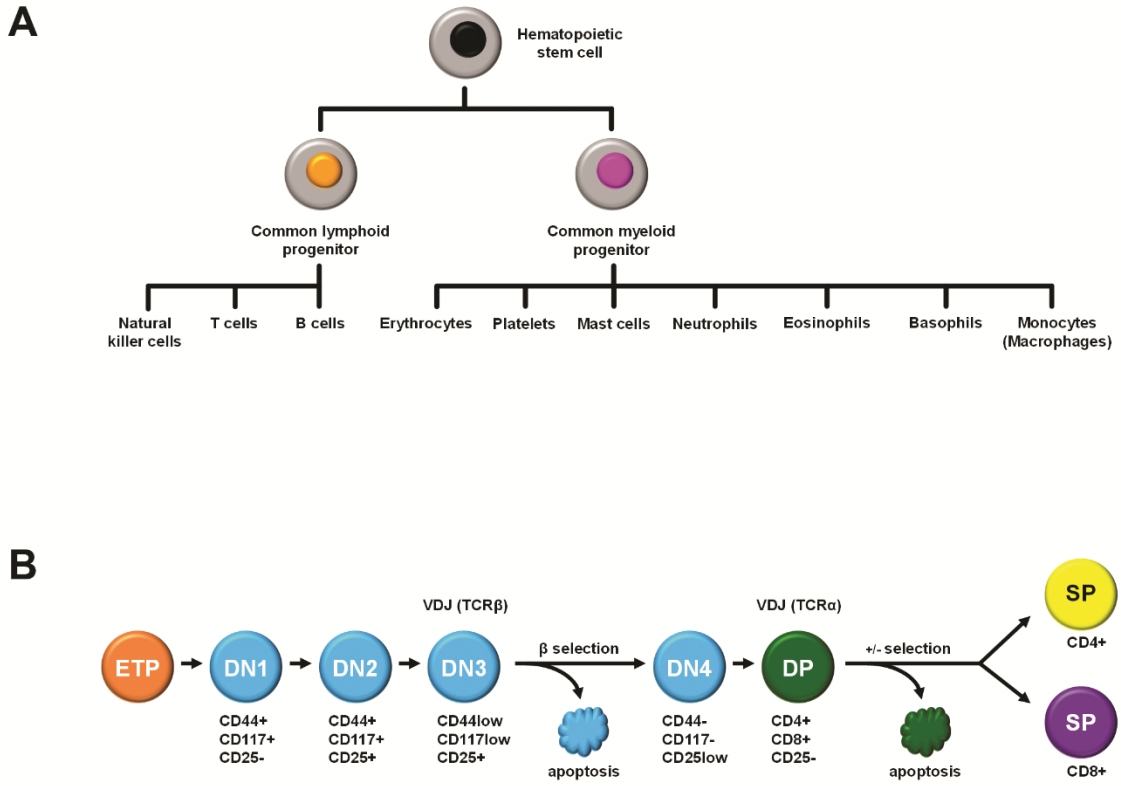

Figure 1-2. Schematic of hematopoiesis and thymocyte maturation.
(A) Differentiation of the lymphoid and myeloid lineages. (B) Differentiation of αβ T cells from an early thymic progenitor (ETP) into DN (double negative, $CD4^{-}CD8^{-}$), DP (double positive, $CD4^{+}CD8^{+}$), and SP (single positive, $CD4^{+}CD8^{-}$ or $CD4^{-}CD8^{+}$) thymocytes. Cell surface markers for each stage are indicated. VDJ recombination of the β and α TCR (T-cell receptor) precedes the β selection and positive selection events respectively. Figures adapted from (Janeway et al., 2005; Naito et al., 2011; Yui and Rothenberg, 2014).

Many of the mutations contributing to T-ALL involve oncogenic translocation events at the TCR loci and tumours are considered to be developmentally arrested when oncogenesis occurs (Van Vlierberghe and Ferrando, 2012).

T-ALL mutations are categorized in two groups: (i) those that initiate oncogenesis and define the molecular-genetic subtype of the tumour, and (ii) mutations that are recurrent (Van Vlierberghe and Ferrando, 2012). Major T-ALL subtypes are defined by aberrant oncogenic activation or chromosomal translocation events in genes coding for bHLH proteins (e.g. TAL1), LMO proteins (e.g. LMO1), homeobox proteins (e.g. TLX1, TLX3), or proto-oncogenes (e.g. c-MYB), while recurrent mutations target cell signaling pathways (e.g. NOTCH1, signal transduction), cell cycle regulatory mechanisms, and tumour suppressors (i.e. for inactivation) (Van Vlierberghe and Ferrando, 2012).

Interestingly, *PHF6* mutations are associated with tumours expressing the *TLX1* and *TLX3* oncogenes (Van Vlierberghe et al., 2010). Consistent with this observation, *PHF6* is highly expressed in DP cells, the stage at which *TLX1*-induced tumours most commonly experience developmental arrest (Ferrando et al., 2002; Van Vlierberghe et al., 2010). Moreover, *PHF6* has also been demonstrated to be a direct target for *TLX1*-mediated repression (De Keersmaecker et al., 2010). *PHF6* mutations are also co-expressed with JAK1 mutations, SET-NUP214 translocations, and activating *NOTCH1* mutations (Huh et al., 2013; Wang et al., 2011). Activating *NOTCH1* mutations occur in over half of all T-ALL patients and *PHF6* has previously been shown to be one of its downstream targets through ChIP (Palomero et al., 2006; Weng et al., 2004). Furthermore, *PHF6* is silenced by other mechanisms in T-ALL, such as oncogenic microRNAs (miR-20a, miR-26a, and miR-128-3p) and by DNA methylation in its

promoter (Kraszewska et al., 2012; Mavrakis et al., 2011; Mets et al., 2014). Collectively, these data illustrate a role for *PHF6* as a tumour suppressor during T-cell development.

1.2.4 PHF6 mutations in acute myeloid leukemia

PHF6 mutations have also been identified in AML patients (Van Vlierberghe et al., 2011). AML is a heterogeneous cancer that develops in multiple progenitor cell types of the myeloid lineage (see Figure 1-2A). Recent profiling of the AML cancer genome with next-generation sequencing has demonstrated that most AML mutations are recurrent, consisting primarily of chromosomal translocation events at specific loci and targeted mutations among a group of 23 genes, including epigenetic regulators such as DNMT3A, TET2, and RUNX1 (Cancer Genome Atlas Research, 2013). Van Vlierberghe et al. found *PHF6* mutations in 10/353 patients, with only one female. Similar to T-ALL, *PHF6* mutations primarily consisted of deletions, frameshifts, nonsense mutations and missense mutations targeting zinc ion-stabilizing residues from the second ZaP domain. Additional AML screens by other groups found *PHF6* mutations within 3% of screened tumours (Cancer Genome Atlas Research, 2013). Additionally, *PHF6* mutations correlated with reduced overall survival in adult patients and were observed to be co-expressed with *RUNX1* mutations (Cancer Genome Atlas Research, 2013; Patel et al., 2012). As of yet, tumours expressing *PHF6* mutations have not been correlated with any specific myeloid progenitor cell type, however *PHF6* expression levels were observed to be higher in hematopoietic stem cells and megakaryocyte/erythroid progenitors than in common myeloid progenitors or granulocyte/macrophage progenitors (Van Vlierberghe et al., 2011). It should be noted that in addition to mutations in AML, there is an isolated

report of *PHF6* mutations arising in chronic myeloid leukemia (CML) patients undergoing blast crisis (Li et al., 2013).

1.2.5 Understanding how PHF6 mutations contribute to BFLS, T-ALL, and AML

In BFLS, attempts to identify genotype-phenotype correlations between specific *PHF6* mutations and the severity of intellectual disability have not been successful (Carter et al., 2009; Zweier et al., 2014). Regardless, the distribution of mutations across the entire *PHF6* gene suggests that the phenotypes arise from a loss of PHF6 function. Given the prevalence and occurrence of common sites of PHF6 mutations in T-ALL and AML patients with those that have BFLS (e.g. R342X), it is surprising that not all BFLS patients develop leukemia. Towards this end, Chapter 2 describes a BFLS patient that acquired T-ALL.

Additionally, murine *Phf6* expression patterns (e.g. brain/CNS, embryonic limb buds) and high *PHF6* expression in human DP thymocytes correlate with the onset of BFLS and T-ALL respectively (Van Vlierberghe et al., 2010; Voss et al., 2007). To better understand the molecular mechanisms by which PHF6 may execute its function in these or other tissues, I identified PHF6 interaction partners in Chapter 3.

1.3 EPIGENETIC REGULATION OF rRNA SYNTHESIS IN THE NUCLEOLUS

1.3.1 Background

First described by Felice Fontana in 1781, the nuclear body responsible for producing the ribosomes upon which the process of translation depends was termed the "nucleolus" (meaning: little nucleus) by Gustav Valentin in 1839, as recounted by an early literature review that provided an extensive overview of nucleolar morphology across several organisms (Montgomery, 1898). Within these collected observations, many of the key properties of the nucleolus had already become apparent, including its lack of a membrane, its increased density relative to the nucleoplasm, and the dispersal of its material into chromatin when the nucleolus disappears at the onset of mitosis.

Further understanding of the reemergence of nucleoli during late mitosis occurred in 1934, when Barbara McClintock described their points of origin on mitotic maize chromosomes as nucleolar organizing bodies or regions (NORs) (McClintock, 1934). In *Drosophila*, NORs were later demonstrated to originate from DNA sites with homology to rRNA (Ritossa and Spiegelman, 1965), confirming earlier suspicions of nucleolar involvement in ribosome biogenesis (Perry, 1962). These so-called rDNA genes were found to exist as tandem repeats and in humans, are localized on the short arms of the five acrocentric chromosomes (13, 14, 15, 21, and 22) (Henderson et al., 1972), where approximately 300-400 rDNA genes occupy the region between the telomere and the centromere in a head-to-tail formation. Each rDNA gene consists of a 13.3 kb coding sequence, flanked by a 30 kb intergenic spacer (IGS) region (see Figure 1-3).

In the ensuing decades, many steps of nucleolus-mediated ribosome biogenesis

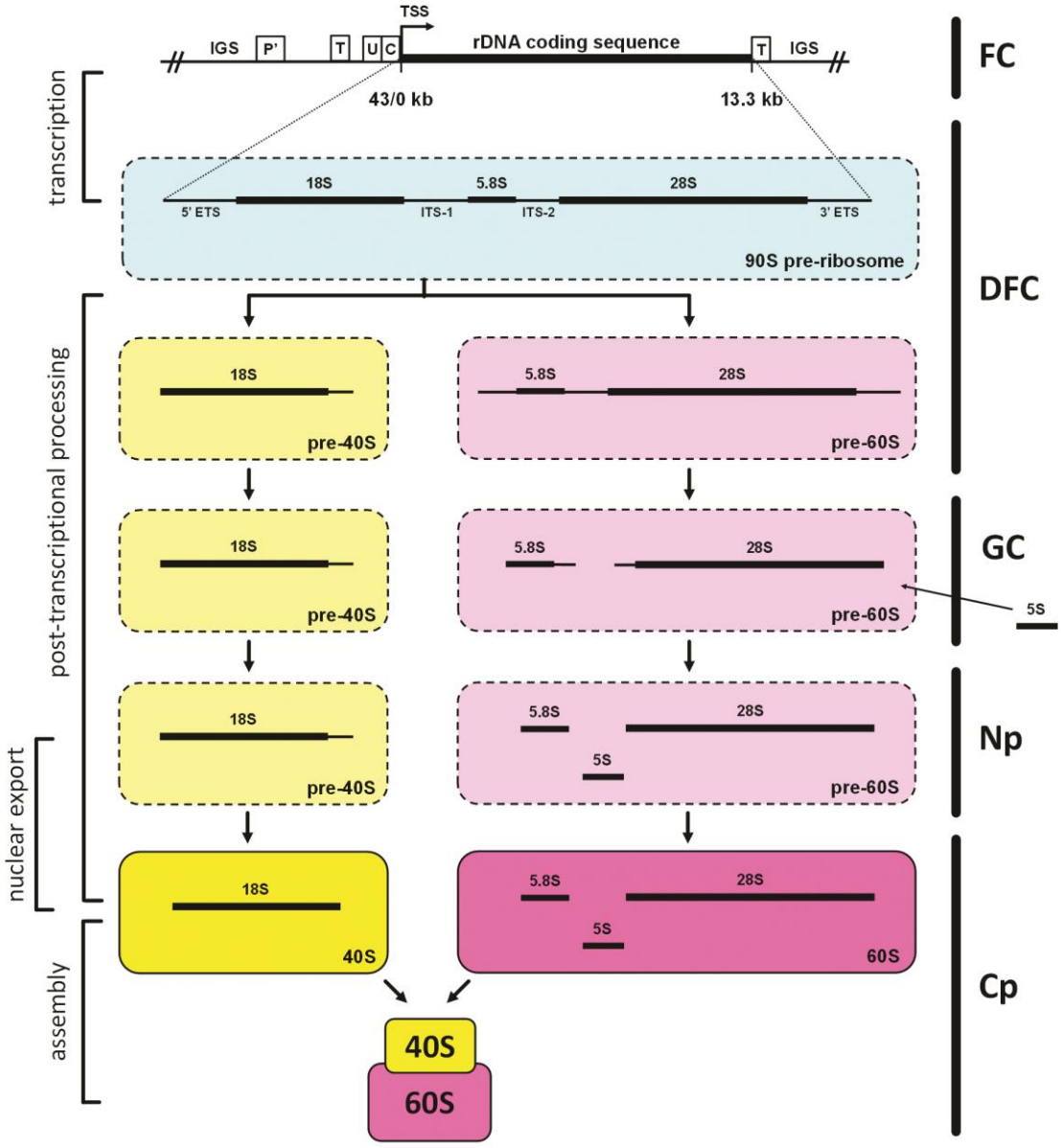

Figure 1-3. Schematic of ribosome biogenesis.
The rDNA coding sequence is 13.3 kb. The proximal promoter includes a core promoter element (-45/+18, C) and an upstream control element (-156/-107, U), as well as a terminator sequence (T) to which TTF-I binds. About 2 kb upstream is another RNA Pol I promoter (P'), from which pRNA is transcribed. Transcription of rRNA occurs at the FC/DFC periphery. Post-transcriptional processing is mediated by ribosomal proteins, snoRNA, and several enzymes which are responsible for packaging the immature ribosomal subunits through endo- and exonuclease cleavage, 5S rRNA incorporation (in the GC), 2'-O-ribose methylation of rRNA, pseudouridylation of rRNA, export from the nucleoplasm (Np), and finally assembly into mature ribosomes in the cytoplasm (Cp). The locations of each external transcribed spacer (ETS) and internal transcribed spacer (ITS) are indicated. Figure adapted from (Bartova et al., 2010; Haltiner et al., 1986; Henras et al., 2008; McStay and Grummt, 2008).

have been elucidated and extensively reviewed (Henras et al., 2008; Tschochner and Hurt, 2003). Ribosome biogenesis is carried out in the fibrillar centre (FC), dense fibrillar component (DFC), and granular component (GC), nucleolar subcompartments which have been defined using electron and fluorescence microscopy (Boisvert et al., 2007). To date, most data describing ribosome biogenesis has been generated from yeast models, and while there is a large degree of conservation amongst all eukaryotes, recent studies have uncovered some differences in the manner with which mammalian nucleoli process rRNA (Figure 1-3) (Mullineux and Lafontaine, 2012; Sloan et al., 2013).

In brief, ribosome biogenesis begins with the transcription of 47S pre-rRNA by RNA Polymerase I at the interface between the FC, which houses the rDNA genes and the transcriptional machinery, and the DFC, into which nascent transcripts emerge for post-transcriptional processing. 47S pre-rRNA is a polycistronic transcript from which 18S, 5.8S, and 28S rRNA are derived. In the DFC, 47S pre-rRNA is initially incorporated into a 90S pre-ribosome, then subsequently cleaved by endo- and exonucleases to liberate 18S rRNA for incorporation into the pre-40S ribosomal subunit, with 5.8S and 28S rRNA becoming incorporated within the pre-60S ribosomal subunit alongside 5S rRNA, which is transcribed by RNA Pol II and imported into the nucleolus. Further maturation of the pre-40S and pre-60S ribosomal subunits proceeds within the GC and nucleoplasm, prior to export and assembly of the mature ribosomes in the cytoplasm.

In its entirety, ribosome biogenesis requires the concerted coordination of over 200 factors (e.g. enzymes, ribosomal proteins, snoRNAs), many of which have been identified through mass spectrometry-based protein identification analyses (Henras et al., 2008). The involvement of so many factors in ribosome biogenesis necessitates a

tremendous expenditure of cellular resources (Warner, 1999). In order to conserve such resources, epigenetic regulation of the rDNA gene has emerged as an important means by which a cell can efficiently control the rate of ribosome biogenesis that it may require.

1.3.2 The epigenetics of rDNA transcription

Early investigations into the rDNA activation status utilized psoralen, which intercalates into dsDNA but not if it is associated with nucleosomes, and crosslinking, observing that coding rDNA exists in one of two states: transcriptionally accessible rDNA (nucleosome-free) and inaccessible rDNA (nucleosome-dense) (Conconi et al., 1989; Dammann et al., 1993). Further studies demonstrated that inaccessible rDNA corresponded with enhanced methylation of CpG dinucleotides in the promoter, and that the inhibition of cytosine methylation with 5-aza-2'-deoxycytidine caused an upregulation in the transcription of rDNA (Santoro and Grummt, 2001). More recently, ChIP-sequencing of rDNA genes in human cell lines identified an active chromatin signature at the rDNA promoter (e.g. H3K4me1/2/3, H3K9ac, H3K27ac) and that the active rDNA coding sequence was generally nucleosome-free (Zentner et al., 2011). Repressive chromatin marks (H3K9me1, H3K27me3, H4K20me1) were observed to have a broader distribution throughout rDNA, particularly within the IGS. Notably, Zentner et al. refer to the similarity of active chromatin signatures among their different cell models, while repressive marks exhibited more heterogeneous distribution patterns, suggesting a greater degree of functional redundancy in the mechanisms that govern rDNA repression vs. activation (see Figure 1-4).

RNA Pol I is a 14 subunit protein complex (Kuhn et al., 2007) whose sole identified function is to transcribe rDNA, consistent with its ChIP-Seq binding profile

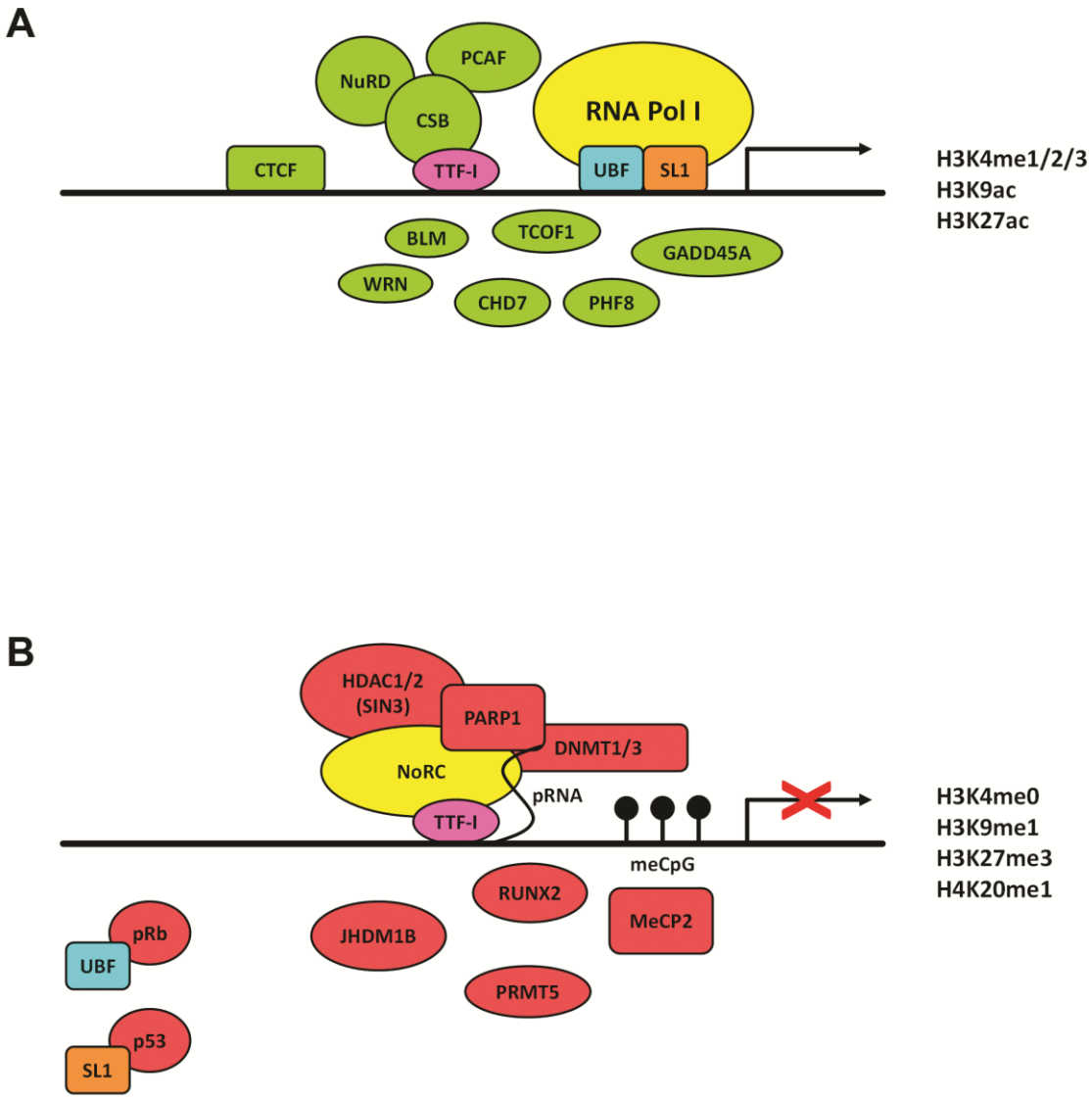

Figure 1-4. Epigenetic regulation of rRNA transcription.
(A) Transcriptionally active rDNA.
(B) Transcriptionally silenced rDNA.

(Zentner et al., 2011). Like mRNA transcription, RNA Pol I-mediated transcription consists of an initiation, elongation, and termination phase (Denissov et al., 2011; McStay and Grummt, 2008; Nemeth et al., 2013; Schneider, 2012). RNA Pol I is recruited to rDNA by the pre-initiation complex (PIC), which consists of upstream binding factor (UBF) and selectivity factor (SL1) (Learned et al., 1986), as well as their collective recruitment of TIF-IA (Yuan et al., 2002). SL1 contributes to promoter recognition through its TATA-binding protein (TBP) subunit and UBF is a transcriptional activator for RNA Pol I (Bell et al., 1988). Interestingly, the activity of UBF was proposed to be mediated by its ability to outcompete linker histone H1, thereby preventing condensed chromatin from forming (Kermekchiev et al., 1997). In addition, UBF is a target for extracellular-signal-regulated kinases (ERKs) to regulate the rate of RNA Pol I transcription during elongation (Stefanovsky et al., 2006).

Interestingly, both the binding of the CTCF insulator protein between the IGS and the rDNA promoter as well as the binding of the transcription termination factor (TTF-I) to the rDNA promoter is necessary for the respective recruitment of UBF (van de Nobelen et al., 2010; Zentner et al., 2011) and activation of RNA Pol I (Langst et al., 1998). Indeed, studies into the mechanisms that underlie ribosomopathies, developmental diseases that negatively affect ribosome biogenesis, have uncovered the contributions of numerous chromatin remodeling proteins towards the transcriptional activation of rDNA, including BLM (Bloom's syndrome) (Grierson et al., 2012), CHD7 (CHARGE syndrome) (Zentner et al., 2010), CSB (Cockayne syndrome) (Bradsher et al., 2002), PHF8 (Siderius XLID) (Feng et al., 2010; Zhu et al., 2010), TCOF1 (Treacher Collins) (Valdez et al., 2004), and WRN (Werner syndrome) (Shiratori et al., 2002).

The activation of transcriptionally open rDNA is also dependent on the proper silencing of a sufficient level of the remaining rDNA repeats. Indeed the derepression of NORs correlates with an increase in genomic instability (Ide et al., 2010) and ribosome biogenesis is commonly hyperactivated in cancer (Hannan et al., 2013; Montanaro et al., 2008). Moreover, the presence of heterochromatin at the nucleolar periphery contributes to the stability of nucleolar structure and function (McStay and Grummt, 2008). One important factor in mediating the establishment of this heterochromatin (Guetg et al., 2010) is the nucleolar remodeling complex (NoRC). NoRC consists of the TTF-I-interacting protein 5 (TIP5) and the SNF2H ATPase and its role has primarily been established in the silencing of rDNA (Strohner et al., 2001; Strohner et al., 2004)

As members of NoRC, SNF2H engages in ATP-dependent nucleosome remodeling to disfavour PIC recruitment, while TIP5 is a large scaffolding subunit that engages in both the targeting of NoRC to the rDNA promoter, via its interaction with TTF-I, as well as the recruitment of additional chromatin repressors, such as DNA methyltransferases (DNMT1, DNMT3) and HDACs (SIN3 co-repressor) (McStay and Grummt, 2008; Santoro et al., 2002; Zhou et al., 2002). More recently, the association of NoRC to rDNA was found to be dependent upon an interaction with a promoter-associated non-coding RNA (pRNA) that is transcribed by RNA Pol I from an alternative promoter that is 2 kb upstream of the coding rDNA TSS (Mayer et al., 2006). The dual presence of pRNA and TIP5 has further been demonstrated to be co-operational in localizing DNMT3B (Schmitz et al., 2010) and PARP1 (Guetg et al., 2012), which poly (ADP) ribosylates DNA, to the rDNA promoter to promote silencing.

Interestingly, NoRC-mediated rDNA repression appears to be dynamic and subject to competition or reversal by other chromatin regulators. For instance, Cockayne syndrome protein B (CSB) competes with TIP5 in the binding of TTF-I, resulting in the recruitment of PCAF histone acetyltransferase to rDNA, which may counter SIN3-mediated histone deacetylation (Shen et al., 2013; Xie et al., 2012). Furthermore, CSB has been shown to interact with NuRD in the activation of rDNA (Xie et al., 2012), and NuRD additionally represses TIF5 at the transcriptional level (Ling et al., 2013). In addition, the CpG methylation deposited by NoRC may also be reversible, as evidenced by the ability of GADD45A to remove methylated cytosines at the rDNA promoter through the induction of nucleotide excision repair mechanisms (Schmitz et al., 2009).

Additional factors that participate in the regulation of rRNA synthesis continue to be identified in the literature and participate in transcriptional regulation (e.g. RUNX2) or the deposition (e.g. PRMT5), removal (e.g. JHDM1B), and reading (e.g. MBD) of chromatin marks (Ali et al., 2012; Frescas et al., 2007; Ghoshal et al., 2004; Majumder et al., 2010; Young et al., 2007). These processes act in concert to determine both whether the PIC will recruit RNA Pol I, but also maintain the ultrastructure of the NOR. Adding an additional layer of regulatory complexity, rDNA activity has also been shown to be influenced by the cell cycle and environmental stress.

1.3.3 Nucleolar regulation by the cell cycle and environmental stress

The influence of the cell cycle in mediating nucleolar structure and function is well demonstrated by its Cyclin B-CDK1-mediated disassembly during mitotic prophase and its PP1/PP2A-mediated reassembly during telophase and early G_1 (Hernandez-Verdun, 2011). Following reassembly, nucleolar regulation continues to be subject to cell

cycle regulation between G_1 and G_2 phase, during which rRNA synthesis is progressively upregulated in a controlled manner in preparation for cell division (Montanaro et al., 2008). In cancer, this process is accelerated through the activation of oncogenes like c-Myc to promote rRNA synthesis (Grandori et al., 2005). On the other hand, inactivating tumour suppressors like pRB and p53 act in limiting the amount of PIC that is loaded onto the rDNA promoter (Montanaro et al., 2008).

Active UBF levels positively correlate with the rate of rDNA transcription (Sanij et al., 2008). During early G_1, unphosphorylated pRB binds UBF and prevents it from binding SL1 to form the PIC (Cavanaugh et al., 1995; Hannan et al., 2000; Montanaro et al., 2008). One recognized function of pRB is to mediate progression through the G_1/S checkpoint (Chen et al., 2009). Through most of G_1, hypophosphorylated pRB is bound to E2F transcription factors thereby preventing them from activating their target genes to favour S phase entry. However, as the cell cycle progresses towards the G_1/S transition, Cyclin D and E levels are progressively induced and their associated kinases, CDK4/6 and CDK2 respectively, hyperphosphorylate pRB to release the E2Fs. Likewise, Cyclin D-CDK4 and Cyclin E-CDK2 favour the release of UBF from pRB by hyperphosphorylating these targets, resulting in the upregulation of rRNA synthesis (Montanaro et al., 2008; Voit et al., 1999).

Similar inhibition of rRNA synthesis is achieved by p53 (Bieging et al., 2014; Golomb et al., 2014). Systematic p53 turnover is regulated by MDM2, which targets p53 for proteasomal degradation under normal conditions, thereby preventing p53 from initiating cell cycle arrest or apoptosis (Haupt et al., 1997; Kubbutat et al., 1997). However during cellular stress, MDM2 becomes immobilized within the nucleolus (e.g.

via interactions with ARF and PML), releasing activated p53 which binds SL1 to prevent PIC formation, thereby repressing rDNA (Bernardi et al., 2004; Rubbi and Milner, 2003; Weber et al., 1999; Zhai and Comai, 2000). Interestingly, lncRNA transcripts expressed from the rDNA IGS region have been demonstrated to immobilize MDM2 and other proteins (e.g. VHL, HSP70, RNA Pol I subunits) in response to cellular stress (e.g. DNA damage, hypoxia, heat shock) in a recently defined nucleolar detention pathway (NoDP) (Audas et al., 2012; Jacob et al., 2013). The NoDP may partially account for the many proteins with no known nucleolar functions that have been identified from mass spectrometry-based characterizations of the nucleolar proteome (Ahmad et al., 2009).

1.3.4 PHF6 in the nucleolus

PHF6 has an NoLS that is necessary for its localization into the nucleolus (Lower et al., 2002), but no role has so far been identified in the contribution of PHF6 towards ribosome biogenesis. The presence of PHD-like zinc finger domains in the PHF6 structure could suggest an interaction with chromatin at the NOR. Indeed, JMJD2B and G2E3, which contain similar zinc fingers, are also found in the nucleolus, but it remains unclear whether their zinc fingers are responsible for this localization (Bartova et al., 2011; Brooks et al., 2007). In Chapter 4 of the thesis, I provide further characterization of nucleolar PHF6 interactions towards the identification of its cellular function.

1.4 RATIONALE, HYPOTHESIS, AND SPECIFIC AIMS

The association of *PHF6* mutations with BFLS, T-ALL, AML, and CML suggests a role for PHF6 as a developmental regulator and tumour suppressor. Prior to the work presented in this thesis, *PHF6* mutations were not yet linked with T-ALL, PHF6 had no known protein interactions, and the role of nucleolar PHF6 was uncharacterized. My **overarching hypothesis** was that PHF6 functions within a protein complex to promote transcriptional regulation. Moreover, mutations in *PHF6* impair neuronal and lymphoid differentiation, resulting in BFLS or leukemia. To address this global hypothesis, I proposed the following **specific aims**:

1.4.1 To understand how PHF6 mutations may predispose BFLS patients to T-ALL:

Based on the association between murine *Phf6* and T-cell lymphoma, NOTCH1-binding to *PHF6*, and the occurrence of another hematopoietic cancer (Hodgkin lymphoma) in a BFLS patient, it was **hypothesized** that *PHF6* mutations may predispose BFLS patients to T-ALL. To address this hypothesis, PCR screens were performed on BFLS and T-ALL patients.

1.4.2 To identify and characterize PHF6 protein interactions:

PHF6 shares structural features with known chromatin remodeling proteins, including those that directly interact with histones, but very little was known regarding its functions or the downstream cellular processes that it regulates. Based on its zinc finger domains and its role in BFLS and leukemia, PHF6 was **hypothesized** to interact with one or more chromatin remodeling complexes that impinge upon proper development during

embryogenesis and hematopoiesis. To address this hypothesis, recombinant PHF6 was immunoprecipitated and co-eluting proteins were identified by mass spectrometry.

1.4.3 To identify a nucleolar function for PHF6:

Despite observations in the literature of its strong nucleolar association, the specific role of PHF6 in the nucleolus was unknown. Because PHF6 interacted with both chromatin remodeling and ribosomal factors in the previous aim, it was **hypothesized** that PHF6 regulated rRNA synthesis at either the transcriptional or post-transcriptional level. To address this hypothesis, the localization of PHF6 to specific subnucleolar compartments was assessed by the immunofluorescent analysis of chemically disrupted nucleoli and by chromatin immunoprecipitation.

CHAPTER 2

T-Cell Acute Lymphoblastic Leukemia in Association with Börjeson–Forssman–Lehmann Syndrome Due To a Mutation in PHF6

Purpose

To understand how PHF6 mutations may predispose BFLS patients to T-ALL.

Submission Information

Submitted: 27 December 2009
Accepted: 16 March 2010
Published: 5 May 2010

Reprinted with permission from "**Pediatric Blood & Cancer, Chao M.M., Todd M.A., Kontny U., Neas K., Sullivan M.J., Hunter A.G., Picketts D.J., and Kratz C.P., T-cell acute lymphoblastic leukemia in association with Börjeson-Forssman-Lehmann syndrome due to a mutation in PHF6, 2010, Volume 55 (4), pp 722-724**." Copyright © 2010 Wiley-Liss, Inc.

Contribution of Co-Authors

Matthew A.M. Todd prepared pediatric patient lymphoblast DNA for sequencing to identify *PHF6* mutations (see supplementary information on pages 45-47). Note that these supplementary data were not shown in the original publication.

Mwe Mwe Chao characterized the clinical features of the BFLS patient shown in Figure 2-1. Udo Kontny provided pediatric patient lymphoblast DNA. The manuscript was jointly written by Christian P. Kratz and David J. Picketts.

ABSTRACT

Börjeson–Forssman–Lehmann syndrome (BFLS) is a rare X-linked mental retardation syndrome that is caused by germline mutations in PHF6. We describe a 9-year-old male with BFLS, who developed T- cell acute lymphoblastic leukemia (T-ALL). The PHF6 gene is located on the X chromosome and encodes a protein with two PHD-type zinc finger domains and four nuclear localization sequences. Previously, overexpression of Phf6 was observed in murine T-cell lymphomas. Our observation indicates that BFLS may represent a cancer predisposition syndrome and that mutations of PHF6 contribute to T-ALL.

INTRODUCTION

Several onco- and tumor suppressor genes that are somatically altered in cancer have also been found to be mutated in the germline of individuals with inherited conditions, supporting the notion that, at least in part, oncogenesis and embryogenesis share common pathways. Examples include germline mutations in the oncogene KRAS in patients with Noonan syndrome (Schubbert et al., 2006), germline HRAS mutations in patients with Costello syndrome (Aoki et al., 2005), and germline mutations of the tumor suppressor gene PTEN in individuals with Cowden disease (Liaw et al., 1997). Moreover, constitutional mutations have been uncovered in several leukemia-associated transcription factors such as RUNX1 (Song et al., 1999) (familial thrombocytopenia with propensity to AML) and GATA1 (congenital dyserythropoietic anemia with macrothrombocytopenia) (Nichols et al., 2000). Not surprisingly, inherited conditions that are caused by germline mutations of cancer-related genes are often associated with a spectrum of malignancies occurring at variable frequencies (Aoki et al., 2005; Liaw et al., 1997; Schubbert et al., 2006; Song et al., 1999). Patients with genetic developmental disorders who develop cancer are of scientific interest because the mutated gene underlying their condition may confer a cancer predisposition. Additionally, disease causative genes of such inherited conditions may be somatically mutated in cancer. In this regard, germline mutations of the ATRX gene are the causes of several X-linked intellectual disability syndromes while somatic mutations have been identified in patients with preleukemic alpha-thalassemia myelodysplastic syndrome (ATMDS) (Gibbons et al., 2008). Thus, the clinical description of such rare associations may have broad

implications in the understanding of cancer biology and lead to the focused identification of novel cancer genes.

CASE REPORT AND RESULTS

We report on a 9-year-old male with Börjeson-Forssman-Lehmann syndrome (BFLS; OMIM 301900) (Figure 1), a rare X-linked disorder associated with intellectual disability, distinctive facial features, truncal obesity, and gynecomastia, which is caused by germline mutations of PHF6, reviewed in (Gecz et al., 2006). Our patient was diagnosed with T-cell acute lymphoblastic leukemia (T-ALL) at age 7 when he presented with hyperleukocytosis and enlarged cervical lymph nodes. Flow cytometric study of bone marrow cells showed blast cells expressing CD45, CD5, CD4, CD8, CD2, CD7, CD9, CD1a, and cytoplasmic CD3 consistent with T-cell phenotype. Cytogenetic analysis of leukemia cells revealed a normal male karyotype. Treatment (high-risk arm of ANZCCSG ALL Study VII) was complicated by transient liver failure during the induction phase; however, the patient recovered and is currently receiving maintenance chemotherapy. Mutation analysis of DNA extracted from peripheral blood taken during remission showed a mutation of PHF6, NM_032458.2: c.1024C>T, that results in a premature termination codon (p.R342X) within exon 10. Leukemia cells were not available for analysis.

Figure 2-1. Patient with T-ALL and Börjeson–Forssman–Lehmann syndrome, 9 years.
Note deep-set eyes, large, fleshy, posteriorly rotated ears, central obesity, breast enlargement, and tapering fingers.

DISCUSSION

The PHF6 gene is a member of a large family of zinc-finger genes and is ubiquitously expressed. The gene product, a 365-amino-acid protein, contains four nuclear localization sequences but its function remains unknown. Expression of green fluorescent-labeled PHF6 showed subcellular localization to the nucleus and nucleolus, reviewed in (Gecz et al., 2006). The latter serves as a key organelle in the synthesis and assembly of ribosomal subunits and is linked to cell growth and proliferation. PHF6 also contains two imperfect plant homeodomain-type zinc fingers (PHD), resembling transcriptional regulators such as MLL, which is frequently disrupted by leukemia-associated translocations (Gecz et al., 2006). The data suggest a role for PHF6 as a transcriptional regulator. There are less than 30 unrelated cases of BFLS with confirmed PHF6 mutations reported in the literature. Germline mutations associated with BFLS are predominantly missense and truncation mutations in and around exons 2 and 10 (Gecz et al., 2006). The c.1024C>T (p.R342X) mutation found in our patient results in a premature termination within exon 10, affecting the 5'-CpG dinucleotide codon for the amino acid arginine which was previously identified in the original BFLS family and is a recurrent mutation in BFLS (Lower et al., 2004). Although BFLS is not recognized as a cancer predisposition syndrome, another patient with BFLS has been reported to have developed Hodgkin lymphoma (Carter et al., 2009). Interestingly, a study by Landais et al. (Landais et al., 2005) implicated Phf6 overexpression in T-cell lymphoma in mice. Specifically, the highly leukemogenic radiation leukemia retrovirus VL3 (RadLV/VL3) induced T-cell lymphoma in a murine model by retroviral integrations in c-myc, Pim1, Notch1, and Kis2 (Kaplan Integration Site 2) loci. Kis2 rearrangements occurred in 11%

of murine lymphomas and resulted in the overexpression of the nearby Phf6 gene implicating a role for Phf6 in T-cell lymphoma development (Landais et al., 2005). Moreover, in another study, comparative genomic hybridization (CGH) identified DNA imbalances in 7 of 37 (19%) human T-cell lymphoma samples from 29 patients with gains related to either the whole or part of the X chromosome that includes bands Xq26-27 containing the PHF6 gene locus (Renedo et al., 2001). Lastly, in gene expression profiling PHF6 has been identified as a direct target gene of NOTCH1, which is frequently mutated in T-ALL (Palomero et al., 2006). Murine Phf6 protein expression analysis demonstrated mild-to-moderate levels of expression of Phf6 in many adult organs including the thymus and spleen (Voss et al., 2007). Taken together, these observations suggest a role of PHF6 in T- cell ALL/lymphoma tumorigenesis. Moreover, because the gene is located on the X chromosome, this may explain the preponderance of T-ALL/lymphoma in males. Ongoing and future functional and genetic studies such as PHF6 mutation analysis in primary human T-ALL/lymphoma cells are necessary to further characterize the role of PHF6 in human cancer.

ADDENDUM

In a pilot study we sequenced DNA from pediatric cases of T-ALL for somatic mutations in PHF6. We screened nine unselected patients who had been treated at the Division of Pediatric Hematology and Oncology, Department of Pediatrics and Adolescent Medicine, University of Freiburg, Germany. Notably, in blast cells from one male pediatric patient with T-ALL we found a novel mutation of PHF6 (NM_032458.2: c.987T>A) predicting a p.H329Q substitution. After submission of this article, a report from Van Vlierberghe and colleagues described somatic mutations and deletions of PHF6 in patients with T-ALL (Van Vlierberghe et al., 2010).

ACKNOWLEDGMENTS

C.P.K.'s work was supported by the Intramural Research Program of the National Cancer Institute, National Institutes of Health. D.J.P.'s work is funded by grants from the Canadian Institutes of Health Research. We thank Lemuel Racacho for technical assistance.

SUPPLEMENTARY INFORMATION

SUPPLEMENTARY MATERIALS AND METHODS

PHF6 patient mutation analysis

Lymphoblast DNA samples from nine pediatric patients affected with T-ALL (Division of Pediatric Hematology and Oncology, Department of Pediatrics and Adolescent Medicine, University of Freiburg, Germany) were screened for somatic PHF6 mutations. Genomic DNA from the affected individuals was used to amplify each exon of the PHF6 gene with forward and reverse primers that annealed to flanking intron sequences, with genomic DNA from an unaffected individual representing a control for each PCR reaction. Exons 2+3 were amplified in a single product, as were exons 4+5 and exons 6+7. For each PCR reaction, 100 ng of template DNA was amplified over 30 cycles, then submitted to the laboratory of Dr. Dennis Bulman for DNA purification and sequencing. For primer sequences and the annealing temperatures used, see Table 2-S1. Sequence files were processed and annotated with Applied Biosystems Sequence Scanner v1.0 software, and alignments with wild type PHF6 cDNA were performed using the NCBI BLAST algorithm (http://blast.ncbi.nlm.nih.gov/Blast.cgi) to identify mutations.

SUPPLEMENTARY RESULTS

Figure 2-S1 presents the data described in the Chapter 2 Addendum section. DNA from the blast cells of a male pediatric T-ALL patient contained a novel c.987T>A mutation in the *PHF6* gene (Figure 2-S1A). This mutation is predicted to cause a p.H329Q missense mutation in the protein, resulting in the loss of a key zinc ion stabilizing histidine residue in the second ZaP domain (Figure 2-S1B, C).

Table 2-S1. List of PHF6 primers used for DNA sequencing.*

Primer name	Sequence	Annealing temp. (ºC)
BFLS-1F	5'-TGGTTTCTGCACATGCGCTG	57
BFLS-1R	5'- CCAAGAGTCCCCTTTAACAA	
BFLS-2F	5'- AAAATTAACATTGTCGCCCTTC	57
BFLS-2R	5'- GAACATTCATGTGTTATTAAGAG	
BFLS-3F	5'- GCCATTTTTACTAGAAAATTACC	57
BFLS-3R	5'- TTCTCAAGAGGCAGAAATACC	
BFLS-4F	5'- TTTTCAATAACCAATTTGTTTTCC	57
BFLS-4R	5'- TTTTTACAAAAGCCCAAAGAAAG	
BFLS-5F	5'- TTGGGTGAAGTGTACTGCTC	57
BFLS-5R	5'- GAATGTTGAGATATGTCTTATGG	
BFLS-6F	5'- AACTAATACTTATTTTGAGATTGG	57
BFLS-6R	5'- CATTTCAAATGATGAACTTTACC	
BFLS-7F	5'-ATGTTAAGTAAGCTTGAAATACC	57
BFLS-7R	5'- CAAAATTGGGCTTAAAAGAACC	
BFLS-8F	5'- CATTTAATGTTTCTCTCATAAGG	57
BFLS-8R	5'- ACTTTAAATTTTCTGATGACTGG	
BFLS-9F	5'-TCTTTTTCAATAGAAAATAGCTG	57
BFLS-9R	5'-TAAACTAATGTCATCTATTTAAGG	
BFLS-10F	5'-CATCCACTAATGTTGGCAGG	57
BFLS-10R	5'-ATATATCAGTGTGTATTGTATCC	

* Product sizes: BFLS1F/1R (395 bp), BFLS2F/3R (598 bp), BFLS4F/5R (672 bp), BFLS6F/7R (562 bp), BFLS8F/8R (266 bp), BFLS9F/9R (276 bp), and BFLS10F/10R (261 bp).

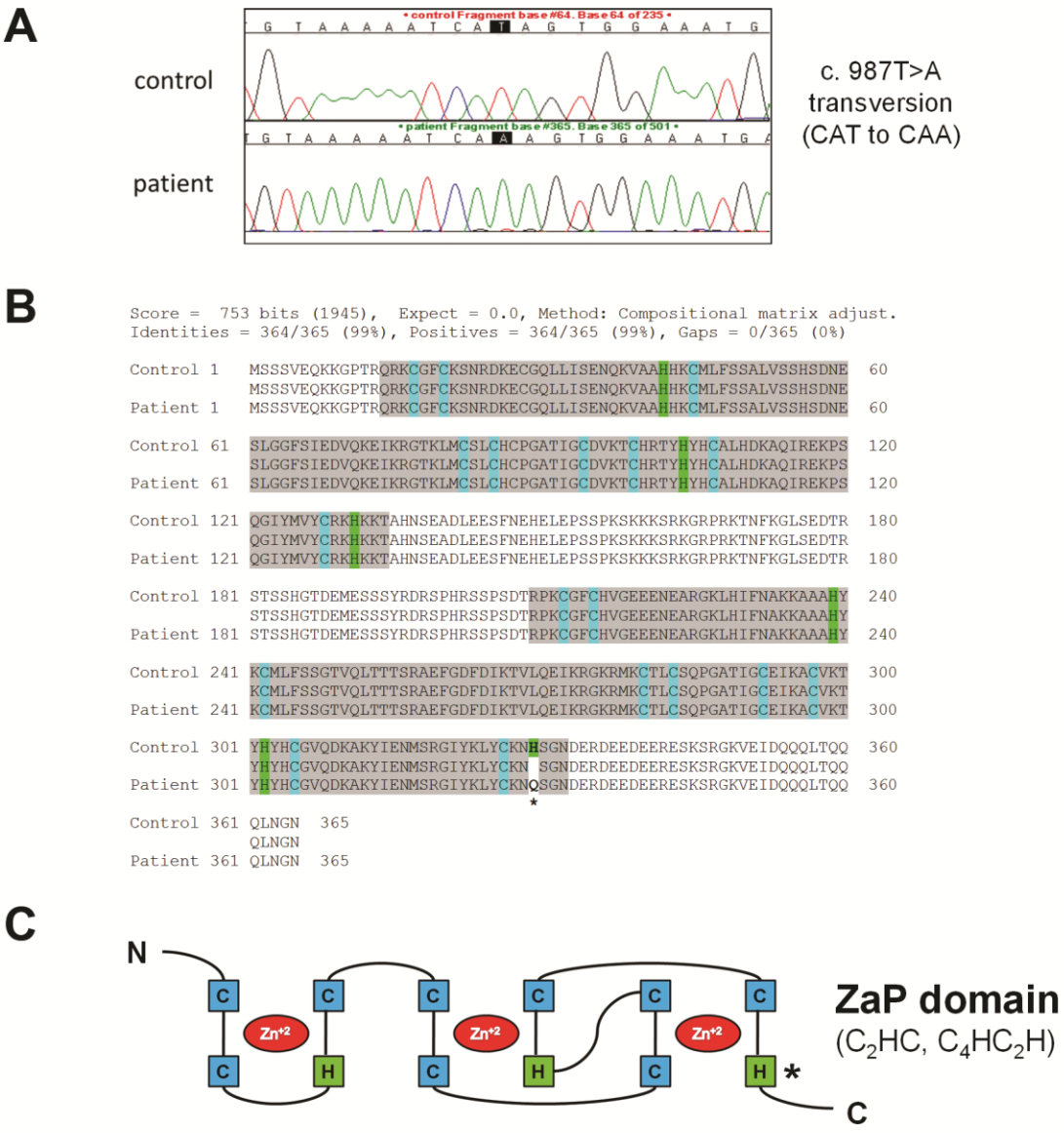

Figure 2-S1. Pediatric T-ALL patient with a novel somatic PHF6 mutation.
(A) DNA sequencing chromatograms from an unaffected control patient and a pediatric T-ALL patient demonstrate a c.987T>A transversion. (B) Protein BLAST alignment of the known amino acid sequence for PHF6 (Uniprot: Q8IWS0) and the PHF6 amino acid sequence that was computationally translated from the T-ALL patient. Zinc ion stabilizing residues of the ZaP domain are indicated in blue (cysteine) and green (histidine). Here, it is evident that the c.987T>A transversion predicts a p.H329Q substitution, indicating that the patient may have a compromised ZaP domain structure. (C) Schematic of the ZaP domain illustrating how the indicated cysteine and histidine residues from (B) participate in zinc ion stabilization (Capili et al., 2001; Liu et al., 2014). The position of the mutated amino acid residue is indicated with an asterisk (*).

CHAPTER 3

PHF6 interacts with the Nucleosome Remodeling and Deacetylation (NuRD) complex

Purpose

To identify and characterize the proteins that interact with PHF6 by using tandem mass spectrometry to identify co-eluting peptides following Flag immunoprecipitation of recombinant PHF6 protein.

Submission Information

Submitted: 11 May 2012
Accepted: 21 June 2012
Published: 3 August 2012

Contribution of Co-Authors

Matthew A.M. Todd performed all of the experimental work and analysis. The manuscript was written by Matthew A.M. Todd and edited by David J. Picketts.

ABSTRACT

Mutations in *PHF6* are the cause of Börjeson-Forssman-Lehman syndrome (BFLS), an X-linked intellectual disability (XLID) disorder, and both T-cell acute lymphoblastic leukemia (T-ALL) and acute myeloid leukemia (AML). The *PHF6* gene encodes a protein with two PHD-like zinc finger domains. As many PHD-like domains function to target chromatin remodelers to post-translationally modified histones, this suggests a role for PHF6 in chromatin regulation. However, PHD domains are usually found in association with a catalytic domain, a feature that is lacking in PHF6. This distinct domain structure and the minimal information on its cellular function prompted us to perform a proteomic screen to identify PHF6 binding partners. We expressed recombinant Flag-tagged PHF6 in HEK 293T cells for co-immunoprecipitation, and analyzed the purified products by mass spectrometry. We identified proteins involved in ribosome biogenesis, RNA splicing, and chromatin regulation, consistent with PHF6 localization to both the nucleoplasm and nucleolus. Notably, PHF6 co-purified with multiple constituents of the Nucleosome Remodeling and Deacetylation (NuRD) complex, including CHD4, HDAC1, and RBBP4. We demonstrate that this PHF6-NuRD complex is not present in the nucleolus but is restricted to the nucleoplasm. The association with NuRD represents the first known interaction for PHF6 and implicates it in chromatin regulation.

INTRODUCTION

PHF6 is a ubiquitously expressed 41 kDa protein that is conserved and vertebrate-specific. In mouse, Phf6 is predominantly expressed in the brain, central nervous system, and a number of embryonic tissues including the pharyngeal arches, nasal processes, anterior pituitary, and limb buds (Voss et al., 2007). In humans, PHF6 is most highly expressed in the thymus, with moderate expression in thyroid, ovary, testis, and adipose tissue (Van Vlierberghe et al., 2010). Structurally, PHF6 possesses two PHD-like zinc fingers and localization sequences for the nucleus and nucleolus (Lower et al., 2002).

PHD-like zinc fingers are common structural components of chromatin remodeling proteins, serving as epigenetic reader domains that interact with post-translationally modified histones. For instance, the PHD domains of Bromodomain and PHD Finger-containing Transcription Factor (BPTF) and Inhibitor of Growth 2 (ING2) bind to H3K4me3, while the PHD domains of Chromodomain-Helicase-DNA-binding protein 4 (CHD4) bind to H3K4me0/H3K9me3, indicating that there is a degree of variability to the post-translational modifications that are recognized by different PHD domains (Li et al., 2006; Mansfield et al., 2011; Shi et al., 2006). Along with other chromatin reading domains, PHD fingers facilitate the targeting of chromatin remodeling proteins to specific genomic loci to regulate gene expression and chromatin structure by engaging enzymatic mechanisms that involve DNA methylation, covalent histone modifications, and the ATP-dependent relocation of nucleosomes. Not surprisingly, genetic mutations in chromatin remodeling proteins have been identified as a cause of human developmental disease, including X-linked intellectual disability (XLID) disorders (e.g. ATRX, MECP2) (Amir et al., 1999; Gibbons et al., 1995).

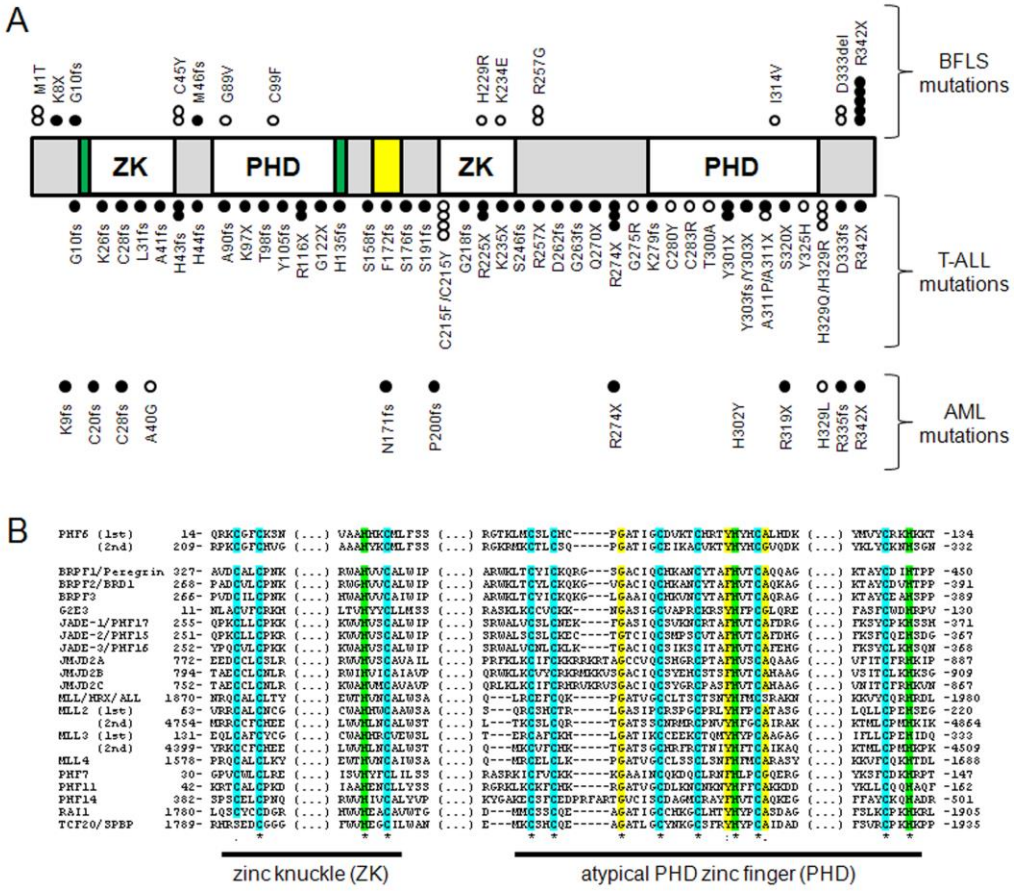

Figure 3-1. PHF6 is a PHD-like zinc finger protein that is mutated in BFLS and T-ALL.

(A) Schematic of the PHF6 protein detailing its two C_2H_2 zinc knuckles (ZK) with an atypical PHD domain (PHD), that we collectively term the ZaP domain. PHF6 also has two nuclear localization sequences (green) and a nucleolar localization sequence (yellow). Known point mutations for BFLS (Chao et al., 2010; Gecz et al., 2006; Mangelsdorf et al., 2009), T-ALL (Chao et al., 2010; Van Vlierberghe et al., 2010; Wang et al., 2011; Yoo et al., 2012), and AML (Van Vlierberghe et al., 2011; Yoo et al., 2012) are shown in relation to the structural features of PHF6. Closed circles represent frameshift and/or truncating mutations, while open circles indicate missense mutations or single amino acid deletions. (B) An alignment of the ZaP domain from human proteins using the ClustalW 1.83 algorithm (Thompson et al., 1994). Zinc ion-stabilizing cysteine (blue) and histidine (green) residues are indicated. Additional conserved residues are highlighted in yellow. Amino acid positions are indicated.

("*" = identical, ":" = conserved substitution, "." = semi-conserved substitution)

Mutations in *PHF6* (Figure 3-1A) cause BFLS (Lower et al., 2002), an XLID disorder further characterized by truncal obesity, gynaecomastia, hypogonadism, facial dysmorphia, digit abnormalities, hypogonadism, and large ears (Gecz et al., 2006). We have reported upon BFLS patients that have also developed bone marrow cancers (Carter et al., 2009; Chao et al., 2010), and more recently, somatic mutations of *PHF6* have been found in patients with T-ALL (Van Vlierberghe et al., 2010) and AML (Van Vlierberghe et al., 2011). Mutations within PHF6 are located throughout the gene and include missense, nonsense, frameshift, and small deletion alterations. One striking difference is that leukemic PHF6 mutations predominantly result in a frameshift or truncation whereas BFLS mutations are largely missense changes. Moreover, PHF6 has been shown to be inactivated by DNA methylation and miRNA silencing in T-ALL (Kraszewska et al., 2012; Mavrakis et al., 2011).

Other than its similarity to chromatin-interacting proteins and its subnuclear localization, very little is known about the functional role of PHF6 or the pathophysiological mechanism underlying *PHF6* mutations. To address this lack of knowledge, we sought to identify PHF6 interacting proteins by co-immunoprecipitation coupled with mass spectrometry identification. Here, we present our findings that PHF6 is a novel interactor with the NuRD complex and that PHF6 also co-purifies with histones, ribosomal assembly subunits, and multiple nucleolar proteins. The PHF6-NuRD complex was enriched in the nucleoplasm, suggesting that distinct PHF6 complexes define functionally specific roles in the nucleoplasm and nucleolus. Moreover, these findings confirm a role for PHF6 in modifying chromatin structure and suggest a general function in gene regulation.

MATERIALS AND METHODS

Generation of plasmid constructs

A cDNA fragment comprising the entire *PHF6* ORF was amplified from a pEGFP-C3-PHF6 expression plasmid (Vallee et al., 2004) using the following primers: PHF6-EcoRI-Fwd (5'-gctgaattcatgtcaagctcagttg-3'), and PHF6-XhoI-Rev (5'-gctctcgaggtttccattaagttg-3'). PCR products were purified and digested with EcoR I and Xho I, then directionally cloned into the pBRIT-LoxP-NTAP and pBRIT-LoxP-CTAP retroviral plasmid vectors (Figure 3-3A), which have been previously described (McKinnell et al., 2008). For each vector, *PHF6* was cloned in-frame with a TAP tag, which consists of a 6X His tag, a tobacco etch virus (TEV) sequence, and a 3X Flag tag. Protein expression is driven by a cytomegalovirus (CMV) promoter, and the vector contains resistance genes for puromycin and ampicillin. pBRIT-LoxP-NTAP vector was used as an empty vector control.

Cell culture

HEK 293T cells were cultured in DMEM (Dulbecco's Modified Eagle Medium), supplemented with 10% FBS (fetal bovine serum) and 1% penicillin-streptomycin (Invitrogen). Expression plasmids were transfected into HEK 293T for 6 hours with Lipofectamine 2000 (Invitrogen) according to the manufacturer's protocol. Following transfection, cells were allowed to recover for 24 hours, then stably selected for expression with 1.5 μg/μL puromycin (Sigma) for 2 weeks prior to colony selection. PHF6 expression in each clone was assessed by Western blot, and cell lines derived from the colonies were cultured in selection media for all subsequent experiments.

Antibodies

See Table 3-S1 for information regarding primary and secondary antibodies.

Immunocytochemistry

HEK 293T cells were trypsinized and washed with PBS on ice prior to cytocentrifugation using the Cytospin system (Thermo Shandon). Approximately 15 000 cells were applied per slide following centrifugation at 800 g for 5 minutes. Cells were then fixed for 10 minutes on ice in 2-4% paraformaldehyde in either PBS or CSK (10 mM PIPES pH 6.8, 10 mM NaCl, 300 mM sucrose, 3 mM $MgCl_2$, 2 mM EDTA) buffer, then washed with PBS before permeabilizing for 10 minutes with 0.5% Triton X in PBS at room temperature. For blocking, cells were incubated for 1 hour at room temperature in PBS with 20% horse serum and 0.5% FBS. Primary antibodies were incubated overnight at 4°C in a humidified box using the appropriate antibody dilution (Table 3-S1) in PBS. Secondary antibodies were applied at a 1:4000 dilution (in PBS) for 40 minutes at room temperature. To visualize chromatin, cells were incubated with 100 ng/mL DAPI (in PBS) for 3 minutes prior to mounting with DAKO Fluorescent Mounting Medium. Fluorescent images were obtained using an Imager M1 microscope (Zeiss) and processed with AxioVision version 4.6 software (Zeiss).

Cell fractionation

Cytoplasmic, nuclear, and nucleolar lysates were isolated from HEK 293T cells by adapting a previously described method (Chamousset et al., 2010b). Briefly, adherent HEK 293T cells (90-95% confluency) were scraped from 10 x 15 cm plates, washed in PBS, resuspended in 10 mL of buffer A (20 mM Tris-HCl pH 7.8, 1.5 mM $MgCl_2$, 5 mM KCl, 0.5 mM DTT), and incubated at 4°C for 15 minutes. NP-40 was then added to a

final concentration of 0.15%, and the lysate was incubated for an additional 15 minutes. The cytoplasmic and nuclear protein fractions were then collected as described, adjusted by adding 5X RIPA (250 mM Tris HCl pH 7.8, 750 mM NaCl, 5% NP-40, 2.5% sodium deoxycholate, 0.5% SDS) or 2X buffer B to a final concentration of 1X, followed by centrifugation at 15 000 g for 30 minutes to remove insoluble protein. The nucleolar pellet was isolated as described and resuspended in 1 mL buffer B (20 mM Tris-HCl pH 7.8, 1.5 mM $MgCl_2$, 400 mM NaCl, 25% glycerol, 5 mM Na-citrate, 10 μM $ZnCl_2$), sonicated (6 x 10 second pulses, 30% amplitude), incubated at 4°C for 30 minutes, and centrifugated at 15 000 g for 30 minutes to pellet insoluble protein.

Glycerol density gradient sedimentation

Protein from nuclear and nucleolar fractionated lysates was separated by glycerol density gradient sedimentation according to a previously described protocol (Lessard et al., 2007). Nuclear and nucleolar fractionated lysates (1 mg each) were diluted in HEM buffer (37.5 mM HEPES-KOH pH 7.8, 50 μM EDTA, 6.25 mM $MgCl_2$, 100 mM KCl, 0.75 mM DTT) with the glycerol concentration reduced to 10% in a final volume of 3 mL that was then layered over a 10 mL 10-30% glycerol gradient of HEM buffer. Samples were ultracentrifugated at 32 000 rpm for 20 hours at 4°C in an SW 41 Ti Beckman Coulter rotor and fractions (500 μL each) were collected from the top (#1) to the bottom (#23). Fractions were then concentrated by centrifugal filtration (MWCO 10 kDa Microcon, Millipore), with equal volumes analyzed by SDS-PAGE.

Immunoprecipitation

HEK 293T nuclei were harvested as described for cell fractionation. After incubation with buffer A (with 0.15% NP-40), nuclei were pelleted and given an

additional 10 mL wash in the hypotonic buffer. Re-pelleted nuclei were then homogenized in 5 mL of buffer B, sonicated, incubated at 4°C for 30 minutes, and centrifugated at 3 000 g for 30 minutes to remove insoluble protein, then diluted 1:10 in binding buffer (20 mM Tris-HCl pH 7.8, 1.5 mM $MgCl_2$, 137 mM NaCl, 10% glycerol, 5 mM Na-citrate, 10 μM $ZnCl_2$). Input for the 3X Flag immunoprecipitations (IPs) for purification and mass spectrometry varied from 20-30 mg per experiment, but was always equivalent for the empty vector, PHF6-NTAP, and PHF6-CTAP samples. For the validation of PHF6 interactions by endogenous IPs, the input was 1-7 mg per experiment. For both pre-clearing and endogenous IPs, 1 μg of mouse/rabbit IgG or antibody and 10 μL of pre-blocked Protein G-agarose (mouse, Santa Cruz)/Protein A-sepharose (rabbit, GE Healthcare) 25% slurry was applied for every 1 mg of lysate, and all washes were performed in binding buffer. When pre-clearing, the IgG and bead slurry incubations were each performed at 4°C for 1 hour. For the endogenous IPs, antibodies were incubated with the lysate at 4°C for 16 hours, followed by incubation with the bead slurry for 1 hour. The beads were then given 5 x 10 minute washes with 1 mL of binding buffer. Proteins were eluted by applying a 1:1 mixture of binding buffer and 4X Novex loading buffer (Invitrogen) to the beads, and incubating at 100°C for 5 minutes. Equal volumes for each sample were analyzed by SDS-PAGE.

For the 3X Flag IPs, 150 μL of 50% M2-Flag agarose (Sigma) bead slurry was added to each pre-cleared lysate and incubated for 16 hours at 4°C. The beads were then given 5 x 10 minute washes with 1 mL of binding buffer. Elution was achieved using 3X Flag peptide (Sigma) competition (1st wash: 400 μg/mL in 400 μL binding buffer at 4°C for 16 hours; 2nd-5th washes: 200 μg/mL in 200 μL binding buffer at 4°C for 30

minutes). The combined elution volumes were then concentrated by centrifugal filtration, with equal volumes for each sample loaded onto the SDS-PAGE gel for band identification and extraction for mass spectrometry.

Western blotting

Cell lysates, 3X Flag IP products, endogenous IP products, or glycerol density gradient fractions were resolved by SDS-PAGE (4-12% Bis-Tris Novex gel, Invitrogen) and transferred onto PVDF membranes (Millipore). Membranes were blocked in 1X TBST with 5% milk for 2 hours at room temperature, then incubated with primary antibody overnight at 4°C in 1X TBST with 5% BSA. Following three 10 minute 1X TBST washes, membranes were incubated with secondary antibody in blocking solution for 45 minutes at room temperature. Development of the membranes was achieved using enhanced chemiluminescence (GE Healthcare) and an SRX-101A (Raytech) film developer. Consult Table 3-S1 for appropriate antibody concentrations.

Mass spectrometry

3X Flag products were resolved by 4-12% SDS-PAGE gel and stained by colloidal blue Coomassie (Invitrogen). Gel slices containing protein were manually excised and submitted to the McGill University and Génome Québec Innovation Centre for reduction, cysteine-alkylation, and in-gel tryptic digestion using an automated MassPrep workstation (Micromass), as previously described (Wasiak et al., 2002). Extracted peptides were injected onto a 300 µm x 5 mm Zorbax C18 trapping column and subsequently resolved on a 10 cm x 75 µm PicoFrit column packed with 5 µm BioBasic C18 beads. Using an Agilent 1100 series HPLC (Agilent Technologies), peptides were eluted from the column using a 30 minute gradient of 10-95% acetonitrile containing

0.1% formic acid at a flow rate of 200 nL/min, and electrosprayed upon exit from the column.

Mass spectrometric data were acquired on a QTRAP 4000 (SCIEX/ABI) using the Information Dependent Analysis (IDA) feature of Analyst 1.4.1 software (ABI). Precursor ion selection for subsequent tandem MS fragmentation analysis was done using predefined IDA criteria. Briefly, up to three doubly, triply or quadruply charged ions of intensity greater than 2 x 10^6 counts per second from each enhanced-MS survey scan were selected for passage into a collision cell. Collision-induced dissociation was facilitated by collision with nitrogen gas; fragment ions were trapped in Q3 and scanned. Three enhanced-product ion scans (EPI) at a speed of 400 amu/second from 70 m/z to 1700 m/z were averaged for each selected precursor ion. Accumulation time used for EPI scans was 20 ms with Q0 trapping activated. Peak lists were generated using Distiller version 2.3.2.0 (Matrix Science) software with peak picking parameters set at 1 as for Signal Noise Ratio (SNR) and at 0.3 for Correlation Threshold (CT).

The peak-listed data was then searched against a copy of the Universal Protein Resource (UniProt) database (version: September 17, 2010) by using MASCOT version 2.3.01 (Matrix Science) and X! Tandem version 2007.01.01.1 (Global Proteome Machine). MASCOT and X! Tandem were set up to search the *Homo sapiens* (taxon ID 9606) database (88352 entries) assuming the digestion enzyme as trypsin with the maximum number of missed cleavages set at 1. MASCOT and X! Tandem were searched with a fragment ion mass tolerance of 0.80 Da, a parent ion tolerance of 1.5 Da, with the iodoacetamide derivative of cysteine specified as a fixed modification, and with methionine oxidation set as a variable modification. In X! Tandem, pyro-glutamine and

asparagine deamidation were also set as variable modifications. Scaffold version 2.06.02 (Proteome Software) was used to validate the MS/MS based peptide and protein identifications. Peptide identifications were accepted if they could be established at greater than 95% probability as specified by the Peptide Prophet algorithm (Keller et al., 2002). Protein identifications were accepted if they could be established at greater than 95% probability and contained at least 1 identified peptide. Protein probabilities were assigned by the Protein Prophet algorithm (Nesvizhskii and Aebersold, 2004). Annotated tandem mass spectra for protein identifications based on a single peptide assignment are provided in Figure 3-S1.

RESULTS

PHF6 has two atypical PHD zinc fingers which represent a conserved motif

PHD domains have been shown to interact with different histone lysine methylation marks, which are partially attributed to the variation in these domains. The canonical PHD domain is a C_4HC_3-type zinc finger (Aasland et al., 1995), which is capable of stabilizing two zinc ions to create protein-protein interaction surfaces (Capili et al., 2001). Variations of the PHD finger include the ADD domain (Aapola et al., 2000), which consists of a C_2C_2 GATA finger followed by a C_4C_4 atypical PHD finger, and the PZP motif (Perry, 2006), which consists of a canonical PHD finger followed by a C_2HC zinc knuckle and a C_4HC_2H atypical PHD zinc finger.

To further characterize the PHF6 zinc finger domain, we performed alignments using the ClustalW algorithm (Thompson et al., 1994). We found the two zinc fingers of PHF6 to be nearly identical and that both domains correspond to a degenerate version of the PZP motif, possessing only the C2HC zinc knuckle and the C4HC2H atypical PHD, which we refer to as the ZaP domain. We subsequently performed alignments to identify all human proteins that possess a ZaP domain (Figure 3-1B) and observed that PHF6 shares homology with several chromatin remodeling proteins, including members of histone acetyltransferase complexes (BRPF1-3, JADE1-3), histone methyltransferases (MLL1-4), histone demethylases (JMJD2A-C), an E3-ubiquitin ligase (G2E3), and transcription factors (RAI1, TCF20). Additional proteins that were aligned (PHF7, PHF11, PHF14) remain uncharacterized. Unlike the PHD and ADD domains, the functional role of the ZaP domain is unclear. Nonetheless, we predicted that the presence of two ZaP domains in PHF6 was indicative of its participation in a chromatin

remodeling/transcriptional regulation complex and subsequently proceeded to further characterize the protein by identifying its interaction partners.

PHF6 is expressed equally in the nucleoplasm and nucleolus of HEK 293T cells

Prior to purifying PHF6 from HEK 293T cells, we assessed its expression levels and subcellular localization in this model cell line. The PHF6 protein contains nuclear and nucleolar targeting sequences and we have previously reported upon the nucleolar concentration of overexpressed GFP-tagged PHF6 in HeLa cells (Vallee et al., 2004). Consistent with this, large-scale mass spectrometry analyses of the nucleolar proteome in immortalized human cell lines have also identified PHF6 peptides in the nucleolus (Ahmad et al., 2009). Nonetheless, quantitative comparisons of nucleolar vs. nucleoplasmic PHF6 have not been performed in any model. Thus, we performed cellular fractionation to isolate cytoplasmic, nucleoplasmic, and nucleolar protein fractions from HEK 293T cells, which were analyzed by western blot (Figure 3-2A; Figure 3-S2). It is evident that most of the PHF6 protein is found in the nucleoplasm, with a significant level also present in the nucleolus and only trace amounts in the cytoplasm. Similarly, the presence of both nucleoplasmic and nucleolar PHF6 was observed qualitatively by immunocytochemistry, as shown in Figure 3-2B. Further subcellular localization analyses revealed that the expression levels of nuclear and nucleolar PHF6 remained unchanged relative to one another during the cell cycle, except during mitosis, where PHF6 fails to co-localize with chromatin until telophase (Figure 3-S3A,B). Because PHF6 is primarily localized to nuclear compartments, we restricted the purification of PHF6 interactors to nuclear lysates.

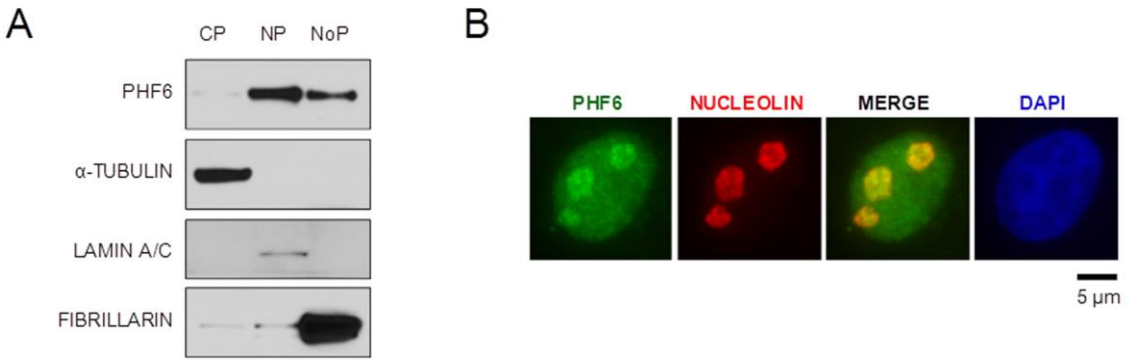

Figure 3-2. PHF6 is localized primarily to the nucleoplasmic and nucleolar cell fractions.
(A) Cell lysates were isolated from HEK 293T cells and fractionated into cytoplasmic protein (CP), nuclear protein (NP), and nucleolar protein (NoP). Equal amounts of protein from each fraction (10 µg) were separated by SDS-PAGE and immunoblotted with anti-PHF6 for a comparative analysis of PHF6 expression. Antibodies for α-tubulin, lamin A/C, and fibrillarin were used as control markers for the CP, NP, and NoP fractions respectively. Additional subcellular fractionation controls are presented in Figure 3-S2. (B) HEK 293T cells were immunofluorescently stained with antibodies to PHF6 (green) and nucleolin (red). Cells were counterstained with DAPI to visualize nuclei. PHF6 localizes to both the nucleoplasm and nucleolus (merge). This image is representative of all non-mitotic cells.

Novel PHF6 binding partners were identified by co-immunoprecipitation

To identify PHF6 interaction partners, we subcloned the coding sequence of *PHF6* cDNA into the respective multiple cloning sites of the pBRIT-LoxP-NTAP and -CTAP vectors, which have previously been used to identify Pax7 and Smn interacting partners (McKinnell et al., 2008; Shafey et al., 2010). A schematic of the PHF6 fusion proteins containing a tandem affinity purification (TAP) tag (6X His, tobacco etch virus cleavage site, 3X Flag) is presented in Figure 3-3A. PHF6 was tagged at both the N- and C-terminal ends as a precaution against mislocalization or impaired interactions of either fusion protein. The fusion proteins were stably expressed in HEK 293T cells using puromycin selection following transfection, with empty NTAP vector transfections serving as a negative control. A total of 16 PHF6-NTAP and 21 PHF6-CTAP clones were selected and analyzed for expression by western blot (Figure 3-S4). The clones showed variable levels of expression and two clones with expression levels equal to or lower than endogenous PHF6 protein levels were chosen for further analysis and purification (Figure 3-3B). Consistent with endogenous expression, the expression of the PHF6 fusion proteins was confined to the nucleus and nucleolus, as shown by immunofluorescence using a Flag antibody (Figure 3-3C).

To identify novel interacting proteins, we immunoprecipitated PHF6 fusion proteins from nuclear lysates using Flag purification, with the products of the purification separated by 4-12% gradient SDS-PAGE and visualized by colloidal Coomassie staining (Figure 3-4A). A band migrating just below M2-Flag heavy chain IgG and corresponding to the PHF6 fusion protein was visible in the PHF6-NTAP and -CTAP lanes but not the empty vector lane. Additional bands corresponding to proteins co-eluting with the PHF6

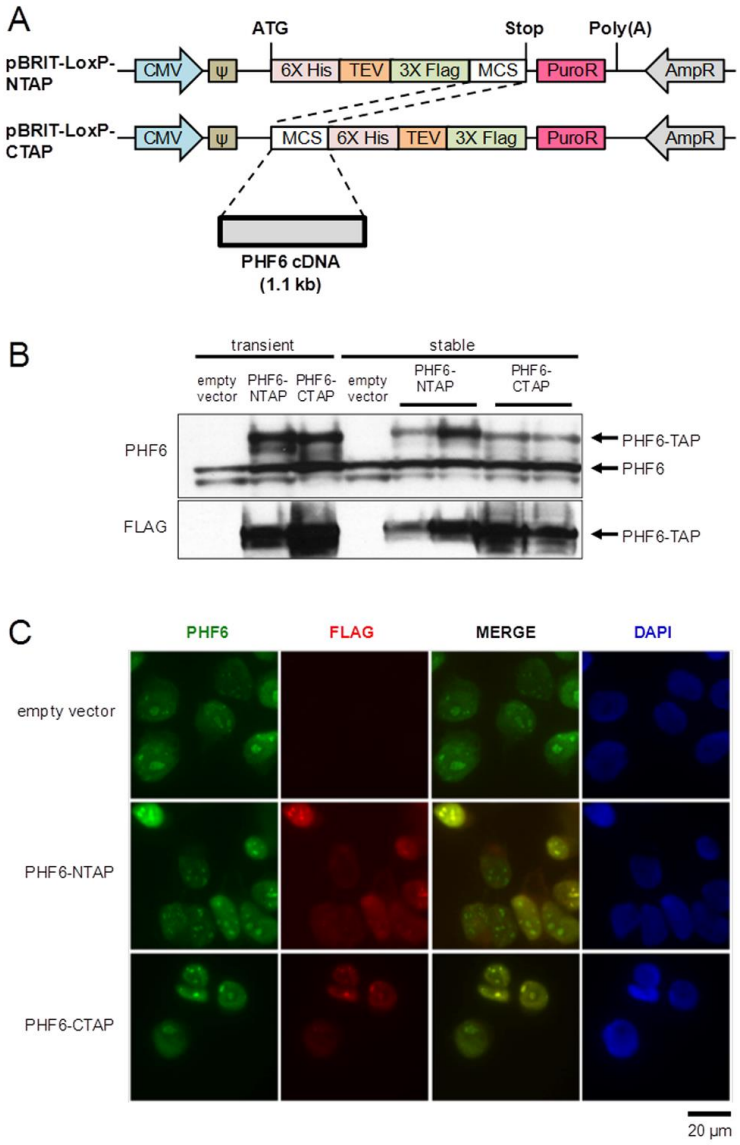

Figure 3-3. Recombinant PHF6-TAP was stably expressed in HEK 293T cells and was localized to both the nucleus and nucleolus.
(A) Schematic diagram of the pBRIT-LoxP-NTAP and pBRIT-LoxP-CTAP TAP-tag vectors used to express the PHF6 cDNA. For each construct, the 3X Flag tag was used for purification. (B) Immunoblots for PHF6 and Flag demonstrating transgene expression after both transient and stable transfection into HEK 293T cells. Endogenous PHF6 has a molecular weight of 41 kDa, while recombinant PHF6 has a molecular weight of 47 kDa. (C) Immunocytochemistry was performed on stable HEK 293T cell lines expressing empty vector, PHF6-NTAP, or PHF6-CTAP using antibodies for PHF6 and Flag. Flag was found to co-localize with nuclear and nucleolar PHF6 in cell lines expressing exogenous PHF6-TAP, but was absent in the cell line expressing only the empty vector.

fusion proteins, but not the empty vector, are also identified in Figure 3-4A (labeled #1-4), and gel slices corresponding to these bands, including the PHF6 gel slice (band 2), were excised and submitted for tryptic digestion and mass spectrometry analysis for protein identification. Equivalent gel slices were also excised from the empty vector control lane to allow for background subtraction. It should be noted that PHF6 was purified following TAP purification but the His tag purification conditions were too stringent to preserve many of the interactions obtained by Flag-purification alone (see Appendix A).

From this analysis, we identified 15 peptides corresponding to PHF6 observing >50% sequence coverage. Proteins that uniquely co-purified with both PHF6-NTAP and -CTAP, but not the empty vector, are presented in Table 3-1. They included histones, splicing factors, 40S ribosomal proteins, 60S ribosomal proteins, and several other nucleolar proteins consistent with the nucleolar distribution of PHF6. Of most interest was the identification of multiple components of the Nucleosome Remodeling and Deacetylation (NuRD) complex. In this regard, the highest score (1453) and most peptides (27) were attributed to CHD4. Additional identified constituents of NuRD included CHD3 (396, 8), RBBP4 (295, 5), and RBBP7 (224, 4). We also identified two peptides for MBD3, another NuRD subunit, however this data was excluded due to low confidence scores (data not shown). The identification of multiple constituents of the NuRD complex strongly suggests that PHF6 interacts with this chromatin remodeling complex. Moreover, since the NuRD complex is known to be critically involved in both development and hematopoiesis, key features associated with *PHF6* mutations, we selected this interaction for further validation and characterization.

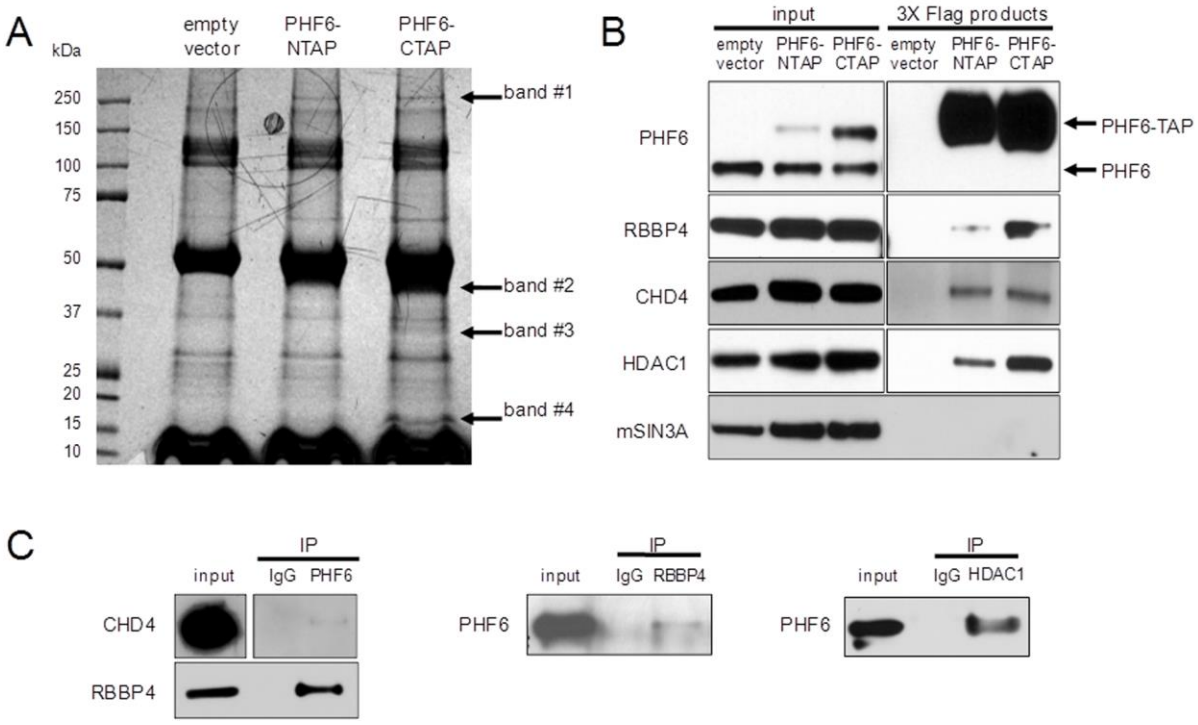

Figure 3-4. PHF6 co-purifies with core constituents of the NuRD complex.
(A) Colloidal Coomassie stained gel of Flag-IP purified proteins. Purified products present in the PHF6-NTAP and PHF6-CTAP eluates, but not the empty vector, were isolated and subject to mass spectrometry (bands #1-4). PHF6-TAP is present in band #2. Equivalent gel slices from the empty vector purification were also submitted to allow for the subtraction of background peptides. (B) Analysis of Flag-IP products by immunoblotting with antibodies for PHF6, RBBP4, CHD4, HDAC1, and mSIN3A. Input represents approximately 0.05% of the Flag-IP protein lysate. Flag-IP products represent 5% of the total recovered product following immunoprecipitation. (C) Endogenous IPs were performed in untransfected HEK 293T cells using antibodies for PHF6, RBBP4, and HDAC1. The PHF6 IP was analyzed by immunoblotting with anti-CHD4 and anti-RBBP4, with the input representing 0.14% of the protein lysate. RBBP4 and HDAC1 IPs were analyzed by immunoblotting with anti-PHF6, with the input representing 1% of the protein lysate. IgG-IPs were also performed as a negative control.

PHF6 co-purifies with the NuRD complex, but not SIN3A

To validate the interaction between PHF6 and NuRD, we performed western blots of Flag-purified PHF6-NTAP, PHF6-CTAP, and empty vector following co-immunoprecipitation (Figure 3-4B). Illustrating the specificity of the Flag pull down, abundant amounts of exogenous PHF6 were detected, but endogenous PHF6 was not pulled down suggesting that PHF6 does not function as a dimer. The immunoblots also clearly demonstrate that CHD4 and RBBP4 are able to co-purify with both N- and C-terminally Flag-tagged PHF6, but not with immunoprecipitation by Flag alone, indicative of the specificity for the purification of NuRD with PHF6.

HDAC1, which interacts with RBBP4 as part of the core HDAC sub-complex within NuRD, also co-immunoprecipitated with PHF6. Interestingly, the core HDAC complex is known to associate with other co-repressing chromatin remodeling complexes, including SIN3 (Silverstein and Ekwall, 2005). However, our western blots indicated that mSIN3A does not co-purify with PHF6, further confirming the specificity of the association between PHF6 and NuRD.

To further confirm the interaction, we performed co-immunoprecipitations of endogenous PHF6, RBBP4, and HDAC1 from the nuclear lysates of untreated HEK 293T cells. As shown in Figure 3-4C, RBBP4 is pulled down in abundance with the PHF6 antibody, while IgG alone did not pull down the protein. Likewise, PHF6 is detected in the reciprocal pull down with RBBP4, albeit in a lesser amount, which may reflect either the relatively small proportion of RBBP4 that interacts with PHF6 or the inefficiency of the monoclonal RBBP4 antibody used for immunoprecipitation. Similarly, we could detect a weak interaction of endogenous PHF6 with CHD4, further confirming the

Table 3-1. Proteins detected by ESI LC-MS/MS following Flag immunoprecipitation of recombinant PHF6.[1]

	accession	protein name	mass (kDa)	# peptides[2]	% sequence coverage	protein score	band #
PHF6	QIWS0	PHD finger protein 6	41	15	56	969	2
Nucleosome Remodeling and Deacetylation (NuRD) complex							
CHD4 (Mi-2β)	Q14839	chromodomain-helicase-DNA-binding protein 4	218	27	15	1453	1
CHD3 (Mi-2α)	Q12873	chromodomain-helicase-DNA-binding protein 3	227	8	4	396	1
RBBP4	Q09028	retinoblastoma-binding protein 4	48	5	12	295	2
RBBP7	Q16576	retinoblastoma-binding protein 7	48	4	10	224	2
Histone proteins							
H1.2	P16403	histone H1.2	21	7	20	414	3
H2B.1	P33778	histone H2B type 1-B	14	5	36	328	4
H2A.Z	P0C0S5	histone H2A.Z	14	3	29	197	4
H3.1	P68431	histone H3.1	15	3	17	133	4
Splicing factors							
SNRNP200[3]	O75643	U5 small nuclear ribonucleoprotein 200 kDa helicase	245	19	10	1099	1
PRPF8	Q6P2Q9	pre-mRNA-processing-splicing factor 8	270	12	5	595	1
HNRNPA2B1[4]	P22626	heterogeneous nuclear ribonucleoproteins A2/B1	37	7	27	436	3
HNRNPH3	P31942	heterogeneous nuclear ribonucleoprotein H3	37	4	13	269	3
HNRNPU	Q00839	heterogeneous nuclear ribonucleoprotein U	80	3	6	190	1
RALY	Q9UKM9	RNA-binding protein, autoantigen p542	32	3	10	172	3
HNRNPA3	P51991	heterogeneous nuclear ribonucleoprotein	40	2	5	127	3

		A3					
PCBP2	Q15366	poly(rC)-binding protein 2	39	2	7	117	3
HNRNPC	P07910	heterogeneous nuclear ribonucleoproteins C1/C2	34	2	7	106	3
MAGOH[5]	P61326	protein mago nashi homolog	17	1	8	57	4
40S/60S Ribosomal proteins							
RPLP0	P05388	60S acidic ribosomal protein P0	34	5	15	265	3
RPS18	P62269	40S ribosomal protein S18	18	3	18	198	4
RPS25	P62851	40S ribosomal protein S25	14	3	22	174	4
RPL22	P35268	60S ribosomal protein L22	15	2	19	170	4
RPL4	P36578	60S ribosomal protein L4	48	2	8	123	2
RPL30	P62888	60S ribosomal protein L30	13	2	21	122	4
Nucleolar proteins							
LYAR	Q9NX58	cell growth-regulating nucleolar protein	44	3	12	173	2
FBL	P22087	rRNA 2'-O-methyltransferase fibrillarin	34	2	8	104	3
NPM1[5]	P06748	nucleolar phosphoprotein B23	33	1	4	51	3
Other proteins							
TUBA1C	Q9BQE3	tubulin alpha-1C chain	50	2	6	132	2
PIP	P12273	prolactin-inducible protein	17	2	18	130	4
SRP14	P37108	signal recognition particle 14 kDa protein	15	2	15	93	4

[1] See Table 3-S2 for the chromosomal location of genes corresponding to proteins listed in this table.
[2] Only peptides with ≥95% confidence in Scaffold are listed in this table.
[3] Empty vector control had 11 peptides with a score of 614 and 5% coverage.
[4] Empty vector control had 3 peptides with a score of 173 and 10% coverage.
[5] Annotated tandem mass spectra for protein identifications based on a single peptide assignment are provided in Figure 3-S1.

validity of our mass spectrometry results. Additionally, PHF6 co-immunoprecipitated specifically with an HDAC1 pull down, but not with IgG. While these reciprocal co-immunoprecipitations experiments confirm a nuclear interaction between PHF6 and NuRD, they were unable to define whether the interaction was primarily nucleoplasmic or nucleolar.

PHF6 and NuRD interact in the nucleoplasm

Previous studies have suggested that NuRD is also localized to the nucleolus (Ahmad et al., 2009; Shimono et al., 2005). To investigate the localization of the PHF6-NuRD complex, we performed subcellular fractionation. We observed the majority of CHD4 to have nucleoplasmic localization, with only trace levels in the nucleolus (Figure 3-5A). Similarly, RBBP4 and HDAC1 have higher concentrations in the nucleoplasm with lower expression in the cytoplasm, and very little nucleolar expression. Therefore, it suggests that the PHF6-NuRD complex is not nucleolar but resides in the nucleoplasm. To confirm these observations, we performed immunocytochemistry to observe co-localization between the nucleolus and NuRD constituents. We observed that CHD4 and HDAC1 do not co-localize with nucleolin, a protein strictly localized to the nucleolus, whereas HDAC1 and RBBP4 showed significant co-localization with PHF6 in the nucleoplasm (Figure 3-5B).

To further elucidate the composition of PHF6 nuclear and nucleolar complexes, we performed glycerol density gradient co-sedimentation of fractionated nuclear and nucleolar lysates (Figure 3-5C). For the nuclear lysates, PHF6 was found to co-sediment with both RBBP4 and CHD4 in fractions #4-12, consistent with where the lowest

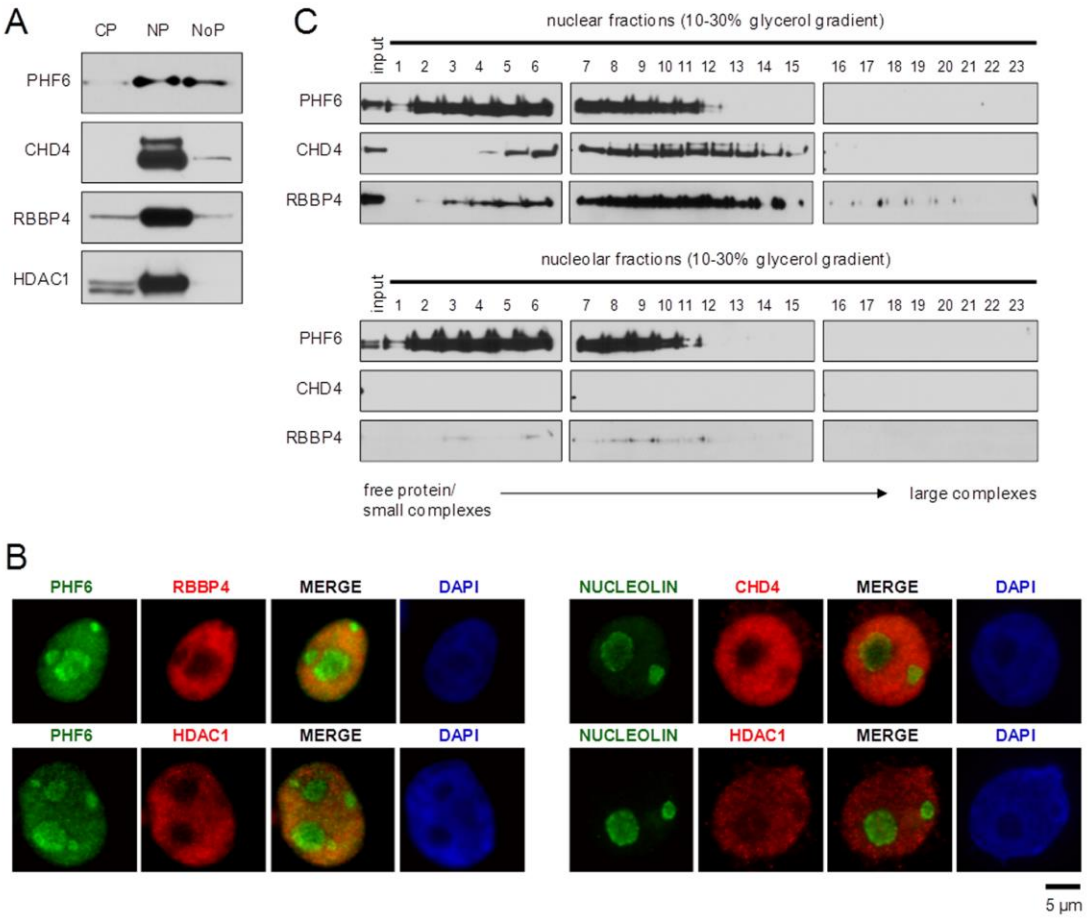

Figure 3-5. PHF6 interacts with the NuRD complex in the nucleus, but not the nucleolus.

(A) Subcellular fractionation analysis demonstrating that the NuRD constituents that interact with PHF6 are primarily localized in the nucleoplasm, with trace levels in the nucleolus. (B) HEK 293T cells were labeled with anti-PHF6, anti-CHD4, anti-RBBP4, and anti-HDAC1 by immunocytochemistry. PHF6 demonstrates strong nuclear and nucleolar localization (left panels), however the NuRD constituents are primarily localized to the nucleoplasm with very little (if any) nucleolar localization. These cells were also labeled with nucleolin as a marker for nucleoli (right panels). (C) Nuclear and nucleolar cell lysate fractions were separated by glycerol density gradient centrifugation. Following centrifugation, fractions were collected from the gradient and analyzed by immunoblotting with antibodies for PHF6, CHD4, and RBBP4. The numbering of the fractions corresponds to an increase in the mass of proteins or protein complexes that are found within the fraction. PHF6 was found to co-elute with the NuRD constituents in nucleoplasmic fractions, but not in nucleolar fractions. Input represents 1% of the nuclear or nucleolar lysate prior to centrifugation.

molecular weight NuRD complexes were expected. The peak of NuRD complex formation appears to occur in fractions #10-12. In larger fractions, where no PHF6 was observed, CHD4 and RBBP4 are likely co-sedimenting with higher molecular weight chromatin remodeling complexes. In contrast, CHD4 protein levels were undetectable and RBBP4 levels were low in the nucleolar lysate fractions, despite the detection of PHF6 in fractions #2-11. We conclude from these experiments that the PHF6-NuRD complex is restricted to the nucleoplasm and that PHF6 interacts with other proteins in the nucleolus and thus, likely has unique functions in these distinct nuclear compartments.

DISCUSSION

The NuRD complex is a multifunctional epigenetic regulator that engages in several catalytic functions, including ATP-dependent nucleosome remodeling, histone deacetylation, and H3K4 demethylation (Tong et al., 1998; Wang et al., 2009; Zhang et al., 1998). We have identified PHF6 as a novel NuRD interactor and subsequent validation of this interaction demonstrated that endogenous PHF6 co-purifies with CHD4, RBBP4, and HDAC1. While PHF6 displayed strong distribution within the nucleoplasm and the nucleolus, the NuRD complex was not abundant in the nucleoli, suggesting that PHF6 co-localizes with NuRD in the nucleoplasm. The interactions with 40S/60S ribosomal proteins, splicing factors, and other nucleolar proteins confirm a role for PHF6 in the nucleolus. Nonetheless, future studies are required to define the function of PHF6 within the nucleolus and determine how it contributes to the BFLS and T-ALL phenotypes.

NuRD regulates developmental pathways that are affected by PHF6 mutations

NuRD regulates critical developmental events that mediate cell proliferation and lineage commitment. Some of the developmental pathways mediated by NuRD include embryogenesis (Hendrich et al., 2001), oncogenesis (Lai and Wade, 2011), neurogenesis (Potts et al., 2011), and hematopoiesis (Yoshida et al., 2008; Zhang et al., 2012a), making PHF6-NuRD an exciting interaction to explain the mechanism responsible for the phenotype that arises when *PHF6* is mutated in BFLS and T-ALL. The specificity of NuRD towards its targets is achieved by the use of interchangeable core constituents that are mutually exclusive (e.g. MTA1/2/3, MBD2/3) (Hendrich and Bird, 1998; Yao and

Yang, 2003). These differential subunits interact uniquely with other proteins, many of which possess a zinc finger, to target NuRD to specific genomic loci.

During T-cell development, where immature $CD4^{-}CD8^{-}$ double-negative thymocytes differentiate into double-positive, and then single-positive mature T-cells, NuRD actively participates in transcriptional activation and repression (Cismasiu et al., 2005; Williams et al., 2004). In some instances, the transcriptional outcome is influenced through the interaction between NuRD and a transient binding partner. For example, NuRD has been shown to promote the active transcription of the T-cell differentiation marker CD4, but the same gene is repressed by Ikaros-NuRD targeting (Naito et al., 2007). Further study of the Ikaros-NuRD interaction has demonstrated that it stably associates at transcriptionally active genes in double-positive thymocytes, and that the ablation of Ikaros leads to NuRD-mediated silencing at genes normally bound by Ikaros (Zhang et al., 2012a). Additionally, the NuRD complex becomes redistributed to other Ikaros-independent sites where it reactivates genes involved in proliferation. Similarly during neurogenesis, chromatin immunoprecipitation and target gene expression studies have demonstrated the contribution of NuRD toward the regulation of genes that contribute to neuronal development in the brain and peripheral nerve myelination, with a loss of NuRD leading to enhanced proliferation (Hung et al., 2012; Potts et al., 2011).

Like NuRD, PHF6 is expressed in both the brain/CNS (Voss et al., 2007) and double-positive thymocytes (Van Vlierberghe et al., 2010). The co-expression of PHF6 and NuRD in these tissues suggests that PHF6 could be directing NuRD to a subset of gene targets that promote the development of these tissues though lineage commitment or maturation. While this is an enticing model for consideration, we cannot attribute the

development of these tissues or the disease phenotypes solely to a PHF6-NuRD complex, as aberrant splicing or ribosome production from a lack of PHF6 in the nucleolus could just as likely account for the malignancy or neurodevelopmental defects. However, transcriptional regulation represents only one known function of the NuRD complex and thus, the contribution of PHF6 towards alternative chromatin remodeling events regulated by NuRD should not be ignored.

Another major function of NuRD involves its localization to active replication forks on pericentromeric heterochromatin during DNA replication where it facilitates DNA repair (Helbling Chadwick et al., 2009; Sims and Wade, 2011). The loss of NuRD constituents leads to defects in the maintenance of pericentromeric heterochromatin, an S phase delay, and the accumulation of DNA damage (Pegoraro et al., 2009; Sims and Wade, 2011). Interestingly, an increase in the γH2AX DNA damage marker has been observed after PHF6 loss in HEK 293T cells (Van Vlierberghe et al., 2010). Moreover, both PHF6 and NuRD are targets of the ATM DNA damage checkpoint kinase (Matsuoka et al., 2007; Polo et al., 2010). Thus, the PHF6-NuRD complex could function in either transcriptional regulation or in active DNA repair. As such, future work must focus on the identification of specific genomic targets and the mechanisms that direct PHF6 to such loci.

PHF6 as a targeting protein for NuRD

PHF6 does not contain DNA sequence recognition domains, thus its interactions with chromatin are most likely determined by its ZaP domains. While the functional role of these zinc fingers is unknown, the ZaP domain has been reported to participate in histone interactions (Darvekar et al., 2012; Saksouk et al., 2009). NuRD itself

preferentially binds H3K4me0/H3K9me3 (Mansfield et al., 2011), and many of its known binding partners (e.g. BRG1, MLL, JARID1B) interact with modified histones to target NuRD to silenced or permissive chromatin (Li et al., 2011; Nakamura et al., 2002; Shimono et al., 2003). Similarly, PHF6 may be targeting NuRD to genomic target sites with a specific histone code signature.

Another possible role for the ZaP domain is in mediating protein-protein interactions, which has been reported for TCF20 and JADE-1 (Sjottem et al., 2007; Zhou et al., 2004). For PHF6, the ZaP domains may be required for the stable association with core subunits of the NuRD complex. Interestingly, several better characterized NuRD interacting proteins (e.g. BCL11B, FOG-1, SALL1) possess an N-terminal C_2HC zinc finger, similar to the zinc knuckle from the first PHF6 ZaP domain, that has been proposed to interact with the GATA-like zinc finger present in the MTA proteins (Cismasiu et al., 2005; Kowalski et al., 2002). Therefore, in addition to targeting NuRD to chromatin, future studies should consider that the PHF6 ZaP domains could also be acting as a primary interface for the interaction with NuRD.

CONCLUSION

In this study, we have identified a novel interaction between PHF6 and several components of the NuRD chromatin remodeling complex. The interaction with the NuRD complex represents the first PHF6 protein complex and it confirms that PHF6 is a chromatin interacting protein. We have demonstrated that while PHF6 is distributed almost equally between the nucleoplasm and the nucleolus, the PHF6-NuRD complex is specific to the nucleoplasm, suggesting that PHF6 has additional functions and interactions that pertain to the nucleolus. Further characterization of the PHF6-NuRD complex will need to be focused on the identification of target genes and the mechanisms that target PHF6 to specific genomic loci. These targets will need to be analyzed within the context of spatiotemporal developmental pathways, such as neurogenesis and hematopoiesis, in order to fully understand the contribution of PHF6 to BFLS and T-ALL.

ACKNOWLEDGEMENTS

We thank Laura Trinkle-Mulcahy for reagents and technical advice with mass spectrometry analysis and nucleolar fractionation; Vahab Soleimani for advice with the Flag-IP experiments; Michael Rudnicki and Iain McKinnell for providing the pBRIT-LoxP-NTAP and pBRIT-LoxP-CTAP vectors; Jozef Gécz for providing the monoclonal PHF6 antibody; and Rashmi Kothary and Michael Huh for comments on the manuscript. This work was supported by operating grants from the Canadian Institutes of Health Research. MAMT was supported by a Natural Sciences and Engineering Research Council of Canada Postgraduate Scholarship and by an Ontario Graduate Scholarship.

SUPPLEMENTARY INFORMATION

SUPPLEMENTARY MATERIALS AND METHODS

Analysis of soluble and insoluble subcellular fractionation products by SDS-PAGE

HEK 293T whole cell lysates were fractionated into cytoplasmic, nuclear, and nucleolar fractions, as described by (Chamousset et al., 2010b) and in the Materials and Methods section. Following the pelleting of insoluble protein from each fraction, the supernatants were collected as lysate fractions while the pellets were re-solubilized in 8M urea at an equivalent volume to the corresponding lysate. Additionally, the supernatant was collected at steps following the wash and subsequent pelleting of the nuclei (wash #1) and nucleoli (wash #2). These supernatants were diluted 1:5 in 5X RIPA and centrifugated at 15 000 g for 30 minutes at 4°C to pellet insoluble protein. For wash #1, the pellet was isolated from the supernatant and re-solubilized in 8 M urea at an equivalent volume to the supernatant. For wash #2, no pellet was discernible. Cytoplasmic, nucleoplasmic, nucleolar, and wash fractions were then prepared for SDS-PAGE analysis. For lysates (cytoplasmic, nucleoplasmic, nucleolar) and the wash #1 supernatant, equivalent amounts (10 µg each) were loaded onto the SDS-PAGE gel. For resuspended pellets, equivalent volumes to the corresponding loaded volumes of lysate were loaded onto the gel. For wash #2, an equivalent volume to the loaded volume of nucleolar lysate was loaded onto the gel.

Immunocytochemistry for BrdU-labeled HEK 293T cells

Asynchronous HEK 293T cells were incubated with 30 µg/mL bromodeoxyuridine (BrdU) in DMEM with 10% FBS for 30 minutes prior to cytocentrifugation and fixation. Immunocytochemistry was performed as described in the

Materials and Methods section, with the following additional step. After permeabilization and blocking, HEK 293T cells were washed with DNase I buffer (20 mM Tris-HCl pH 7.8, 140 mM NaCl, 1 mM $MgSO_4$) and incubated for 30 minutes at 37°C in the presence of 10 µg/mL DNase I. Following DNase I incubation, cells were washed with PBS, then incubated with primary antibody, as described. All subsequent steps remained identical to the aforementioned protocol.

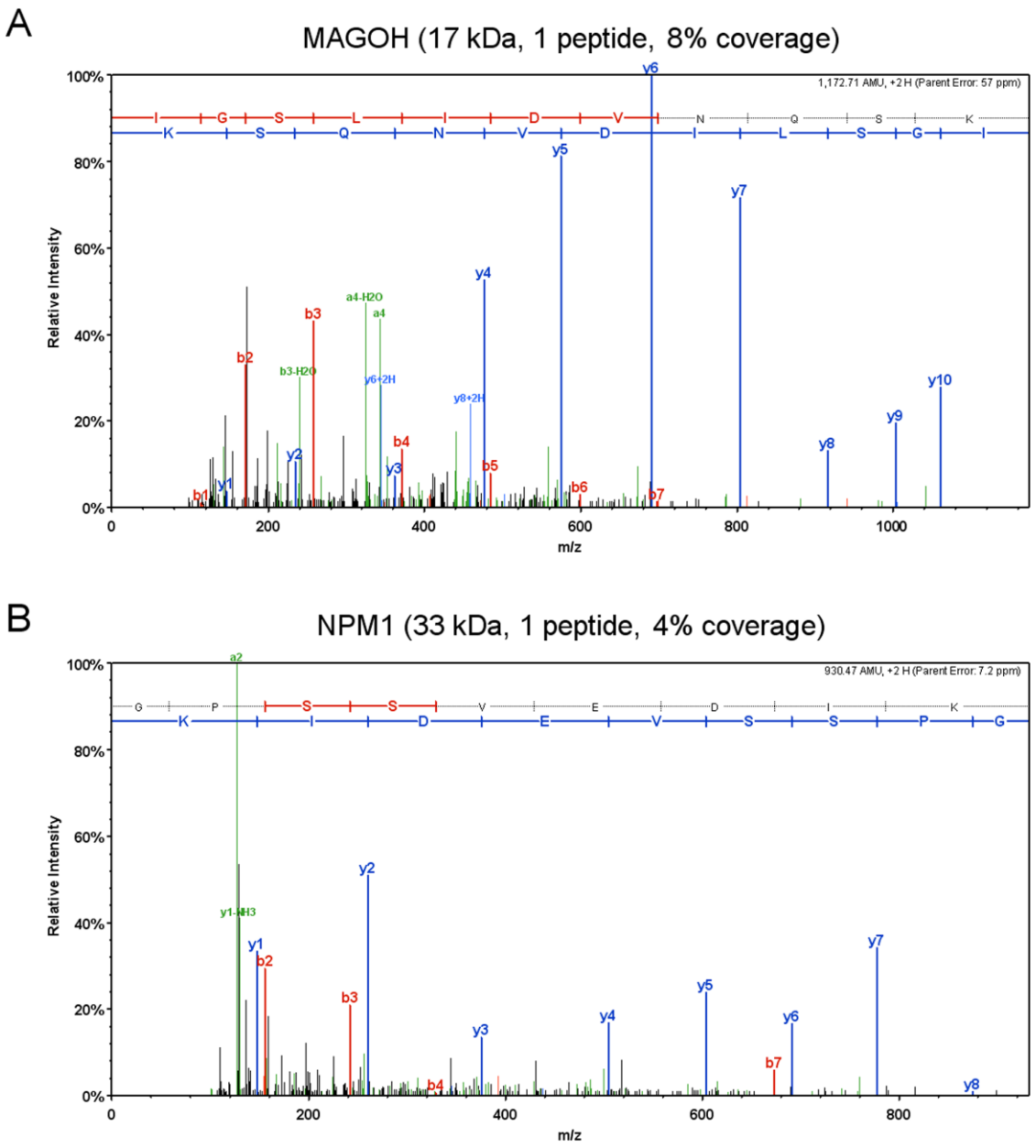

Figure 3-S1. Annotated tandem mass spectra for MAGOH (A) and NPM1 (B) single peptide assignments. Annotated spectra were generated by Scaffold version 2.06.02 (Proteome Software) with y-ions indicated in blue and b-ions indicated in red. Corresponding amino acid sequences are indicated at the top of each panel.

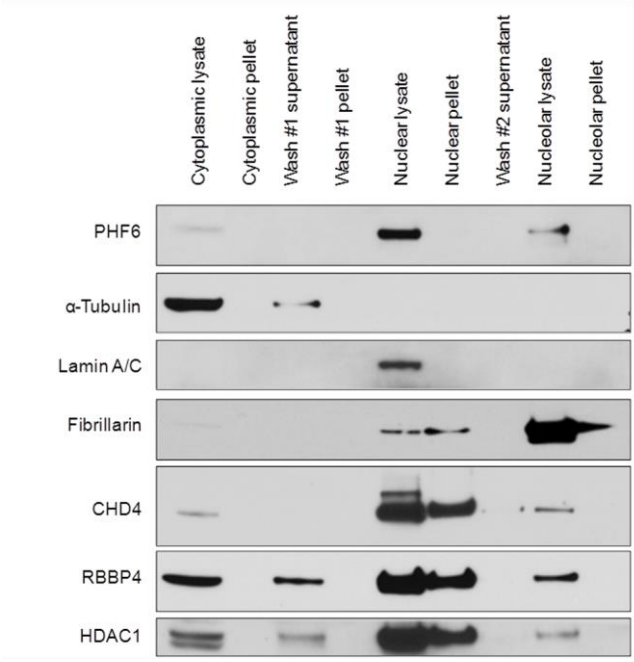

Figure 3-S2. PHF6 is present in only the soluble fractions following subcellular fractionation. Whole cell lysates from HEK 293T were fractionated into soluble (lysate or supernatant) and insoluble (pellet) cytoplasmic, nucleoplasmic, nucleolar, and wash fractions. Soluble fractions (except wash #2) were loaded at equivalent amounts (10 μg), while insoluble fractions were loaded at equivalent volumes to the corresponding soluble fraction. Wash #2 was loaded at an equivalent volume to the nucleolar lysate fraction. Immunoblotting was performed using antibodies to detect PHF6, α-Tubulin, Lamin A/C, Fibrillarin, CHD4, RBBP4, and HDAC1. PHF6 was only detected in soluble fractions, with strong levels detected in the nucleoplasmic and nucleolar lysates. Trace levels of PHF6 were also detected in the cytoplasmic lysate. By comparison, NuRD proteins (CHD4, RBBP4, HDAC1) are most highly detected in the soluble and insoluble nucleoplasmic fractions, with lower levels present in the cytoplasmic and nucleolar soluble fractions. α-Tubulin, Lamin A/C, and Fibrillarin are markers for the cytoplasm, nucleoplasm, and nucleolus respectively.

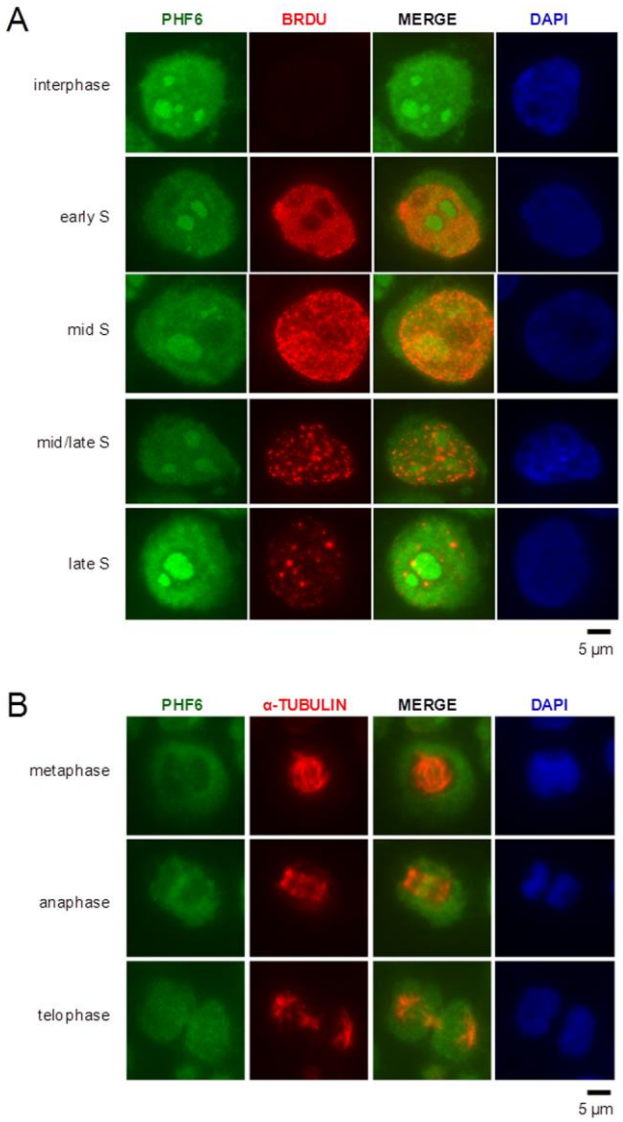

Figure 3-S3. PHF6 is co-localized with DNA throughout the cell cycle, except during mitosis.

(A) HEK 293T cells were briefly pulsed with BrdU to mark regions of active DNA replication prior to immunocytochemistry using antibodies to detect PHF6 and BrdU. PHF6 is expressed in the nucleoplasm and nucleoli during interphase and throughout S-phase. (B) HEK 293T cells were co-labeled with PHF6 and α-Tubulin antibodies by immunocytochemistry. α-Tubulin marks the mitotic spindle, and mitotic chromosomes are observed by DAPI staining. While PHF6 does not co-localize with mitotic chromosomes during metaphase and anaphase, it does so during telophase.

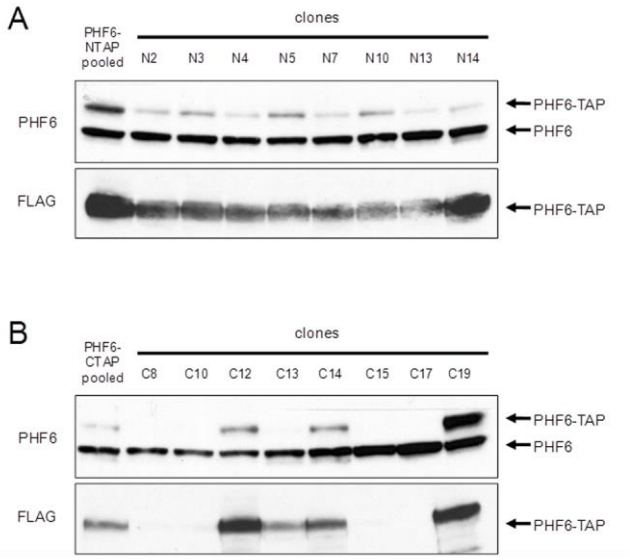

Figure 3-S4. Expression levels of PHF6-TAP in clonally derived cell lines. HEK 293T cells stably expressing PHF6-NTAP (A) or PHF6-CTAP (B) were clonally derived and whole cell lysates were analyzing by immunoblotting with antibodies for PHF6 and Flag. Whole cell lysates from pooled PHF6-NTAP and PHF6-CTAP cell lines were simultaneously analyzed by immunoblotting to provide a comparative analysis of expression levels.

Table 3-S1. Summary of antibodies used for Western blotting (W), immunocytochemistry (ICC), and immunoprecipitation (IP).

Antibody	Source	Application
Primary antibodies		
PHF6 (rabbit)[a]	Bethyl Labs (A301-450A)	ICC (1:500) (not shown)
	Bethyl Labs (A301-451A)	W (1:5000)
	Bethyl Labs (A301-452A)	W (1:2000), IP (not shown)
	Sigma (HPA001023)	W (1:5000), ICC (1:1000), IP
PHF6 (mouse, clone 4B1B6)	Josef Gecz (University of Adelaide)	W (1:1000)
BrdU (mouse)	BD Biosciences (347580)	ICC (1:500)
CHD4 (mouse)	Abcam (ab54603)	W (1:500)
CHD4 (rabbit)	Abcam (ab72418)	ICC (1:500)
Fibrillarin (mouse)	Abcam (ab18380)	W (1:10000), ICC (1:1000)
HDAC1 (mouse, clone 10E2)	Abcam (ab46985)	ICC (1:250)
HDAC1 (rabbit), H51	Santa Cruz (sc-7872)	W (1:1000), ICC (1:50), IP
Lamin A/C (mouse)	Santa Cruz (sc-7293)	W (1:1000)
M2-Flag (mouse)	Sigma (F1804)	ICC (1:500)
M5-Flag (mouse)	Sigma (F4042)	W (1:10000)
Nucleolin (mouse)	Upstate (05-565)	W (1:4000), ICC (1:500)
RBBP4 (mouse, clone 13D10)	Upstate (05-524) Abcam (ab86)	W (1:5000), ICC (1:50), IP
SIN3A (rabbit)	Santa Cruz (sc-994)	W (1:1000)
α-tubulin (mouse, clone DM1A)	Sigma (T6199)	W (1:10000), ICC (1:1000)
Secondary antibodies		
Anti-mouse HRP	Sigma (A5906)	W (1:10000)
Anti-rabbit HRP	Sigma (A4914)	W (1:10000)
Anti-mouse 488 Alexa Fluor	Invitrogen (A21202)	ICC (1:4000)
Anti-mouse 594 Alexa Fluor	Invitrogen (A21203)	ICC (1:4000)
Anti-rabbit 488 Alexa Fluor	Invitrogen (A21206)	ICC (1:4000)
Anti-rabbit 594 Alexa Fluor	Invitrogen (A21207)	ICC (1:4000)

[a] Sigma antibody was used for all experiments shown, except Figure 3-3B (WB, Bethyl 451A), Figure 3-4C (WB, HDAC1 IP, clone 4B1B6), and Figure 3-S3 (Bethyl 451A).

Table 3-S2. List of human genes corresponding to Flag-immunoprecipitated proteins identified in Table 3-1.

protein	gene	chromosome location
PHF6	*PHF6*	Xq26.2
Nucleosome Remodeling and Deacetylation (NuRD) complex		
CHD4 (Mi-2β)	*CHD4*	12p13.3
CHD3 (Mi-2α)	*CHD3*	17p13.1
RBBP4	*RBBP4*	1p35.1
RBBP7	*RBBP7*	Xp22.2
Histone proteins		
H1.2	*HIST1H1C*	6p22.2
H2B.1	*HIST1H2BB*	6p22.2
H2A.Z	*H2AFZ*	4q23
H3.1	*HIST1H3C*	6p22.2
Splicing factors		
SNRNP200	*SNRNP200*	2q11.2
PRPF8	*PRPF8*	17p13.3
HNRNPA2B1	*HNRNPA2B1*	7p15.2
HNRNPH3	*HNRNPH3*	10q21.3
HNRNPU	*HNRNPU*	1q44
RALY	*RALY*	20q11.2
HNRNPA3	*HNRNPA3*	2q31.2
PCBP2	*PCBP2*	12q13.1
HNRNPC	*HNRNPC*	14q11.2
MAGOH	*MAGOH*	1p32.3
40S/60S Ribosomal proteins		
RPLP0	*RPLP0*	12q24.2
RPS18	*RPS18*	6p21.3
RPS25	*RPS25*	11q23.3
RPL22	*RPL22*	1p36.3
RPL4	*RPL4*	15q22.3
RPL30	*RPL30*	8q22.2
Nucleolar proteins		
LYAR	*LYAR*	4p16.3
FBL	*FBL*	19q13.2
NPM1	*NPM1*	5q35.1
Other proteins		
TUBA1C	*TUBA1C*	12q13.1
PIP	*PIP*	7q34
SRP14	*SRP14*	15q15.1

CHAPTER 4

RNA tethers PHF6 to the nucleolus to mediate rDNA transcript levels

Purpose

To observe how PHF6 is recruited to the nucleolus, identify the nucleolar sub-compartments to which it is localized, and determine the function of PHF6 with respect to rRNA synthesis.

Submission Information

Manuscript submitted to the *Journal of Medical Genetics* on 10 November 2014.

Contribution of Co-Authors

Matthew A.M. Todd performed all of the experimental work and analysis, with the exception of the Pyronin Y staining shown in Figure 4-S2A, which was carried out by Michael S. Huh. The manuscript was written by Matthew A.M. Todd and edited by David J. Picketts.

ABSTRACT

Background: Ribosomal RNA synthesis occurs in the nucleolus and is a tightly regulated process that is targeted in some developmental diseases and hyperactivated in multiple cancers. Subcellular localization and immunoprecipitation coupled mass spectrometry demonstrated that a proportion of plant homeodomain (PHD) finger protein 6 (PHF6) protein is localized within the nucleolus and interacts with proteins involved in ribosomal processing. While *PHF6* mutations cause Börjeson-Forssman-Lehmann syndrome (BFLS, MIM#301900) and occur in cases of T-cell acute lymphoblastic (MIM#613065) and acute myeloid leukemia (MIM#601626), very little is known about its cellular function including its nucleolar role. **Methods:** HEK 293T cells were treated with RNase A, DNase I, actinomycin D, or 5,6-dichloro-β-D-ribofuranosylbenzimadole, followed by immunocytochemistry to determine PHF6 sub-nucleolar localization. Stable cell lines that overexpress or knockdown PHF6 were used for ChIP-qPCR and qRT-PCR studies to determine the effect on rDNA expression. **Results:** We observed the RNA-dependent localization of PHF6 to the subnucleolar fibrillar center and dense fibrillar component, at whose interface rRNA transcription occurs. Subsequent analysis by ChIP-qPCR revealed strong enrichment of PHF6 across the entire rDNA coding sequence, but not in the intergenic spacer (IGS) region. When rRNA levels were quantified in a PHF6 gain-of-function model, we observed an overall decrease of 47S pre-rRNA and 28S rRNA. These losses were accompanied by a modest increase in repressive promoter-associated RNA (pRNA) and a significant increase in the levels of IGS_{36}RNA and IGS_{39}RNA. **Conclusions:** Collectively, our results demonstrate a role for PHF6 in carefully mediating the overall levels of ribosome biogenesis within a cell.

INTRODUCTION

Mutations in the X-linked gene coding for PHF6 are associated with both germline and acquired human disease. *PHF6* mutations are the only known cause of BFLS (MIM#301900), a congenital disorder characterized by intellectual disability, truncal obesity, gynaecomastia, hypogonadism, as well as facial and digit abnormalities (Gecz et al., 2006; Lower et al., 2002). Somatic *PHF6* mutations also frequently occur in cases of T-ALL (~20-40%), AML (~3%), and CML (~2%) (Grossmann et al., 2013; Huether et al., 2014; Huh et al., 2013; Li et al., 2013; Patel et al., 2012; Van Vlierberghe et al., 2010; Van Vlierberghe et al., 2011; Yoo et al., 2012). In comparison, BFLS mutations are largely missense mutations whereas leukemic *PHF6* mutations overwhelmingly consist of truncations, frameshifts, and deletions, suggesting that severe loss-of-function mutations may favour oncogenesis (Todd and Picketts, 2012; Van Vlierberghe et al., 2010). In this regard, few BFLS patients develop leukemia although we have reported bone marrow cancers, including T-ALL, in two BFLS patients (Carter et al., 2009; Chao et al., 2010). Nonetheless, whether PHF6 loss is a primary or secondary event to the onset of leukemia remains to be determined.

Structurally, the PHF6 protein consists of two ZaP domains (Zinc knuckle, atypical PHD) as well as both nuclear and nucleolar localization sequences (Todd and Picketts, 2012). While the specific function of PHF6 remains unclear, we have previously shown that PHF6 co-purifies with multiple constituents (CHD4, RBBP4, HDAC1) of the nucleosome remodeling and deacetylation (NuRD) complex, an important developmental regulator of gene expression during embryogenesis and lineage commitment, with particularly well characterized responsibilities during lymphogenesis (Todd and Picketts,

2012; Zhang et al., 2012a). While NuRD is known to regulate transcription in both the nucleoplasm and nucleolus (Xie et al., 2012), we found that the PHF6-NuRD interaction was restricted to the nucleoplasm. These findings have since been validated by Liu et al., who confirmed a direct interaction between PHF6 and RBBP4 (Liu et al., 2014). More recently, an association between PHF6 and the PAF1 transcriptional elongation complex was reported (Zhang et al., 2013). The PHF6-PAF1 complex was essential for allowing the complete transcription of targets such as *NGC/CSPG5*, thus ensuring proper neuronal migration in murine cerebral cortices. Other studies have shown that the second ZaP domain of PHF6 interacts with double-stranded DNA, indicating that PHF6 may serve as a targeting molecule for these transcriptional regulatory complexes (Liu et al., 2014).

In addition, a significant proportion of the PHF6 protein is localized within the nucleolus, where it interacts with several nucleolar proteins (Todd and Picketts, 2012). Nucleoli are subnuclear compartments that form around nucleolar organizer regions (NORs) at rDNA tandem repeats. Each 43 kb rDNA gene repeat (GenBank, U13369) consists of a coding sequence for the 13 kb polycistronic 47S pre-rRNA transcript followed by a 30 kb intergenic spacer (IGS) region. Nucleoli primarily serve as centers for ribosome biogenesis, during which 47S pre-rRNA is transcribed, processed into 18S, 5.8S, and 28S rRNA, and incorporated into 60S and 40S ribosomes (Tschochner and Hurt, 2003). Ribosomal output is directly proportional to nucleolar size, and large nucleoli have been correlated with poor cancer prognoses (Derenzini et al., 2009). Furthermore, nucleolar dysregulation is linked to several human developmental diseases, including those with intellectual disability, and neurological disorders such as Alzheimer's and Parkinson's disease (Hannan et al., 2013; Hetman and Pietrzak, 2012).

Structurally, the nucleolus consists of three compartments (Figure 4-1A): the fibrillar center (FC), where rDNA is located, the dense fibrillar center (DFC), where early rRNA processing occurs, and the granular component (GC), where later rRNA processing occurs, with the actual transcription of pre-rRNA occurring at the interface between the FC and the DFC (Boisvert et al., 2007; Denissov et al., 2011). In this regard, both PHF6-containing complexes NuRD and PAF1 are known to mediate RNA Pol I-dependent rRNA transcription in addition to their RNA Pol II targets, suggesting that PHF6 may regulate rDNA transcription (Xie et al., 2012; Zhang et al., 2010b). Moreover, PHF6 can be recruited to the rDNA promoter by upstream binding factor (UBF), a major transcriptional activator during rRNA synthesis (Wang et al., 2013). In contrast, proteomic studies from our lab identified interactions between PHF6 and ribosomal proteins involved in rRNA processing, indicating that further studies are required to fully dissect the specific nucleolar responsibilities with which PHF6 is tasked.

The objective of this study was to utilize subnucleolar fractionation to further elucidate the role of PHF6 in regulating rDNA expression. We observed that nucleolar PHF6 is localized within both the FC and DFC compartments, where it binds to transcribed regions of rDNA and suppresses rRNA transcription. We also report the novel findings that PHF6 is recruited to the nucleolus by an RNA tethering mechanism and that the suppression of rRNA was coincidental with elevated levels of the non-coding IGS_{36}RNA, IGS_{39}RNA, and unprocessed promoter RNA (pre-pRNA) transcripts. Overall, our findings confirm a specific role for PHF6 in modulating the expression of multiple transcripts from rDNA repeats.

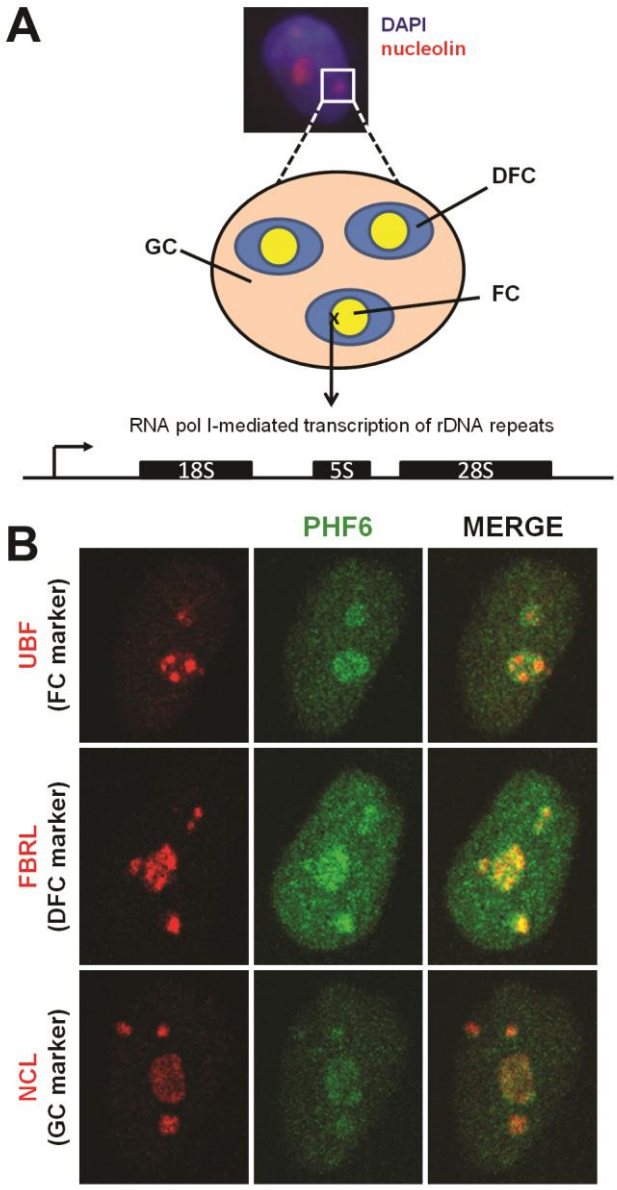

Figure 4-1. A subset of nuclear PHF6 localizes to the nucleolus.
(A) The nucleolus consists of three subnucleolar compartments: the fibrillar centre (FC), the dense fibrillar component (DFC), and the granular component (GC). The rDNA is located within the FC and 47S pre-rRNA is transcribed at the FC/DFC interface. rRNA processing occurs within the DFC and GC. (B) Confocal imaging of HeLa cells immunofluorescently stained with antibodies to PHF6 (green) and subnucleolar markers (red) representing the FC (UBF), DFC (FBRL), or GC (NCL). PHF6 partially co-localizes with markers for each subnucleolar compartment in intact nucleoli from untreated cells. Representative cell images are shown.

MATERIALS AND METHODS

Cell culture and chemical treatments

HeLa and HEK 293T cells were cultured at 37º C in DMEM supplemented with 10% FBS and 1% penicillin-streptomycin (Life Technologies). For chemical treatment assays, cultures were supplemented with either, 0.5 μg/mL ActD (Sigma), 25 μg/mL and 5,6-dichloro-β-D-ribofuranosylbenzimadole (DRB, Sigma), or 5 μg/mL α-amanitin (Sigma) for two hours, then immediately harvested for immunocytochemistry. As a control, some DRB treated cells were cultured for an additional 2 hours in DRB-free media prior to fixation. The generation of HEK 293T stable cell lines expressing either the pBRIT-LoxP-PHF6-NTAP or pBRIT-LoxP-PHF6-CTAP plasmids was previously described (Todd and Picketts, 2012), and these cells were cultured in the DMEM media additionally supplemented with 1.5 μg/μL puromycin (Sigma).

Immunocytochemistry

Chemically treated cells were trypsinized and washed with PBS on ice prior to cytocentrifugation using the Cytospin system (Thermo Shandon). Approximately 15 000 cells were applied per slide by centrifugation at 800 g for 5 minutes. Cells were fixed for 10 minutes on ice in 4% paraformaldehyde in CSK buffer (10 mM PIPES pH 6.8, 10 mM NaCl, 300 mM sucrose, 3 mM MgCl2, 2 mM EDTA), then washed with PBS before permeabilizing for 10 minutes with 0.5% Triton X in PBS at room temperature. Cells were blocked for 1 hour at room temperature in PBS with 20% horse serum and 0.5% FBS. PHF6 (Sigma, HPA001023; 1:1000), UBF (Santa Cruz, sc-13125; 1:1000), fibrillarin (Abcam, ab4566; 1:1000), coilin (BD Biosciences, 612074; 1:1000), and nucleolin (Millipore, 05-565; 1:250) primary antibodies were diluted in PBS and

incubated with the fixed cells overnight at 4°C in a humidifying chamber. Alexa Fluor 488 (A21202) and 594 (A21207) secondary antibodies (Life Technologies; 1:4000) were incubated for 40 minutes at room temperature, prior to washing and mounting slides (DAKO) for microscopy.

Nuclease treatments

Nuclease treatments were adapted from the previously described method of (Chamousset et al., 2010a). Briefly, slides containing HEK 293T (~15 000) cells were rinsed once with PBS and once with ASE buffer (20 mM Tris pH 7.5, 5 mM $MgCl_2$, 0.5 mM EGTA), then permeabilized (5 min, room temperature) in ASE buffer containing 0.1% Triton X-100. Cells were then incubated (20 min, room temperature) with 10 µg/mL DNase I or 100 µg/mL RNase A in ASE buffer. Untreated control incubations were performed in nuclease-free ASE buffer. Cells were prepared for immunocytochemistry as described above. DAPI (100 ng/mL, 3 min, room temperature) staining was used to visualize DNA, while RNA was visualized by incubating cells with 10 µM Pyronin Y for 10 minutes (after DAPI).

Image acquisition and processing

All cell images were captured with a Plan-Apochromat 63x/1.40 Oil DIC M27 objective on a Zeiss LSM 510 laser scanning confocal microscope, equipped with UV (405 nm), argon (488 nm), and helium/neon (546 nm) lasers. Images were initially acquired with Zeiss ZEN 2009 software using a zoom factor of 1.5, then exported to Zeiss LSM Image Browser v.4.2.0.121 software for contrast processing and cropping.

Chromatin immunoprecipitation

Chromatin immunoprecipitation (ChIP) was performed using the EZ-ChIP protocol (Millipore, #17-371). Briefly, adherent HEK 293T cells were grown on 10 cm tissue culture plates (80-90% confluency), crosslinked with 1% formaldehyde for 10 minutes at room temperature, washed with ice cold PBS, and scraped. Harvested cells were resuspended in SDS lysis buffer (50 mM Tris-HCl pH 7.8, 10 mM EDTA, 1% SDS; 1 mL buffer for every 10^7 cells), then sonicated (5 x 10 second pulses, 30% amplitude). The average chromatin fragment size was determined to be about 400-500 bp as confirmed by agarose gel electrophoresis. Sonicated lysates were centrifugated at 10 000 g for 10 minutes to pellet insoluble material and divided into 100 µL aliquots (~10^6 cells), then 900 µL of ChIP dilution buffer was added to each aliquot (16.7 mM Tris-HCl pH 7.8, 167 mM NaCl, 1.2 mM EDTA, 1.1% Triton X-100, 0.01% SDS). Diluted lysates were pre-cleared, then 10 µL of the sample was removed as 1% input. The remaining aliquot was then incubated with 1 µg of mouse/rabbit IgG (Jackson) or one of the PHF6, CTCF (Millipore, 07-729), UBF, or histone H3 (Abcam, ab1791) primary antibodies overnight at 4º C with rotation. Antibody-protein complexes were then captured by adding 60 µL (25% slurry) of pre-blocked Protein G-agarose (Santa Cruz, for mouse)/Protein A-sepharose (GE Healthcare, for rabbit), and beads were subsequently washed once with low salt wash buffer (20 mM Tris-HCl pH 7.8, 150 mM NaCl, 2 mM EDTA, 1% Triton X-100, 0.1% SDS), once with high salt wash buffer(20 mM Tris-HCl pH 7.8, 500 mM NaCl, 2 mM EDTA, 1% Triton X-100, 0.1% SDS), once with LiCl wash buffer (10 mM Tris-HCl pH 7.8, 1 mM EDTA, 1% deoxycholate, 1% Nonidet P-40, 250 mM LiCl), and twice in Tris-EDTA buffer. An equivalent volume of elution

buffer (1% SDS, 100 mM $NaHCO_3$) was then added to the washed beads and 1% input aliquots, followed by an overnight at 65º C in the presence of 200 mM NaCl to reverse the crosslinks. Residual RNA and protein were eliminated by digesting with 10 μg of RNase A and 10 μg of proteinase K respectively. Final DNA products were purified by phenol-chloroform extraction and resuspended in Tris-EDTA buffer in preparation for subsequent qPCR analysis.

RNA extraction and quantitative real-time PCR

RNA extractions were performed from 10^6 cells (per experiment) using an RNeasy Mini Kit (Qiagen). Total RNA (1 μg) was used for reverse transcription (RT) with random primers and SuperScript III enzyme (Life Technologies) to generate cDNA. ChIP-DNA or RT samples were prepared for qPCR using SYBR Green Advantage qPCR premix (Clontech) and reactions performed on an Mx3000P system (Stratagene). All primer sets are listed in Table 4-S1. For ChIP-qPCR reactions, rDNA fold changes between ChIP products and 1% input were calculated using the following equation: fold change = $2^{-(\text{input Ct - ChIP Ct})}$. For qRT-PCR reactions, fold changes were calculated with the ΔΔCt method using GAPDH as an internal control.

Statistics

Statistical analyses were performed in Microsoft Excel. Two-tailed t tests, 95% confidence intervals, and 99% confidence intervals were used to determine significance.

RESULTS

PHF6 localizes to the nucleolar FC and DFC

We previously performed cellular fractionation studies indicating that PHF6 is present within the nucleoplasm and nucleolus (Todd and Picketts, 2012). To better understand the nucleolar role of PHF6 and its subnucleolar localization, we performed immunocytochemistry to determine if PHF6 co-localizes with any markers for the nucleolar subcompartments: UBF (FC marker), fibrillarin (FBRL, DFC marker), or nucleolin (NCL) (GC marker). As shown in Figure 4-1B, these initial studies showed some overlap of PHF6 localization with each marker, yet they were inconclusive in distinguishing a specific compartment within which PHF6 resides. As such, we proceeded to use chemical-based treatments as a more definitive means of achieving separation between the nucleolar subcompartments.

To better delineate how PHF6 localizes within the nucleolus, HEK 293T cells were treated with actinomycin D (ActD) and DRB to induce nucleolar reorganization, as previously described (Chamousset et al., 2010a). Briefly, ActD induces nucleolar disassembly by inhibiting RNA Pol I, thereby arresting pre-rRNA transcription, while DRB inhibits casein kinase 2 to uncouple the rRNA processing machinery from RNA Pol I-mediated transcription. Unlike the ActD treatment, the effects of DRB are reversible upon its removal, and RNA Pol I will continue to transcribe pre-rRNA upon nucleolar disassembly (Scheer et al., 1984). Studies of nucleolar disassembly in response to chemical treatments and during mitosis have previously demonstrated that proteins found in particular nucleolar compartments remain associated with one another during nucleolar reorganization, thus the co-localization of PHF6 with particular markers before and after

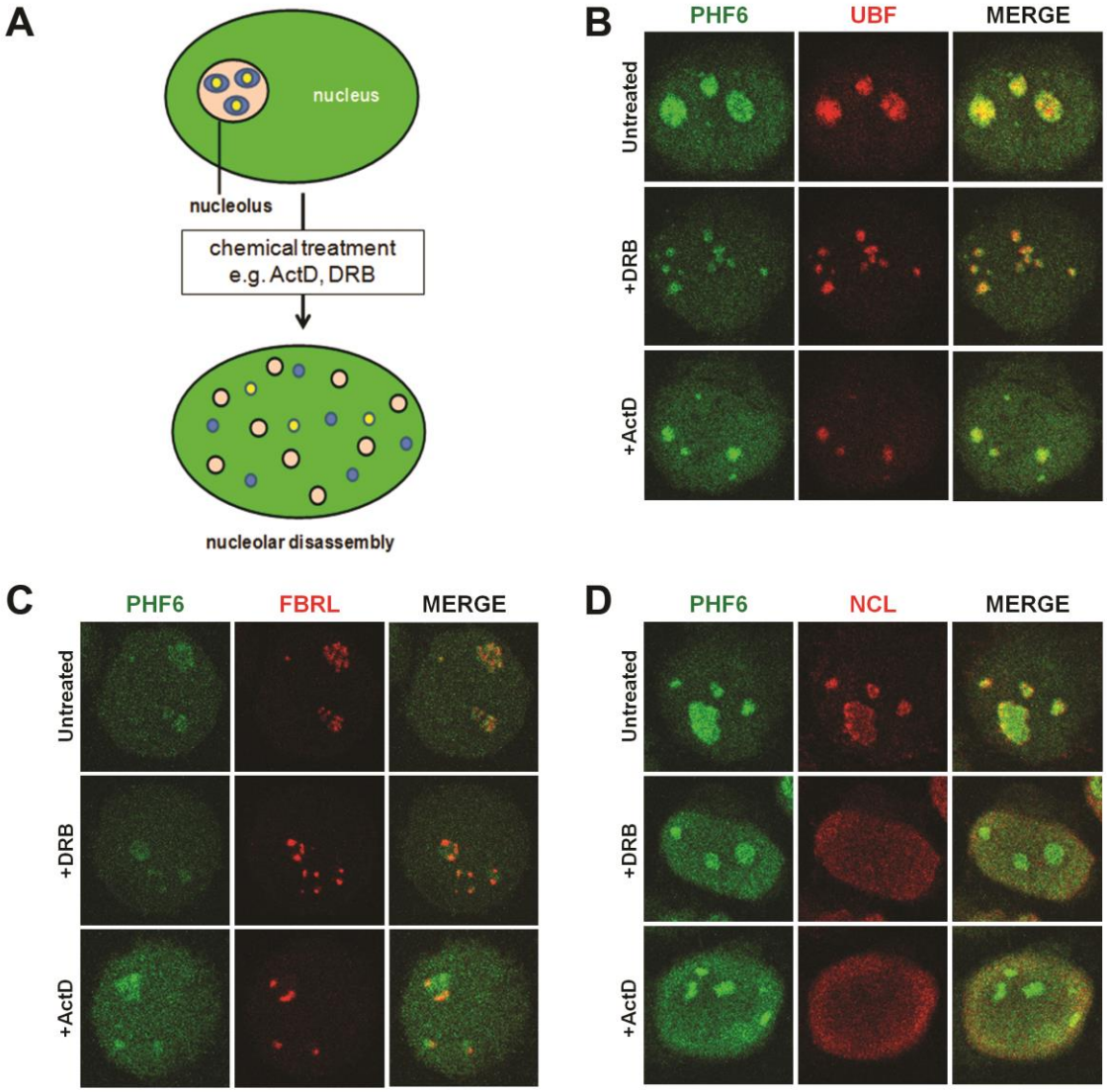

Figure 4-2. PHF6 co-localizes with the nucleolar FC and partially co-localizes with the DFC.

(A) Nucleoli can be partially or completely disassembled in response to chemical treatment. 5,6-dichloro-1-beta-D-ribofuranosylbenzimidazole (DRB) causes the uncoupling of rRNA processing from rDNA transcription, while actinomycin D (ActD) inhibits RNA pol I at low concentrations. During nucleolar reorganization, proteins that are found in the same nucleolar compartments commonly remain associated in the same nascent foci. HEK 293T cells were treated with either 25 µg/mL DRB or 0.5 µg/mL Act D for 2 hours. Cells were then fixed and labeled with antibodies to PHF6 (green) and either (B) UBF, (C) FBRL, or (D) NCL (red), then visualized by confocal microscopy. PHF6 strongly co-localizes with UBF in both the DRB and ActD treatments, and also partially co-localizes with FBRL foci. Representative cell images are shown. Additional controls for these chemical treatments are shown in Figure 4-S1.

treatment would imply its association with that particular nucleolar compartment (Figure 4-2A) (Dundr et al., 2000; Scheer et al., 1993; Weisenberger and Scheer, 1995).

HEK 293T cells were treated with 0.5 μg/mL ActD or 25 μg/mL DRB for 2 hours prior to immunocytochemistry and confocal microscopy, with untreated cells serving as a negative control (Figure 4-2B,C,D) (Scheer et al., 1984; Zandomeni et al., 1986). In both the ActD and DRB treatments, PHF6 was found to co-localize with UBF (Figure 4-2B) and partially co-localize with FBRL (Figure 4-2C), but did not co-localize with NCL (Figure 4-2D). Because ActD (at higher concentrations) and DRB are known to inhibit RNA Pol II, we also treated HEK 293T cells with α-amanitin (5 μg/mL, 2 hours), which specifically inhibits RNA Pol II but not RNA Pol I (Lindell et al., 1970). As shown in Figure 4-S1A, the α-amanitin treatment did not induce nucleolar reorganization. Additionally, HEK 293T cells that were treated with 25 μg/mL DRB for 2 hours were also grown in untreated media (without DRB) for a further 2 hours to assess the reversibility of the DRB-induced nucleolar disassembly. Indeed, the DRB-induced PHF6 reorganization proved to be reversible (Figure 4-S1A).

Cajal bodies exist as known sites for snRNP/snoRNP biogenesis, and are recruited to nucleoli in response to DRB exposure as well as other instances of nucleolar stress (Boulon et al., 2010). To rule out the possibility that PHF6 was associating with Cajal bodies, we also co-labeled ActD and DRB treated cells with PHF6 and COILIN, a marker for Cajal bodies. However, for each treatment, we did not observe any co-localization between PHF6 and COILIN (Figure 4-S1B). Thus from these experiments, we conclude that PHF6 is most likely localized to the interface between the FC and the DFC, where rDNA is transcribed.

PHF6 localization to the nucleolus is RNA-dependent

The FC/DFC interface is the site where 47S pre-rRNA is transcribed from rDNA, and harbours proteins with the ability to interact with DNA and/or RNA. Since PHF6 was reported to bind to dsDNA and be recruited to the rRNA promoter, we expected the nucleolar recruitment of PHF6 to be DNA-dependent (Liu et al., 2014; Wang et al., 2013). To test this hypothesis, HEK 293T cells were permeabilized and digested with 10 μg/mL of DNase I or 100 μg/mL of RNase A prior to fixation and immunocytochemistry using confocal microscopy for PHF6 and UBF (DNA-dependent marker) or nucleolin (RNA-dependent marker) (Figure 4-3A,B). UBF binds coding rDNA as a transcriptional activator. The DNase treatment resulted in the loss of UBF binding in the nucleolus, but RNase treatment had no effect (Figure 4-3A). DNA loss is apparent with DNase, as demonstrated by reduced DAPI staining (Figure 4-3A). To our surprise, nucleolar PHF6 remained in the nucleolus after the DNase treatment (Figure 4-3A,B), but was lost following RNase treatment, suggesting that PHF6 is mainly associated with the nucleolus through an RNA-based mechanism. As expected, we observed nucleolin localization to be dependent on RNA, but not DNA (Figure 4-3B). As a control, treated cells were stained with Pyronin Y to label RNA, demonstrating rRNA loss in the RNase treatment, but not with DNase (Figure 4-S2A). Fibrillarin was also found to be significantly depleted from nucleoli following RNase treatment, but not with DNase (Figure 4-S2B). Taken together, we conclude that PHF6 requires an association with RNA in order to be localized within the nucleolus. Since fibrillarin associates with both rDNA and rRNA in the nucleolus, but was only lost after the RNase treatment in our hands, we cannot exclude the possibility that PHF6 interacts with both DNA and RNA (Ochs et al., 1985).

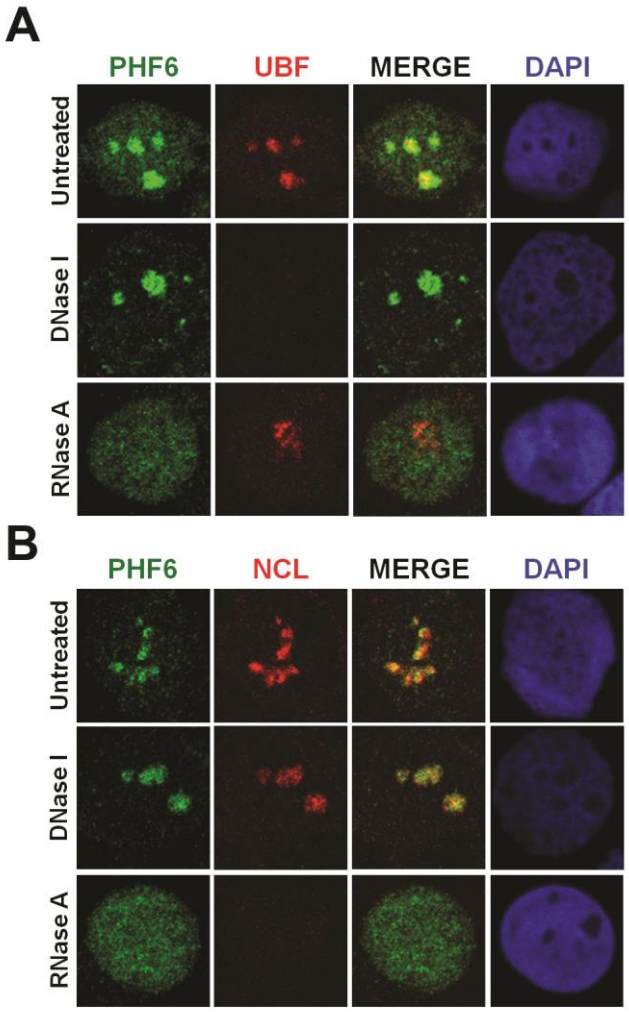

Figure 4-3. The nucleolar localization of PHF6 is RNA-dependent.
(A, B) HEK 293T cells were treated with either DNase I (10 µg/mL) or RNase A (100 µg/mL) then immunofluorescently stained with antibodies to PHF6 (green) and UBF (A; red), or NCL (B; red). DAPI counterstain was used to visualize DNA within the nuclei. Treatment with RNase A results in the near loss of PHF6 from the nucleolus. Conversely, nucleolar PHF6 expression is not affected following treatment with DNase I. The efficacy of the DNase I treatment is confirmed by accompanying reduction in DAPI intensity. Representative cell images are shown. PHF6 co-localization controls with Pyronin Y (to visualize RNA) and FBRL are shown in Figure 4-S2.

PHF6 binds to the rDNA transcribed regions

The localization of PHF6 to the FC and DFC strongly implicates a role for PHF6 in the regulation of rRNA transcription, which occurs at the boundary separating these two nucleolar compartments. As such, we sought to determine if (i) PHF6 binds rDNA itself, and (ii) if PHF6 binds to the pre-rRNA coding sequence or to IGS sequences, by performing chromatin immunoprecipitation followed by quantitative PCR (ChIP-qPCR) using previously described primer pairs along the entire length of the 43 kb rDNA gene (Figure 4-4A) (Zhu et al., 2010). It has long been known that the IGS contains multiple RNA Pol I responsive promoters, which can be correlated with the recent identification of multiple non-coding IGS transcripts (Cassidy et al., 1987; Jacob et al., 2012; Kuhn and Grummt, 1987; Moss and Birnstiel, 1979; Moss et al., 1980). In one such instance, an IGS transcript originates from a promoter ~2 kb upstream from the rRNA TSS and is processed into 150-250 nt RNA molecules which are complementary to the rDNA promoter itself (Mayer et al., 2006). These so-called promoter-associated RNAs (pRNA) can subsequently silence rRNA transcription through the recruitment of the nucleolar remodeling complex (NoRC) and DNMT3B (Mayer et al., 2006; Schmitz et al., 2010). In another example, non-coding IGS_{16}RNA/IGS_{22}RNA, and IGS_{28}RNA (each numbered with respect to its downstream position from the TSS in kb) become induced in response to environmental stress (e.g. heat shock, acidosis), binding HSP70 and VHL respectively, sequestering these proteins in a nucleolar detention center whose formation leads to an arrest in rRNA synthesis (Audas et al., 2012; Jacob et al., 2013). The identification of these transcripts may indeed be the tip of the iceberg as multiple non-coding RNAs appear to be expressed across the entire IGS (Audas et al., 2012).

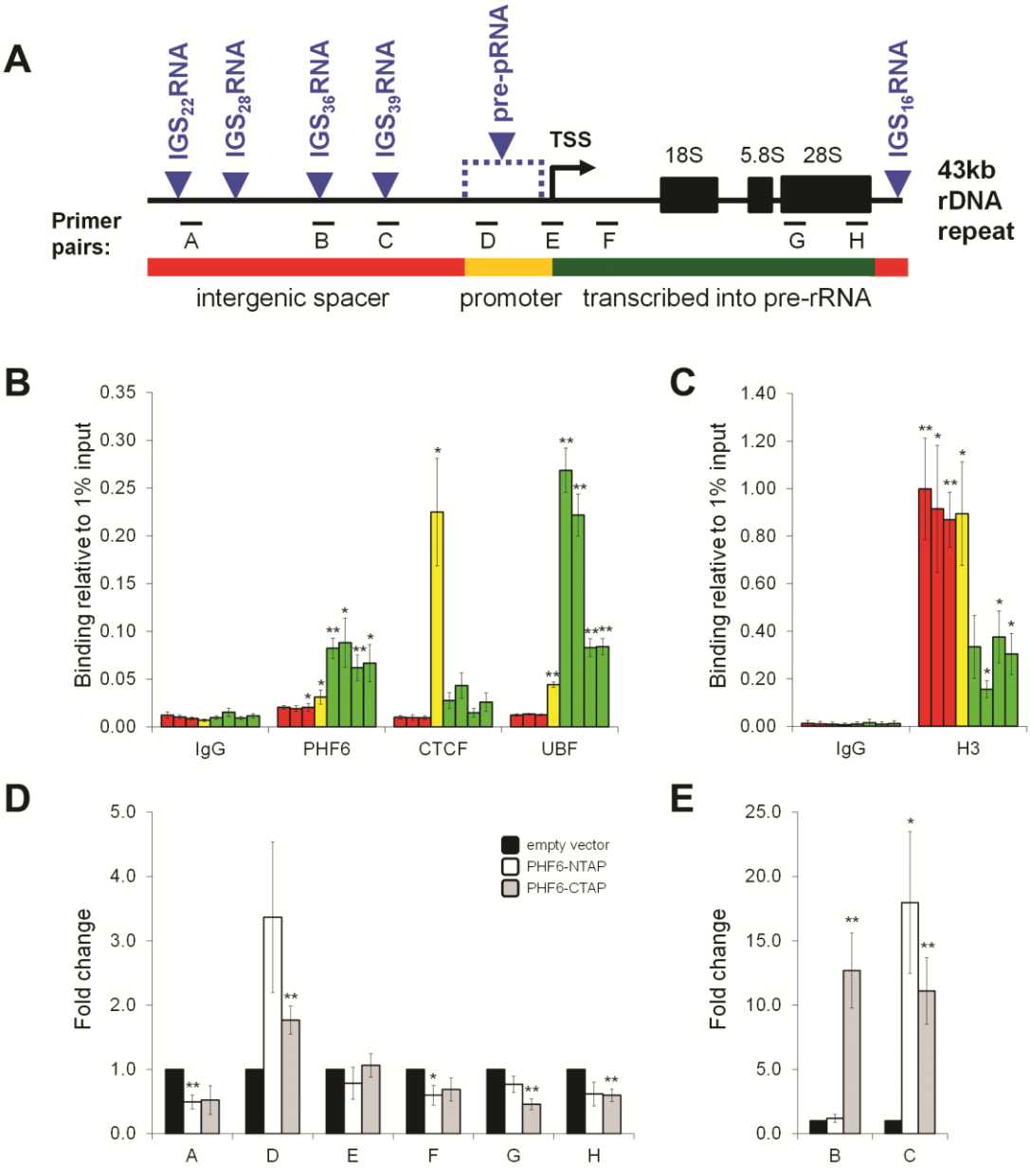
A
IGS22RNA
IGS28RNA
IGS36RNA
IGS39RNA
pre-pRNA
TSS
18S
5.8S
28S
IGS16RNA
43kb rDNA repeat
Primer pairs:
A
B
C
D
E
F
G
H
intergenic spacer
promoter
transcribed into pre-rRNA
B
Binding relative to 1% input
IgG
PHF6
CTCF
UBF
C
Binding relative to 1% input
IgG
H3
D
Fold change
empty vector
PHF6-NTAP
PHF6-CTAP
A
D
E
F
G
H
E
Fold change
B
C

Figure 4-4. PHF6 binds to the transcribed regions of rDNA repeats to mediate the expression of rDNA coding and non-coding transcripts.

(A) Schematic diagram of the rDNA gene repeat, showing the intergenic spacer (IGS) region (red), the rDNA promoter (yellow), and the rRNA coding region (green). Primer pairs were designed to amplify IGS sequences (A,-20188/-20077; B,-6942/-6839; C,-3712/-3610), the promoter sequence (D,-1017/-924), and the coding sequences (E,-47/+32; F,+307/+445; G,+8204/+8300; H,+12855/+12970) for ChIP-qPCR (panels B, C) or qRT-PCR (panels D, E) experiments. The locations of sequences corresponding to non-coding IGS and unprocessed pRNA (pre-pRNA) transcripts are indicated in blue. (B) PHF6 enrichment throughout the rDNA repeat was determined by ChIP-qPCR (n=5) analysis performed from approximately 10^6 HEK 293T cells (per experiment). CTCF (n=3) and UBF (n=4) ChIP-qPCR products were quantitated as controls for binding to the coding rDNA promoter and transcribed regions, respectively. For each antibody, the individual bars on the graph represent the binding (relative to 1% input) for individual primer sets in sequential order: IGS (primer sets A-C, red), promoter (primer set D, yellow), and transcribed (primer sets E-H, green). (C) Histone H3 (n=3) ChIP-qPCR was performed as an additional positive control. (D, E) qRT-PCR analysis (n=5) of RNA isolated from HEK 293T cell lines expressing empty vector or PHF6 overexpression cell lines (PHF6-NTAP, PHF6-CTAP). Given the large fold changes observed with primer sets B and C, these samples were plotted separately (panel E). All Ct values were normalized to GAPDH amplification and fold changes are calculated relative to the empty vector dCt value for all treatments. Bars represent standard error (*$p<0.05$, **$p<0.01$, two-tailed student's t-test). For the quantification of rRNA under conditions of PHF6 knockdown, see Figure 4-S5B.

As shown in Figure 4-4B, ChIP-qPCR for endogenous PHF6 demonstrated significant enrichment of PHF6 at the transcriptional start site (TSS) and in the rDNA coding sequence (-47/+32; +307/+445; +8204/8300; +12855/12970 primer sets), with less binding at the promoter (-1017/-924 primer set), and little to no binding in the IGS (-20188/-20077; -6942/-6839; -3712/-3610 primer sets) in comparison to IgG ChIP-qPCR. To confirm the specificity of the purified DNA fragments, we also performed ChIP-qPCR for CTCF, which preferentially marks the boundaries between active and inactive chromatin, and UBF (Figure 4-4B) (Barski et al., 2007). Consistent with previous reports, CTCF only bound the rRNA promoter sequence, while UBF was bound to the entire rDNA coding sequence, and most highly enriched at the 5' end (van de Nobelen et al., 2010). Histone H3 ChIP-qPCR was performed as an additional positive control, demonstrating strong enrichment throughout the rDNA repeat, including the IGS sequences (Figure 4-4C). Knowing now that PHF6 preferentially binds actively transcribed rDNA coding region, we next sought to determine how this bound PHF6 may contribute to the synthesis of rRNA.

PHF6 overexpression represses rRNA and activates non-coding IGS transcripts

PHF6 has previously been linked to RNA Pol II-mediated transcription through its nucleoplasmic associations with NuRD and PAF1. Knowing that PHF6 binds the rDNA coding sequence, we next asked whether this binding serves to enhance or repress rRNA expression by quantitating rRNA levels in a PHF6 gain-of-function model. For our model, we utilized stable cell lines overexpressing N- or C-terminally Flag-tagged PHF6 (PHF6-NTAP, PHF6-CTAP), which we previously employed to co-purify PHF6-NuRD (Todd and Picketts, 2012). As an additional control, PHF6 shRNA knockdown was stably

achieved using pGIPZ lentivirus (Open Biosystems) in three cell lines, each expressing a different shRNA sequence. PHF6 overexpression or knockdown in these cell lines was confirmed at both the mRNA and protein levels (Figure 4-S3A,B,C). Previously, the knockdown of PHF6 in HeLa cells was reported to cause a reduction in cell proliferation and with an associated cell cycle arrest at G_2/M (Wang et al., 2013). However, we did not observe any noticeable changes in the proliferation rates of our PHF6 shRNA cell lines after seeding our cell lines at a low confluency and monitoring cell proliferation over five days (Figure 4-S3D). Furthermore, when PHF6 shRNA cell lines were given a 1 hour pulse of 30 μM BrdU, then quantitated for BrdU and propidium iodide over a 24 hour time course, no obvious cell cycle delays were apparent (Figure 4-S4). Conversely, we observed reduced rates of cell proliferation in our overexpression model after five days (Figure 4-S3E), which seems consistent with the perceived role of PHF6 as a tumour suppressor.

To quantitate rRNA, overexpression and knockdown cell lines were seeded at a low confluency and total RNA was isolated after two days for qRT-PCR analysis using the primer sets indicated in Figure 4-4A, which account for the following potential transcripts: 28S rRNA (+8204/8300; +12855/12970), 47S pre-rRNA (+307/+445), unprocessed pre-pRNA (-1017/-924), IGS_{23}RNA (-20188/-20077), IGS_{36}RNA (-6942/-6839), and IGS_{39}RNA (-3712/-3610). When normalized to pre-pRNA, levels of the 47S pre-rRNA transcripts were about 100-fold higher, consistent with previous observations (Mayer et al., 2006), while levels of 28S rRNA are approximately 10^4-10^6 times more elevated than pre-pRNA (Figure 4-S5A). When rRNA levels were quantitated in the PHF6 overexpression cell lines, statistically significant decreases in the relative amounts

of 47S pre-rRNA and 28S rRNA were observed for the +307/+445, +8204/8300, and +12855/12970 primer sets (Figure 4-4D), indicative of a reduction in the transcription of rRNA. There was also a reduction in IGS_{23}RNA transcript levels for which no function has yet been attributed. Unexpectedly, we also observed elevated transcript levels for pre-pRNA (Figure 4-4D) as well as the IGS_{36}RNA and IGS_{39}RNA transcripts (Figure 4-4E). Indeed, levels of the IGS_{39}RNA transcript were only 2-5X lower than those of the 47S pre-rRNA in our overexpression cell lines (Figure 4-S5A). Thus we observe that the outcome of enhanced PHF6 binding to the rDNA coding sequence is a reduction in rRNA synthesis and an activation of pre-pRNA and IGS RNA approximately 3.5-7 kb upstream of the TSS. In contrast to our overexpression model, no consistent or significant changes were observed amongst rDNA transcript levels following PHF6 knockdown (Figure 4-S5B).

DISCUSSION

Mutations in genes encoding chromatin remodeling proteins are well appreciated as a cause of developmental disorders and many of these genes are now being increasingly identified as altered in various cancers. In this regard, PHF6 mutations are the cause of BFLS and have been identified in T-ALL, AML, and CML. Despite the dual disease role for PHF6 very little is known about its function and how mutations can contribute to disease pathology. Previously, we demonstrated that PHF6 is localized both in the nucleoplasm and in the nucleolus suggesting that it may have distinct subnuclear functions. We now report that nucleolar PHF6 localizes to the FC and DFC of the nucleolus, at whose interface rRNA transcription and early rRNA splicing occurs. Interestingly, PHF6 requires RNA to localize to the nucleolus, but once properly localized, it binds to rDNA coding sequences. Upon the overexpression of PHF6, we observed a decrease in overall 47S pre-rRNA and 28S rRNA levels, which coincided with enhanced expression of repressive pre-pRNA and non-coding IGS RNA in a region approximately 3.5-7 kb upstream of the rDNA TSS, suggesting that PHF6 mediates overall levels of ribosome biogenesis.

RNA Pol I-mediated elongation of pre-rRNA is a key regulatory step during ribosome biogenesis and is coupled with the downstream processing of rRNA (Schneider, 2012; Schneider et al., 2007). Previous work has shown that PHF6 interacts with the PAF1 transcriptional elongation complex to mediate RNA Pol II transcription (Zhang et al., 2013). Other studies have also shown that the PAF1 complex activates RNA Pol I-mediated elongation during rRNA synthesis (Zhang et al., 2010b). Taken together, it suggests that PHF6 may be interacting with PAF1 to mediate transcriptional elongation

of the rDNA gene. Consistent with this idea, our ChIP-qPCR results demonstrated strong enrichment of PHF6 protein at the TSS and across the entire rDNA gene body, which differs from one other study that found PHF6 only at the promoter region (Wang et al., 2013). Nonetheless, this study suggested that PHF6 was a suppressor of rRNA synthesis. Indeed, we demonstrated that overexpression of PHF6 reduced 47S pre-rRNA and 28S rRNA levels further suggesting that PHF6 may have a repressive effect on RNA Pol I-mediated elongation and a consequent uncoupling with rRNA processing.

When PHF6 is overexpressed, we also observed increased expression levels of pre-pRNA, IGS_{36}RNA, and IGS_{39}RNA transcripts. It has been well documented that pRNA contributes to the epigenetic silencing of rRNA through direct interactions with NoRC and DNMT3B, which methylate histones and DNA respectively (Mayer et al., 2006; Schmitz et al., 2010). While the roles of IGS_{36}RNA and IGS_{39}RNA transcripts are not as well characterized, they are upregulated under conditions of transcriptional stress (Audas et al., 2012). Since PHF6 does not bind to these regions, one possible explanation is that RNA Pol I transcription is redirected to these regions to further promote rDNA gene silencing when rRNA elongation is repressed.

Finally, we observed that PHF6 localization to the nucleolus was an RNA-dependent process despite its binding to the rDNA locus. Interestingly, this finding is similar to fibrillarin, which also localizes to the FC/DFC boundary and associates with rRNA and rDNA (Ochs et al., 1985). Since rRNA transcription and early processing events occur at the FC/DFC boundary, it suggests that the ability of PHF6 to interact with both RNA and DNA may be critical for ribosome biogenesis regulation. PHF6 contains two ZaP nucleic acid interaction domains, and the second of these domains is known to

bind dsDNA (Liu et al., 2012; Liu et al., 2014). Interestingly, point mutations within the first ZaP domain of PHF6 were shown to be essential for nucleolar localization, although it was proposed to be an interaction surface for UBF and thus, indirect recruitment (Wang et al., 2013). Given that both ZaP domains of PHF6 share strong homology, we propose that PHF6 may interact with nascent pre-rRNA through its first ZaP domain, while binding to rDNA through its second ZaP domain. In this way, PHF6 may potentially serve as a scaffolding bridge between the processes of elongation and early rRNA processing within the FC and DFC.

Abnormal nucleoli are a hallmark of several developmental and acquired human diseases, including intellectual disability and cancer, respectively. Dysfunctional ribosome biogenesis results from mutations that target key aspects in the regulation of rDNA, including epigenetic activation/silencing, the RNA Pol I transcriptional machinery, or the post-transcriptional processing of pre-ribosomes and maturing rRNA transcripts (Hannan et al., 2013). We have provided evidence that PHF6 is localized to the FC/DFC boundary within the nucleolus where it is likely involved in the regulation of rRNA transcriptional elongation and early rRNA processing events. Future efforts should be directed at defining its specific role in ribosome biogenesis and delineating how PHF6 mutations promote disease pathogenesis.

ACKNOWLEDGEMENTS

Laura Trinkle-Mulcahy, Robin Parks, Keqin Yan, Jeff Hamill, Matias Alvarez-Saavedra, Danton Ivanochko, and Lemuel Racacho provided reagents and/or technical advice. Confocal microscopy support was provided by staff at the University of Ottawa Cell Biology & Image Acquisition Core Facility. MAMT was supported by an Ontario Graduate Scholarship. This work was supported by operating grants to DJP from the Canadian Institutes of Health Research (MOP-97764, MOP-133586) and an operating grant from the Cancer Research Society, University of Ottawa, and Ottawa Hospital Research Institute partnership program.

SUPPLEMENTARY INFORMATION

SUPPLEMENTARY MATERIALS AND METHODS

PHF6 Knockdown

Stable PHF6 shRNA knockdown cell lines were generated using the GIPZ PHF6 shRNA Viral Particle Starter Kit (Open Biosystems, VGH5526-EG84295). Briefly, HEK 293T cells, seeded the day before transduction at 5 x 10^4 cells per well, were transduced for 6 hours at 37º C in serum-free media containing 4 x 10^4 lentivirus particles and 8 μg/μL polybrene then allowed to recover in growth media (DMEM, 10% FBS, 1% penicillin-streptomycin) for 72 hours, prior to selection in 1.5 μg/μL puromycin. The following antisense sequences were used for PHF6 shRNA mediated knockdown: KD #1 (5'-TCAAAGTCTCCAAATTCTG, catalogue # V2LHS_138602), KD #2 (5'-TTTCCTCGTTTAATCTCCT, catalogue # V3LHS_350404), and KD #3 (5'-AAAACTTTCTTCTAAATCA, catalogue # V3LHS_350403). PHF6 knockdown was confirmed both by qRT-PCR (Figure 4-S3B) and Western blot (Figure 4-S3C). HEK 293T cell lines stably infected with the empty GIPZ vector were used as a negative control.

Western blotting

Transformed HEK 293T cells were harvested on ice and lysed in radioimmunoprecipitation assay buffer (RIPA; 50 mM Tris HCl pH 7.8, 150 mM NaCl, 1% Nonidet P-40, 0.5% sodium deoxycholate, 0.1% sodium dodecyl sulphate), resolved by SDS-PAGE (3-8% Tris-Acetate Novex gel, Life Technologies), and transferred onto a PVDF membrane (Millipore). Membranes were blocked in 1X TBST with 5% milk for 2 hours at room temperature, then incubated with primary antibody for PHF6 (HPA001023,

Sigma, 1:5000 dilution) or α-tubulin (T9026, Sigma, 1:10 000 dilution) overnight at 4°C in 1X TBST with 5% BSA. Following three 1X TBST washes, membranes were incubated with the appropriate anti-rabbit (A4914, Sigma) or anti-mouse (A5906, Sigma) secondary antibody (1:10 000 dilution) in blocking solution for 45 minutes at room temperature. Development of the membranes was achieved using enhanced chemiluminescence (GE Healthcare) and an SRX-101A (Raytech) film developer.

Cell proliferation assay

Transformed HEK 293T cell lines were seeded on 10 cm plates (10^5 cells per plate) and cultured at 37º C. Cells were harvested by trypsin digest at 24 hrs (day 1), 48 hrs (day 2), 72 hrs (day 3), 96 hrs (day 4), and 120 hrs (day 5) after seeding and the concentration of viable cells for each sample was measured using the Vi-CELL XR system (Beckman Coulter). Cumulative population doubling was used to measure cellular growth rates with the following formula: counts per day = [log(day X concentration)-log(day 1 concentration)]/log(2).

BrdU pulse-chase cell cycle assay

This BrdU protocol was adapted from (Huh et al., 2012). Briefly, stable HEK 293T cells expressing PHF6 shRNA (KD #1, KD#2, KD#3) or empty GIPZ vector were seeded at a confluency of 2 x 10^5 cells on a 10 cm tissue culture plate and cultured for 48 hours at 37º C, then pulsed with 30 μM BrdU for 1 hour at 37º C. Cells were provided three PBS washes to remove PBS, then grown in fresh selection media and harvested at the following timepoints (measured upon BrdU removal): 0 hrs, 4 hrs, 8 hrs, 12 hrs, 16 hrs, 20 hrs, and 24 hrs. Cells were fixed in ice cold 70% ethanol and prepared for flow cytometry analysis as described (Huh et al., 2012; Stubbert et al., 2007), including

labeling with a 1:100 dilution of BrdU primary antibody (BD Biosciences, 347580), 1:500 diluted Alexa Fluor 488 secondary antibody, and propidium iodide (Sigma). Flow cytometry was performed using a Beckman Coulter FACS Station and data analysis was performed with Flowing software version 2.5.1 (04-Nov-2013, created by Perttu Terho at the Turku Centre for Biotechnology, http://www.flowingsoftware.com/).

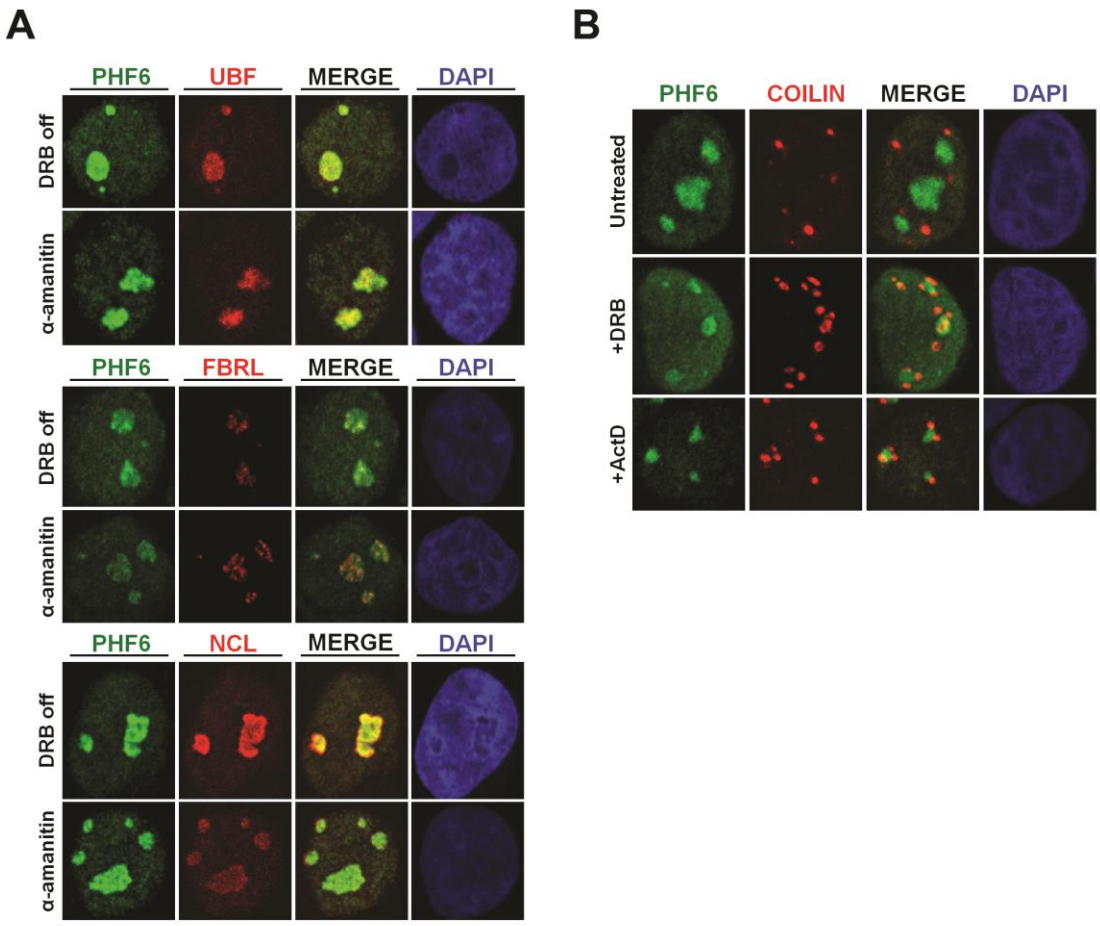

Figure 4-S1. PHF6 co-localizes with the nucleolar FC and partially co-localizes with the DFC.

(A) To demonstrate the reversibility of the DRB treatment, HEK 293T cells were treated with 25 µg/mL DRB for 2 hours and allowed to recover for 2 hours (DRB off). HEK 293T cells were also treated with 5 µg/mL of α-amanitin, an RNA pol II inhibitor, to confirm if the ActD-mediated nucleolar disassembly observed in Figure 4-2 was indeed specific to RNA pol I inhibition. Cells were then fixed and labeled with antibodies to PHF6 (green) and either UBF, FBRL, or NCL (red), then visualized by confocal microscopy. Cells were counterstained with DAPI to visualize nuclei. (B) HEK 293T cells were treated with either 25 µg/mL DRB or 0.5 µg/mL Act D for 2 hours. Cells were then fixed and labeled with antibodies to PHF6 (green) and COILIN (red), a marker for Cajal bodies. Representative cell images are shown. This supplementary figure is an accompaniment for Figure 4-2.

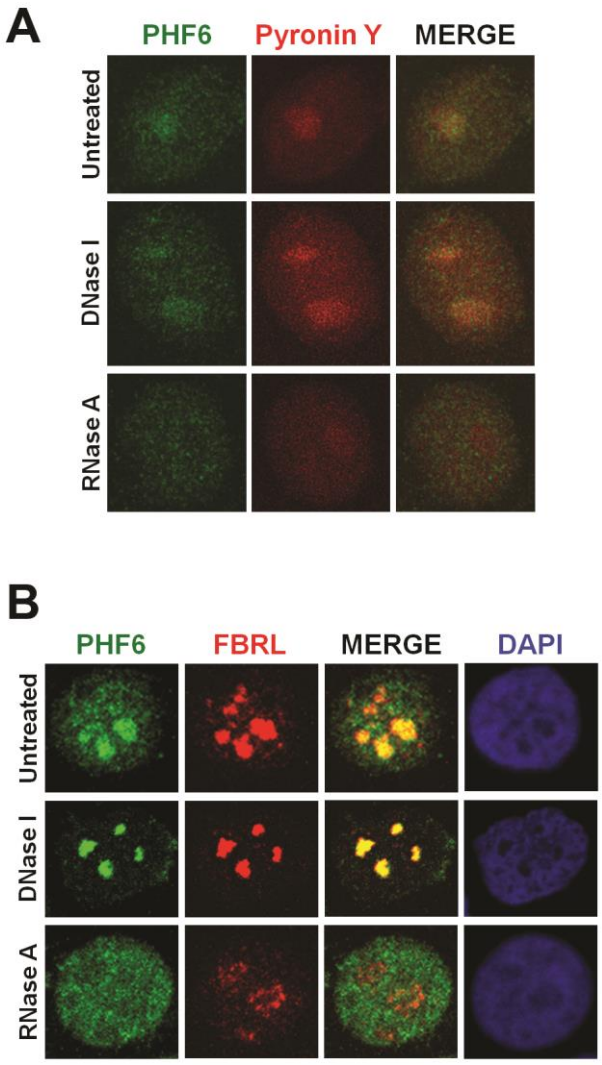

Figure 4-S2. The nucleolar localization of PHF6 is RNA-dependent.
(A, B) HEK 293T cells were digested with either DNase I (10 μg/mL) or RNase A (10 μg/mL) and compared with untreated cells by immunocytochemistry. Cells were immunofluorescently stained with antibodies to PHF6 (green) and counterstained with (A) Pyronin Y to label RNA, or (B) FBRL, a DFC marker. Treatment with RNase A results in the loss of PHF6 from the nucleolus, as indicated by the loss of co-localization between PHF6 and Pyronin Y. The efficacy of the RNase A treatment is confirmed by an accompanying reduction in Pyronin Y intensity. Conversely, nucleolar PHF6 expression is not affected following treatment with DNase I. Like PHF6, the nucleolar localization of FBRL is unaffected by DNase I digestion, yet severely reduced in the RNase A treatment. Representative cell images are shown. This supplementary figure is an accompaniment for Figure 4-3.

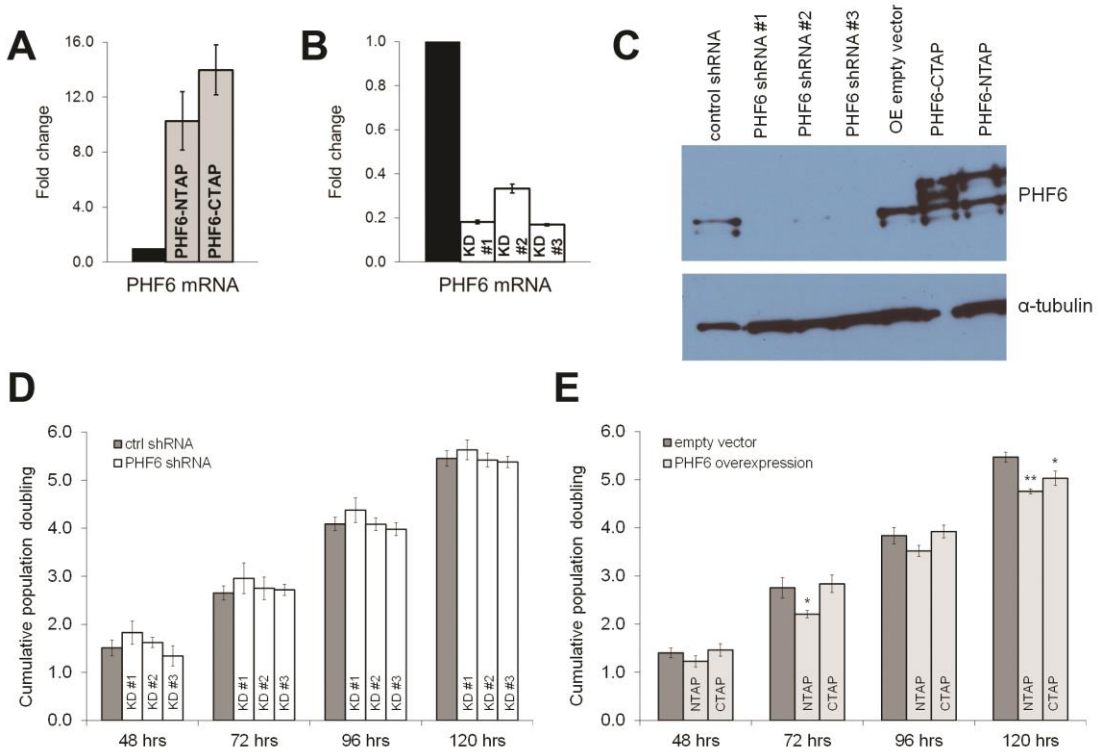

Figure 4-S3. Characterization of the PHF6 overexpression and knockdown cell lines. (A-C) PHF6 levels were quantified from overexpression (PHF6-NTAP, PHF6-CTAP) and shRNA knockdown cell lines (KD #1, KD #2, KD #3) using qRT-PCR (A, B) with primers to amplify PHF6 mRNA (normalized to GAPDH mRNA levels); and by Western blot (C) with antibodies directed against PHF6 and α-tubulin (loading control). Note that the Flag-PHF6 protein is detected above the endogenous PHF6 band. (D, E) Cumulative population doubling values were calculated from cell counts for cell lines (D) overexpressing PHF6 (n=5), or (E) PHF6 shRNA knockdown (n=4). Bars represent standard error (*$p<0.05$, **$p<0.01$, two-tailed student's t-test). [OE = overexpression]

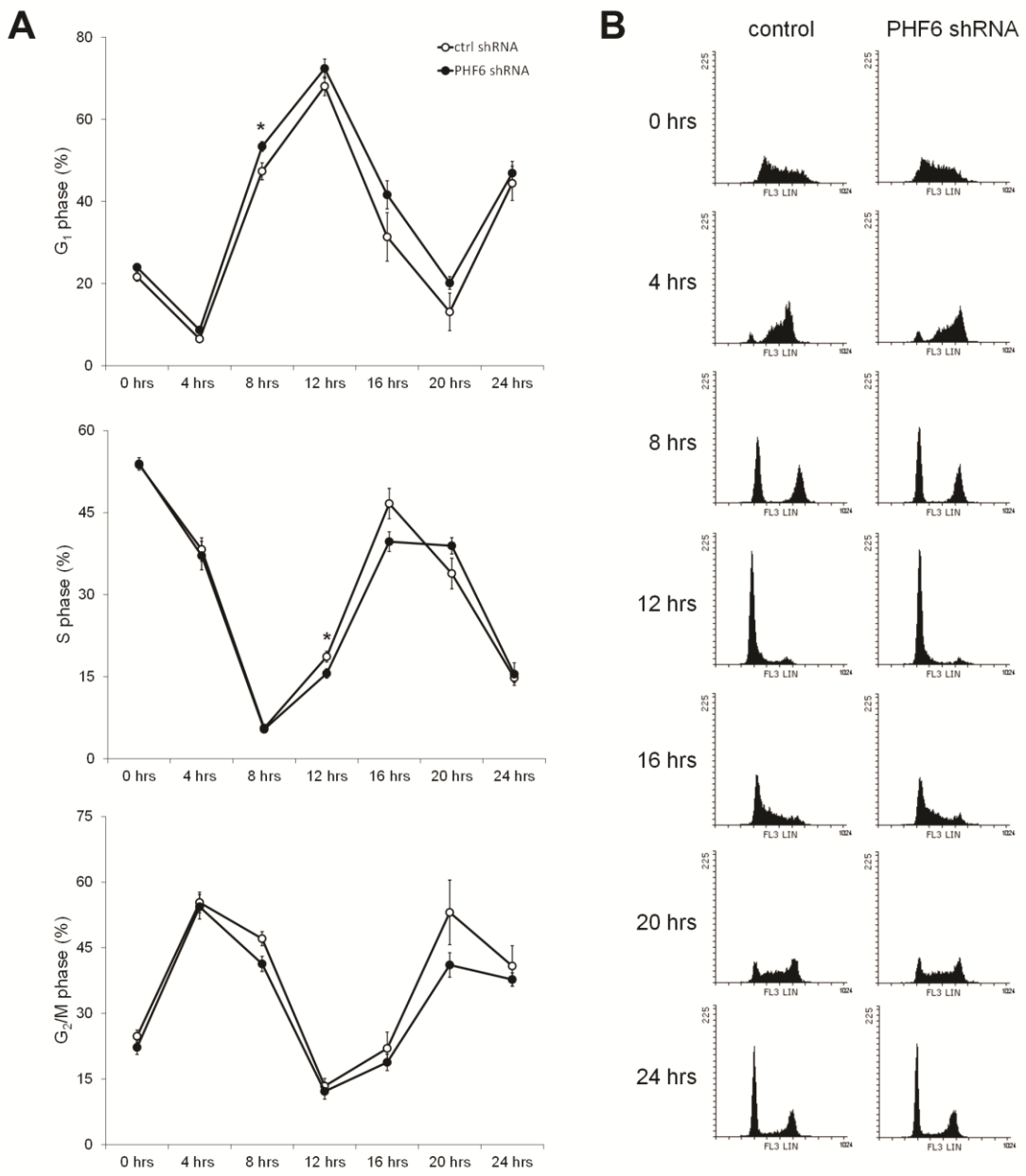

Figure 4-S4. Flow cytometry cell cycle progression analyses and histograms of the BrdU-positive population during PHF6 knockdown.

(A) Flow cytometry cell cycle progression analysis was performed in HEK 293T cells lines expressing either empty pGIPZ vector (control, n=4) or PHF6 shRNA (n=6). Graphs represent the percentage of BrdU-positive cells in the G_1, S, and G_2/M gates at the indicated time points after the moment of BrdU removal (0 hours), following a 1 hour pulse with 30 μM BrdU in unsynchronized cells. Bars represent standard error (*$p<0.05$, **$p<0.01$, two-tailed student's t-test). (B) Representative histograms for each time point (control or PHF6 shRNA), demonstrating the relative proportions of BrdU positive cells (y-axis) with respect to the propidium iodide (PI)-labeled DNA content (x-axis).

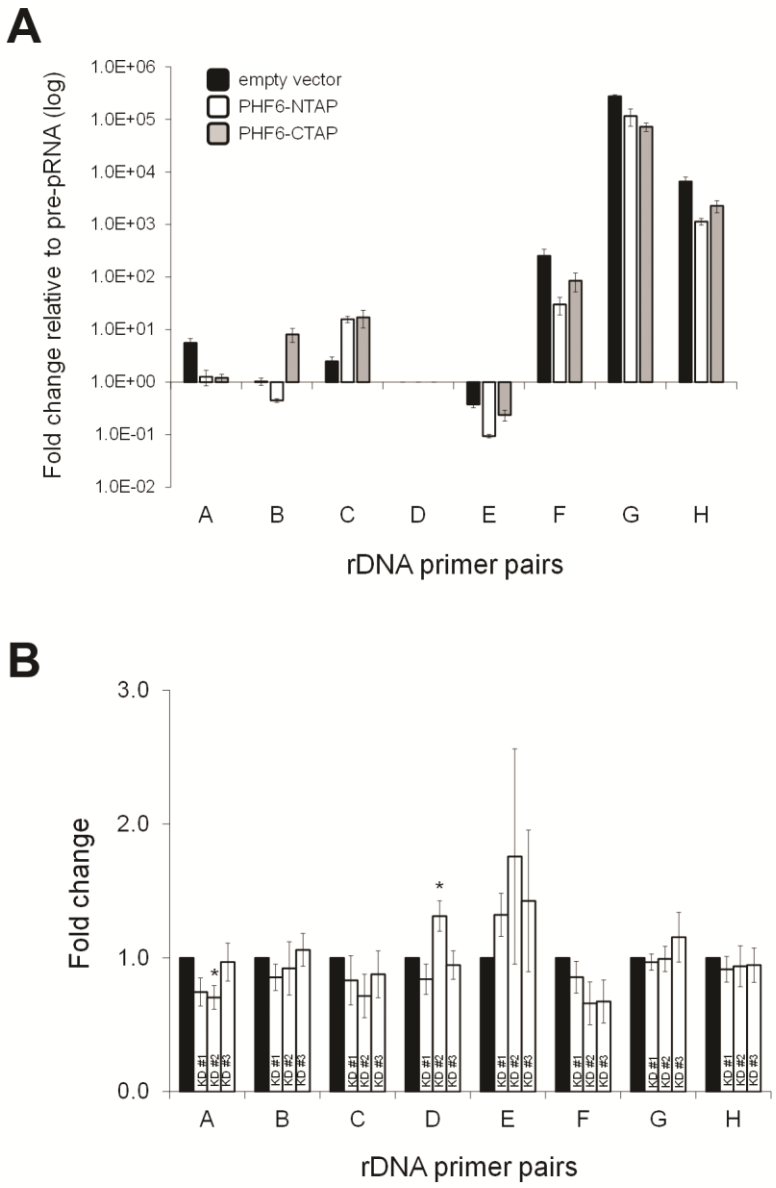

Figure 4-S5. Relative abundance of RNA transcripts quantified from the rDNA gene.

(A) qRT-PCR products from Figure 4-4D,E were re-analyzed with normalization performed against pre-pRNA levels (primer set D product,-1017/-924) from the same RNA sample (n=5). The y-axis is logarithmic (base 10). (B) Quantification of rRNA (primer sets E-H) and non-coding IGS RNA (primer sets A-D) from the rDNA gene was performed for PHF6 shRNA knockdown cell lines (n=4) by qRT-PCR, as described in Figure 4-4D,E. Bars represent standard error (*p<0.05, **p<0.01, two-tailed student's t-test).

Table 4-S1. Primer sequences for ChIP-qPCR and qRT-PCR.

Primer name*	Sequence	Annealing temp. (ºC)
rDNA forward primer A	5'- CCTTCCACGAGAGTGAGAAGC	57
rDNA reverse primer A	5'- TCGACCTCCCGAAATCGTAC	
rDNA forward primer B	5'- TGCTCGGATGCCCCGAGTGA	57
rDNA reverse primer B	5'- ACGTGTGTCCCGAGCTCCTGT	
rDNA forward primer C	5'- CCCCGGGAGACAGACCCTGG	57
rDNA reverse primer C	5'- CGAGGCGGAAGAGTCCACGC	
rDNA forward primer D	5'- AGAGGGGCTGCGTTTTCGGCC	70
rDNA reverse primer D	5'- CGAGACAGATCCGGCTGGCAG	
rDNA forward primer E	5'- GGTATATCTTTCGCTCCGAG	57
rDNA reverse primer E	5'- GACGACAGGTCGCCAGAGGA	
rDNA forward primer F	5'- TGTCAGGCGTTCTCGTCTC	57
rDNA reverse primer F	5'- GAGAGCACGACGTCACCAC	
rDNA forward primer G	5'- AGTCGGGTTGCTTGGGAATGC	57
rDNA reverse primer G	5'- CCCTTACGGTACTTGTTGACT	
rDNA forward primer H	5'- ACCTGGCGCTAAACCATTCGT	57
rDNA reverse primer H	5'- GGACAAACCCTTGTGTCGAGG	
GAPDH forward primer	5'-AAGGTGAAGGTCGGAGTCAAC	57
GAPDH reverse primer	5'-CAGGGATGATGTTCTGGAGA	
PHF6 forward primer	5'-GAAAACTGCACATAACTC	57
PHF6 reverse primer	5'-TGTGTGGAGACCTATC	

* Note: rDNA primer sets A-H were derived from (Zhu et al., 2010).

CHAPTER 5

General Discussion

5. GENERAL DISCUSSION

5.1 Overview of Findings

The advent of next-generation sequencing technologies has greatly facilitated whole genome mutation screening in many human cancers. Consequently, chromatin remodeling proteins that were originally established in the etiology of rare human developmental diseases are now increasingly being identified as targets for oncogenesis (You and Jones, 2012). Fitting this paradigm, germline *PHF6* mutations remain the sole known cause of BFLS, a rare developmental disease that has been diagnosed in fewer than 30 families, yet somatic *PHF6* mutations were recently observed to occur with greater frequency in patients who have acquired T-ALL, AML, or CML (Chao et al., 2010; Li et al., 2013; Van Vlierberghe et al., 2010; Van Vlierberghe et al., 2011). One of these publications, demonstrating the presence of a novel H329Q missense mutation in a T-ALL patient, is presented in Chapter 2. This chapter further describes a pediatric BFLS patient with an R342X frameshift mutation who acquired T-ALL, corresponding to a T-ALL frequency of 3% among all BFLS families, indicating that germline *PHF6* mutations may confer susceptibility to leukemia.

In both BFLS and leukemia, *PHF6* mutations limit the function of the protein. Prior to the work presented in this thesis, the consequences of these mutations with respect to the onset of disease, and even the function of the PHF6 protein itself, were largely unknown. PHF6 was known simply to possess nuclear and nucleolar localization and was classified as a chromatin remodeling protein based on the homology of its zinc finger domains to similar domains in protein families such as MLL or JMJD2. Unlike these known chromatin remodelers, however, PHF6 lacks catalytic domains that could

serve as a means of identifying its function. Moreover the significance of its localization within both the nucleoplasm and nucleolus remained undefined. These concerns are addressed in the work presented in Chapters 3 and 4.

In order to identify a function for PHF6, an IP-MS/MS based proteomic screen was performed under the premise that the activities of its putative interaction partners could be attributed to PHF6 itself. Most notably, PHF6 was found to interact with multiple constituents of the NuRD chromatin remodeling complex, a transcriptional regulator that participates in lineage commitment during development, indicating that PHF6 may in fact be targeting NuRD to specific transcriptional targets. Enrichment of the PHF6-NuRD complex was restricted to the nucleoplasm, although the proteomic screen yielded putative interactions between PHF6 and several proteins involved in ribosome biogenesis and RNA splicing as well, suggesting the existence of distinct PHF6 complexes with different functional roles in the nucleoplasm and nucleolus.

The implication for having two subnuclear pools of PHF6 is the need for an intrinsic mechanism to shuttle PHF6 between the nucleus and nucleolus as required. The identification of PHF6 serine phosphorylation sites in the expanded mass spectrometry dataset (see Appendix A) provides one potential clue as to how such a mechanism might occur. In total, three phosphorylation sites were identified: S145, S154, and S155. Peptides were observed to be singly phosphorylated at either S154 or S155 alone, however S145 phosphorylation was only observed in combination with phosphorylation at S155. Each of these serine phosphorylation sites are documented in the literature and are particularly elevated during mitosis or in response to TCR signaling (Dephoure et al., 2008; Mayya et al., 2009). While definitive experiments to identify the responsible

kinases have not yet been performed, high throughput screens indicate that S145 is phosphorylated by Polo-like kinase 1 (PLK1) (Kettenbach et al., 2011). Supporting this putative mechanism is the fact that S145 is situated within a PLK1 consensus sequence and phosphorylation at S155 provides a binding site for the polo binding domain of PLK1 (PBD) (Elia et al., 2003; Nakajima et al., 2003). The Appendix A dataset and the literature show that S145 is never phosphorylated on its own, suggesting a mechanism whereby phosphorylation at S155 primes S145 for PLK1-mediated phosphorylation. Supporting this model, two studies demonstrated that PLK1 inhibition not only led to a decrease in S145/S155 phosphorylation, but also an accumulation of the singularly phosphorylated S155 peptide (Grosstessner-Hain et al., 2011; Kettenbach et al., 2011). Interestingly, another screen identified S155 as a candidate substrate for CDK2 phosphorylation (Chi et al., 2008). Moreover, roscovitine-mediated CDK2 inhibition interferes with the ability of PHF6 to localize to the nucleolus (Kustatscher et al., 2014). PLK1 and CDK2 are highly active during S and G_2 phase, when nucleolar size and the rate of ribosome biogenesis is higher relative to G_1 (Lapenna and Giordano, 2009; Montanaro et al., 2008), indicating that PHF6 may be recruited to compensate for the increased rates of rRNA synthesis that precede cytokinesis.

Interestingly, these phosphorylated residues are adjacent to an NoLS sequence, a motif that is thought to promote localization to the nucleolus through direct and/or indirect interactions with nucleolar material (e.g. nucleic acid or protein) (Emmott and Hiscox, 2009). In Chapter 4, further investigation of the nucleolar portion of PHF6 indeed indicated the requirement for RNA in the localization of PHF6 to the nucleolus. PHF6 was also observed to localize to the FC and DFC nucleolar subcompartments at

whose interface rRNA transcription occurs. ChIP-qPCR analyses were performed, demonstrating that PHF6 is bound to the rDNA TSS and gene body. Quantitative rDNA transcript analyses showed that PHF6 overexpression correlates with a decrease in rRNA levels and an increase in repressive IGS RNA levels, suggesting a role for PHF6 in limiting the rate of rRNA synthesis.

5.2 Modelling PHF6 gene targets

From Chapter 2 and other case studies of BFLS and leukemia, PHF6 has been classified as a developmental regulator and tumour suppressor. While PHF6 is ubiquitously expressed, it is particularly elevated in embryonic tissues, immature thymocytes, and in the postnatal brain/CNS (Van Vlierberghe et al., 2010; Voss et al., 2007). In Chapter 3, PHF6 was demonstrated to interact with the NuRD complex, a transcriptional regulator with several gene targets that influence embryogenesis, oncogenesis, neurogenesis, and hematopoiesis (Hendrich et al., 2001; Lai and Wade, 2011; Potts et al., 2011; Yoshida et al., 2008), and a later publication described the association of PHF6 with the PAF1 transcriptional elongation complex (Zhang et al., 2013). Thus it is possible that PHF6, as a member of these complexes, regulates its own gene targets. Therefore the identification of any such gene targets provides a better means of understanding the disease mechanisms underlying the BFLS and T-ALL phenotypes.

The NuRD core complex has the ability to catalyze ATP-dependent nucleosome remodeling and histone deacetylation at its gene targets through its CHD and HDAC subunits respectively (Tong et al., 1998; Zhang et al., 1998), but the transcriptional outcome of its targets is dependent upon its collective associations with other activators (e.g. P300) and repressors (e.g. LSD1) (Wang et al., 2009; Williams et al., 2004). Several

NuRD interactors also possess zinc finger domains with the ability to target the complex to gene targets through DNA sequence-specific interactions (e.g. IKAROS, SALL1, BCL11B) (Lauberth et al., 2007; Molnar and Georgopoulos, 1994; Tang et al., 2011; Yamashita et al., 2007). As such, the PHF6 ZaP domain was discussed in Chapter 3 as a potential mediator for the associations between PHF6, NuRD, and chromatin.

The ZaP domain contains an atypical PHD domain, which was speculated to interact with post-translationally modified histones, and a C2HC zinc knuckle, which was discussed as a potential interaction surface with the MTA NuRD subunits, similar to known associations by BCL11B, FOG-1, and SALL1. These other NuRD interactors also possess a conserved N-terminal 12 amino acid sequence that fits into the binding pocket of the β propeller of another NuRD subunit, RBBP4 (Lauberth and Rauchman, 2006; Lejon et al., 2011). Indeed, following the publication of Chapter 3, another group demonstrated that PHF6 amino acid residues 152-171 directly interact with RBBP4 and furthermore that this sequence is highly similar to the conserved 12 amino acid sequence from BCL11B, FOG-1, and SALL-1 (Liu et al., 2014). Moreover, this group determined that the second ZaP domain of PHF6 does not bind histones but in fact binds dsDNA, providing further support for the classification of PHF6 as a transcription factor.

As an initial means of identifying potential PHF6 gene targets, microarray hybridization and qRT-PCR analyses were performed upon RNA samples derived from HEK 293T cell lines expressing either PHF6 shRNA knockdown or PHF6 overexpression (see Appendix A). From these analyses, *SPARC* was identified as a candidate for PHF6 repression. *SPARC* encodes a secreted collagen-binding glycoprotein that counters cell adhesion by interfering with the manner in which cells interact with the

extracellular matrix (Bradshaw, 2009). While ubiquitous, *SPARC* levels are noticeably present among astroglial cells in the developing and postnatal brain (Mendis and Brown, 1994; Mendis et al., 1995; Vincent et al., 2008), and particularly elevated during obesity and in several cancers (Kos and Wilding, 2010). Indeed, as is the case with PHF6 mutations, *SPARC* upregulation correlates with reduced overall survival in AML (Alachkar et al., 2014; Patel et al., 2012). As such, *SPARC* makes for an exciting candidate in attempting to resolve the pathogenic phenotypes that accompany PHF6 mutations in both BFLS and leukemia.

The manner in which PHF6 regulates *SPARC* remains inconclusive. Luciferase reporter assays (see Appendix A) indicate that the putative mechanism for the PHF6-related SPARC repression does not occur through the *SPARC* promoter. These results illustrate the need for further in-depth ChIP sequencing to catalogue genomic binding sites for PHF6 in relevant tissues, as has been performed for other NuRD interactors such as IKAROS and BCL11B (Kastner et al., 2010; Novershtern et al., 2011).

From these studies, it has been demonstrated that such transcription factors can greatly influence the ability of NuRD to activate or repress its target genes. For instance, CD4 is normally activated by NuRD, but repressed by IKAROS-NuRD (Naito et al., 2007). In another example, ChIP-seq analyses showed BCL11B-NuRD to bind target genes that were repressed in DP thymocytes, yet activated in SP cells (e.g. *RUNX3*) (Kastner et al., 2010). A later study determined that BCL11B was being dephosphorylated and sumoylated to recruit P300, which in turn led to the activation of the previously repressed target gene (Zhang et al., 2012b). Interestingly, PHF6 has

multiple phosphorylation sites in the interaction domain with RBBP4, although it is unclear whether this affects its association with NuRD (Kettenbach et al., 2011).

In carrying out future PHF6 ChIP-seq analyses, it will be important to compare primary sets of PHF6 binding sites with PHF6 null RNA expression datasets as well as with known binding sites for NuRD subunits (e.g. CHD4, MBD3), many of which have already been characterized in the literature (Reynolds et al., 2012b; Yoshida et al., 2008; Zhang et al., 2012a). PHF6 binding patterns can also be correlated with DNA methylation and histone PTM patterns in future assessments defining the role of PHF6 in the transcriptional activation or repression of specific targets. The possibility for PHF6 to have NuRD-independent targets should also be recognized, as evidenced by its regulation of rDNA described in Chapter 4.

5.3 Modelling the contribution of ribosome biogenesis to BFLS and leukemia

While additional PHF6 gene targets await characterization, ChIP-qPCR and RNA expression data from Chapter 4 demonstrate that rDNA, whose synthesis accounts for as much as half of all cellular transcription (Hamperl et al., 2013), is a key target for PHF6 repression. Moreover, PHF6 was demonstrated to associate with RNA in the nucleolus, and several nucleolar proteins based on IP-MS/MS data. As such, nucleolar ribosome biogenesis represents a major cellular pathway in the disease pathologies of BFLS and leukemia following PHF6 loss.

Ribosome biogenesis rates positively correlate with nucleolar size. In general, proliferating cells possess large nucleoli to accommodate the metabolic requirements of successive passages through the cell cycle, and over the course of differentiation, rDNA genes become increasingly silenced in an allelic manner (Schlesinger et al., 2009). Not

surprisingly, cancer cells with large nucleoli correlate with poor clinical outcomes (Derenzini et al., 2009). Large nucleoli are also present in terminally differentiated cells that possess hypertrophic cytoplasmic volumes. In neurons, such nucleoli are necessary for supplying a sufficient amount of ribosomes to growing neurites to accommodate local demands for translation (Gomes et al., 2011). Indeed many developmental intellectual disability diseases (e.g. Cockayne syndrome, Rett syndrome) and acquired neurodegenerative disorders (e.g. Alzheimer's, Parkinson's) are associated with reduced levels of ribosome biogenesis (Hannan et al., 2013; Hetman and Pietrzak, 2012).

In Chapter 4, PHF6 overexpression yielded reduced rRNA levels. If indeed a repressor, PHF6 loss in T-ALL, AML, and CML is consistent with a model in which the hyperactivation of ribosome biogenesis is favoured. However such a role is not consistent with the paradigm of reduced ribosome biogenesis in intellectual disability diseases like BFLS. A similar paradox is represented by the loss of MeCP2, which is responsible for Rett syndrome (Amir et al., 1999). MeCP2 binds methylated CpG DNA, a mark for rDNA silencing (Santoro and Grummt, 2001), and contributes to heterochromatin formation (Brero et al., 2005); yet, rather than hyperactivating rRNA synthesis, its loss correlates with reduced nucleolar size (Singleton et al., 2011). In addressing this dilemma, it is important to consider the regulation of cell cycle checkpoints.

Reports in the literature identify PHF6 as a target of the ATM DNA damage checkpoint kinase (Matsuoka et al., 2007) and its loss correlates with the accumulation of phosphorylated γH2AX (Van Vlierberghe et al., 2010; Wang et al., 2013). The ATM pathway has been shown to inhibit RNA Pol I (Kruhlak et al., 2007). Moreover, rDNA transcriptional stress activates other checkpoints that can shut down nucleolar activities,

trigger cell cycle arrest, or even induce apoptosis (Grummt, 2013). Notably, the pRB and p53 master checkpoint proteins are key negative regulators of rRNA transcription (Montanaro et al., 2008). Interestingly, the p53 guardian protein MDM2 is immobilized in the NoDP by non-coding IGS transcripts, including IGS_{36}RNA, under conditions of transcriptional stress (Audas et al., 2012). Thus, altered levels of PHF6 may instigate DNA repair or cell cycle checkpoint mechanisms in the absence of secondary mutations.

The epigenetic landscapes of cancers such as T-ALL and AML are defined by frequent and co-occurring mutations to favour both unrestricted proliferation and tumour survival (Cancer Genome Atlas Research, 2013; Van Vlierberghe et al., 2008). In T-ALL, *PHF6* mutations co-occur with mutations in *TLX1*, *TLX3*, *NOTCH1*, *JAK1*, as well as *SET-NUP214* translocations (Van Vlierberghe et al., 2010; Wang et al., 2011). In AML, *PHF6* mutations co-occur with *RUNX1* mutations (Cancer Genome Atlas Research, 2013). While the advantages conferred by these co-occurring mutations in specific T-ALL/AML lineages is not yet clear, this pathogenic model is similar to the example provided by BCL11B in developing thymocytes, in which the loss of BCL11B on its own induces massive apoptosis during β-selection (Wakabayashi et al., 2003), yet also favours T-ALL progression when lost in combination with other oncogenically favourable events (De Keersmaecker et al., 2010).

Taken together, the presence of established checkpoints may explain how a loss of rDNA repression causes reduced ribosome biogenesis in developing tissues, yet hyperactivates ribosome biogenesis in cancer cells with deactivated checkpoints. It is worth noting that the contribution of PHF6 mutations towards other forms of neoplasia has not yet been well investigated, however in contrast to T-ALL and AML, the shRNA-

mediated depletion of *Phf6* in a murine B-ALL model corresponded to a reduction in the rate of tumorigenic growth (Meacham et al., 2015). As such, these results suggest the downstream functions of PHF6 are variable among different cell types, or perhaps there are differences in the cell cycle or developmental checkpoints that become compromised in combination with *PHF6* loss-of-function in T-ALL and AML vs. B-ALL or other forms of neoplasia. Thus, future investigations need to be considerate of the potential for the PHF6 protein to have tissue-specific functional roles or for its expression to be subject to different tissue-specific regulatory mechanisms.

5.4 Developing biological therapies for BFLS and T-ALL

In working towards future therapies for BFLS, T-ALL, AML, and CML, future research needs to utilize mammalian models so that the loss of PHF6, and the subsequent impact on gene expression or ribosome biogenesis, can be studied in populations of primary cells that are relevant to the onset of disease. Even though many developmental features are established by birth, much of the developmental delay among BFLS patients only becomes apparent postnatally (Gecz et al., 2006), perhaps indicative of the importance of nucleoli toward supporting post-mitotic neuronal activities and the potential for some level of rescue. Such optimism is reinforced by recent publications in which neurological deficits were partially rescued with statins in mouse models for both Rett syndrome and Fragile X syndrome (Buchovecky et al., 2013; Osterweil et al., 2013), as well as the existence of ongoing clinical trials of mGluR5 antagonists in the treatment of Fragile X (Jacquemont et al., 2014; Pop et al., 2014)

In treating leukemia, identifying established gene targets may represent new pathways for inhibition. In fact, SPARC and the HDAC subunits of NuRD are known

targets for bortezomib and SAHA, respectively (Alachkar et al., 2014; Finnin et al., 1999). Novel anti-cancer therapeutics that target ribosome biogenesis have also recently been developed, including CX-5461 and BMH-21, which act by repressing RNA Pol I and stimulating p53-dependent apoptosis (Bywater et al., 2012; Peltonen et al., 2014).

5.5 Conclusion

The body of work in this thesis includes the first description of a BFLS patient to develop T-ALL, the first identification of a protein complex (NuRD) that associates with PHF6, the first endogenous ChIP-qPCR mapping of PHF6 binding sites across the rDNA gene, and the first demonstration of RNA-dependent localization of PHF6 to the nucleolar FC/DFC. Taken together, these data present a model whereby PHF6 executes its function through participation in the transcriptional regulation of mRNA and rRNA gene targets.

REFERENCES

Aapola, U., Kawasaki, K., Scott, H.S., Ollila, J., Vihinen, M., Heino, M., Shintani, A., Minoshima, S., Krohn, K., Antonarakis, S.E., et al. (2000). Isolation and initial characterization of a novel zinc finger gene, DNMT3L, on 21q22.3, related to the cytosine-5-methyltransferase 3 gene family. Genomics 65, 293-298.

Aasland, R., Gibson, T.J., and Stewart, A.F. (1995). The PHD finger: implications for chromatin-mediated transcriptional regulation. Trends in biochemical sciences 20, 56-59.

Adams-Cioaba, M.A., and Min, J. (2009). Structure and function of histone methylation binding proteins. Biochemistry and cell biology = Biochimie et biologie cellulaire 87, 93-105.

Ahmad, Y., Boisvert, F.M., Gregor, P., Cobley, A., and Lamond, A.I. (2009). NOPdb: Nucleolar Proteome Database--2008 update. Nucleic Acids Res 37, D181-184.

Alachkar, H., Santhanam, R., Maharry, K., Metzeler, K.H., Huang, X., Kohlschmidt, J., Mendler, J.H., Benito, J.M., Hickey, C., Neviani, P., et al. (2014). SPARC promotes leukemic cell growth and predicts acute myeloid leukemia outcome. J Clin Invest 124, 1512-1524.

Alberts, B., Johnson, A., Lewis, J., Raff, M., Roberts, K., and Walter, P. (2002). Molecular Biology of the Cell, 4 edn (New York, NY: Garland Science).

Ali, S.A., Dobson, J.R., Lian, J.B., Stein, J.L., van Wijnen, A.J., Zaidi, S.K., and Stein, G.S. (2012). A RUNX2-HDAC1 co-repressor complex regulates rRNA gene expression by modulating UBF acetylation. Journal of cell science 125, 2732-2739.

Amir, R.E., Van den Veyver, I.B., Wan, M., Tran, C.Q., Francke, U., and Zoghbi, H.Y. (1999). Rett syndrome is caused by mutations in X-linked MECP2, encoding methyl-CpG-binding protein 2. Nat Genet 23, 185-188.

Aoki, Y., Niihori, T., Kawame, H., Kurosawa, K., Ohashi, H., Tanaka, Y., Filocamo, M., Kato, K., Suzuki, Y., Kure, S., et al. (2005). Germline mutations in HRAS proto-oncogene cause Costello syndrome. Nat Genet 37, 1038-1040.

Audas, T.E., Jacob, M.D., and Lee, S. (2012). Immobilization of proteins in the nucleolus by ribosomal intergenic spacer noncoding RNA. Mol Cell 45, 147-157.

Baba, A., Ohtake, F., Okuno, Y., Yokota, K., Okada, M., Imai, Y., Ni, M., Meyer, C.A., Igarashi, K., Kanno, J., et al. (2011). PKA-dependent regulation of the histone lysine demethylase complex PHF2-ARID5B. Nat Cell Biol 13, 668-675.

Bannister, A.J., and Kouzarides, T. (2011). Regulation of chromatin by histone modifications. Cell Res 21, 381-395.

Barski, A., Cuddapah, S., Cui, K., Roh, T.Y., Schones, D.E., Wang, Z., Wei, G., Chepelev, I., and Zhao, K. (2007). High-resolution profiling of histone methylations in the human genome. Cell 129, 823-837.

Bartova, E., Horakova, A.H., Uhlirova, R., Raska, I., Galiova, G., Orlova, D., and Kozubek, S. (2010). Structure and epigenetics of nucleoli in comparison with non-nucleolar compartments. J Histochem Cytochem 58, 391-403.

Bartova, E., Stixova, L., Galiova, G., Harnicarova Horakova, A., Legartova, S., and Kozubek, S. (2011). Mutant genetic background affects the functional rearrangement and kinetic properties of JMJD2b histone demethylase. Journal of molecular biology 405, 679-695.

Baumstark, A., Lower, K.M., Sinkus, A., Andriuskeviciute, I., Jurkeniene, L., Gecz, J., and Just, W. (2003). Novel PHF6 mutation p.D333del causes Borjeson-Forssman-Lehmann syndrome. J Med Genet 40, e50.

Baylin, S.B., and Jones, P.A. (2011). A decade of exploring the cancer epigenome - biological and translational implications. Nat Rev Cancer 11, 726-734.

Bell, S.P., Learned, R.M., Jantzen, H.M., and Tjian, R. (1988). Functional cooperativity between transcription factors UBF1 and SL1 mediates human ribosomal RNA synthesis. Science 241, 1192-1197.

Berland, S., Alme, K., Brendehaug, A., Houge, G., and Hovland, R. (2011). PHF6 Deletions May Cause Borjeson-Forssman-Lehmann Syndrome in Females. Mol Syndromol 1, 294-300.

Bernardi, R., Scaglioni, P.P., Bergmann, S., Horn, H.F., Vousden, K.H., and Pandolfi, P.P. (2004). PML regulates p53 stability by sequestering Mdm2 to the nucleolus. Nat Cell Biol 6, 665-672.

Bernstein, E., Duncan, E.M., Masui, O., Gil, J., Heard, E., and Allis, C.D. (2006). Mouse polycomb proteins bind differentially to methylated histone H3 and RNA and are enriched in facultative heterochromatin. Mol Cell Biol 26, 2560-2569.

Bieging, K.T., Mello, S.S., and Attardi, L.D. (2014). Unravelling mechanisms of p53-mediated tumour suppression. Nat Rev Cancer 14, 359-370.

Boisvert, F.M., Ahmad, Y., Gierlinski, M., Charriere, F., Lamont, D., Scott, M., Barton, G., and Lamond, A.I. (2012). A quantitative spatial proteomics analysis of proteome turnover in human cells. Mol Cell Proteomics 11, M111 011429.

Boisvert, F.M., van Koningsbruggen, S., Navascues, J., and Lamond, A.I. (2007). The multifunctional nucleolus. Nat Rev Mol Cell Biol 8, 574-585.

Borjeson, M., Forssman, H., and Lehmann, O. (1962). An X-linked, recessively inherited syndrome characterized by grave mental deficiency, epilepsy, and endocrine disorder. Acta medica Scandinavica 171, 13-21.

Borrow, J., Stanton, V.P., Jr., Andresen, J.M., Becher, R., Behm, F.G., Chaganti, R.S., Civin, C.I., Disteche, C., Dube, I., Frischauf, A.M., et al. (1996). The translocation t(8;16)(p11;p13) of acute myeloid leukaemia fuses a putative acetyltransferase to the CREB-binding protein. Nat Genet 14, 33-41.

Boulon, S., Westman, B.J., Hutten, S., Boisvert, F.M., and Lamond, A.I. (2010). The nucleolus under stress. Mol Cell 40, 216-227.

Bradshaw, A.D. (2009). The role of SPARC in extracellular matrix assembly. Journal of cell communication and signaling 3, 239-246.

Bradsher, J., Auriol, J., Proietti de Santis, L., Iben, S., Vonesch, J.L., Grummt, I., and Egly, J.M. (2002). CSB is a component of RNA pol I transcription. Mol Cell 10, 819-829.

Brero, A., Easwaran, H.P., Nowak, D., Grunewald, I., Cremer, T., Leonhardt, H., and Cardoso, M.C. (2005). Methyl CpG-binding proteins induce large-scale chromatin reorganization during terminal differentiation. J Cell Biol 169, 733-743.

Brookes, E., and Shi, Y. (2014). Diverse epigenetic mechanisms of human disease. Annual review of genetics 48, 237-268.

Brooks, W.S., Banerjee, S., and Crawford, D.F. (2007). G2E3 is a nucleo-cytoplasmic shuttling protein with DNA damage responsive localization. Exp Cell Res 313, 665-676.

Buchovecky, C.M., Turley, S.D., Brown, H.M., Kyle, S.M., McDonald, J.G., Liu, B., Pieper, A.A., Huang, W., Katz, D.M., Russell, D.W., et al. (2013). A suppressor screen in Mecp2 mutant mice implicates cholesterol metabolism in Rett syndrome. Nat Genet 45, 1013-1020.

Bywater, M.J., Poortinga, G., Sanij, E., Hein, N., Peck, A., Cullinane, C., Wall, M., Cluse, L., Drygin, D., Anderes, K., et al. (2012). Inhibition of RNA polymerase I as a therapeutic strategy to promote cancer-specific activation of p53. Cancer Cell 22, 51-65.

Campos, E.I., and Reinberg, D. (2009). Histones: annotating chromatin. Annual review of genetics 43, 559-599.

Cancer Genome Atlas Research, N. (2013). Genomic and epigenomic landscapes of adult de novo acute myeloid leukemia. N Engl J Med 368, 2059-2074.

Capili, A.D., Schultz, D.C., Rauscher, I.F., and Borden, K.L. (2001). Solution structure of the PHD domain from the KAP-1 corepressor: structural determinants for PHD, RING and LIM zinc-binding domains. Embo J 20, 165-177.

Carter, M.T., Picketts, D.J., Hunter, A.G., and Graham, G.E. (2009). Further clinical delineation of the Borjeson-Forssman-Lehmann syndrome in patients with PHF6 mutations. Am J Med Genet A 149A, 246-250.

Cassidy, B.G., Yang-Yen, H.F., and Rothblum, L.I. (1987). Additional RNA polymerase I initiation site within the nontranscribed spacer region of the rat rRNA gene. Mol Cell Biol 7, 2388-2396.

Cavanaugh, A.H., Hempel, W.M., Taylor, L.J., Rogalsky, V., Todorov, G., and Rothblum, L.I. (1995). Activity of RNA polymerase I transcription factor UBF blocked by Rb gene product. Nature 374, 177-180.

Chamousset, D., De Wever, V., Moorhead, G.B., Chen, Y., Boisvert, F.M., Lamond, A.I., and Trinkle-Mulcahy, L. (2010a). RRP1B targets PP1 to mammalian cell nucleoli and is associated with Pre-60S ribosomal subunits. Mol Biol Cell 21, 4212-4226.

Chamousset, D., Mamane, S., Boisvert, F.M., and Trinkle-Mulcahy, L. (2010b). Efficient extraction of nucleolar proteins for interactome analyses. Proteomics 10, 3045-3050.

Chao, M.M., Todd, M.A., Kontny, U., Neas, K., Sullivan, M.J., Hunter, A.G., Picketts, D.J., and Kratz, C.P. (2010). T-cell acute lymphoblastic leukemia in association with Borjeson-Forssman-Lehmann syndrome due to a mutation in PHF6. Pediatr Blood Cancer 55, 722-724.

Chen, H.Z., Tsai, S.Y., and Leone, G. (2009). Emerging roles of E2Fs in cancer: an exit from cell cycle control. Nat Rev Cancer 9, 785-797.

Chi, Y., Welcker, M., Hizli, A.A., Posakony, J.J., Aebersold, R., and Clurman, B.E. (2008). Identification of CDK2 substrates in human cell lysates. Genome biology 9, R149.

Chiurazzi, P., Schwartz, C.E., Gecz, J., and Neri, G. (2008). XLMR genes: update 2007. Eur J Hum Genet 16, 422-434.

Cismasiu, V.B., Adamo, K., Gecewicz, J., Duque, J., Lin, Q., and Avram, D. (2005). BCL11B functionally associates with the NuRD complex in T lymphocytes to repress targeted promoter. Oncogene 24, 6753-6764.

Clark, D.E., Errington, T.M., Smith, J.A., Frierson, H.F., Jr., Weber, M.J., and Lannigan, D.A. (2005). The serine/threonine protein kinase, p90 ribosomal S6 kinase, is an important regulator of prostate cancer cell proliferation. Cancer Res 65, 3108-3116.

Conconi, A., Widmer, R.M., Koller, T., and Sogo, J.M. (1989). Two different chromatin structures coexist in ribosomal RNA genes throughout the cell cycle. Cell 57, 753-761.

Crawford, J., Lower, K.M., Hennekam, R.C., Van Esch, H., Megarbane, A., Lynch, S.A., Turner, G., and Gecz, J. (2006). Mutation screening in Borjeson-Forssman-Lehmann syndrome: identification of a novel de novo PHF6 mutation in a female patient. J Med Genet 43, 238-243.

Dalgliesh, G.L., Furge, K., Greenman, C., Chen, L., Bignell, G., Butler, A., Davies, H., Edkins, S., Hardy, C., Latimer, C., et al. (2010). Systematic sequencing of renal carcinoma reveals inactivation of histone modifying genes. Nature 463, 360-363.

Dammann, R., Lucchini, R., Koller, T., and Sogo, J.M. (1993). Chromatin structures and transcription of rDNA in yeast Saccharomyces cerevisiae. Nucleic Acids Res 21, 2331-2338.

Darvekar, S., Johnsen, S.S., Eriksen, A.B., Johansen, T., and Sjottem, E. (2012). Identification of two independent nucleosome-binding domains in the transcriptional co-activator SPBP. Biochem J 442, 65-75.

De Keersmaecker, K., Real, P.J., Gatta, G.D., Palomero, T., Sulis, M.L., Tosello, V., Van Vlierberghe, P., Barnes, K., Castillo, M., Sole, X., et al. (2010). The TLX1 oncogene drives aneuploidy in T cell transformation. Nat Med 16, 1321-1327.

Denissov, S., Lessard, F., Mayer, C., Stefanovsky, V., van Driel, M., Grummt, I., Moss, T., and Stunnenberg, H.G. (2011). A model for the topology of active ribosomal RNA genes. EMBO Rep 12, 231-237.

Dephoure, N., Zhou, C., Villen, J., Beausoleil, S.A., Bakalarski, C.E., Elledge, S.J., and Gygi, S.P. (2008). A quantitative atlas of mitotic phosphorylation. Proc Natl Acad Sci U S A 105, 10762-10767.

Derenzini, M., Montanaro, L., and Trere, D. (2009). What the nucleolus says to a tumour pathologist. Histopathology 54, 753-762.

Dhalluin, C., Carlson, J.E., Zeng, L., He, C., Aggarwal, A.K., and Zhou, M.M. (1999). Structure and ligand of a histone acetyltransferase bromodomain. Nature 399, 491-496.

Dhayalan, A., Rajavelu, A., Rathert, P., Tamas, R., Jurkowska, R.Z., Ragozin, S., and Jeltsch, A. (2010). The Dnmt3a PWWP domain reads histone 3 lysine 36 trimethylation and guides DNA methylation. J Biol Chem 285, 26114-26120.

Di Donato, N., Isidor, B., Lopez Cazaux, S., Le Caignec, C., Klink, B., Kraus, C., Schrock, E., and Hackmann, K. (2014). Distinct phenotype of PHF6 deletions in females. Eur J Med Genet 57, 85-89.

Dundr, M., Misteli, T., and Olson, M.O. (2000). The dynamics of postmitotic reassembly of the nucleolus. J Cell Biol 150, 433-446.

Ehrlich, M., Buchanan, K.L., Tsien, F., Jiang, G., Sun, B., Uicker, W., Weemaes, C.M., Smeets, D., Sperling, K., Belohradsky, B.H., et al. (2001). DNA methyltransferase 3B mutations linked to the ICF syndrome cause dysregulation of lymphogenesis genes. Hum Mol Genet 10, 2917-2931.

Elia, A.E., Cantley, L.C., and Yaffe, M.B. (2003). Proteomic screen finds pSer/pThr-binding domain localizing Plk1 to mitotic substrates. Science 299, 1228-1231.

Emmott, E., and Hiscox, J.A. (2009). Nucleolar targeting: the hub of the matter. EMBO Rep 10, 231-238.

Encode Project, C. (2012). An integrated encyclopedia of DNA elements in the human genome. Nature 489, 57-74.

Eustermann, S., Yang, J.C., Law, M.J., Amos, R., Chapman, L.M., Jelinska, C., Garrick, D., Clynes, D., Gibbons, R.J., Rhodes, D., et al. (2011). Combinatorial readout of histone H3 modifications specifies localization of ATRX to heterochromatin. Nat Struct Mol Biol 18, 777-782.

Feinberg, A.P., Ohlsson, R., and Henikoff, S. (2006). The epigenetic progenitor origin of human cancer. Nat Rev Genet 7, 21-33.

Feng, W., Yonezawa, M., Ye, J., Jenuwein, T., and Grummt, I. (2010). PHF8 activates transcription of rRNA genes through H3K4me3 binding and H3K9me1/2 demethylation. Nat Struct Mol Biol 17, 445-450.

Ferrando, A.A., Neuberg, D.S., Staunton, J., Loh, M.L., Huard, C., Raimondi, S.C., Behm, F.G., Pui, C.H., Downing, J.R., Gilliland, D.G., et al. (2002). Gene expression signatures define novel oncogenic pathways in T cell acute lymphoblastic leukemia. Cancer Cell 1, 75-87.

Finnin, M.S., Donigian, J.R., Cohen, A., Richon, V.M., Rifkind, R.A., Marks, P.A., Breslow, R., and Pavletich, N.P. (1999). Structures of a histone deacetylase homologue bound to the TSA and SAHA inhibitors. Nature 401, 188-193.

Frescas, D., Guardavaccaro, D., Bassermann, F., Koyama-Nasu, R., and Pagano, M. (2007). JHDM1B/FBXL10 is a nucleolar protein that represses transcription of ribosomal RNA genes. Nature 450, 309-313.

Gecz, J., Turner, G., Nelson, J., and Partington, M. (2006). The Borjeson-Forssman-Lehman syndrome (BFLS, MIM #301900). Eur J Hum Genet 14, 1233-1237.

Gedeon, A.K., Kozman, H.M., Robinson, H., Pilia, G., Schlessinger, D., Turner, G., and Mulley, J.C. (1996). Refinement of the background genetic map of Xq26-q27 and gene localisation for Borjeson-Forssman-Lehmann Syndrome. American journal of medical genetics 64, 63-68.

Georgel, P.T., Horowitz-Scherer, R.A., Adkins, N., Woodcock, C.L., Wade, P.A., and Hansen, J.C. (2003). Chromatin compaction by human MeCP2. Assembly of novel secondary chromatin structures in the absence of DNA methylation. J Biol Chem 278, 32181-32188.

Gerhard, D.S., Wagner, L., Feingold, E.A., Shenmen, C.M., Grouse, L.H., Schuler, G., Klein, S.L., Old, S., Rasooly, R., Good, P., et al. (2004). The status, quality, and expansion of the NIH full-length cDNA project: the Mammalian Gene Collection (MGC). Genome research 14, 2121-2127.

Ghoshal, K., Majumder, S., Datta, J., Motiwala, T., Bai, S., Sharma, S.M., Frankel, W., and Jacob, S.T. (2004). Role of human ribosomal RNA (rRNA) promoter methylation and of methyl-CpG-binding protein MBD2 in the suppression of rRNA gene expression. J Biol Chem 279, 6783-6793.

Gibbons, R.J., Picketts, D.J., Villard, L., and Higgs, D.R. (1995). Mutations in a putative global transcriptional regulator cause X-linked mental retardation with alpha-thalassemia (ATR-X syndrome). Cell 80, 837-845.

Gibbons, R.J., Wada, T., Fisher, C.A., Malik, N., Mitson, M.J., Steensma, D.P., Fryer, A., Goudie, D.R., Krantz, I.D., and Traeger-Synodinos, J. (2008). Mutations in the chromatin-associated protein ATRX. Human mutation 29, 796-802.

Gibson, W.T., Hood, R.L., Zhan, S.H., Bulman, D.E., Fejes, A.P., Moore, R., Mungall, A.J., Eydoux, P., Babul-Hirji, R., An, J., et al. (2012). Mutations in EZH2 cause Weaver syndrome. American journal of human genetics 90, 110-118.

Goll, M.G., and Bestor, T.H. (2005). Eukaryotic cytosine methyltransferases. Annu Rev Biochem 74, 481-514.

Golomb, L., Volarevic, S., and Oren, M. (2014). p53 and ribosome biogenesis stress: the essentials. FEBS Lett 588, 2571-2579.

Gomes, C., Smith, S.C., Youssef, M.N., Zheng, J.J., Hagg, T., and Hetman, M. (2011). RNA polymerase 1-driven transcription as a mediator of BDNF-induced neurite outgrowth. J Biol Chem 286, 4357-4363.

Grandori, C., Gomez-Roman, N., Felton-Edkins, Z.A., Ngouenet, C., Galloway, D.A., Eisenman, R.N., and White, R.J. (2005). c-Myc binds to human ribosomal DNA and stimulates transcription of rRNA genes by RNA polymerase I. Nat Cell Biol 7, 311-318.

Greer, E.L., and Shi, Y. (2012). Histone methylation: a dynamic mark in health, disease and inheritance. Nat Rev Genet 13, 343-357.

Grierson, P.M., Lillard, K., Behbehani, G.K., Combs, K.A., Bhattacharyya, S., Acharya, S., and Groden, J. (2012). BLM helicase facilitates RNA polymerase I-mediated ribosomal RNA transcription. Hum Mol Genet 21, 1172-1183.

Grossmann, V., Haferlach, C., Weissmann, S., Roller, A., Schindela, S., Poetzinger, F., Stadler, K., Bellos, F., Kern, W., Haferlach, T., et al. (2013). The molecular profile of adult T-cell acute lymphoblastic leukemia: mutations in RUNX1 and DNMT3A are associated with poor prognosis in T-ALL. Genes Chromosomes Cancer 52, 410-422.

Grossmann, V., Tiacci, E., Holmes, A.B., Kohlmann, A., Martelli, M.P., Kern, W., Spanhol-Rosseto, A., Klein, H.U., Dugas, M., Schindela, S., et al. (2011). Whole-exome sequencing identifies somatic mutations of BCOR in acute myeloid leukemia with normal karyotype. Blood 118, 6153-6163.

Grosstessner-Hain, K., Hegemann, B., Novatchkova, M., Rameseder, J., Joughin, B.A., Hudecz, O., Roitinger, E., Pichler, P., Kraut, N., Yaffe, M.B., et al. (2011). Quantitative phospho-proteomics to investigate the polo-like kinase 1-dependent phospho-proteome. Mol Cell Proteomics 10, M111 008540.

Grummt, I. (2013). The nucleolus-guardian of cellular homeostasis and genome integrity. Chromosoma 122, 487-497.

Guetg, C., Lienemann, P., Sirri, V., Grummt, I., Hernandez-Verdun, D., Hottiger, M.O., Fussenegger, M., and Santoro, R. (2010). The NoRC complex mediates the heterochromatin formation and stability of silent rRNA genes and centromeric repeats. EMBO J 29, 2135-2146.

Guetg, C., Scheifele, F., Rosenthal, F., Hottiger, M.O., and Santoro, R. (2012). Inheritance of silent rDNA chromatin is mediated by PARP1 via noncoding RNA. Mol Cell 45, 790-800.

Haltiner, M.M., Smale, S.T., and Tjian, R. (1986). Two distinct promoter elements in the human rRNA gene identified by linker scanning mutagenesis. Mol Cell Biol 6, 227-235.

Hamperl, S., Wittner, M., Babl, V., Perez-Fernandez, J., Tschochner, H., and Griesenbeck, J. (2013). Chromatin states at ribosomal DNA loci. Biochim Biophys Acta 1829, 405-417.

Hannan, K.M., Hannan, R.D., Smith, S.D., Jefferson, L.S., Lun, M., and Rothblum, L.I. (2000). Rb and p130 regulate RNA polymerase I transcription: Rb disrupts the interaction between UBF and SL-1. Oncogene 19, 4988-4999.

Hannan, K.M., Sanij, E., Rothblum, L.I., Hannan, R.D., and Pearson, R.B. (2013). Dysregulation of RNA polymerase I transcription during disease. Biochim Biophys Acta 1829, 342-360.

Hargreaves, D.C., and Crabtree, G.R. (2011). ATP-dependent chromatin remodeling: genetics, genomics and mechanisms. Cell Res 21, 396-420.

Haupt, Y., Maya, R., Kazaz, A., and Oren, M. (1997). Mdm2 promotes the rapid degradation of p53. Nature 387, 296-299.

He, Y.F., Li, B.Z., Li, Z., Liu, P., Wang, Y., Tang, Q., Ding, J., Jia, Y., Chen, Z., Li, L., et al. (2011). Tet-mediated formation of 5-carboxylcytosine and its excision by TDG in mammalian DNA. Science 333, 1303-1307.

Helbling Chadwick, L., Chadwick, B.P., Jaye, D.L., and Wade, P.A. (2009). The Mi-2/NuRD complex associates with pericentromeric heterochromatin during S phase in rapidly proliferating lymphoid cells. Chromosoma 118, 445-457.

Henderson, A.S., Warburton, D., and Atwood, K.C. (1972). Location of ribosomal DNA in the human chromosome complement. Proc Natl Acad Sci U S A 69, 3394-3398.

Hendrich, B., and Bird, A. (1998). Identification and characterization of a family of mammalian methyl-CpG binding proteins. Mol Cell Biol 18, 6538-6547.

Hendrich, B., Guy, J., Ramsahoye, B., Wilson, V.A., and Bird, A. (2001). Closely related proteins MBD2 and MBD3 play distinctive but interacting roles in mouse development. Genes Dev 15, 710-723.

Henras, A.K., Soudet, J., Gerus, M., Lebaron, S., Caizergues-Ferrer, M., Mougin, A., and Henry, Y. (2008). The post-transcriptional steps of eukaryotic ribosome biogenesis. Cell Mol Life Sci 65, 2334-2359.

Hernandez-Verdun, D. (2011). Assembly and disassembly of the nucleolus during the cell cycle. Nucleus 2, 189-194.

Hetman, M., and Pietrzak, M. (2012). Emerging roles of the neuronal nucleolus. Trends in neurosciences 35, 305-314.

Huether, R., Dong, L., Chen, X., Wu, G., Parker, M., Wei, L., Ma, J., Edmonson, M.N., Hedlund, E.K., Rusch, M.C., et al. (2014). The landscape of somatic mutations in epigenetic regulators across 1,000 paediatric cancer genomes. Nat Commun 5, 3630.

Huh, H.J., Lee, S.H., Yoo, K.H., Sung, K.W., Koo, H.H., Jang, J.H., Kim, K., Kim, S.J., Kim, W.S., Jung, C.W., et al. (2013). Gene mutation profiles and prognostic implications in Korean patients with T-lymphoblastic leukemia. Ann Hematol 92, 635-644.

Huh, M.S., Price O'Dea, T., Ouazia, D., McKay, B.C., Parise, G., Parks, R.J., Rudnicki, M.A., and Picketts, D.J. (2012). Compromised genomic integrity impedes muscle growth after Atrx inactivation. J Clin Invest 122, 4412-4423.

Hung, H., Kohnken, R., and Svaren, J. (2012). The nucleosome remodeling and deacetylase chromatin remodeling (NuRD) complex is required for peripheral nerve myelination. J Neurosci 32, 1517-1527.

Ide, S., Miyazaki, T., Maki, H., and Kobayashi, T. (2010). Abundance of ribosomal RNA gene copies maintains genome integrity. Science 327, 693-696.

Ito, S., Shen, L., Dai, Q., Wu, S.C., Collins, L.B., Swenberg, J.A., He, C., and Zhang, Y. (2011). Tet proteins can convert 5-methylcytosine to 5-formylcytosine and 5-carboxylcytosine. Science 333, 1300-1303.

Iwase, S., Xiang, B., Ghosh, S., Ren, T., Lewis, P.W., Cochrane, J.C., Allis, C.D., Picketts, D.J., Patel, D.J., Li, H., et al. (2011). ATRX ADD domain links an atypical histone methylation recognition mechanism to human mental-retardation syndrome. Nat Struct Mol Biol 18, 769-776.

Jacob, M.D., Audas, T.E., Mullineux, S.T., and Lee, S. (2012). Where no RNA polymerase has gone before: novel functional transcripts derived from the ribosomal intergenic spacer. Nucleus 3, 315-319.

Jacob, M.D., Audas, T.E., Uniacke, J., Trinkle-Mulcahy, L., and Lee, S. (2013). Environmental cues induce a long noncoding RNA-dependent remodeling of the nucleolus. Mol Biol Cell 24, 2943-2953.

Jacobs, S.A., and Khorasanizadeh, S. (2002). Structure of HP1 chromodomain bound to a lysine 9-methylated histone H3 tail. Science 295, 2080-2083.

Jacquemont, S., Berry-Kravis, E., Hagerman, R., von Raison, F., Gasparini, F., Apostol, G., Ufer, M., Des Portes, V., and Gomez-Mancilla, B. (2014). The challenges of clinical trials in fragile X syndrome. Psychopharmacology 231, 1237-1250.

Jaju, R.J., Fidler, C., Haas, O.A., Strickson, A.J., Watkins, F., Clark, K., Cross, N.C., Cheng, J.F., Aplan, P.D., Kearney, L., et al. (2001). A novel gene, NSD1, is fused to NUP98 in the t(5;11)(q35;p15.5) in de novo childhood acute myeloid leukemia. Blood 98, 1264-1267.

Janeway, C.A., Travers, P., Walport, M., and Shlomchik, M.J. (2005). Immunobiology: The immune system in health and disease, 6th edn (New York, NY: Garland Science Publishing).

Jensen, L.R., Amende, M., Gurok, U., Moser, B., Gimmel, V., Tzschach, A., Janecke, A.R., Tariverdian, G., Chelly, J., Fryns, J.P., et al. (2005). Mutations in the JARID1C gene, which is involved in transcriptional regulation and chromatin remodeling, cause X-linked mental retardation. American journal of human genetics 76, 227-236.

Jiao, Y., Shi, C., Edil, B.H., de Wilde, R.F., Klimstra, D.S., Maitra, A., Schulick, R.D., Tang, L.H., Wolfgang, C.L., Choti, M.A., et al. (2011). DAXX/ATRX, MEN1, and mTOR pathway genes are frequently altered in pancreatic neuroendocrine tumors. Science 331, 1199-1203.

Kastner, P., Chan, S., Vogel, W.K., Zhang, L.J., Topark-Ngarm, A., Golonzhka, O., Jost, B., Le Gras, S., Gross, M.K., and Leid, M. (2010). Bcl11b represses a mature T-cell gene expression program in immature CD4(+)CD8(+) thymocytes. European journal of immunology 40, 2143-2154.

Katzaki, E., Morin, G., Pollazzon, M., Papa, F.T., Buoni, S., Hayek, J., Andrieux, J., Lecerf, L., Popovici, C., Receveur, A., et al. (2010). Syndromic mental retardation with thrombocytopenia due to 21q22.11q22.12 deletion: Report of three patients. Am J Med Genet A 152A, 1711-1717.

Keller, A., Nesvizhskii, A.I., Kolker, E., and Aebersold, R. (2002). Empirical statistical model to estimate the accuracy of peptide identifications made by MS/MS and database search. Anal Chem 74, 5383-5392.

Kent, W.J., Sugnet, C.W., Furey, T.S., Roskin, K.M., Pringle, T.H., Zahler, A.M., and Haussler, D. (2002). The human genome browser at UCSC. Genome research 12, 996-1006.

Kermekchiev, M., Workman, J.L., and Pikaard, C.S. (1997). Nucleosome binding by the polymerase I transactivator upstream binding factor displaces linker histone H1. Mol Cell Biol 17, 5833-5842.

Kettenbach, A.N., Schweppe, D.K., Faherty, B.K., Pechenick, D., Pletnev, A.A., and Gerber, S.A. (2011). Quantitative phosphoproteomics identifies substrates and functional modules of Aurora and Polo-like kinase activities in mitotic cells. Science signaling 4, rs5.

Klose, R.J., and Bird, A.P. (2006). Genomic DNA methylation: the mark and its mediators. Trends in biochemical sciences 31, 89-97.

Kohli, R.M., and Zhang, Y. (2013). TET enzymes, TDG and the dynamics of DNA demethylation. Nature 502, 472-479.

Kornberg, R.D. (1974). Chromatin structure: a repeating unit of histones and DNA. Science 184, 868-871.

Kos, K., and Wilding, J.P. (2010). SPARC: a key player in the pathologies associated with obesity and diabetes. Nature reviews Endocrinology 6, 225-235.

Kouzarides, T. (2007). Chromatin modifications and their function. Cell 128, 693-705.

Kowalski, K., Liew, C.K., Matthews, J.M., Gell, D.A., Crossley, M., and Mackay, J.P. (2002). Characterization of the conserved interaction between GATA and FOG family proteins. J Biol Chem 277, 35720-35729.

Kraszewska, M.D., Dawidowska, M., Larmonie, N.S., Kosmalska, M., Sedek, L., Szczepaniak, M., Grzeszczak, W., Langerak, A.W., Szczepanski, T., and Witt, M. (2012). DNA methylation pattern is altered in childhood T-cell acute lymphoblastic leukemia patients as compared with normal thymic subsets: insights into CpG island methylator phenotype in T-ALL. Leukemia 26, 367-371.

Kruhlak, M., Crouch, E.E., Orlov, M., Montano, C., Gorski, S.A., Nussenzweig, A., Misteli, T., Phair, R.D., and Casellas, R. (2007). The ATM repair pathway inhibits RNA polymerase I transcription in response to chromosome breaks. Nature 447, 730-734.

Kubbutat, M.H., Jones, S.N., and Vousden, K.H. (1997). Regulation of p53 stability by Mdm2. Nature 387, 299-303.

Kuhn, A., and Grummt, I. (1987). A novel promoter in the mouse rDNA spacer is active in vivo and in vitro. EMBO J 6, 3487-3492.

Kuhn, C.D., Geiger, S.R., Baumli, S., Gartmann, M., Gerber, J., Jennebach, S., Mielke, T., Tschochner, H., Beckmann, R., and Cramer, P. (2007). Functional architecture of RNA polymerase I. Cell 131, 1260-1272.

Kurotaki, N., Imaizumi, K., Harada, N., Masuno, M., Kondoh, T., Nagai, T., Ohashi, H., Naritomi, K., Tsukahara, M., Makita, Y., et al. (2002). Haploinsufficiency of NSD1 causes Sotos syndrome. Nat Genet 30, 365-366.

Kustatscher, G., Hegarat, N., Wills, K.L., Furlan, C., Bukowski-Wills, J.C., Hochegger, H., and Rappsilber, J. (2014). Proteomics of a fuzzy organelle: interphase chromatin. EMBO J 33, 648-664.

Lai, A.Y., and Wade, P.A. (2011). Cancer biology and NuRD: a multifaceted chromatin remodelling complex. Nat Rev Cancer 11, 588-596.

Landais, S., Quantin, R., and Rassart, E. (2005). Radiation leukemia virus common integration at the Kis2 locus: simultaneous overexpression of a novel noncoding RNA and of the proximal Phf6 gene. J Virol 79, 11443-11456.

Langst, G., Becker, P.B., and Grummt, I. (1998). TTF-I determines the chromatin architecture of the active rDNA promoter. EMBO J 17, 3135-3145.

Lapenna, S., and Giordano, A. (2009). Cell cycle kinases as therapeutic targets for cancer. Nature reviews Drug discovery 8, 547-566.

Lauberth, S.M., Bilyeu, A.C., Firulli, B.A., Kroll, K.L., and Rauchman, M. (2007). A phosphomimetic mutation in the Sall1 repression motif disrupts recruitment of the nucleosome remodeling and deacetylase complex and repression of Gbx2. J Biol Chem 282, 34858-34868.

Lauberth, S.M., and Rauchman, M. (2006). A conserved 12-amino acid motif in Sall1 recruits the nucleosome remodeling and deacetylase corepressor complex. J Biol Chem 281, 23922-23931.

Learned, R.M., Learned, T.K., Haltiner, M.M., and Tjian, R.T. (1986). Human rRNA transcription is modulated by the coordinate binding of two factors to an upstream control element. Cell 45, 847-857.

Lee, M.G., Villa, R., Trojer, P., Norman, J., Yan, K.P., Reinberg, D., Di Croce, L., and Shiekhattar, R. (2007). Demethylation of H3K27 regulates polycomb recruitment and H2A ubiquitination. Science 318, 447-450.

Lejon, S., Thong, S.Y., Murthy, A., AlQarni, S., Murzina, N.V., Blobel, G.A., Laue, E.D., and Mackay, J.P. (2011). Insights into association of the NuRD complex with FOG-1 from the crystal structure of an RbAp48.FOG-1 complex. J Biol Chem 286, 1196-1203.

Lessard, J., Wu, J.I., Ranish, J.A., Wan, M., Winslow, M.M., Staahl, B.T., Wu, H., Aebersold, R., Graef, I.A., and Crabtree, G.R. (2007). An essential switch in subunit composition of a chromatin remodeling complex during neural development. Neuron 55, 201-215.

Li, H., Ilin, S., Wang, W., Duncan, E.M., Wysocka, J., Allis, C.D., and Patel, D.J. (2006). Molecular basis for site-specific read-out of histone H3K4me3 by the BPTF PHD finger of NURF. Nature 442, 91-95.

Li, Q., Shi, L., Gui, B., Yu, W., Wang, J., Zhang, D., Han, X., Yao, Z., and Shang, Y. (2011). Binding of the JmjC demethylase JARID1B to LSD1/NuRD suppresses angiogenesis and metastasis in breast cancer cells by repressing chemokine CCL14. Cancer Res 71, 6899-6908.

Li, X., Yao, H., Chen, Z., Wang, Q., Zhao, Y., and Chen, S. (2013). Somatic mutations of PHF6 in patients with chronic myeloid leukemia in blast crisis. Leuk Lymphoma 54, 671-672.

Liang, G., Chan, M.F., Tomigahara, Y., Tsai, Y.C., Gonzales, F.A., Li, E., Laird, P.W., and Jones, P.A. (2002). Cooperativity between DNA methyltransferases in the maintenance methylation of repetitive elements. Mol Cell Biol 22, 480-491.

Liaw, D., Marsh, D.J., Li, J., Dahia, P.L., Wang, S.I., Zheng, Z., Bose, S., Call, K.M., Tsou, H.C., Peacocke, M., et al. (1997). Germline mutations of the PTEN gene in Cowden disease, an inherited breast and thyroid cancer syndrome. Nat Genet 16, 64-67.

Lindell, T.J., Weinberg, F., Morris, P.W., Roeder, R.G., and Rutter, W.J. (1970). Specific inhibition of nuclear RNA polymerase II by alpha-amanitin. Science 170, 447-449.

Ling, T., Xie, W., Luo, M., Shen, M., Zhu, Q., Zong, L., Zhou, T., Gu, J., Lu, Z., Zhang, F., et al. (2013). CHD4/NuRD maintains demethylation state of rDNA promoters through inhibiting the expression of the rDNA methyltransferase recruiter TIP5. Biochem Biophys Res Commun 437, 101-107.

Liu, L., Qin, S., Zhang, J., Ji, P., Shi, Y., and Wu, J. (2012). Solution structure of an atypical PHD finger in BRPF2 and its interaction with DNA. Journal of structural biology 180, 165-173.

Liu, Z., Li, F., Ruan, K., Zhang, J., Mei, Y., Wu, J., and Shi, Y. (2014). Structural and functional insights into the human Borjeson-Forssman-Lehmann syndrome-associated protein PHF6. J Biol Chem 289, 10069-10083.

Lower, K.M., Solders, G., Bondeson, M.L., Nelson, J., Brun, A., Crawford, J., Malm, G., Borjeson, M., Turner, G., Partington, M., et al. (2004). 1024C> T (R342X) is a recurrent PHF6 mutation also found in the original Borjeson-Forssman-Lehmann syndrome family. Eur J Hum Genet 12, 787-789.

Lower, K.M., Turner, G., Kerr, B.A., Mathews, K.D., Shaw, M.A., Gedeon, A.K., Schelley, S., Hoyme, H.E., White, S.M., Delatycki, M.B., et al. (2002). Mutations in PHF6 are associated with Borjeson-Forssman-Lehmann syndrome. Nat Genet 32, 661-665.

Maecker, H.T., McCoy, J.P., and Nussenblatt, R. (2012). Standardizing immunophenotyping for the Human Immunology Project. Nature reviews Immunology 12, 191-200.

Majumder, S., Alinari, L., Roy, S., Miller, T., Datta, J., Sif, S., Baiocchi, R., and Jacob, S.T. (2010). Methylation of histone H3 and H4 by PRMT5 regulates ribosomal RNA gene transcription. J Cell Biochem 109, 553-563.

Mangelsdorf, M., Chevrier, E., Mustonen, A., and Picketts, D.J. (2009). Borjeson-Forssman-Lehmann Syndrome due to a novel plant homeodomain zinc finger mutation in the PHF6 gene. J Child Neurol 24, 610-614.

Mansfield, R.E., Musselman, C.A., Kwan, A.H., Oliver, S.S., Garske, A.L., Davrazou, F., Denu, J.M., Kutateladze, T.G., and Mackay, J.P. (2011). Plant homeodomain (PHD) fingers of CHD4 are histone H3-binding modules with preference for unmodified H3K4 and methylated H3K9. J Biol Chem 286, 11779-11791.

Mathews, K.D., Ardinger, H.H., Nishimura, D.Y., Buetow, K.H., Murray, J.C., and Bartley, J.A. (1989). Linkage localization of Borjeson-Forssman-Lehmann syndrome. American journal of medical genetics 34, 470-474.

Matsuoka, S., Ballif, B.A., Smogorzewska, A., McDonald, E.R., 3rd, Hurov, K.E., Luo, J., Bakalarski, C.E., Zhao, Z., Solimini, N., Lerenthal, Y., et al. (2007). ATM and ATR substrate analysis reveals extensive protein networks responsive to DNA damage. Science 316, 1160-1166.

Mavrakis, K.J., Van Der Meulen, J., Wolfe, A.L., Liu, X., Mets, E., Taghon, T., Khan, A.A., Setty, M., Rondou, P., Vandenberghe, P., et al. (2011). A cooperative microRNA-tumor suppressor gene network in acute T-cell lymphoblastic leukemia (T-ALL). Nat Genet 43, 673-678.

Mayer, C., Schmitz, K.M., Li, J., Grummt, I., and Santoro, R. (2006). Intergenic transcripts regulate the epigenetic state of rRNA genes. Mol Cell 22, 351-361.

Mayya, V., Lundgren, D.H., Hwang, S.I., Rezaul, K., Wu, L., Eng, J.K., Rodionov, V., and Han, D.K. (2009). Quantitative phosphoproteomic analysis of T cell receptor signaling reveals system-wide modulation of protein-protein interactions. Science signaling 2, ra46.

McCabe, M.T., Brandes, J.C., and Vertino, P.M. (2009). Cancer DNA methylation: molecular mechanisms and clinical implications. Clin Cancer Res 15, 3927-3937.

McClintock, B. (1934). The relation of a particular chromosomal element to the development of the nucleoli in Zea mays. Zeitschrift für Zellforschung und Mikroskopische Anatomie 21, 294-328.

McGinty, R.K., Kim, J., Chatterjee, C., Roeder, R.G., and Muir, T.W. (2008). Chemically ubiquitylated histone H2B stimulates hDot1L-mediated intranucleosomal methylation. Nature 453, 812-816.

McKinnell, I.W., Ishibashi, J., Le Grand, F., Punch, V.G., Addicks, G.C., Greenblatt, J.F., Dilworth, F.J., and Rudnicki, M.A. (2008). Pax7 activates myogenic genes by recruitment of a histone methyltransferase complex. Nat Cell Biol 10, 77-84.

McStay, B., and Grummt, I. (2008). The epigenetics of rRNA genes: from molecular to chromosome biology. Annual review of cell and developmental biology 24, 131-157.

Meacham, C.E., Lawton, L.N., Soto-Feliciano, Y.M., Pritchard, J.R., Joughin, B.A., Ehrenberger, T., Fenouille, N., Zuber, J., Williams, R.T., Young, R.A., et al. (2015). A genome-scale in vivo loss-of-function screen identifies Phf6 as a lineage-specific regulator of leukemia cell growth. Genes Dev 29, 483-488.

Mendis, D.B., and Brown, I.R. (1994). Expression of the gene encoding the extracellular matrix glycoprotein SPARC in the developing and adult mouse brain. Brain research Molecular brain research 24, 11-19.

Mendis, D.B., Malaval, L., and Brown, I.R. (1995). SPARC, an extracellular matrix glycoprotein containing the follistatin module, is expressed by astrocytes in synaptic enriched regions of the adult brain. Brain Res 676, 69-79.

Mets, E., Van Peer, G., Van der Meulen, J., Boice, M., Taghon, T., Goossens, S., Mestdagh, P., Benoit, Y., De Moerloose, B., Van Roy, N., et al. (2014). MicroRNA-128-3p is a novel oncomiR targeting PHF6 in T-cell acute lymphoblastic leukemia. Haematologica.

Metzker, M.L. (2010). Sequencing technologies - the next generation. Nat Rev Genet 11, 31-46.

Min, J., Feng, Q., Li, Z., Zhang, Y., and Xu, R.M. (2003a). Structure of the catalytic domain of human DOT1L, a non-SET domain nucleosomal histone methyltransferase. Cell 112, 711-723.

Min, J., Zhang, Y., and Xu, R.M. (2003b). Structural basis for specific binding of Polycomb chromodomain to histone H3 methylated at Lys 27. Genes Dev 17, 1823-1828.

Molnar, A., and Georgopoulos, K. (1994). The Ikaros gene encodes a family of functionally diverse zinc finger DNA-binding proteins. Mol Cell Biol 14, 8292-8303.

Montanaro, L., Trere, D., and Derenzini, M. (2008). Nucleolus, ribosomes, and cancer. The American journal of pathology 173, 301-310.

Montgomery, T.H. (1898). Comparative cytological studies, with especial regard to the morphology of the nucleolus. J Morphol 15, 265-565.

Moran, V.A., Perera, R.J., and Khalil, A.M. (2012). Emerging functional and mechanistic paradigms of mammalian long non-coding RNAs. Nucleic Acids Res 40, 6391-6400.

Morin, R.D., Johnson, N.A., Severson, T.M., Mungall, A.J., An, J., Goya, R., Paul, J.E., Boyle, M., Woolcock, B.W., Kuchenbauer, F., et al. (2010). Somatic mutations altering EZH2 (Tyr641) in follicular and diffuse large B-cell lymphomas of germinal-center origin. Nat Genet 42, 181-185.

Moss, T., and Birnstiel, M.L. (1979). The putative promoter of a Xenopus laevis ribosomal gene is reduplicated. Nucleic Acids Res 6, 3733-3743.

Moss, T., Boseley, P.G., and Birnstiel, M.L. (1980). More ribosomal spacer sequences from Xenopus laevis. Nucleic Acids Res 8, 467-485.

Mullineux, S.T., and Lafontaine, D.L. (2012). Mapping the cleavage sites on mammalian pre-rRNAs: where do we stand? Biochimie 94, 1521-1532.

Naito, T., Gomez-Del Arco, P., Williams, C.J., and Georgopoulos, K. (2007). Antagonistic interactions between Ikaros and the chromatin remodeler Mi-2beta determine silencer activity and Cd4 gene expression. Immunity 27, 723-734.

Naito, T., Tanaka, H., Naoe, Y., and Taniuchi, I. (2011). Transcriptional control of T-cell development. International immunology 23, 661-668.

Nakajima, H., Toyoshima-Morimoto, F., Taniguchi, E., and Nishida, E. (2003). Identification of a consensus motif for Plk (Polo-like kinase) phosphorylation reveals Myt1 as a Plk1 substrate. J Biol Chem 278, 25277-25280.

Nakamura, T., Mori, T., Tada, S., Krajewski, W., Rozovskaia, T., Wassell, R., Dubois, G., Mazo, A., Croce, C.M., and Canaani, E. (2002). ALL-1 is a histone methyltransferase that assembles a supercomplex of proteins involved in transcriptional regulation. Mol Cell 10, 1119-1128.

Nemeth, A., Perez-Fernandez, J., Merkl, P., Hamperl, S., Gerber, J., Griesenbeck, J., and Tschochner, H. (2013). RNA polymerase I termination: Where is the end? Biochim Biophys Acta 1829, 306-317.

Nesvizhskii, A.I., and Aebersold, R. (2004). Analysis, statistical validation and dissemination of large-scale proteomics datasets generated by tandem MS. Drug discovery today 9, 173-181.

Ng, D., Thakker, N., Corcoran, C.M., Donnai, D., Perveen, R., Schneider, A., Hadley, D.W., Tifft, C., Zhang, L., Wilkie, A.O., et al. (2004). Oculofaciocardiodental and Lenz microphthalmia syndromes result from distinct classes of mutations in BCOR. Nat Genet 36, 411-416.

Ng, S.B., Bigham, A.W., Buckingham, K.J., Hannibal, M.C., McMillin, M.J., Gildersleeve, H.I., Beck, A.E., Tabor, H.K., Cooper, G.M., Mefford, H.C., et al. (2010). Exome sequencing identifies MLL2 mutations as a cause of Kabuki syndrome. Nat Genet 42, 790-793.

Nichols, K.E., Crispino, J.D., Poncz, M., White, J.G., Orkin, S.H., Maris, J.M., and Weiss, M.J. (2000). Familial dyserythropoietic anaemia and thrombocytopenia due to an inherited mutation in GATA1. Nat Genet 24, 266-270.

Novershtern, N., Subramanian, A., Lawton, L.N., Mak, R.H., Haining, W.N., McConkey, M.E., Habib, N., Yosef, N., Chang, C.Y., Shay, T., et al. (2011). Densely interconnected transcriptional circuits control cell states in human hematopoiesis. Cell 144, 296-309.

Ochs, R.L., Lischwe, M.A., Spohn, W.H., and Busch, H. (1985). Fibrillarin: a new protein of the nucleolus identified by autoimmune sera. Biol Cell 54, 123-133.

Okano, M., Xie, S., and Li, E. (1998). Cloning and characterization of a family of novel mammalian DNA (cytosine-5) methyltransferases. Nat Genet 19, 219-220.

Olsen, J.V., Vermeulen, M., Santamaria, A., Kumar, C., Miller, M.L., Jensen, L.J., Gnad, F., Cox, J., Jensen, T.S., Nigg, E.A., et al. (2010). Quantitative phosphoproteomics reveals widespread full phosphorylation site occupancy during mitosis. Science signaling 3, ra3.

Ooi, S.K., Qiu, C., Bernstein, E., Li, K., Jia, D., Yang, Z., Erdjument-Bromage, H., Tempst, P., Lin, S.P., Allis, C.D., et al. (2007). DNMT3L connects unmethylated lysine 4 of histone H3 to de novo methylation of DNA. Nature 448, 714-717.

Osterweil, E.K., Chuang, S.C., Chubykin, A.A., Sidorov, M., Bianchi, R., Wong, R.K., and Bear, M.F. (2013). Lovastatin corrects excess protein synthesis and prevents epileptogenesis in a mouse model of fragile X syndrome. Neuron 77, 243-250.

Palomero, T., Lim, W.K., Odom, D.T., Sulis, M.L., Real, P.J., Margolin, A., Barnes, K.C., O'Neil, J., Neuberg, D., Weng, A.P., et al. (2006). NOTCH1 directly regulates c-MYC and activates a feed-forward-loop transcriptional network promoting leukemic cell growth. Proc Natl Acad Sci U S A 103, 18261-18266.

Parsons, D.W., Li, M., Zhang, X., Jones, S., Leary, R.J., Lin, J.C., Boca, S.M., Carter, H., Samayoa, J., Bettegowda, C., et al. (2011). The genetic landscape of the childhood cancer medulloblastoma. Science 331, 435-439.

Patel, J.P., Gonen, M., Figueroa, M.E., Fernandez, H., Sun, Z., Racevskis, J., Van Vlierberghe, P., Dolgalev, I., Thomas, S., Aminova, O., et al. (2012). Prognostic relevance of integrated genetic profiling in acute myeloid leukemia. N Engl J Med 366, 1079-1089.

Pegoraro, G., Kubben, N., Wickert, U., Gohler, H., Hoffmann, K., and Misteli, T. (2009). Ageing-related chromatin defects through loss of the NURD complex. Nat Cell Biol 11, 1261-1267.

Peltonen, K., Colis, L., Liu, H., Trivedi, R., Moubarek, M.S., Moore, H.M., Bai, B., Rudek, M.A., Bieberich, C.J., and Laiho, M. (2014). A targeting modality for destruction of RNA polymerase I that possesses anticancer activity. Cancer Cell 25, 77-90.

Perry, J. (2006). The Epc-N domain: a predicted protein-protein interaction domain found in select chromatin associated proteins. BMC genomics 7, 6.

Perry, R.P. (1962). The Cellular Sites of Synthesis of Ribosomal and 4s Rna. Proc Natl Acad Sci U S A 48, 2179-2186.

Petrij, F., Giles, R.H., Dauwerse, H.G., Saris, J.J., Hennekam, R.C., Masuno, M., Tommerup, N., van Ommen, G.J., Goodman, R.H., Peters, D.J., et al. (1995). Rubinstein-Taybi syndrome caused by mutations in the transcriptional co-activator CBP. Nature 376, 348-351.

Picketts, D.J., Higgs, D.R., Bachoo, S., Blake, D.J., Quarrell, O.W., and Gibbons, R.J. (1996). ATRX encodes a novel member of the SNF2 family of proteins: mutations point to a common mechanism underlying the ATR-X syndrome. Hum Mol Genet 5, 1899-1907.

Plass, C., Pfister, S.M., Lindroth, A.M., Bogatyrova, O., Claus, R., and Lichter, P. (2013). Mutations in regulators of the epigenome and their connections to global chromatin patterns in cancer. Nat Rev Genet 14, 765-780.

Polo, S.E., Kaidi, A., Baskcomb, L., Galanty, Y., and Jackson, S.P. (2010). Regulation of DNA-damage responses and cell-cycle progression by the chromatin remodelling factor CHD4. Embo J 29, 3130-3139.

Pop, A.S., Gomez-Mancilla, B., Neri, G., Willemsen, R., and Gasparini, F. (2014). Fragile X syndrome: a preclinical review on metabotropic glutamate receptor 5 (mGluR5) antagonists and drug development. Psychopharmacology 231, 1217-1226.

Potts, R.C., Zhang, P., Wurster, A.L., Precht, P., Mughal, M.R., Wood, W.H., 3rd, Zhang, Y., Becker, K.G., Mattson, M.P., and Pazin, M.J. (2011). CHD5, a brain-specific paralog of Mi2 chromatin remodeling enzymes, regulates expression of neuronal genes. PLoS One 6, e24515.

Puig, O., Caspary, F., Rigaut, G., Rutz, B., Bouveret, E., Bragado-Nilsson, E., Wilm, M., and Seraphin, B. (2001). The tandem affinity purification (TAP) method: a general procedure of protein complex purification. Methods (San Diego, Calif 24, 218-229.

Qin, S., and Min, J. (2014). Structure and function of the nucleosome-binding PWWP domain. Trends in biochemical sciences 39, 536-547.

Qiu, Y., Zhang, W., Zhao, C., Wang, Y., Wang, W., Zhang, J., Zhang, Z., Li, G., Shi, Y., Tu, X., et al. (2012). Solution structure of the Pdp1 PWWP domain reveals its unique binding sites for methylated H4K20 and DNA. Biochem J 442, 527-538.

Ragvin, A., Valvatne, H., Erdal, S., Arskog, V., Tufteland, K.R., Breen, K., AM, O.Y., Eberharter, A., Gibson, T.J., Becker, P.B., et al. (2004). Nucleosome binding by the bromodomain and PHD finger of the transcriptional cofactor p300. Journal of molecular biology 337, 773-788.

Renedo, M., Martinez-Delgado, B., Arranz, E., Garcia, M., Urioste, M., Martinez-Ramirez, A., Rivas, C., Cigudosa, J.C., and Benitez, I. (2001). Chromosomal changes pattern and gene amplification in T cell non-Hodgkin's lymphomas. Leukemia 15, 1627-1632.

Reynolds, N., Latos, P., Hynes-Allen, A., Loos, R., Leaford, D., O'Shaughnessy, A., Mosaku, O., Signolet, J., Brennecke, P., Kalkan, T., et al. (2012a). NuRD suppresses pluripotency gene expression to promote transcriptional heterogeneity and lineage commitment. Cell Stem Cell 10, 583-594.

Reynolds, N., Salmon-Divon, M., Dvinge, H., Hynes-Allen, A., Balasooriya, G., Leaford, D., Behrens, A., Bertone, P., and Hendrich, B. (2012b). NuRD-mediated deacetylation of H3K27 facilitates recruitment of Polycomb Repressive Complex 2 to direct gene repression. EMBO J 31, 593-605.

Richmond, T.J., and Davey, C.A. (2003). The structure of DNA in the nucleosome core. Nature 423, 145-150.

Ritossa, F.M., and Spiegelman, S. (1965). Localization of DNA Complementary to Ribosomal Rna in the Nucleolus Organizer Region of Drosophila Melanogaster. Proc Natl Acad Sci U S A 53, 737-745.

Rubbi, C.P., and Milner, J. (2003). Disruption of the nucleolus mediates stabilization of p53 in response to DNA damage and other stresses. EMBO J 22, 6068-6077.

Saito, M., and Ishikawa, F. (2002). The mCpG-binding domain of human MBD3 does not bind to mCpG but interacts with NuRD/Mi2 components HDAC1 and MTA2. J Biol Chem 277, 35434-35439.

Saksouk, N., Avvakumov, N., Champagne, K.S., Hung, T., Doyon, Y., Cayrou, C., Paquet, E., Ullah, M., Landry, A.J., Cote, V., et al. (2009). HBO1 HAT complexes target chromatin throughout gene coding regions via multiple PHD finger interactions with histone H3 tail. Mol Cell 33, 257-265.

Sanij, E., Poortinga, G., Sharkey, K., Hung, S., Holloway, T.P., Quin, J., Robb, E., Wong, L.H., Thomas, W.G., Stefanovsky, V., et al. (2008). UBF levels determine the number of active ribosomal RNA genes in mammals. J Cell Biol 183, 1259-1274.

Santoro, R., and Grummt, I. (2001). Molecular mechanisms mediating methylation-dependent silencing of ribosomal gene transcription. Mol Cell 8, 719-725.

Santoro, R., Li, J., and Grummt, I. (2002). The nucleolar remodeling complex NoRC mediates heterochromatin formation and silencing of ribosomal gene transcription. Nat Genet 32, 393-396.

Sarraf, S.A., and Stancheva, I. (2004). Methyl-CpG binding protein MBD1 couples histone H3 methylation at lysine 9 by SETDB1 to DNA replication and chromatin assembly. Mol Cell 15, 595-605.

Scheer, U., Hugle, B., Hazan, R., and Rose, K.M. (1984). Drug-induced dispersal of transcribed rRNA genes and transcriptional products: immunolocalization and silver staining of different nucleolar components in rat cells treated with 5,6-dichloro-beta-D-ribofuranosylbenzimidazole. J Cell Biol 99, 672-679.

Scheer, U., Thiry, M., and Goessens, G. (1993). Structure, function and assembly of the nucleolus. Trends Cell Biol 3, 236-241.

Schlesinger, S., Selig, S., Bergman, Y., and Cedar, H. (2009). Allelic inactivation of rDNA loci. Genes Dev 23, 2437-2447.

Schmitz, K.M., Mayer, C., Postepska, A., and Grummt, I. (2010). Interaction of noncoding RNA with the rDNA promoter mediates recruitment of DNMT3b and silencing of rRNA genes. Genes Dev 24, 2264-2269.

Schmitz, K.M., Schmitt, N., Hoffmann-Rohrer, U., Schafer, A., Grummt, I., and Mayer, C. (2009). TAF12 recruits Gadd45a and the nucleotide excision repair complex to the promoter of rRNA genes leading to active DNA demethylation. Mol Cell 33, 344-353.

Schneider, D.A. (2012). RNA polymerase I activity is regulated at multiple steps in the transcription cycle: recent insights into factors that influence transcription elongation. Gene 493, 176-184.

Schneider, D.A., Michel, A., Sikes, M.L., Vu, L., Dodd, J.A., Salgia, S., Osheim, Y.N., Beyer, A.L., and Nomura, M. (2007). Transcription elongation by RNA polymerase I is linked to efficient rRNA processing and ribosome assembly. Mol Cell 26, 217-229.

Schubbert, S., Zenker, M., Rowe, S.L., Boll, S., Klein, C., Bollag, G., van der Burgt, I., Musante, L., Kalscheuer, V., Wehner, L.E., et al. (2006). Germline KRAS mutations cause Noonan syndrome. Nat Genet 38, 331-336.

Schullek, J.R., and Wilson, I.B. (1988). The binding of zinc to angiotensin-converting enzyme. Archives of biochemistry and biophysics 265, 346-350.

Schwartzentruber, J., Korshunov, A., Liu, X.Y., Jones, D.T., Pfaff, E., Jacob, K., Sturm, D., Fontebasso, A.M., Quang, D.A., Tonjes, M., et al. (2012). Driver mutations in histone H3.3 and chromatin remodelling genes in paediatric glioblastoma. Nature 482, 226-231.

Shafey, D., Boyer, J.G., Bhanot, K., and Kothary, R. (2010). Identification of novel interacting protein partners of SMN using tandem affinity purification. J Proteome Res 9, 1659-1669.

Shahbazian, M.D., and Grunstein, M. (2007). Functions of site-specific histone acetylation and deacetylation. Annu Rev Biochem 76, 75-100.

Shen, M., Zhou, T., Xie, W., Ling, T., Zhu, Q., Zong, L., Lyu, G., Gao, Q., Zhang, F., and Tao, W. (2013). The chromatin remodeling factor CSB recruits histone acetyltransferase PCAF to rRNA gene promoters in active state for transcription initiation. PLoS One 8, e62668.

Shi, X., Hong, T., Walter, K.L., Ewalt, M., Michishita, E., Hung, T., Carney, D., Pena, P., Lan, F., Kaadige, M.R., et al. (2006). ING2 PHD domain links histone H3 lysine 4 methylation to active gene repression. Nature 442, 96-99.

Shi, Y., Lan, F., Matson, C., Mulligan, P., Whetstine, J.R., Cole, P.A., Casero, R.A., and Shi, Y. (2004). Histone demethylation mediated by the nuclear amine oxidase homolog LSD1. Cell 119, 941-953.

Shimono, K., Shimono, Y., Shimokata, K., Ishiguro, N., and Takahashi, M. (2005). Microspherule protein 1, Mi-2beta, and RET finger protein associate in the nucleolus and up-regulate ribosomal gene transcription. J Biol Chem 280, 39436-39447.

Shimono, Y., Murakami, H., Kawai, K., Wade, P.A., Shimokata, K., and Takahashi, M. (2003). Mi-2 beta associates with BRG1 and RET finger protein at the distinct regions with transcriptional activating and repressing abilities. J Biol Chem 278, 51638-51645.

Shiratori, M., Suzuki, T., Itoh, C., Goto, M., Furuichi, Y., and Matsumoto, T. (2002). WRN helicase accelerates the transcription of ribosomal RNA as a component of an RNA polymerase I-associated complex. Oncogene 21, 2447-2454.

Silverstein, R.A., and Ekwall, K. (2005). Sin3: a flexible regulator of global gene expression and genome stability. Curr Genet 47, 1-17.

Sims, J.K., and Wade, P.A. (2011). Mi-2/NuRD complex function is required for normal S phase progression and assembly of pericentric heterochromatin. Mol Biol Cell 22, 3094-3102.

Singleton, M.K., Gonzales, M.L., Leung, K.N., Yasui, D.H., Schroeder, D.I., Dunaway, K., and LaSalle, J.M. (2011). MeCP2 is required for global heterochromatic and nucleolar changes during activity-dependent neuronal maturation. Neurobiology of disease 43, 190-200.

Sjottem, E., Rekdal, C., Svineng, G., Johnsen, S.S., Klenow, H., Uglehus, R.D., and Johansen, T. (2007). The ePHD protein SPBP interacts with TopBP1 and together they co-operate to stimulate Ets1-mediated transcription. Nucleic Acids Res 35, 6648-6662.

Sloan, K.E., Mattijssen, S., Lebaron, S., Tollervey, D., Pruijn, G.J., and Watkins, N.J. (2013). Both endonucleolytic and exonucleolytic cleavage mediate ITS1 removal during human ribosomal RNA processing. J Cell Biol 200, 577-588.

Song, W.J., Sullivan, M.G., Legare, R.D., Hutchings, S., Tan, X., Kufrin, D., Ratajczak, J., Resende, I.C., Haworth, C., Hock, R., et al. (1999). Haploinsufficiency of CBFA2 causes familial thrombocytopenia with propensity to develop acute myelogenous leukaemia. Nat Genet 23, 166-175.

Stefanovsky, V., Langlois, F., Gagnon-Kugler, T., Rothblum, L.I., and Moss, T. (2006). Growth factor signaling regulates elongation of RNA polymerase I transcription in mammals via UBF phosphorylation and r-chromatin remodeling. Mol Cell 21, 629-639.

Stender, J.D., Pascual, G., Liu, W., Kaikkonen, M.U., Do, K., Spann, N.J., Boutros, M., Perrimon, N., Rosenfeld, M.G., and Glass, C.K. (2012). Control of proinflammatory gene programs by regulated trimethylation and demethylation of histone H4K20. Mol Cell 48, 28-38.

Stephens, P.J., Tarpey, P.S., Davies, H., Van Loo, P., Greenman, C., Wedge, D.C., Nik-Zainal, S., Martin, S., Varela, I., Bignell, G.R., et al. (2012). The landscape of cancer genes and mutational processes in breast cancer. Nature 486, 400-404.

Stevenson, R.E., Schwartz, C.E., and Rogers, R.C. (2013). Malformations among the X-linked intellectual disability syndromes. Am J Med Genet A 161A, 2741-2749.

Strahl, B.D., and Allis, C.D. (2000). The language of covalent histone modifications. Nature 403, 41-45.

Strohner, R., Nemeth, A., Jansa, P., Hofmann-Rohrer, U., Santoro, R., Langst, G., and Grummt, I. (2001). NoRC--a novel member of mammalian ISWI-containing chromatin remodeling machines. EMBO J 20, 4892-4900.

Strohner, R., Nemeth, A., Nightingale, K.P., Grummt, I., Becker, P.B., and Langst, G. (2004). Recruitment of the nucleolar remodeling complex NoRC establishes ribosomal DNA silencing in chromatin. Mol Cell Biol 24, 1791-1798.

Stubbert, L.J., Hamill, J.D., Spronck, J.C., Smith, J.M., Becerril, C., and McKay, B.C. (2007). DDB2-independent role for p53 in the recovery from ultraviolet light-induced replication arrest. Cell cycle 6, 1730-1740.

Suva, M.L., Riggi, N., and Bernstein, B.E. (2013). Epigenetic reprogramming in cancer. Science 339, 1567-1570.

Tahiliani, M., Koh, K.P., Shen, Y., Pastor, W.A., Bandukwala, H., Brudno, Y., Agarwal, S., Iyer, L.M., Liu, D.R., Aravind, L., et al. (2009). Conversion of 5-methylcytosine to 5-hydroxymethylcytosine in mammalian DNA by MLL partner TET1. Science 324, 930-935.

Talbert, P.B., and Henikoff, S. (2010). Histone variants--ancient wrap artists of the epigenome. Nat Rev Mol Cell Biol 11, 264-275.

Tang, B., Di Lena, P., Schaffer, L., Head, S.R., Baldi, P., and Thomas, E.A. (2011). Genome-wide identification of Bcl11b gene targets reveals role in brain-derived neurotrophic factor signaling. PLoS One 6, e23691.

Thompson, J.D., Higgins, D.G., and Gibson, T.J. (1994). CLUSTAL W: improving the sensitivity of progressive multiple sequence alignment through sequence weighting, position-specific gap penalties and weight matrix choice. Nucleic Acids Res 22, 4673-4680.

Todd, M.A., and Picketts, D.J. (2012). PHF6 interacts with the nucleosome remodeling and deacetylation (NuRD) complex. J Proteome Res 11, 4326-4337.

Tong, J.K., Hassig, C.A., Schnitzler, G.R., Kingston, R.E., and Schreiber, S.L. (1998). Chromatin deacetylation by an ATP-dependent nucleosome remodelling complex. Nature 395, 917-921.

Trivier, E., De Cesare, D., Jacquot, S., Pannetier, S., Zackai, E., Young, I., Mandel, J.L., Sassone-Corsi, P., and Hanauer, A. (1996). Mutations in the kinase Rsk-2 associated with Coffin-Lowry syndrome. Nature 384, 567-570.

Tschochner, H., and Hurt, E. (2003). Pre-ribosomes on the road from the nucleolus to the cytoplasm. Trends Cell Biol 13, 255-263.

Tsukada, Y., Fang, J., Erdjument-Bromage, H., Warren, M.E., Borchers, C.H., Tempst, P., and Zhang, Y. (2006). Histone demethylation by a family of JmjC domain-containing proteins. Nature 439, 811-816.

Turner, G., Gedeon, A., Mulley, J., Sutherland, G., Rae, J., Power, K., and Arthur, I. (1989). Borjeson-Forssman-Lehmann syndrome: clinical manifestations and gene localization to Xq26-27. American journal of medical genetics 34, 463-469.

Turner, G., Lower, K.M., White, S.M., Delatycki, M., Lampe, A.K., Wright, M., Smith, J.C., Kerr, B., Schelley, S., Hoyme, H.E., et al. (2004). The clinical picture of the Borjeson-Forssman-Lehmann syndrome in males and heterozygous females with PHF6 mutations. Clin Genet 65, 226-232.

Valdez, B.C., Henning, D., So, R.B., Dixon, J., and Dixon, M.J. (2004). The Treacher Collins syndrome (TCOF1) gene product is involved in ribosomal DNA gene transcription by interacting with upstream binding factor. Proc Natl Acad Sci U S A 101, 10709-10714.

Vallee, D., Chevrier, E., Graham, G.E., Lazzaro, M.A., Lavigne, P.A., Hunter, A.G., and Picketts, D.J. (2004). A novel PHF6 mutation results in enhanced exon skipping and mild Borjeson-Forssman-Lehmann syndrome. J Med Genet 41, 778-783.

van Bokhoven, H. (2011). Genetic and epigenetic networks in intellectual disabilities. Annual review of genetics 45, 81-104.

van de Nobelen, S., Rosa-Garrido, M., Leers, J., Heath, H., Soochit, W., Joosen, L., Jonkers, I., Demmers, J., van der Reijden, M., Torrano, V., et al. (2010). CTCF regulates the local epigenetic state of ribosomal DNA repeats. Epigenetics Chromatin 3, 19.

Van Vlierberghe, P., and Ferrando, A. (2012). The molecular basis of T cell acute lymphoblastic leukemia. J Clin Invest 122, 3398-3406.

Van Vlierberghe, P., Palomero, T., Khiabanian, H., Van der Meulen, J., Castillo, M., Van Roy, N., De Moerloose, B., Philippe, J., Gonzalez-Garcia, S., Toribio, M.L., et al. (2010). PHF6 mutations in T-cell acute lymphoblastic leukemia. Nat Genet 42, 338-342.

Van Vlierberghe, P., Patel, J., Abdel-Wahab, O., Lobry, C., Hedvat, C.V., Balbin, M., Nicolas, C., Payer, A.R., Fernandez, H.F., Tallman, M.S., et al. (2011). PHF6 mutations in adult acute myeloid leukemia. Leukemia 25, 130-134.

Van Vlierberghe, P., Pieters, R., Beverloo, H.B., and Meijerink, J.P. (2008). Molecular-genetic insights in paediatric T-cell acute lymphoblastic leukaemia. Br J Haematol 143, 153-168.

Vincent, A.J., Lau, P.W., and Roskams, A.J. (2008). SPARC is expressed by macroglia and microglia in the developing and mature nervous system. Developmental dynamics : an official publication of the American Association of Anatomists 237, 1449-1462.

Voit, R., Hoffmann, M., and Grummt, I. (1999). Phosphorylation by G1-specific cdk-cyclin complexes activates the nucleolar transcription factor UBF. Embo J 18, 1891-1899.

Voss, A.K., Gamble, R., Collin, C., Shoubridge, C., Corbett, M., Gecz, J., and Thomas, T. (2007). Protein and gene expression analysis of Phf6, the gene mutated in the Borjeson-Forssman-Lehmann Syndrome of intellectual disability and obesity. Gene Expr Patterns 7, 858-871.

Wakabayashi, Y., Watanabe, H., Inoue, J., Takeda, N., Sakata, J., Mishima, Y., Hitomi, J., Yamamoto, T., Utsuyama, M., Niwa, O., et al. (2003). Bcl11b is required for differentiation and survival of alphabeta T lymphocytes. Nat Immunol 4, 533-539.

Wang, J., Leung, J.W., Gong, Z., Feng, L., Shi, X., and Chen, J. (2013). PHF6 regulates cell cycle progression by suppressing ribosomal RNA synthesis. J Biol Chem 288, 3174-3183.

Wang, Q., Qiu, H., Jiang, H., Wu, L., Dong, S., Pan, J., Wang, W., Ping, N., Xia, J., Sun, A., et al. (2011). Mutations of PHF6 are associated with mutations of NOTCH1, JAK1 and rearrangement of SET-NUP214 in T-cell acute lymphoblastic leukemia. Haematologica 96, 1808-1814.

Wang, Y., Zhang, H., Chen, Y., Sun, Y., Yang, F., Yu, W., Liang, J., Sun, L., Yang, X., Shi, L., et al. (2009). LSD1 is a subunit of the NuRD complex and targets the metastasis programs in breast cancer. Cell 138, 660-672.

Warner, J.R. (1999). The economics of ribosome biosynthesis in yeast. Trends in biochemical sciences 24, 437-440.

Wasiak, S., Legendre-Guillemin, V., Puertollano, R., Blondeau, F., Girard, M., de Heuvel, E., Boismenu, D., Bell, A.W., Bonifacino, J.S., and McPherson, P.S. (2002). Enthoprotin: a novel clathrin-associated protein identified through subcellular proteomics. J Cell Biol 158, 855-862.

Watt, F., and Molloy, P.L. (1988). Cytosine methylation prevents binding to DNA of a HeLa cell transcription factor required for optimal expression of the adenovirus major late promoter. Genes Dev 2, 1136-1143.

Weber, J.D., Taylor, L.J., Roussel, M.F., Sherr, C.J., and Bar-Sagi, D. (1999). Nucleolar Arf sequesters Mdm2 and activates p53. Nat Cell Biol 1, 20-26.

Weisenberger, D., and Scheer, U. (1995). A possible mechanism for the inhibition of ribosomal RNA gene transcription during mitosis. J Cell Biol 129, 561-575.

Weng, A.P., Ferrando, A.A., Lee, W., Morris, J.P.t., Silverman, L.B., Sanchez-Irizarry, C., Blacklow, S.C., Look, A.T., and Aster, J.C. (2004). Activating mutations of NOTCH1 in human T cell acute lymphoblastic leukemia. Science 306, 269-271.

Wieczorek, D., Bogershausen, N., Beleggia, F., Steiner-Haldenstatt, S., Pohl, E., Li, Y., Milz, E., Martin, M., Thiele, H., Altmuller, J., et al. (2013). A comprehensive molecular study on Coffin-Siris and Nicolaides-Baraitser syndromes identifies a broad molecular and clinical spectrum converging on altered chromatin remodeling. Hum Mol Genet 22, 5121-5135.

Williams, C.J., Naito, T., Arco, P.G., Seavitt, J.R., Cashman, S.M., De Souza, B., Qi, X., Keables, P., Von Andrian, U.H., and Georgopoulos, K. (2004). The chromatin remodeler Mi-2beta is required for CD4 expression and T cell development. Immunity 20, 719-733.

Xie, W., Ling, T., Zhou, Y., Feng, W., Zhu, Q., Stunnenberg, H.G., Grummt, I., and Tao, W. (2012). The chromatin remodeling complex NuRD establishes the poised state of rRNA genes characterized by bivalent histone modifications and altered nucleosome positions. Proc Natl Acad Sci U S A 109, 8161-8166.

Xu, C., Bian, C., Yang, W., Galka, M., Ouyang, H., Chen, C., Qiu, W., Liu, H., Jones, A.E., MacKenzie, F., et al. (2010a). Binding of different histone marks differentially regulates the activity and specificity of polycomb repressive complex 2 (PRC2). Proc Natl Acad Sci U S A 107, 19266-19271.

Xu, Y.Z., Heravi, M., Thuraisingam, T., Di Marco, S., Muanza, T., and Radzioch, D. (2010b). Brg-1 mediates the constitutive and fenretinide-induced expression of SPARC in mammary carcinoma cells via its interaction with transcription factor Sp1. Molecular cancer 9, 210.

Yamashita, K., Sato, A., Asashima, M., Wang, P.C., and Nishinakamura, R. (2007). Mouse homolog of SALL1, a causative gene for Townes-Brocks syndrome, binds to A/T-rich sequences in pericentric heterochromatin via its C-terminal zinc finger domains. Genes Cells 12, 171-182.

Yao, Y.L., and Yang, W.M. (2003). The metastasis-associated proteins 1 and 2 form distinct protein complexes with histone deacetylase activity. J Biol Chem 278, 42560-42568.

Yildirim, O., Li, R., Hung, J.H., Chen, P.B., Dong, X., Ee, L.S., Weng, Z., Rando, O.J., and Fazzio, T.G. (2011). Mbd3/NURD complex regulates expression of 5-hydroxymethylcytosine marked genes in embryonic stem cells. Cell 147, 1498-1510.

Yoder, J.A., Soman, N.S., Verdine, G.L., and Bestor, T.H. (1997). DNA (cytosine-5)-methyltransferases in mouse cells and tissues. Studies with a mechanism-based probe. Journal of molecular biology 270, 385-395.

Yoo, N.J., Kim, Y.R., and Lee, S.H. (2012). Somatic mutation of PHF6 gene in T-cell acute lymphoblatic leukemia, acute myelogenous leukemia and hepatocellular carcinoma. Acta Oncol 51, 107-111.

Yoshida, T., Hazan, I., Zhang, J., Ng, S.Y., Naito, T., Snippert, H.J., Heller, E.J., Qi, X., Lawton, L.N., Williams, C.J., et al. (2008). The role of the chromatin remodeler Mi-2beta in hematopoietic stem cell self-renewal and multilineage differentiation. Genes Dev 22, 1174-1189.

You, J.S., and Jones, P.A. (2012). Cancer genetics and epigenetics: two sides of the same coin? Cancer Cell 22, 9-20.

Young, D.W., Hassan, M.Q., Pratap, J., Galindo, M., Zaidi, S.K., Lee, S.H., Yang, X., Xie, R., Javed, A., Underwood, J.M., et al. (2007). Mitotic occupancy and lineage-specific transcriptional control of rRNA genes by Runx2. Nature 445, 442-446.

Yuan, X., Zhao, J., Zentgraf, H., Hoffmann-Rohrer, U., and Grummt, I. (2002). Multiple interactions between RNA polymerase I, TIF-IA and TAF(I) subunits regulate preinitiation complex assembly at the ribosomal gene promoter. EMBO Rep 3, 1082-1087.

Yui, M.A., and Rothenberg, E.V. (2014). Developmental gene networks: a triathlon on the course to T cell identity. Nature reviews Immunology 14, 529-545.

Zandomeni, R., Zandomeni, M.C., Shugar, D., and Weinmann, R. (1986). Casein kinase type II is involved in the inhibition by 5,6-dichloro-1-beta-D-ribofuranosylbenzimidazole of specific RNA polymerase II transcription. J Biol Chem 261, 3414-3419.

Zentner, G.E., Layman, W.S., Martin, D.M., and Scacheri, P.C. (2010). Molecular and phenotypic aspects of CHD7 mutation in CHARGE syndrome. Am J Med Genet A 152A, 674-686.

Zentner, G.E., Saiakhova, A., Manaenkov, P., Adams, M.D., and Scacheri, P.C. (2011). Integrative genomic analysis of human ribosomal DNA. Nucleic Acids Res 39, 4949-4960.

Zhai, W., and Comai, L. (2000). Repression of RNA polymerase I transcription by the tumor suppressor p53. Mol Cell Biol 20, 5930-5938.

Zhang, C., Mejia, L.A., Huang, J., Valnegri, P., Bennett, E.J., Anckar, J., Jahani-Asl, A., Gallardo, G., Ikeuchi, Y., Yamada, T., et al. (2013). The X-linked intellectual disability protein PHF6 associates with the PAF1 complex and regulates neuronal migration in the mammalian brain. Neuron 78, 986-993.

Zhang, J., Jackson, A.F., Naito, T., Dose, M., Seavitt, J., Liu, F., Heller, E.J., Kashiwagi, M., Yoshida, T., Gounari, F., et al. (2012a). Harnessing of the nucleosome-remodeling-deacetylase complex controls lymphocyte development and prevents leukemogenesis. Nat Immunol 13, 86-94.

Zhang, L.J., Vogel, W.K., Liu, X., Topark-Ngarm, A., Arbogast, B.L., Maier, C.S., Filtz, T.M., and Leid, M. (2012b). Coordinated regulation of transcription factor Bcl11b activity in thymocytes by the mitogen-activated protein kinase (MAPK) pathways and protein sumoylation. J Biol Chem 287, 26971-26988.

Zhang, Y., Jurkowska, R., Soeroes, S., Rajavelu, A., Dhayalan, A., Bock, I., Rathert, P., Brandt, O., Reinhardt, R., Fischle, W., et al. (2010a). Chromatin methylation activity of Dnmt3a and Dnmt3a/3L is guided by interaction of the ADD domain with the histone H3 tail. Nucleic Acids Res 38, 4246-4253.

Zhang, Y., LeRoy, G., Seelig, H.P., Lane, W.S., and Reinberg, D. (1998). The dermatomyositis-specific autoantigen Mi2 is a component of a complex containing histone deacetylase and nucleosome remodeling activities. Cell 95, 279-289.

Zhang, Y., Ng, H.H., Erdjument-Bromage, H., Tempst, P., Bird, A., and Reinberg, D. (1999). Analysis of the NuRD subunits reveals a histone deacetylase core complex and a connection with DNA methylation. Genes Dev 13, 1924-1935.

Zhang, Y., Smith, A.D.t., Renfrow, M.B., and Schneider, D.A. (2010b). The RNA polymerase-associated factor 1 complex (Paf1C) directly increases the elongation rate of RNA polymerase I and is required for efficient regulation of rRNA synthesis. J Biol Chem 285, 14152-14159.

Zhou, M.I., Wang, H., Foy, R.L., Ross, J.J., and Cohen, H.T. (2004). Tumor suppressor von Hippel-Lindau (VHL) stabilization of Jade-1 protein occurs through plant homeodomains and is VHL mutation dependent. Cancer Res 64, 1278-1286.

Zhou, Y., Santoro, R., and Grummt, I. (2002). The chromatin remodeling complex NoRC targets HDAC1 to the ribosomal gene promoter and represses RNA polymerase I transcription. EMBO J 21, 4632-4640.

Zhu, Z., Wang, Y., Li, X., Xu, L., Wang, X., Sun, T., Dong, X., Chen, L., Mao, H., Yu, Y., et al. (2010). PHF8 is a histone H3K9me2 demethylase regulating rRNA synthesis. Cell Res 20, 794-801.

Zweier, C., Kraus, C., Brueton, L., Cole, T., Degenhardt, F., Engels, H., Gillessen-Kaesbach, G., Graul-Neumann, L., Horn, D., Hoyer, J., et al. (2013). A new face of Borjeson-Forssman-Lehmann syndrome? De novo mutations in PHF6 in seven females with a distinct phenotype. J Med Genet 50, 838-847.

Zweier, C., Rittinger, O., Bader, I., Berland, S., Cole, T., Degenhardt, F., Di Donato, N., Graul-Neumann, L., Hoyer, J., Lynch, S.A., et al. (2014). Females with de novo aberrations in PHF6: clinical overlap of Borjeson-Forssman-Lehmann with Coffin-Siris syndrome. American journal of medical genetics Part C, Seminars in medical genetics 166C, 290-301.

Contributions of Collaborators

The design, performance, analysis, and interpretation of all experimental work was carried out by Matthew A.M. Todd, unless otherwise specified. This thesis was written and prepared by Matthew A.M. Todd and edited by David J. Picketts, with the following exceptions: Chapter 2 was jointly written by Christian P. Kratz and Dr. David J. Picketts; Appendix B was written by David J. Picketts; Appendix C was jointly written by Matthew A.M. Todd and Michael S. Huh, with editing by David J. Picketts; and Appendix D was written by Matias Alvarez-Saavedra and David J. Picketts.

Some work presented in this thesis was generated with the help of collaborators. In Chapter 2, Mwe Mwe Chao (Children's National Medical Center, Washington DC) characterized the clinical features of the BFLS patient shown in Figure 2-1, Udo Kontny (University of Freiburg, Germany) provided lymphoblast patient DNA, and Lemuel Racacho operated the DNA sequencing instrument. In Chapter 3, Michael Rudnicki and Iain McKinnell provided the pBRIT-LoxP-NTAP and pBRIT-LoxP-CTAP vectors, while Jozef Gécz (University of Adelaide, Australia) provided the monoclonal PHF6 antibody. In Chapter 4, Michael S. Huh performed the Pyronin Y staining for Figure 4-S2A.

In Appendix A, Keqin Yan and Alan J. Mears executed the microarray analyses, while Matthew A.M. Todd annotated the data and prepared Table A-2. Also, the pGL4.11 and pGL4.11-SPARC plasmids used in Figure A-4 were provided by Dr. Guido Marcucci (The Ohio State University Comprehensive Cancer Center), while the pGL4.74 plasmid was provided by Dr. Valerie Wallace. The contributions for Appendices B and D are indicated on pages 187 and 209 respectively.

APPENDIX A

Additional Data

SUMMARY

Chapter 3: Detecting phosphorylation of PHF6 serine residues from mass spectra

Several putative PHF6 phosphorylation sites have been identified in the literature through high throughput mass spectrometry-based screens (Dephoure et al., 2008; Matsuoka et al., 2007; Mayya et al., 2009; Olsen et al., 2010). As such, additional parameters of the MASCOT analysis of the mass spectra from the IP-MS/MS experiment in Chapter 3 allowed for the identification of phosphorylated and ubiquitylated peptides. Table A-1 shows all PHF6 phosphopeptides detected within the dataset. Phosphorylated PHF6 peptides were found to either be singularly phosphorylated at S154 or S155, or dually phosphorylated at S145 and S155.

Table A-1. List of phosphorylated PHF6 peptides from IP-MS/MS experiment (see Table 3-1).

Peptide sequence*	Amino acid residue #s
TAHNSEADLEESFNEHELEP**S**SPK	S154
TAHNSEADLEESFNEHELEPS**S**PK	S155
TAHNSEADLEE**S**FNEHELEPS**S**PK	S145, S155

* Note: phosphorylated serine residues are indicated in bold and underlined. PLK1 consensus sequence is highlighted in gray (Nakajima et al., 2003).

Chapter 3: Tandem affinity purification (TAP)

The initial objective of Chapter 3 was to pull down PHF6 interaction partners using TAP (Figure A-1), rather than 3X Flag alone, which has been described (Puig et al., 2001). PHF6-CTAP was nearly completely captured on the M2-Flag beads, as evidenced by the absence of PHF6-CTAP in the first flowthrough lysate (lanes 1-3, Figure A-1A,B). Endogenous PHF6 was not captured, indicating that PHF6-CTAP does not interact with PHF6. The TEV cleavage was also very efficient at eluting recombinant PHF6 from the M2-Flag beads (see lanes 4-7). TEV cleavage also induced a mass shift, as predicted (PHF6-CTAP is 47 kDa, TEV-cleaved PHF6-CTAP is 45 kDa). For the second capture step, recombinant PHF6 was nearly completely captured by the Ni-NTA beads through its 6x His tag (lanes 8-9). Also, the final elution of recombinant PHF6 was very efficient (lanes 10-11). When the TAP purification was scaled up to a starting material of 50 mg nuclear lysate, TAP-purified recombinant PHF6 could easily be visualized by colloidal blue Coomassie (Figure A-1C), and mass spectrometry-based protein identification of the gel slice corresponding to recombinant PHF6 detecting similar sequence coverage to the results presented in Table 3-1. However, the mass spectrometry analysis did not detect significant quantities of peptides for any other proteins (not shown). Following these experiments, it was speculated that of NTA (nitrilotriacetic acid) might be stripping the zinc ions from the ZaP domains of PHF6, based on its high affinity for zinc in other proteins (Schullek and Wilson, 1988). If so, the resulting collapse of the ZaP domains may cause PHF6 to lose its interaction partners. Therefore, the 6x His-tag purification step of the TAP protocol was determined to be too stringent, and 3x Flag purification alone was employed for the IP-MS/MS experiments presented in Chapter 3.

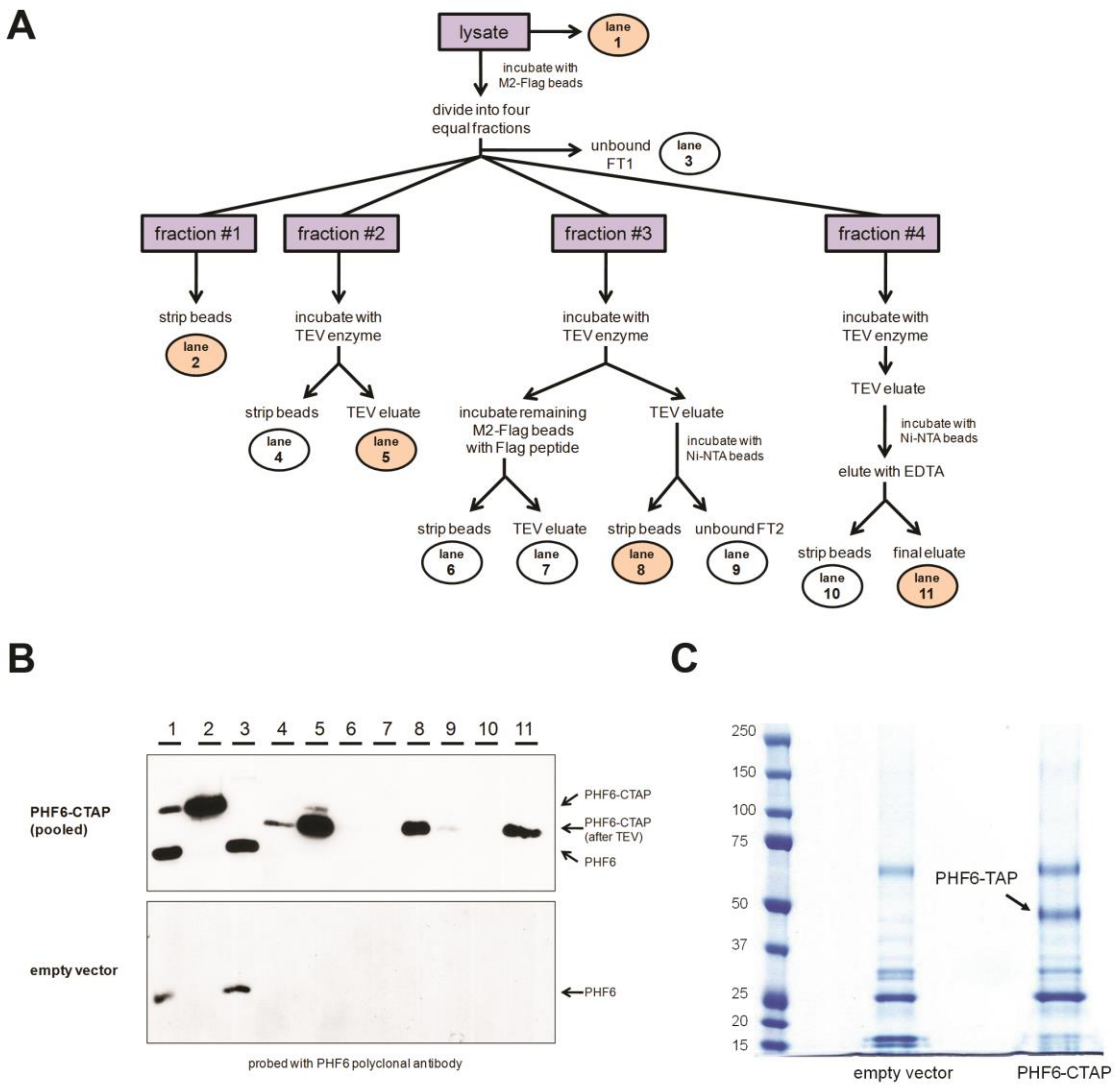

Figure A-1. Tandem affinity purification of PHF6-CTAP in HEK 293T cells.
(A) Schematic diagram for the analysis of PHF6-CTAP and empty vector control samples analyzed by immunoblotting with anti-PHF6 in (B). Pre-cleared nuclear lysates were incubated with M2-Flag agarose beads overnight, then the beads were separated into four equal fractions (#1-4) which were each halted at different steps within the TAP procedure to #1) assess the efficiency of protein capture with the M2-Flag beads (lanes 1-3), #2) assess the efficiency of TEV cleavage (lanes 4-5), #3) assess how much PHF6-CTAP remains bound to the beads after incubating with TEV (lanes 6-7) and to test the efficiency of protein capture with the Ni-NTA beads (lanes 8-9), and #4) to assess the efficiency of the elution (lanes 10-11). Highlighted circles correspond to lanes where PHF6-CTAP is expected to be found. The predicted masses are 42 kDa for PHF6, 47 kDa for PHF6-CTAP, and 45 kDa for PHF6-CTAP after TEV cleavage. FT1 and FT2 refer to the flowthrough, or unbound fraction, after each binding step. Lanes 1 and 3 contain 20 µg of lysate, and total sample was loaded for lanes 2 and 4-11. (C) Colloidal Blue Coomassie stain of purified TAP products from HEK 293T cells expressing empty vector or PHF6-CTAP (~50 mg of nuclear lysate for each sample prior to TAP purification).

Chapter 3 follow-up: Identifying PHF6 gene targets

Chapter 3 describes the interaction between PHF6 and NuRD in the nucleoplasm as well as the nucleolar associations of PHF6. While Chapter 4 goes on to further dissect the nucleolar activities of PHF6, Appendix A describes additional experiments that were performed with the objective of identifying PHF6 gene targets.

To identify potential gene targets, RNA from a HEK 293T cell line overexpressing PHF6 (PHF6-CTAP) and a cell line expressing empty vector was hybridized to a HEEBO microarray, identifying 285 genes with a 2-fold expression change when PHF6 is overexpressed. Gene ontology was performed on the gene list, identifying 22 candidates, summarized in Table A-2, having shared biological processes with PHF6 (e.g. brain development, hematopoiesis, obesity, limb bud development, or association with T-cell and/or myeloid leukemia). Several of these candidates are involved in the regulation of cell proliferation, signal transduction, and cell adhesion/migration processes, however it was unclear which genes could represent direct targets for PHF6 and which genes may simply be upregulated/downregulated in response to the cellular stress induced by overexpressing PHF6.

To increase the probability of identifying direct gene targets, the gene candidates listed in Table A-2 were subjected to validation by qRT-PCR analysis in PHF6 shRNA knockdown and overexpression cell lines (Figure A-2). It was reasoned that direct targets would be upregulated during PHF6 knockdown and downregulated by PHF6 overexpression, and vice versa. The genes with transcript expression levels matching this prediction included *LY6G6D*, *SPARC*, and *EPHB2*. In addition, while *UBF* was not

Table A-2. Gene expression changes resulting from the overexpression of PHF6.*

Accession	Symbol	Fold change	A	P	Cellular role	Brain Development	Hematopoiesis	Obesity	Limb bud development	Cell proliferation	Cell signaling	Cell adhesion/migration	Leukemia
NM_021246.2	*LY6G6D*	8.85	12.07	1.34E-04	Transmembrane protein						■		
NM_001010926	*HES5*	6.65	9.79	1.10E-05	Transcriptional regulation	■	■			■	■	■	■
NM_003467.2	*CXCR4*	6.35	12.62	3.06E-05	Chemokine receptor		■			■	■	■	■
NM_032458.2	*PHF6*	5.91	13.29	3.91E-05	Chromatin-binding	■	■	■	■				■
NM_002133.1	*HMOX1*	4.33	12.53	5.35E-05	Heme oxygenase			■		■	■		■
NM_019845.2	*RPRM*	3.38	11.85	4.88E-04	Cell cycle regulator					■			
NC_000007	*HOXA11-as*	3.00	12.33	3.04E-04	lncRNA								
NM_153715.1	*HOXA10*	2.83	12.49	6.16E-04	Homeobox protein		■		■				■
NM_000937	*POLR2A*	2.57	11.66	8.83E-04	RNA polymerase	■	■	■	■	■			■
NM_002449.3	*MSX2*	2.48	13.44	1.40E-03	Homeobox protein				■	■	■		■
NM_182767.3	*SLC6A15*	2.25	11.25	1.83E-03	Amino acid transporter	■		■					
NM_002467.2	*MYC*	2.09	13.74	2.73E-03	Transcriptional regulation		■			■			■
NM_000522.2	*HOXA13*	2.09	11.96	3.10E-03	Homeobox protein				■		■		■
NM_024014.2	*HOXA6*	2.04	12.68	3.54E-03	Homeobox protein								■
NM_181353.1	*ID1*	1.93	12.84	4.96E-03	DNA-binding protein	■	■				■	■	■
NM_199171.1	*TMEPAI*	-1.98	9.79	4.07E-03	Transmembrane protein		■	■		■	■		■
NM_004442.5	*EPHB2*	-2.86	10.60	3.93E-04	Receptor tyrosine kinase							■	
NM_006908	*RAC1*	-3.11	10.52	3.60E-04	GTP-ase	■					■		
NM_006435	*IFITM2*	-5.25	13.23	4.17E-05	Transmembrane protein						■		
NM_003118.2	*SPARC*	-6.66	12.79	1.15E-05	Extracellular matrix	■	■	■		■	■	■	■
NM_014391.2	*ANKRD1*	-7.09	11.51	1.86E-05	Transcription factor								
NM_031442.2	*TMEM47*	-9.25	9.69	9.43E-06	Transmembrane protein	■							
NM_002468.2	*MYD88*	-9.49	9.81	6.33E-06	TLR Signaling						■	■	

*Note: negative fold changes denote downregulation.

detected in the microarray dataset, its levels appear to negatively correlate with those of PHF6, consistent with observations from the literature (Wang et al., 2013).

To further validate the biological relevance of these candidate gene targets to PHF6, gene expression was quantified in lymphoblast cell lines derived from BFLS patients and wild type controls (Figure A-3). BFLS patient #1 has an R257G missense mutation and BFLS patients #2 and #3 are siblings that express PHF6Δexon3(Vallee et al., 2004). Western blotting with anti-PHF6 demonstrates reduced or absent protein levels of PHF6 in all three BFLS patients, but not the controls (Figure A-3A), while PHF6 mRNA transcripts are only reduced in BFLS patients #2 and #3 (Figure A-3B). From these data, *SPARC* was the only target gene candidate with expression levels in the BFLS cell lines that were most consistent with the observations from Figure A-2, however it should be noted that BFLS patient #3 did not have significantly upregulated *SPARC* levels in comparison to the controls. While *TMEPAI* levels were also elevated in all three BFLS patients, *SPARC* was selected as a candidate for further analyses due to its many shared biological processes with PHF6 (see Table A-2).

SPARC, also known as BM-40 or osteonectin, is a secreted collagen-binding glycoprotein that influences the binding of the cell surface to the extracellular matrix. When SPARC levels increase, the extracellular matrix becomes more fibrotic and cell adhesion is reduced (Bradshaw, 2009). In humans, enhanced expression of *SPARC* correlates with the onset of obesity and more aggressive tumour growth in AML (Alachkar et al., 2014; Kos and Wilding, 2010). Collectively, the microarray and qRT-PCR data is consistent with a model whereby PHF6 represses *SPARC*, however it remains to be determined how PHF6 specifically influences *SPARC* expression.

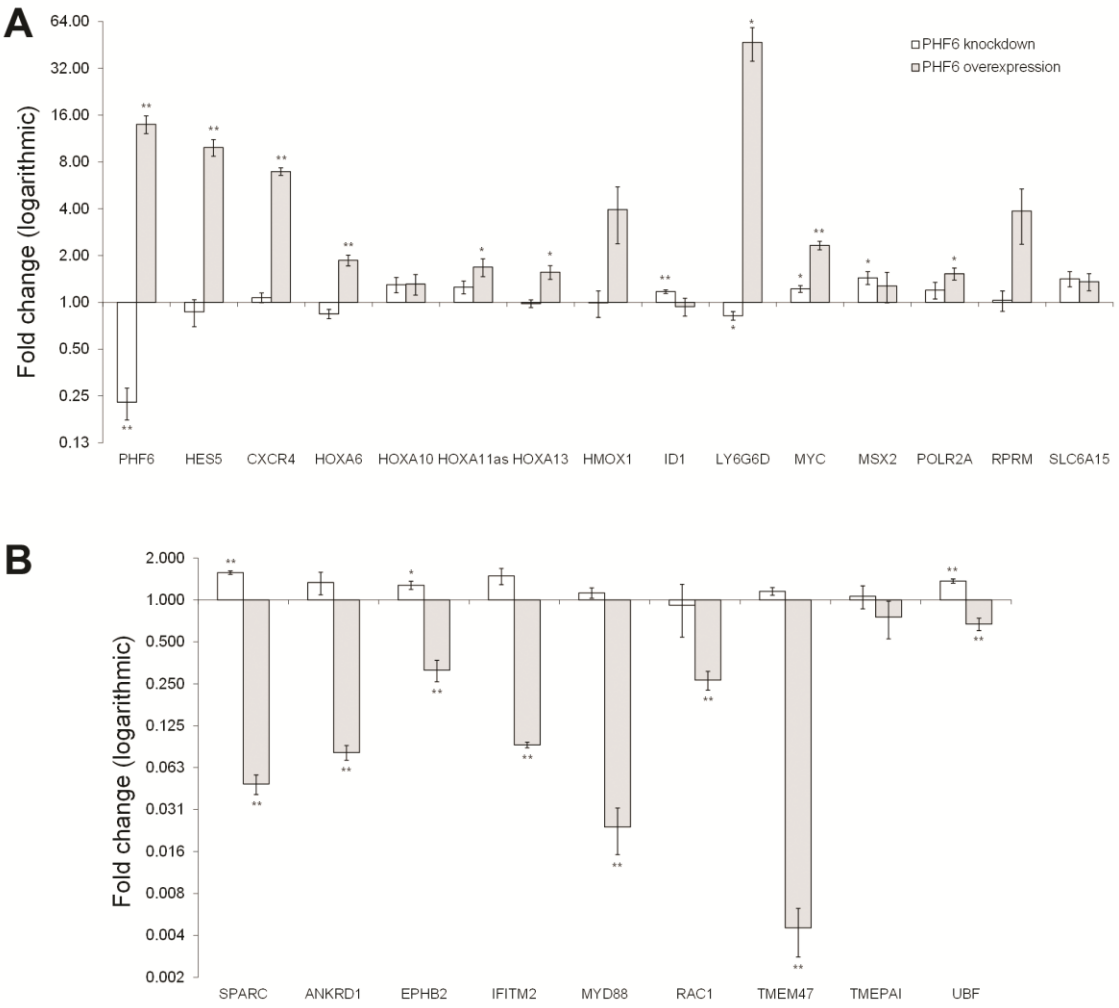

Figure A-2. Validation of PHF6 target genes by qRT-PCR in HEK 293T cells.
(A,B) RNA was harvested from HEK 293T cells expressing PHF6 shRNA or cells overexpressing PHF6, then subjected to qRT-PCR analysis to validate gene expression changes observed from the microarray results shown in Table A-2. Fold changes are represented relative to empty vector controls. GAPDH was used as a reference gene. Bars represent standard error (n=3, *p<0.05, **p<0.01, two-tailed student's t-test). The y axis is logarithmic (base 2).

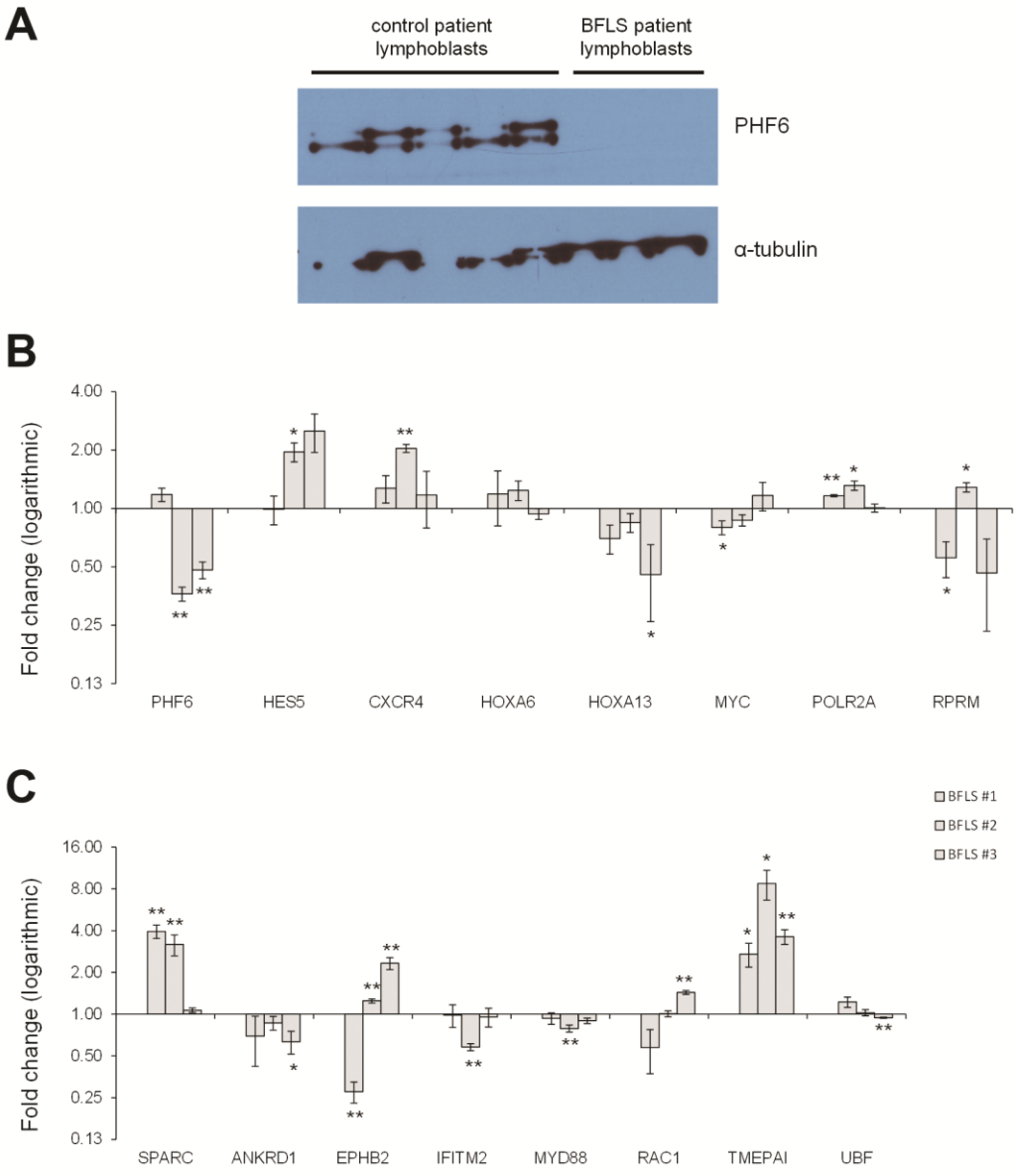

Figure A-3. Validation of PHF6 target genes by qRT-PCR in BFLS patient lymphoblasts.
(A) Western blotting with antibodies directed against PHF6 and α-tubulin (loading control) in RIPA lysates from control and BFLS patient lymphoblasts. BFLS patient #1 has a R257G mutation while patients #2 and #3 are siblings that express PHF6Δexon3. BFLS patients #1, #2, and #3 are loaded in sequential order from left-to-right where indicated. (B,C) RNA was isolated from BFLS patient lymphoblasts and subjected to qRT-PCR to validate gene expression changes observed in HEK 293T-derived cell lines. Bars represent standard error (n=3, *p<0.05, **p<0.01, two-tailed student's t-test). The y axis is logarithmic (base 2).

The *SPARC* promoter (-651/1) region already possesses known binding sites for transcriptional activation by SP1, NFκβ, and BRG1 (Alachkar et al., 2014; Xu et al., 2010b). Moreover RUNX1, which is mutated with PHF6 in both T-ALL and AML (Cancer Genome Atlas Research, 2013; Grossmann et al., 2013) and has also recently been linked with developmental intellectual disability (Katzaki et al., 2010), potently represses *SPARC* through binding to this promoter (Alachkar et al., 2014).

To determine if PHF6 directly (e.g. PHF6-NuRD binding) or indirectly (e.g. affecting the recruitment of SP1, NFκβ, BRG1, or RUNX1) modulates *SPARC*, a luciferase assay was performed by transfecting the pGL4.11 Firefly luciferase plasmid containing the (-651/1) *SPARC* promoter region, or empty vector, into HEK 293T cell lines expressing PHF6 shRNA knockdown or PHF6 overexpression. If PHF6 was indeed repressing *SPARC*, it was expected that the knockdown condition would elicit higher luciferase activity and that PHF6 overexpression would result in a reduction of luciferase activity. As shown in Figure A-4, PHF6 knockdown had no impact on luciferase expression in comparison to the control, while PHF6 overexpression was actually higher for the cell line expressing PHF6-CTAP in comparison to the control.

Thus it was concluded that the means by which PHF6 represses *SPARC* does not occur through binding to the proximal promoter nor by specifically altering the binding of other *SPARC* transcription factors to this region. Future work should focus on identifying PHF6 binding sites by ChIP-sequencing. It is perhaps possible that PHF6 may instead bind *SPARC* coding sequences, which would be consistent with its binding along the rDNA gene, shown in Chapter 4, and with its association with PAF1 in the transcriptional regulation of NGC/CSPG5 (Zhang et al., 2013).

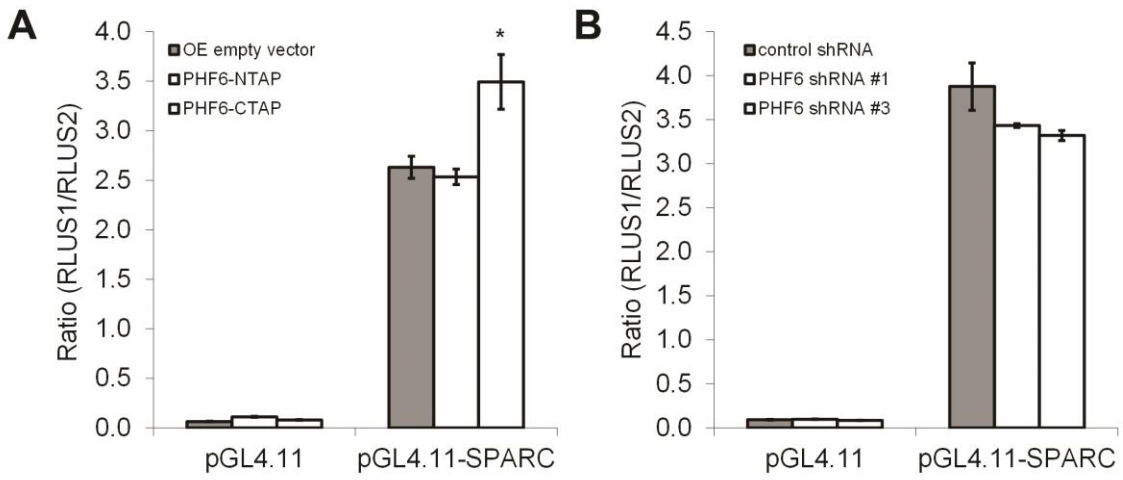

Figure A-4. PHF6 does not induce luciferase repression through the -651/1 SPARC promoter gene element.
Mean ratios (n=3) of Firefly luciferase (RLUS1) to *Renilla* luciferase (RLUS2) levels that were quantified in either (A) PHF6 overexpression (OE) cell lines or (B) PHF6 shRNA knockdown cell lines. Cell lines were transfected with either the empty luciferase vector (pGL4.11) or a plasmid expressing the -651/1 region of the SPARC promoter (pGL4.11-SPARC). Bars represent standard error (*$p<0.05$, **$p<0.01$, two-tailed student's t-test).

MATERIALS AND METHODS

Cell culture, RNA extractions, and Western blot

See Chapters 3 and 4 for a description of the generation of PHF6 overexpression and knockdown HEK 293T-derived cell lines, as well as the necessary cell culture conditions. BFLS patient lymphoblast cell lines #1 (R257G), #2 (PHF6Δexon3), and #3 (PHF6Δexon3), and control lymphoblast cell lines have been previously described (Vallee et al., 2004), and were cultured in RPMI-1640 (Sigma), supplemented with 20% FBS and 1% penicillin-streptomycin. In preparation for the RNA extractions, HEK 293T-derived cell lines were seeded at a confluency of 2 x 10^5 cells per 10 cm tissue culture dish and incubated at 37º C for 48 hours, while 5 x 10^5 lymphoblasts were seeded per 75 mm^2 tissue culture flask and incubated at 37º C for 48 hours. RNA extractions were performed using the RNeasy Mini Kit (Qiagen). Additionally, for lymphoblast cell lines, protein extractions and Western blotting were performed as described in Chapter 4.

Tandem affinity purification (TAP)

HEK 293T nuclear lysates from cells expressing empty vector or PHF6-CTAP were prepared for TAP, a two-step purification method that allows for the high yield purification of protein complexes under native buffer conditions (Puig et al., 2001). The TAP tag expressed in these cell lines consists of a C-terminal 6X His tag, a tobacco etch virus (TEV) sequence, and a 3X Flag tag (see Chapter 3). TAP purification was performed similarly to the 3X Flag purification described in Chapter 3, with the following changes: elution from the M2-Flag beads was performed using two 3 hr elutions at 4º C in the presence of 10U (per mg lysate) of AcTEV protease (Invitrogen) in binding buffer, to cleave the TEV site. Both eluted fractions were combined, then

incubated with 60 µL Ni-NTA bead slurry (50%) for 3 hours at 4º C with rotation in binding buffer containing 20 mM imidazole (Sigma). Ni-NTA beads were then given 5 x 5 min washes in binding buffer containing 20 mM imidazole, then captured protein complexes were eluted with 200 mM EDTA in binding buffer. Eluted products were concentrated by centrifugal filtration (MWCO 10 kDa Microcon, Millipore). Fractions were collected for each step of the purification and analyzed by Western blot, as indicated in Figure A-1A,B. Bead stripping was performed in a 1:1 mixture of 2X Novex buffer (Invitrogen) and binding buffer (with 100 µM DTT added). Final TAP products were also visualized by colloidal blue Coomassie (Invitrogen) (Figure A-1C).

Gene expression (microarrays)

RNA from HEK 293T cell lines stably expressing empty vector (pBRIT-LoxP-NTAP) or overexpressing for PHF6 (PHF6-CTAP) were respectively labelled with Cy3 or Cy5 using a 3DNA Array 900 kit (Genisphere), then co-hybridized to a HEEBO gene expression array (Microarrays Inc., HS1100). Two replicates were performed, with the dyes flipped between control and PHF6-CTAP RNA for the second replicate to counter dye bias. Probe-specific signals were quantified with ScanArray express (Perkin Elmer), and the WEBARRAY online tool (http://www.webarraydb.org/webarray/index.html) was used for data processing and statistics. The following thresholds were applied to the finalized dataset to score a given probe (gene) as being differentially expressed during PHF6 overexpression: $A>9$, $M>0.32$ or $M<-0.32$, and $p<0.01$. Note: $M = \log_2$ ratio of PHF6-CTAP/control signal and $A = \log_2$ average signal strength. Biological processes were attributed to candidate genes by screening the final gene list against publically

available gene ontology datasets with AmiGO 2 software (http://geneontology.org/), and by performing PubMed searches for individual genes.

Quantitative real-time PCR

Reverse transcription and qRT-PCR were performed as described in Chapter 4. All primers (with corresponding annealing temperatures) are listed in Table A-3. Fold changes were calculated with the ΔΔCt method using GAPDH as an internal control. For gene expression analyses from HEK 293T-derived cell lines, three PHF6 shRNA knockdown cell lines (KD #1, KD #2, KD #3; see Chapter 4 supplementary information) were analyzed (three technical replicates each) for a biological n = 3, while three technical replicates of the PHF6-CTAP overexpression cell line are presented as a technical n = 3 in Figure A-2. For gene expression analyses from BFLS patient cell lines, three technical replicates were performed for each BFLS patient (#1, #2, #3) for a technical n = 3. In each technical replicate, fold changes for genes expressed by individual BFLS patient were calculated using an average ΔCt from four control patients that each expressed wild type PHF6. Statistical analyses were performed in Microsoft Excel. Two-tailed t tests, 95% confidence intervals, and 99% confidence intervals were used to determine significance.

SPARC promoter luciferase assay

HEK 293T-derived PHF6 overexpression and knockdown cell lines were seeded at ~80-90% confluency in 6-well tissue culture plates and each well was transfected with 2 µg of a pGL4.11 Firefly luciferase plasmid, expressing either the -651/1 region of the SPARC promoter (pGL4.11-SPARC) or empty vector (pGL4.11), in a 1.2 mL volume for 6 hours at 37º C with Lipofectamine 2000 (Life Technologies) according to the

manufacturer's protocol (Alachkar et al., 2014). As a control, all cells were co-transfected with 10 ng of the pGL4.74 Renilla luciferase plasmid. At 72 hours post-transfection, cells were washed with PBS and luciferase reactions were prepared using the Dual-Luciferase Assay Kit (Promega) according to the manufacturer's protocol, and luciferase signals were quantified on a Lumat LB 9507 luminometer (Eg&G Berthhold) to measure Firefly luciferase activity (RLUS1) and Renilla luciferase activity (RLUS2). Two-tailed t tests and 95% confidence intervals were used to determine significance.

Table A-3. List of primer pairs used for qRT-PCR in HEK293T-derived cell lines and patient lymphoblasts.*

Primer name	Sequence	Annealing temp. (ºC)
SPARC-Fwd	5'- GTGCGAGCTGGATGAGAACA	57
SPARC-Rev	5'- TTGCAAGGCCCGATGTAGTC	
ANKRD1-Fwd	5'- AGACCTCAACGCCAAAGACA	60
ANKRD1-Rev	5'- CCAGATCCATCGGCGTCTTC	
CXCR4-Fwd	5'- AAACCCTCAGCGTCTCAGT	60
CXCR4-Rev	5'- AGTGGGCTAAGGGCACAAGA	
EPHB2-Fwd	5'- GTTCGCCTCTGTGAACATCA	57
EPHB2-Rev	5'- GACCACGACAGGGTAATGCT	
HES5-Fwd	5'- TCGCCTCGTCGCCTGTTC	64
HES5-Rev	5'- CCACGAGTAGCCTTCGCTGTAG	
HOXA6-Fwd	5'- AGGCTGGCTATGACGCGCT	60
HOXA6-Rev	5'- CATGGCTCCCATACACAGCAC	
HOXA10-Fwd	5'- GCCCCTTCCGAGAGCAGCAAAG	57
HOXA10-Rev	5'- AGGTGGACGCTGCGGCTAATCTCTA	
HOXA11as-Fwd	5'- GCTTTAGAGGCGCTGACATC	57
HOXA11as-Rev	5'- GAAATGGAACTCGGACTTGG	
HOXA13-Fwd	5'- GAACGGCCAAATGTACTGCC	57
HOXA13-Rev	5'- CGCCTCCGTTTGTCCTTAGT	
HMOX1-Fwd	5'- TAGAAGAGGCCAAGACTGCG	64
HMOX1-Rev	5'- GCCACCAGAAAGCTGAGTGT	
ID1-Fwd	5'- CTCCAGCACGTCATCGACTA	60
ID1-Rev	5'- CGCTTCAGCGACACAAGAT	
IFITM2-Fwd	5'- GATCACCGCTGGTCACCATGA	57
IFITM2-Rev	5'- TCACGTCGCCAACCATCTTC	
LY6G6D-Fwd	5'- AACCGAATGCGGTGCTACA	64
LY6G6D-Rev	5'- GGGCTGGATAAGTCACGTCT	
MSX2-Fwd	5'- CAGGAACCCGGCCGATATT	57
MSX2-Rev	5'- TGGTCTTGTGTTTCCTCAGGG	
MYC-Fwd	5'- GAGGCTATTCTGCCCATTTG	57
MYC-Rev	5'- CACCGAGTCGTAGTCGAGGT	
MYD88-Fwd	5'- CCTGCAGAGCAAGGAATGTG	64
MYD88-Rev	5'- CAAGGCGAGTCCAGAACCAA	
POLR2A-Fwd	5'- CCCCAACCTCTCCATTGACC	57
POLR2A-Rev	5'- CCCTGCGCACTAGTTCTTGA	
RAC1-Fwd	5'- TACGCCCCCTATCCTATCCG	64
RAC1-Rev	5'- CAATCGGCTTGTCTTTGCCC	
RPRM-Fwd	5'- GCCTGCCTGAGGAGTTACAG	60
RPRM-Rev	5'- AAACGGTGTCACGGATGTCA	
SLC6A15-Fwd	5'- GACGTGGAAGCAGCAAGAGG	57
SLC6A15-Rev	5'- TCCGTATGTCCAGTATTCTGTAGG	

TMEM47-Fwd	5'- ACCTGTTGCGGTCATGCTTT	64
TMEM47-Rev	5'- TGATTGGGTAAAGGACCAGGC	
TMEPAI-Fwd	5'- TGCAAACGCTCTTTGTTCCAG	64
TMEPAI-Rev	5'- ATGAAGGACCGTGCAGACAG	
UBF-Fwd	5'- TGAGCAACCTGGACCTAACC	57
UBF-Rev	5'- TTTCGCTCGAACTCCTGTTT	

* For PHF6 and GAPDH primer sets, see Chapter 4.

ACKNOWLEDGEMENTS

DNA sequencing was carried out by Lemuel Racacho from the lab of (Dr. Dennis Bulman's laboratory, Children's Hospital of Eastern Ontario). The interpretation of peptides containing phosphorylated serine residues was performed by Dr. Hu Zhou in the laboratory of Dr. Daniel Figeys (Ottawa Institute of Systems Biology). Microarrays were prepared by Keqin Yan (Dr. David Picketts' laboratory) and data analysis was performed by Dr. Alan J. Mears (Dr. Valerie Wallace's laboratory, Ottawa Hospital Research Institute). The pGL4.11 and pGL4.11-SPARC plasmids were generously provided by Dr. Guido Marcucci (The Ohio State University Comprehensive Cancer Center), and the pGL4.74 plasmid was provided by the laboratory of Dr. Valerie Wallace.

APPENDIX B

Characterization of novel isoforms and evaluation of SNF2L/SMARCA1 as a candidate gene for X-linked mental retardation in 12 families linked to Xq25-26

Purpose

To screen XLMR patients for *SNF2L/SMARCA1* mutations and to characterize the alternative splicing within exon 24 of *SNF2L/SMARCA1*.

Submission Information

Submitted: 1 November 2007
Accepted: 26 February 2008
Published: 26 February 2008

Contribution of Co-Authors

Matthew A.M. Todd conducted semi-quantitative RT-PCR experiments, as shown in Figure 2B of the article.

Maribeth A. Lazzaro identified the various SNF2L isoforms, generated the preliminary RT-PCR data, and performed the immunofluorescence experiments. Paul Lavigne and Dominic Vallée performed the sequence analysis of the XLMR patients. Adriana De Maria prepared the initial figures and wrote the first draft of the manuscript. David J. Picketts designed the study, participated in its execution and coordination, and wrote the final manuscript.

BMC Medical Genetics

BioMed Central

Research article

Open Access

Characterization of novel isoforms and evaluation of *SNF2L/SMARCA1* as a candidate gene for X-linked mental retardation in 12 families linked to Xq25-26

Maribeth A Lazzaro[1,2], Matthew AM Todd[1], Paul Lavigne[1], Dominic Vallee[1], Adriana De Maria[1,2] and David J Picketts*[1,3]

Address: [1]Ottawa Health Research Institute, 501 Smyth Road, Ottawa, ON K1H 8L6, Canada, [2]Health Canada, Therapeutic Products Directorate, Bureau of Cardiology, Allergy and Neurological Sciences, Tunney's Pasture, Ottawa, Ontario K1A 1B9, Canada and [3]University of Ottawa Centre for Neuromuscular Disease and Departments of Medicine, Biochemistry, Microbiology and Immunology, Ottawa, ON, K1H 8M5, Canada

Email: Maribeth A Lazzaro - maribeth_lazzaro@hc-sc.gc.ca; Matthew AM Todd - mtodd@ohri.ca; Paul Lavigne - lavigne_paul@hotmail.com; Dominic Vallee - dvallee@ohri.ca; Adriana De Maria - adriana_de_maria@hc-sc.gc.ca; David J Picketts* - dpicketts@ohri.ca

* Corresponding author

Published: 26 February 2008

BMC Medical Genetics 2008, **9**:11 doi:10.1186/1471-2350-9-11

Received: 1 November 2007
Accepted: 26 February 2008

This article is available from: http://www.biomedcentral.com/1471-2350/9/11

Abstract

Background: Mutations in genes whose products modify chromatin structure have been recognized as a cause of X-linked mental retardation (XLMR). These genes encode proteins that regulate DNA methylation (*MeCP2*), modify histones (*RSK2* and *JARID1C*), and remodel nucleosomes through ATP hydrolysis (*ATRX*). Thus, genes encoding other chromatin modifying proteins should also be considered as disease candidate genes. In this work, we have characterized the *SNF2L* gene, encoding an ATP-dependent chromatin remodeling protein of the ISWI family, and sequenced the gene in patients from 12 XLMR families linked to Xq25-26.

Methods: We used an *in silico* and RT-PCR approach to fully characterize specific SNF2L isoforms. Mutation screening was performed in 12 patients from individual families with syndromic or non-syndromic XLMR. We sequenced each of the 25 exons encompassing the entire coding region, complete 5' and 3' untranslated regions, and consensus splice-sites.

Results: The *SNF2L* gene spans 77 kb and is encoded by 25 exons that undergo alternate splicing to generate several distinct transcripts. Specific isoforms are generated through the alternate use of exons 1 and 13, and by the use of alternate donor splice sites within exon 24. Alternate splicing within exon 24 removes a NLS sequence and alters the subcellular distribution of the SNF2L protein. We identified 3 single nucleotide polymorphisms but no mutations in our 12 patients.

Conclusion: Our results demonstrate that there are numerous splice variants of SNF2L that are expressed in multiple cell types and which alter subcellular localization and function. *SNF2L* mutations are not a cause of XLMR in our cohort of patients, although we cannot exclude the possibility that regulatory mutations might exist. Nonetheless, *SNF2L* remains a candidate for XLMR localized to Xq25-26, including the Shashi XLMR syndrome.

Background

The isolation of genes underlying X-linked mental retardation (XLMR) disorders has been hampered, in part, by the broad phenotypic variability observed in patients that restricts linkage analysis to large single families or instances where a specific trait facilitates phenotypic splitting. More recently, the use of large scale genomic methods including comparative genome hybridization (CGH) arrays and patient sequencing projects has increased the identification rate of XLMR disease genes. Surprisingly, each gene identified accounts for a small proportion of cases and there remain many conditions for which a gene has not been identified. Nonetheless, several trends have emerged. These include the identification of XLMR genes encoding proteins that modulate chromatin structure [1]. The cloning of the *ATRX* gene as the cause of the α-thalassemia mental retardation (ATR-X) syndrome established the paradigm for chromatin remodeling proteins in neurodevelopmental disorders [2]. This gene, encoding a SWI/SNF-like protein, is also mutated in other severe XLMR syndromes lacking α-thalassemia and in patients with mild-to-moderate XLMR [3]. Subsequently, the *RSK2* gene encoding a histone kinase was identified as the causative gene for Coffin-Lowry syndrome and non-specific XLMR [4,5], and the methyl-CpG-binding protein 2 (*MeCP2*) gene was identified as the causative gene for Rett syndrome [6] and other non-specific male MR [7-9]. More recently, the *PHF6* (Borjeson-Forssman-Lehmann syndrome;[10]), *ZNF41* [11], *ZNF81* [12], and *JARID1C* [13] genes have also been implicated in XLMR and have roles in transcriptional regulation and/or chromatin remodeling. Taken together, these studies suggest that additional chromatin interacting proteins whose genes reside on the X chromosome should be considered as disease candidates for both syndromal and non-specific XLMR disorders.

The Drosophila ISWI gene was identified as a distinct SWI/SNF subclass named the Imitation SWI (ISWI) family [14]. Two human orthologs of *Drosophila* ISWI (dISWI) have been described, *SNF2H* (SMARCA5) which maps to 4q31.1 and *SNF2L* (SMARCA1) which maps to Xq25-26 [15,16]. Moreover, analysis of the murine *Snf2h* and *Snf2l* genes demonstrated that *Snf2h* was expressed in proliferating neuroblast layers whereas *Snf2l* expression was enhanced in differentiating neuronal populations [17]. Indeed, purification of the SNF2L-containing human NURF complex demonstrated that it regulated expression of the *engrailed* genes, which are important in mid/hindbrain development [18]. In addition, the latter study also demonstrated that SNF2L could promote neuronal differentiation when expressed ectopically in neuroblasts [18]. SNF2L was also found to be a component of a second chromatin remodeling complex, called CERF that contains the CECR2 protein, a transcription factor involved in neurulation and a cause of exencephaly in mice when mutated [19]. These studies suggest that *SNF2L* is an excellent candidate gene for the cause of XLMR. In this study, we have characterized multiple splice forms and examined 12 families with XLMR for mutations in *SNF2L*.

Methods

Reverse Transcription-PCR

For cell lines, total RNA was prepared from cell lines by acid phenol extraction of cell lysates [20]. Poly A+ RNA for reverse transcription was purified from total RNA using the PolyATtract mRNA Isolation System (Promega, Nepean, Ontario). Total RNA from human tissues and specific brain regions were obtained commercially (Applied Biosystems Canada, Streetsville, Ontario). Total RNA (2 ug) or Poly A+ RNA (100 ng) was reverse transcribed using Superscript RT (Invitrogen) and a combination of oligo dT and random hexamers. PCR reactions for analysis of *SNF2L* splice variants were at 94°C for 30 seconds, 53°C for 30 seconds and 72°C for 2 minutes for 35 cycles, followed by a final extension of 15 minutes at 72°C. For the 5' splice variants, the following primers were used: 5'UTR SNF2L1 Fwd, 5' CAAACTTGCTGCTAAAGCGCC 3'; 5'UTR SNF2L2 Fwd, 5' GGAATTCATGGAGCAGGACACTGC 3'; SNF2L5'splice variants Rev, 5'CACCAAGACAATTTTTAGTG 3'. For the NLS splice variants: SNF2L NLS Fwd, 5' GGAGGTCATGGAGTATTC 3' and SNF2L NLS Rev, 5'CAGTAGCTGACTCTGCTTTTCTTTTCTGTG 3'.

Patient Material

DNA samples from 12 individuals affected with XLMR and previously mapped to a region encompassing the *SNF2L* gene were used for direct sequencing analysis. Samples from families F85-19 [21], F93-04, and F91-02 were provided by Drs. Ben Hamel and Hans van Bokhoven (University Hospital Nijmegen, Nijmegen, Netherlands). Samples K8045 [22], K8135 [23], K8320, K8395, K8725, K8895 [24], and K8923 were generously provided by Dr. Charles Schwartz (JC Self Research Institute, Greenwood Genetic Center, Greenwood South Carolina). The non-syndromic XLMR sample 24981 was provided by Dr. Judith Allanson (Children's Hospital of Eastern Ontario, Ottawa Ontario). The Pettigrew syndrome DNA sample was prepared from a commercially available EBV transformed lymphoblast cell line (GM12523; Coriell Cell Repository, Camden, NJ).

Plasmid constructs

The SNF2L NLS splice variants were cloned into the pcDNA3 expression plasmid (Invitrogen Canada Inc. Burlington, ON), each with an amino terminal tag encoding the FLAG epitope. Annealed primers encoding the FLAG epitope were inserted in the *Kpn*I and *Eco*RI sites of the pcDNA3 plasmid. The 5' region encoding the amino ter-

minus of the SNF2L2 splice variant (SNF2LB) was engineered with an *Eco*RI restriction site for cloning in frame with the FLAG epitope. The primers used were: FLAG-sense EcoRI, 5'-CCCACCATGGATTACAAGGATGACGACGATAAGG-3' and FLAG-antisense EcoRI, 5'-AATTCCTTATCGTCGTCATCCTTGTAATCCATGGTGGGGTAC-3'. The remainder of each cDNA (+ NLS or -NLS) was inserted in two additional cloning steps to construct plasmids encoding full length SNF2L proteins with and without a nuclear localization signal.

Cell transfections and immunofluorescence

293HEK cells were cultured in EMEM (Eagle's Minimal Essential Medium, Wisent, St Bruno, Quebec) supplemented with 10% fetal bovine serum (FBS) in a humidified 95% air with 5% CO_2 incubator at 37°C. One day prior to transfection, cells were plated on glass coverslips coated with poly D-lysine (100 μg/ml, Sigma, Oakville, Ontario) in 6 well tissue culture plates at a density of approximately 3×10^5 cells/well. Cells were transfected with 5 μg DNA [pcDNA3 control, pcDNA3 FLAG-SNF2LΔNLS, or pcDNA3 FLAG SNF2L] and the Lipofectamine 2000 reagent (Life Technologies, Burlington, Ontario) according to the manufacturer's protocol. After 48 hours, cells were fixed in cold ethanol/methanol (3:1) prior to blocking with 10% FBS diluted in PBS. Coverslips were incubated with diluted primary antibody (murine anti-FLAG monoclonal clone M2, 2 μg/ml, Sigma, Oakville, Ontario) for 1 hour at room temperature, washed and then incubated for 1 hour at room temperature with FITC-conjugated donkey-anti-murine IgG secondary antibody (Sigma) diluted 1:100 in PBS. Cell nuclei were counterstained with 1 μg/ml DAPI (Sigma) and images were captured using a Zeiss Axioplan 2 microcope outfitted with an AxioCam camera and AxioVision software.

SNF2L Mutation Analysis

Genomic DNA from individuals affected with XLMR in each of the 12 families analyzed was used to amplify each exon of the *SNF2L* gene with forward and reverse primers that annealed to flanking intron sequences, approximately 100 bp from each exon/intron boundary (primer sequences available upon request). Genomic DNA from an individual unaffected by XLMR was the control for all PCR reactions. For each reaction, 100–200 ng DNA was combined with 1 μM each of forward and reverse PCR primers, 200 μM dNTPs, 2.5 mM $MgCl_2$, 20 mM Tris-HCl pH 8.4, 50 mM KCl, and 1 unit Taq DNA polymerase in a volume of 100 μl. PCR reactions were incubated at 95°C for 40 seconds, 57°C for 40 seconds and 72°C for 3 minutes for 30 cycles, followed by a final extension of 15 minutes at 72°C. DNA obtained from PCR reactions was purified using the Qiaquick PCR Purification kit (Qiagen, Mississauga, Onatario) and sequenced using Perkin Elmer dye terminator and ABI automated sequencing. Sequences were aligned and compared to sequences obtained from the control DNA and sequence available in public databases to identify mutations.

Results and Discussion

Spatial and temporal expression studies of the *Snf2l* gene in mice and the purification of two human SNF2L-containing complexes have both suggested that the SNF2L protein may have an important role in neurodevelopment and that the *SNF2L* gene is a strong XLMR candidate gene [17-19]. *In silico* analysis demonstrated that the *SNF2L* gene (NM_003069) is highly conserved between mouse and human with a common intron/exon pattern containing 25 exons spanning ~77 kb along the X chromosome within Xq25 (Figure 1A and data not shown). However, the human cDNA and predicted protein sequences showed several significant discrepancies to the mouse *Snf2l* sequence (NM_053123) that required characterization, prior to mutation studies [16,17]. Indeed, we previously reported the presence of a human *SNF2L* variant (SNF2L+13) containing a non-conserved in-frame exon within the SNF2 catalytic domain that abolishes chromatin remodeling activity [25]. In addition, Okabe et al. reported two human cDNA clones with disparate 5' ends [16]. We will refer to these two clones as *SNF2LA* and *SNF2LB*, respectively. *SNF2LB* aligns with the start of the murine cDNA sequence and corresponds to a transcript that would initiate within exon 1 of the human genomic sequence (Figure 1B). The shorter *SNF2LA* isoform results from transcription that initiates within exon 2. The corresponding proteins differ in size at the NH_2-terminus by 78 amino acids with *SNF2LB* corresponding to the published murine sequence (Figure 1B). The *SNF2L*A isoform was not present in mice suggesting that it may be unique to humans. Using RT-PCR, we detected the corresponding transcripts for both 5' variants in human fetal brain and multiple human neuronal cell lines (Figure 1C).

In addition to the variation at the amino-terminus, the human and mouse amino acid sequences also differed at their carboxyl-terminus following Blast tool analysis. The last seven amino acids of the human sequence were not present in the mouse SNF2L protein sequence, but instead were replaced by 23 unique residues (Figure 2A). RT-PCR analysis demonstrated that both 3'-end variants could be detected in a variety of human cell lines, tissues and specific brain regions with the NLS-containing isoform representing the predominant species (Figure 2B). Sequencing demonstrated that the two transcripts are generated by alternative splicing of exons 24 and 25. Inclusion of exons 24 and 25 result in a shorter peptide due to a stop codon located at the start of exon 25. We called this variant SNF2LΔNLS. Alternative use of splice sites within exons 24 and 25 removes 100 bp and generates a transcript that

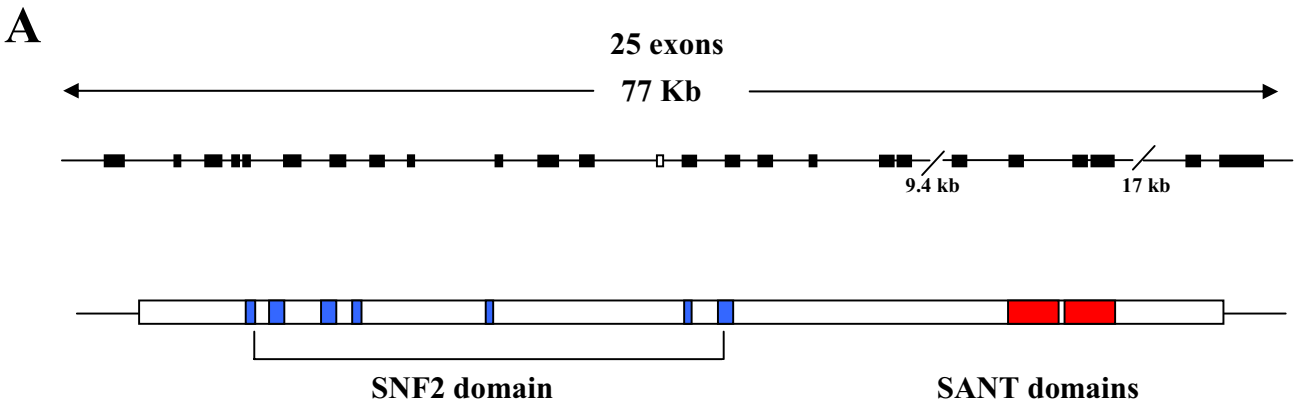

B

```
hSNF2LB      1 MEQDTAAVAATVAAADATATIVVIEDEQPGPSTSQEEGAAAAATEATAAT   50
mSNF2L       1 MEPDTATEAATVAVSDARATVVVVEDEQPGPSTFKEEGAAAAATEGTTAT   50

hSNF2LA      1                                MDPEYEEKMK-----ADRAKRF   17
hSNF2LB     51 EKGEKKKEKNVSSFQLKLAAKAPKSEKEMDPEYEEKMK-----ADRAKRF   95
mSNF2L      51 EKAEKKEKITFSISTQTCLLKLSKSEKEMDPEYEEKMVNMPLKAARAKRF  100
```

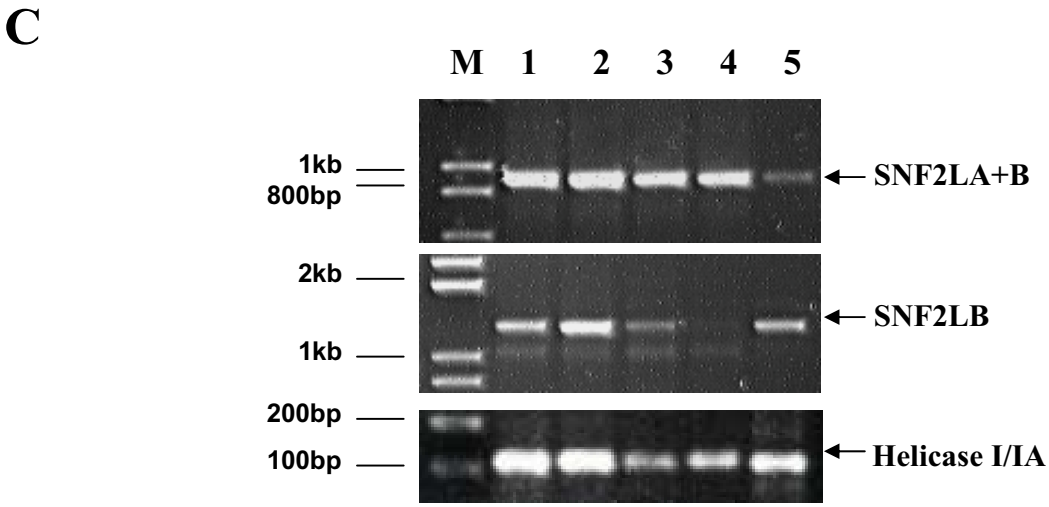

Figure 1

Genomic organization and 5' transcript variants of the human *SNF2L* gene. **A**. Schematic diagram showing the 25 exons (dark boxes; exon 13 is an open box) of the human *SNF2L* gene (top). Below is a schematic diagram of the SNF2L transcript showing the ORF (open box) and the location of the motifs that comprise the SNF2 domain (blue boxes) and the SANT domains (red boxes). **B**. The 5' variants *SNF2LA* and *SNF2L*B provide alternative initiation codons and encode two forms of *SNF2L* with different amino-termini. They are shown aligned to the mouse *Snf2l* sequence. The *SNF2L*B transcript encodes a protein with an amino-terminus similar in length and amino acid composition to the murine Snf2l protein. **C**. RT-PCR analysis showing that both transcript variants are present in human cell lines and fetal brain tissue examined. The helicase I/Ia domain served as control amplification. Lane 1, 293 cells; lane 2, SH-SY5Y cells; lane 3, NT2 cells; lane 4, hNT neurons; and lane 5, human fetal brain. M, molecular weight marker.

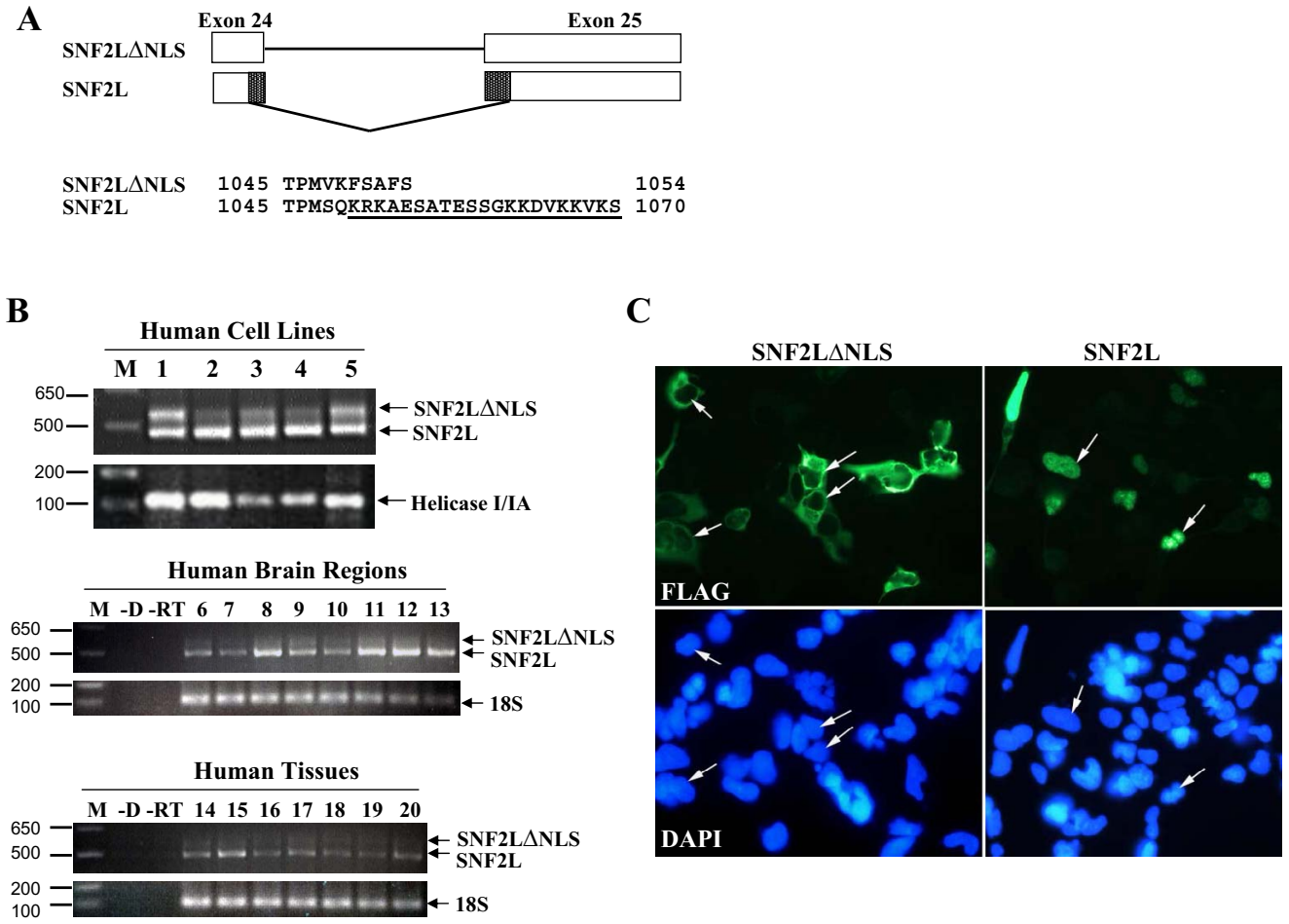

Figure 2

Alternative splicing of exons 24 and 25 generates nuclear and cytoplasmic isoforms of SNF2L. Alternative splicing of the *SNF2L* gene at the 3' end generates a transcript containing either the full sequence of exons 24 and 25, which encodes a shorter form of SNF2L without a nuclear localization signal (SNF2LΔNLS), or a transcript lacking 100 bp that encodes for a larger protein isoform (SNF2L) with an NLS (underlined). **B**. RT-PCR analysis demonstrated that both 3' variants are present in most cells and tissues examined, while the NLS isoform is predominant. M, marker; -D, no DNA template; -RT, no reverse transcriptase. Lanes 1–5, human cell lines and fetal brain sample as follows: 1, 293-HEK cells; 2, SH-SY5Y cells; 3, NT2 cells; 4, hNT neurons; 5, human fetal brain. Lanes 6–13, human brain regions including: 6, amygdala; 7, basal ganglia; 8, caudate nucleus; 9, cerebellum; 10, frontal cortex; 11, hippocampus; 12, pons; 13, thalamus. Lanes 14–20, human tissue samples including: 14, heart; 15, kidney; 16, liver; 17, ovary; 18, placenta; 19, skeletal muscle; and 20, testes. **C**. Indirect immunofluorescence imaging of 293 HEK cells transfected with FLAG-epitope tagged SNF2LΔNLS and SNF2L were stained with anti-flag antibody (green) or DAPI (blue). Note that SNF2LΔNLS encodes a protein that is localized exclusively in the cytoplasm while SNF2L is expressed only in the nucleus (arrows point to nuclei of transfected cells).

contains an additional 23 amino acids similar to the reported mouse protein (and herein called SNF2L). More importantly, we used the PredictNLS program [26] to determine that this alternatively spliced region contained a putative NLS sequence. To verify the importance of the NLS *in vivo*, we transiently transfected 293 HEK cells with FLAG-epitope tagged SNF2L or SNF2LΔNLS and detected the expressed protein by indirect immunofluorescence. As shown in Figure 2C, SNF2LΔNLS localized exclusively in the cytoplasm whereas SNF2L was present in the nucleus.

The *SNF2L* gene undergoes alternative splicing at multiple sites to generate a wide number of different isoforms. Some of these isoforms will affect the activity of the protein. For example, the inclusion of exon 13 abolishes the chromatin remodeling activity [25], and the altered splic-

Table 1: Mutation analysis of 12 families linked to Xq25 revealed 3 SNPs

Location of SNP	SNP	Family	% of control sample with SNP (n = 100)	SNP Heterozygosity (SNP Database No.)
Exon 1 – 5'UTR 29 bp 5' of AUG	CTTGTCCC CTTΔTCCC	F93-04	13%	ND
Intron 13 48 bp 5' of exon14	CAACAGTA CAATAGTA	K8895	15%	0.359 (rs2274093)
Intron 18 74 bp 3' of exon18	CAGATTTAC CAGATTTTC	24981	0%	0.093 (rs3736692)

ing within exons 24/25 removes the NLS resulting in cytoplasmic localization. In the latter case, the SNF2LΔNLS variant was detected in most tissues examined, suggesting that the cytoplasmic isoform of SNF2L may fulfill an alternative role to the chromatin remodeling function of the nuclear isoforms. Alternatively, it could represent a SNF2L dominant negative protein that sequesters other components of the chromatin remodeling complex in the cytoplasm. As such, it will be important to further explore the function of these novel SNF2L isoforms to determine their specific roles, similar to work done with the SNF2L+13 variant. Indeed, with splicing occurring at the 5'-end of the gene (isoforms SNF2LA and B), the 3'-end of the gene (NLS or ΔNLS) and encompassing exon 13 (+exon 13 or -exon 13) there are 8 possible isoforms of the SNF2L protein that can impinge on the function/activity of the protein.

We have demonstrated that expression of the murine *Snf2l* gene increases during development in a manner that is coincident with neuronal maturation and synapse formation [17]. This expression profile is most prevalent in the hippocampus, dentate gyrus and the cerebellum and expression within these structures is maintained in the adult mouse [17]. Given that the hippocampus and dentate gyrus have been implicated in learning and memory, and that mutations in genes involved in chromatin remodeling or modification cause mental retardation, it prompted us to examine the human *SNF2L* gene as a candidate XLMR gene. DNA samples from 12 individuals affected with XLMR and previously mapped to a region encompassing the *SNF2L* gene were used for direct sequencing analysis. We sequenced each of the 25 exons and flanking intron sequences of the *SNF2L* gene and identified 3 different single nucleotide polymorphisms (SNPs), all located in untranslated sequences (Table 1). Screening of 100 unaffected individuals demonstrated that the SNP in the 5' UTR of exon 1 and the polymorphism in intron 13 (rs2274093) had frequencies of 13% and 15% respectively, in our control population. Conversely, the SNP in intron 18 was not found in our control DNA samples, but screening of the SNP database identified it as a polymorphism with a heterozygosity frequency of 0.093 (rs3736692). Overall, the SNP database contains 195 entries for the *SNF2L* gene including 5 in the coding region (exons 1, 10, 16, 17, and 20). The SNP within exon 20 is reported to have a heterozygosity value of 0.026 and would result in an Ala to Gly substitution. While we did not find this change in any of our families, future analysis of this gene should be wary of this polymorphism.

Despite the absence of mutations in these families, SNF2L remains a logical candidate for XLMR localized to Xq25-26 because of (a) its similarity to *ATRX*, a SNF2-domain containing protein mutated in several XLMR disorders; (b) its high expression in the brain including areas important for learning and development; and (c) its ability to induce neuroblastoma cells to undergo differentiation when ectopically expressed [17,18]. In addition, SNF2L has been shown to regulate the engrailed genes, En-1 and En-2, both of which are important for mid/hind-brain development [27,28], the latter of which has been associated with autism in genetic linkage studies [29-31]. Given these criteria and the small sample size available for mutation analysis, other syndromes should be considered for screening, including the Shashi XLMR syndrome [32,33] and a family with syndromal XLMR and late-onset testicular failure (Cillier syndrome) [34] that both map to Xq26. In addition, there are 3 other syndromes (Wilson/MRXS12, Gustavson, and CMTX4/Cowchock-Fishbeck) and 8 MRX families (MRX 27, 35, 42, 62, 70, 71, 75, and 82) that map to this region that should also be considered in future screening endeavors [35]. The generation of a transgenic mouse ablated for the *Snf2l* gene should provide valuable phenotypic insight for its potential involvement in specific XLMR disorders. Together, the analysis of additional samples and the characterization of transgenic mice should define whether the SNF2L gene is a cause of mental retardation.

Conclusion

We have shown that there are multiple SNF2L isoforms that result from alternative splicing of the gene. How these different isoforms are spatially and temporally regulated and defining their specific role during neural development remains to be established. In our collection of 12 patients with XLMR linked to Xq25-26, we did not identify any mutations within the coding region. However, we cannot exclude intronic mutations (outside of the consensus splice sites) that would affect alternative splicing and hence the expression levels of the different isoforms. Similarly, we cannot exclude mutations in regulatory regions

in the 12 families screened for mutations in this gene. Alternatively, our failure to identify mutations may arise from (1) the small sample size which may have prevented us from ascertaining a family with a mutation in this gene, or (2) the possibility that mutations in SNF2L could cause a more severe phenotype that may be lethal in males. Indeed, SNF2L remains a candidate XLMR gene for Xq25-26 linked XLMR families including the Shashi syndrome as well as in sporadic mental retardation cases.

Competing interests

The author(s) declare that they have no competing interests.

Authors' contributions

MAL identified the various SNF2L isoforms, generated the preliminary RT-PCR data and performed the immunofluorescence experiments. MAMT extended the RT-PCR experiments to include the multiple human tissues and brain regions. PL and DV performed the sequence analysis of the XLMR patients. AD prepared the initial figures and wrote the first draft of the manuscript. DJP designed the study, participated in its execution and coordination and wrote the final manuscript. All authors have read and approved the final manuscript.

Acknowledgements

The authors would like to thank Drs. Allanson, Hamel, Schwartz, and Van Bokhoven for their generosity in providing patient DNA samples. This work was supported by grants from the Ontario Mental Health Foundation and the Neuromuscular Research Partnership (JNM-78384), an initiative of the ALS Society of Canada, Muscular Dystrophy Canada, and the Canadian Institutes of Health Research.

References

1. Chelly J, Mandel JL: **Monogenic causes of X-linked mental retardation.** *Nat Rev Genet* 2001, **2(9):**669-680.
2. Gibbons RJ, Picketts DJ, Higgs DR: **Syndromal mental retardation due to mutations in a regulator of gene expression.** *Hum Mol Genet* 1995, **4(Spec No):**1705-1709.
3. Gibbons RJ, Higgs DR: **Molecular-clinical spectrum of the ATR-X syndrome.** *Am J Med Genet* 2000, **97(3):**204-212.
4. Merienne K, Pannetier S, Harel-Bellan A, Sassone-Corsi P: **Mitogen-regulated RSK2-CBP interaction controls their kinase and acetylase activities.** *Mol Cell Biol* 2001, **21(20):**7089-7096.
5. Trivier E, De Cesare D, Jacquot S, Pannetier S, Zackai E, Young I, Mandel JL, Sassone-Corsi P, Hanauer A: **Mutations in the kinase Rsk-2 associated with Coffin-Lowry syndrome.** *Nature* 1996, **384(6609):**567-570.
6. Amir RE, Van den Veyver IB, Wan M, Tran CQ, Francke U, Zoghbi HY: **Rett syndrome is caused by mutations in X-linked MECP2, encoding methyl- CpG-binding protein 2.** *Nat Genet* 1999, **23(2):**185-188.
7. Meloni I, Bruttini M, Longo I, Mari F, Rizzolio F, D'Adamo P, Denvriendt K, Fryns JP, Toniolo D, Renieri A: **A mutation in the Rett syndrome gene, MECP2, causes X-linked mental retardation and progressive spasticity in males.** *Am J Hum Genet* 2000, **67(4):**982-985.
8. Orrico A, Lam C, Galli L, Dotti MT, Hayek G, Tong SF, Poon PM, Zappella M, Federico A, Sorrentino V: **MECP2 mutation in male patients with non-specific X-linked mental retardation.** *FEBS Lett* 2000, **481(3):**285-288.
9. Couvert P, Bienvenu T, Aquaviva C, Poirier K, Moraine C, Gendrot C, Verloes A, Andres C, Le Fevre AC, Souville I, Steffann J, des Portes V, Ropers HH, Yntema HG, Fryns JP, Briault S, Chelly J, Cherif B: **MECP2 is highly mutated in X-linked mental retardation.** *Hum Mol Genet* 2001, **10(9):**941-946.
10. Lower KM, Turner G, Kerr BA, Mathews KD, Shaw MA, Gedeon AK, Schelley S, Hoyme HE, White SM, Delatycki MB, Lampe AK, Clayton-Smith J, Stewart H, van Ravenswaay CM, de Vries BB, Cox B, Grompe M, Ross S, Thomas P, Mulley JC, Gecz J: **Mutations in PHF6 are associated with Borjeson-Forssman-Lehmann syndrome.** *Nat Genet* 2002, **32(4):**661-665.
11. Shoichet SA, Hoffmann K, Menzel C, Trautmann U, Moser B, Hoeltzenbein M, Echenne B, Partington M, Van Bokhoven H, Moraine C, Fryns JP, Chelly J, Rott HD, Ropers HH, Kalscheuer VM: **Mutations in the ZNF41 gene are associated with cognitive deficits: identification of a new candidate for X-linked mental retardation.** *Am J Hum Genet* 2003, **73(6):**1341-1354.
12. Kleefstra T, Yntema HG, Oudakker AR, Banning MJ, Kalscheuer VM, Chelly J, Moraine C, Ropers HH, Fryns JP, Janssen IM, Sistermans EA, Nillesen WN, de Vries LB, Hamel BC, van Bokhoven H: **Zinc finger 81 (ZNF81) mutations associated with X-linked mental retardation.** *J Med Genet* 2004, **41(5):**394-399.
13. Jensen LR, Amende M, Gurok U, Moser B, Gimmel V, Tzschach A, Janecke AR, Tariverdian G, Chelly J, Fryns JP, Van Esch H, Kleefstra T, Hamel B, Moraine C, Gecz J, Turner G, Reinhardt R, Kalscheuer VM, Ropers HH, Lenzner S: **Mutations in the JARID1C Gene, Which Is Involved in Transcriptional Regulation and Chromatin Remodeling, Cause X-Linked Mental Retardation.** *Am J Hum Genet* 2005, **76(2):**227-236.
14. Elfring LK, Deuring R, McCallum CM, Peterson CL, Tamkun JW: **Identification and characterization of Drosophila relatives of the yeast transcriptional activator SNF2/SWI2.** *Mol Cell Biol* 1994, **14(4):**2225-2234.
15. Aihara T, Miyoshi Y, Koyama K, Suzuki M, Takahashi E, Monden M, Nakamura Y: **Cloning and mapping of SMARCA5 encoding hSNF2H, a novel human homologue of Drosophila ISWI.** *Cytogenet Cell Genet* 1998, **81(3-4):**191-193.
16. Okabe I, Bailey LC, Attree O, Srinivasan S, Perkel JM, Laurent BC, Carlson M, Nelson DL, Nussbaum RL: **Cloning of human and bovine homologs of SNF2/SWI2: a global activator of transcription in yeast S. cerevisiae.** *Nucleic Acids Res* 1992, **20(17):**4649-4655.
17. Lazzaro MA, Picketts DJ: **Cloning and characterization of the murine Imitation Switch (ISWI) genes: differential expression patterns suggest distinct developmental roles for Snf2h and Snf2l.** *J Neurochem* 2001, **77(4):**1145-1156.
18. Barak O, Lazzaro MA, Lane WS, Speicher DW, Picketts DJ, Shiekhattar R: **Isolation of human NURF: a regulator of Engrailed gene expression.** *Embo J* 2003, **22(22):**6089-6100.
19. Banting GS, Barak O, Ames TM, Burnham AC, Kardel MD, Cooch NS, Davidson CE, Godbout R, McDermid HE, Shiekhattar R: **CECR2, a protein involved in neurulation, forms a novel chromatin remodeling complex with SNF2L.** *Hum Mol Genet* 2005, **14(4):**513-524.
20. Chomczynski P, Sacchi N: **Single-step method of RNA isolation by acid guanidinium thiocyanate- phenol-chloroform extraction.** *Anal Biochem* 1987, **162(1):**156-159.
21. Hamel BC, Smits AP, Otten BJ, van den Helm B, Ropers HH, Mariman EC: **Familial X-linked mental retardation and isolated growth hormone deficiency: clinical and molecular findings.** *Am J Med Genet* 1996, **64(1):**35-41.
22. Arena JF, Schwartz C, Stevenson R, Lawrence L, Carpenter A, Duara R, Ledbetter D, Huang T, Lehner T, Ott J, *et al.*: **Spastic paraplegia with iron deposits in the basal ganglia: a new X-linked mental retardation syndrome.** *Am J Med Genet* 1992, **43(1-2):**479-490.
23. Cabezas DA, Slaugh R, Abidi F, Arena JF, Stevenson RE, Schwartz CE, Lubs HA: **A new X linked mental retardation (XLMR) syndrome with short stature, small testes, muscle wasting, and tremor localises to Xq24-q25.** *J Med Genet* 2000, **37(9):**663-668.
24. Christianson AL, Stevenson RE, van der Meyden CH, Pelser J, Theron FW, van Rensburg PL, Chandler M, Schwartz CE: **X linked severe mental retardation, craniofacial dysmorphology, epilepsy, ophthalmoplegia, and cerebellar atrophy in a large South African kindred is localised to Xq24-q27.** *J Med Genet* 1999, **36(10):**759-766.
25. Barak O, Lazzaro MA, Cooch NS, Picketts DJ, Shiekhattar R: **A tissue-specific, naturally occurring human SNF2L variant inac-**

tivates chromatin remodeling. *J Biol Chem* 2004, **279(43):**45130-45138.
26. Predict_NLS_program: [http://cubic.bioc.columbia.edu/predictNLS/].
27. Joyner AL, Herrup K, Auerbach BA, Davis CA, Rossant J: **Subtle cerebellar phenotype in mice homozygous for a targeted deletion of the En-2 homeobox.** *Science* 1991, **251(4998):**1239-1243.
28. Wurst W, Auerbach AB, Joyner AL: **Multiple developmental defects in Engrailed-1 mutant mice: an early mid-hindbrain deletion and patterning defects in forelimbs and sternum.** *Development* 1994, **120(7):**2065-2075.
29. Benayed R, Gharani N, Rossman I, Mancuso V, Lazar G, Kamdar S, Bruse SE, Tischfield S, Smith BJ, Zimmerman RA, Dicicco-Bloom E, Brzustowicz LM, Millonig JH: **Support for the homeobox transcription factor gene ENGRAILED 2 as an autism spectrum disorder susceptibility locus.** *Am J Hum Genet* 2005, **77(5):**851-868.
30. Gharani N, Benayed R, Mancuso V, Brzustowicz LM, Millonig JH: **Association of the homeobox transcription factor, ENGRAILED 2, 3, with autism spectrum disorder.** *Mol Psychiatry* 2004, **9(5):**474-484.
31. Kuemerle B, Gulden F, Cherosky N, Williams E, Herrup K: **The mouse Engrailed genes: a window into autism.** *Behav Brain Res* 2007, **176(1):**121-132.
32. Castro NH, dos Santos RC, Nelson R, Becak W, Hane B, Lindsey CJ, Lubs HA, Stevenson RE, Schwartz CE: **Shashi XLMR syndrome: report of a second family.** *Am J Med Genet A* 2003, **118(1):**49-51.
33. Shashi V, Berry MN, Shoaf S, Sciote JJ, Goldstein D, Hart TC: **A unique form of mental retardation with a distinctive phenotype maps to Xq26-q27.** *Am J Hum Genet* 2000, **66(2):**469-479.
34. Cilliers DD, Parveen R, Clayton P, Cairns SA, Clarke S, Shalet SM, Black GC, Newman WG, Clayton-Smith J: **A new X-linked mental retardation (XLMR) syndrome with late-onset primary testicular failure, short stature and microcephaly maps to Xq25-q26.** *Eur J Med Genet* 2007, **50(3):**216-223.
35. Chiurazzi P, Schwartz CE, Gecz J, Neri G: **XLMR genes: update 2007.** *Eur J Hum Genet* 2008.

Pre-publication history

The pre-publication history for this paper can be accessed here:

http://www.biomedcentral.com/1471-2350/9/11/prepub

APPENDIX C

SCO-ping Out the Mechanisms Underlying the Etiology of Hydrocephalus

Purpose

To review the literature concerning the contributions of the subcommissural organ (SCO) and the ventricular ependyma of the brain towards the onset of congenital hydrocephaly in both humans and animal models.

Submission Information

Submitted: December 2008
Accepted: February 2009
Published: 1 April 2009

Reprinted from "**Physiology, Huh, M.S., Todd M.A.M., and Picketts D.J., SCO-ping out the mechanisms underlying the etiology of hydrocephalus, 2009, Volume 24, pp 117-126**," in accordance with the copyright (2009) permission policies of The American Physiological Society.

Contribution of Co-Authors

Matthew A.M. Todd contributed Figure 2 and Table 1 and wrote the following sections: "Signal Transduction and the Regulation of SCO Secretion," "The Contribution of the Ventricular Cilia to CSF Homeostasis," and "Cell Adhesion Molecules and Hydrocephalus."

Michael S. Huh contributed Figure 1 and wrote the "Loss of Developmental Factors Impairs SCO Formation and Function" section. The remaining sections were co-written by all authors. Matthew A.M. Todd and Michael S. Huh contributed equally to the writing of this manuscript, while David J. Picketts edited the manuscript.

PHYSIOLOGY 24: 117–126, 2009; doi:10.1152/physiol.00039.2008

SCO-ping Out the Mechanisms Underlying the Etiology of Hydrocephalus

Michael S. Huh,[1,*] Matthew A. M. Todd,[2,*] and David J. Picketts[2]

[1]Regenerative Medicine Program, Ottawa Health Research Institute, and [2]Department of Biochemistry, Microbiology, and Immunology, University of Ottawa, Ottawa, Ontario, Canada
dpicketts@ohri.ca
*M. S. Huh and M. A. M. Todd contributed equally to this manuscript.

The heterogeneous nature of congenital hydrocephalus has hampered our understanding of the molecular basis of this common clinical problem. However, disease gene identification and characterization of multiple transgenic mouse models has highlighted the importance of the subcommissural organ (SCO) and the ventricular ependymal (vel) cells. Here, we review how altered development and function of the SCO and vel cells contributes to hydrocephalus.

The cerebral spinal fluid (CSF) flow tract is a vital lifeline for supplying the brain with essential nutrients and growth factors throughout development and into adulthood. At the same time, the brain exercises constant control to ensure that the flow of CSF is homeostatic. CSF is secreted by the choroid plexus and moves rostrocaudally through the ventricles and into the subarachnoid space before being drained into the venous circulation (80). Failures within this cerebral irrigation network can lead to a buildup of CSF in the ventricular cavities of the brain, a condition known as hydrocephaly, which is fatal without surgical intervention. Hydrocephalus can result from an overproduction of CSF by the choroid plexus, failure to drain the CSF at the subarachnoid space, and the blockage of CSF flow through the narrow Sylvian aqueduct, which is situated between the third and fourth ventricles. Indeed, stenosis of the Sylvian aqueduct is considered the primary cause of congenital hydrocephalus, which is quite frequent, occurring with an incidence of 0.1–0.3% of live births (80). The causes for this disease are quite heterogeneous and have been linked to a number of genetic mutations, both autosomal and X-linked (112). What is intriguing, though, is that many of these mutations impinge on the development or function of the subcommissural organ (SCO) and the ventricular ependymal (vel) cells that collectively facilitate the flow of CSF through the confining canals of the ventricular system (Table 1).

The goal of this review is to summarize the molecular mechanisms that cause *1*) the SCO to be absent or disorganized, *2*) an inability of the SCO to properly secrete glycoproteins, *3*) primary ciliary dyskinesia (PCD) of the ependymal cells, and *4*) denudation of the neuroependyma. Although it should be noted that not all SCO/vel defects have been proven to precede the onset of hydrocephaly, indeed it is the aberrant execution of these diverse molecular pathways that can lead to stenosis of the aqueduct and contribute to communicating or noncommunicating hydrocephalus.

Loss of Developmental Factors Impairs SCO Formation and Function

The SCO is a small secretory gland positioned in the dorsal caudal aspect of the third ventricle underneath the posterior commissure. The SCO is derived from the neuroepithelial cells that line the lumen of the dorsal-caudal aspect of the diencephalon. This anatomical region is also described as the prosomere 1 (P1), demarcated by the pineal gland and the mesencephalon. The primitive epithelial progenitors of the presumptive SCO are driven toward a specialized secretory ependymal cell fate in response to the inductive Wnt and Bmp signals emanating from the roof plate of the dimesencephalon boundary (FIGURE 1A). Indeed, the roof plate acts as an important organizing center for the secretion of these morphogens that are crucial for establishing the dorsal-lateral identity along the central nervous system (CNS) (31, 58, 59). Although malformation of the SCO during gestation leads to ventricular dilation and aqueductal stenosis before birth (FIGURE 1, B AND C) (32, 80), the involvement of specific factors has been slowly elucidated over the past decade through the analysis of mutant mouse models.

One such protein is Msx1, a critical factor involved in dorsal neural patterning (3, 84). Msx1 along with Msx2 and Msx3 form a family of homeodomain transcriptional repressors (18, 96, 111). The earliest expression of Msx1 is observed at the neural fold stage, along the boundary of the neural plate (17, 38). Upon closure of the neural tube, Msx1 is prominently expressed along the entire length of the dorsal midline of the neural tube. Msx1 is also expressed in the SCO, choroid plexus (CP), and the habenula in the third ventricle (84). Bach et al. clearly demonstrated that homozygous mutants for Msx1 were unable to sustain Wnt1 and Bmp6 expression in the dorsal midline of P1, and histological analysis demonstrated the absence of a SCO and a poorly organized posterior commissure (3, 84). Loss of morphogen induction in P1 consequently downregulated cell fate markers such

1548-9213/09 8.00

as Pax6, Pax7, and Lim1, whereas the P2 marker Gbx2 remained unaffected. The *Msx1* mutant mice developed hydrocephaly, and the interactions of Msx1 with Wnt1 and Pax6 are corroborated by similar hydrocephalic phenotypes in *Wnt1*$^{sw/sw}$ and *Pax6*$^{sey/sey}$ mice (27, 60).

It is also possible that Msx1 may regulate genes that maintain homeostasis in the mature SCO ependymal cells. Msx1 is already known to influence a diverse set of gene expression programs during neuronal development (85). Moreover, the residual ependymal cells of the SCO were not immunoreactive with anti-Reissner's fiber serum (AFRU), suggesting the absence of glycoprotein secretion (84). Although multiple roles are suggestive, additional studies such as temporal inactivation of *Msx1* will be required to determine whether Msx1 directly regulates the expression of secreted glycoproteins and cell adhesion molecules in secretory ependymal cells. *Msx1*$^{+/-}$ mice are viable, but one-third of them develop hydrocephaly, likely due to the reduction in SCO size (29).

The regulatory factor X (Rfx) family represents a second class of transcription factors expressed in the dorsal neural tube, and two family members, Rfx3 and Rfx4_v3, are important for the development of the SCO (2, 11). The Rfx proteins are winged-helix transcription factors that form either homo- or heterodimers to regulate target genes (45, 71, 86) and are known to direct the formation of ciliated cell types in metazoans (1, 12, 26, 35, 52, 97, 101). Both *Rfx3* and *Rfx4_v3* transcripts are expressed embryonically in the dorsal aspect of the neural tube and are highly expressed in the ependymal cells of the SCO in the embryo and adult (2, 11). Additionally, Rfx3 expression is prominent in the ependymal cells of the CP and is sustained in all ciliated ependymal cells from the moment of birth to adulthood (2). Not surprisingly, *Rfx3*$^{-/-}$ mice that come to term invariably develop communicating hydrocephaly (2). In the *Rfx4_v3* mice, congenital non-communicating hydrocephaly was observed in the heterozygous condition (11). The agenesis of the SCO was a common feature found in both *Rfx3*$^{-/-}$ and *Rfx4_v3*$^{+/-}$ mice (2, 11). The absence of a functional SCO was ascertained by the degree of immunoreactivity using anti-SCO-spondin (*Rfx3*$^{-/-}$) and anti-RF (*Rfx4_v3*$^{+/-}$) in the presumptive SCO region. In both studies, the degree of immunoreactivity was significantly reduced. Although both mouse knockout models resulted in the absence of a functional SCO, an intriguing observation was reported in the case of the Rfx3 phenotype. The *Rfx3*$^{-/-}$ mice appeared to have an

Table 1. Mutations that lead to hydrocephaly in the mouse

Gene	Description/Function	SCO/Neuroependymal Phenotype	References
		Developmental defects	
En-1	Transcription factor	Ectopic expression leads to SCO agenesis, ependymal differentiation defects in CP/SCO	60
Hdh	Unknown	SCO agenesis; ependymal differentiation defects	24
Msx1	Transcription factor	SCO agenesis; neuroependymal denudation	3, 29, 84
Pax6	Transcription factor	SCO agenesis	27
Rfx3	Transcription factor	SCO agenesis; neuroependymal defects	2
Rfx4_v3	Transcription factor	SCO agenesis; severe midline structure defects	11
Wnt1	Secreted morphogen	SCO agenesis	60
		Signal transduction defects	
Pac1	G-protein coupled receptor	Overexpression leads to SCO agenesis; ependymal cilia are short and disorganized	50
Socs7	Suppressor of cytokine signaling	SCO cellular structure is disorganized	48
		Cilia structure/function defects	
Hydin	Central pair-dynein adaptor	Missing central pair projection; ciliary motility defects	22, 53
Foxj1/Hfh-4	Transcription factor	Ciliogenesis defects	13, 20
Mdnah5	Dynein heavy chain	Outer dynein arms missing; ciliary motility defects	39, 41
Pcdp1	Unknown; may bind to central pair	Ciliary motility defects	55
Polaris/Ift188	IFT particle protein	Ependymal cells are shorter, disorganized, and beat asynchronously; CP defects	6
Pol λ	DNA repair polymerase	Inner dynein arm abnormalities; ciliary motility defects	47
Spag6	Central pair-dynein adaptor	Ciliary motility defects; Spag16 inactivation increases severity of hydrocephalus	93, 116
		Cell adhesion defects	
L1-cam	Cell adhesion molecule	Defects in neuronal neurite outgrowth; neuroependyma appears normal	90
Nmhc-IIb	Component of apical cell adhesion complex	Neuroependymal denudation	61, 104
Napa/α-Snap	Apical transporter of cell adhesion molecules	Neuroependymal denudation with mutation that causes reduced expression of protein	19, 36

*Unless otherwise stated, all mutations are inactivating.

overall dysfunction in the development of the ciliated ependymal cells. More specifically, the CP was poorly formed or improperly differentiated, with a lack of cilia present on the apical surface. Furthermore, the cell adhesion properties of the CP ependymal cells were compromised since the interdigitations between cells were poorly formed and the basal membrane was not apposed to the basal lamina. This apparent lack of differentiation was also observed in the SCO where its ependymal cells were more cuboidal with many cilia, appearing similar to the ependyma lining the ventricles (2).

In the case of the Rfx4_v3 studies, homozygous knockouts of *Rfx4_v3* strongly suggest its role as a critical mediator of an earlier dorsal midline patterning decision. *Rfx4_v3*$^{-/-}$ mice were embryonic lethal due to catastrophic midline defects. *Rfx4_v3*$^{-/-}$ telencephalon at E12.5 were characterized by hypoplasia of the dorsal midline and adjacent cerebral cortex. The dorsal midline defect was also evident due to the down regulation of *Wnt7a* and *Wnt7b* in the cortical hem, a midline structure that normally produces these transcripts (11). A recent microarray experiment identified components of the Wnt, Bmp, and retinoic acid signaling pathways to be potential targets of Rfx4_v3 in E10.5 brains (110).

From the studies described above, tight regulation along the dorsal midline through Wnt and Bmp signaling pathways is an important regulatory mechanism for the proper development of the differentiated ependymal cells of the SCO and for preventing the onset of hydrocephalus. Indeed, this is also noted in mice that ectopically express Engrailed-1 (En-1), a transcription factor that is important for establishment of the mid-hindbrain boundary, since these animals were presented with hydrocephaly and SCO agenesis in the P1 domain (60). Similarly, a recent report by Dietrich et al. produced a mouse model linking the Huntington's disease gene (*Hdh*) to congenital hydrocephaly (24). In this study, a mid- to hindbrain-specific inactivation of *Hdh* was generated by crossing *Hdh*^{flox} mice with animals that express Cre under the control of a *Wnt1* regulatory element. The *Wnt1-Cre:Hdh*^{flox} mice came to term but displayed reduced growth and progressive wasting due to the build up of excessive CSF, expansion of the ventricles, and the loss of cortical tissue. Histology revealed expansion of the lateral ventricles by E17.5, indicating the congenital nature of the hydrocephaly. Despite the complete absence of huntingtin (htt) in the mutant CP, no gross structural defects were observed using immunohistochemistry for a variety of markers (24). The effect of htt loss was more overt in the mutant SCO. Mutant SCO was ~40% the size of the controls. Serial coronal

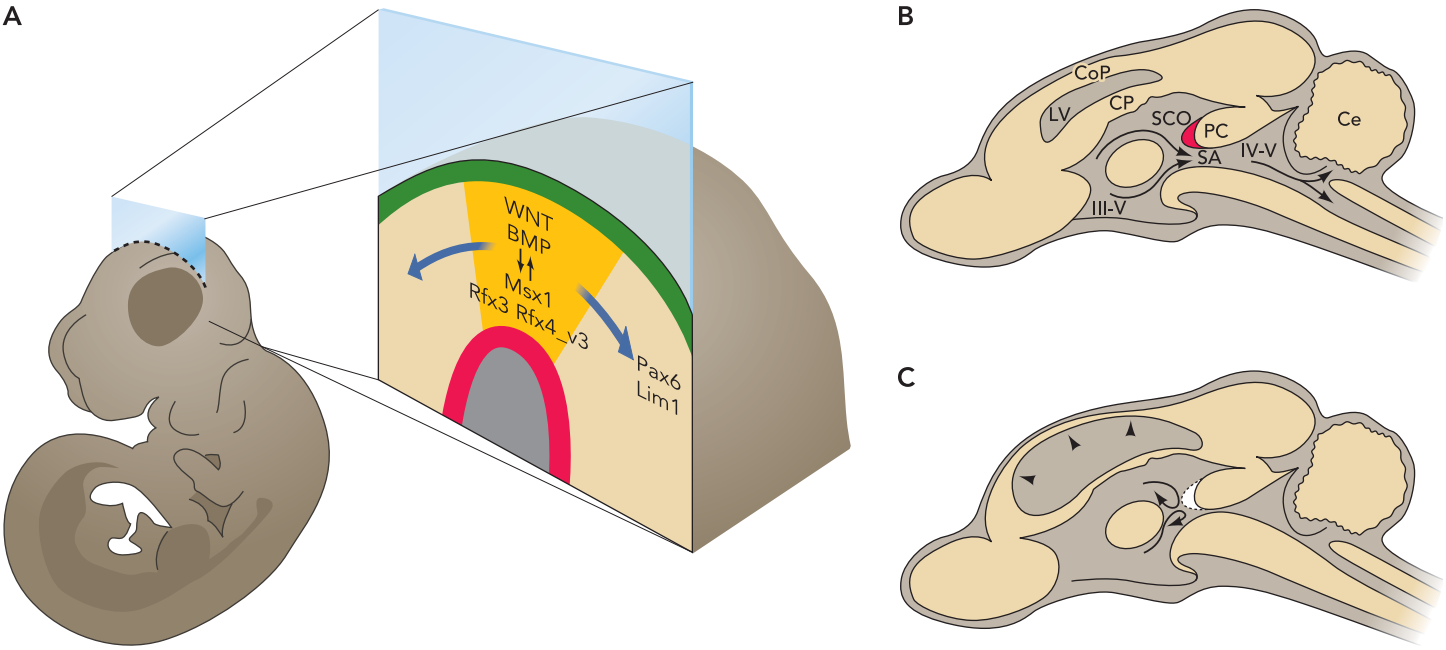

FIGURE 1. **Genetic determinants of congenital hydrocephaly and subcommissural organ agenesis**
A: molecular regulation of dorsal midline patterning in prosomere1 (P1) in an E10.5 mouse embryo. A coronal section of the neural tube through the di-mesencephalic boundary depicts the roof plate in yellow and the underlying dorsal primitive neuroepithelium in red that gives rise to the subcommissural organ (SCO). Msx1 expression in the midline activates the expression of Wnts and Bmps. Wnt and Bmp signaling from the roof plate induces the expression of Pax6 and Lim1 in a dorsal-lateral gradient. Rfx3 and Rfx4_v3 are also expressed at this stage in the dorsal-medial region. *B*: sagittal section of a normal E18.5 mouse brain depicting the cerebral spinal fluid (CSF) flow. The CSF flows unimpeded, circulating from the lateral (LV) and third ventricles (III–V) and in through the Sylvian aqueduct (SA). The SCO (red) is positioned immediately anteriorly to SA and is believed to facilitate the flow of the CSF by the secretion of glycoproteins and the formation of Reissner's fibers (not represented in this figure). Other structures in this panel are cortical plate (CoP), choroid plexus (CP), fourth ventricle (IV–V), posterior commissure (PC), and cerebellum (Ce). *C*: sagittal section depicting a hydrocephalic E18.5 mouse brain. Mutations in genes that regulate the tightly controlled patterning in the dorsal midline of P1 lead to SCO malformation and congenital hydrocephaly. Wnt1, Msx1, Rfx3, Rfx4_v3, Pax6, and Engrailed have been demonstrated to be critical players in this process. Misregulation of these genes frequently leads to agenesis of the SCO (dotted area) and the stenosis of the SA. The closure of the SA causes an accumulation of the CSF resulting in dilatation of the III–V and LV. The enlargement of the ventricles results in a secondary loss of cortical tissue and a characteristic doming of the cortex.

sections revealed that only the rostral portion of the SCO appeared properly differentiated as detected by SCO-spondin staining. Moreover, caudal to the SCO domain, ectopic SCO-spondin expression was detected in the ependymal lining of the Sylvian aqueduct (24). Further characterization of these mice is needed to determine whether the defect lies in inappropriate secretion of glycoproteins from the SCO or altered function of the vel cells lining the aqueduct. Nonetheless, these findings suggest that htt has a role in regulating the function of specialized ependymal cells.

Taken together, the proper development of the SCO is essential for CSF circulation through the narrow Sylvian aqueduct, and other factors that regulate dorsal patterning at or near the mid-hindbrain boundary are potential candidates for genetic causes of congenital hydrocephaly. In this regard, a protein like Snf2l, which modulates chromatin structure and expression of En-1, may potentially have dire consequences for hydrocephaly (8). Although we are only beginning to unravel the multitude of factors that control the cell fate decisions in this region and the terminal differentiation of the specialized cells of the SCO and vel, it is apparent that there is extreme heterogeneity underlying hydrocephalus. It should also be mentioned that other transcription factors, such as Otx2, are known to be associated with hydrocephalus when inactivated in mice; however, such a phenotype is unlikely to be SCO-specific and likely constitutes a more general defect in brain development (62). Although development seems to have a significant role in the etiology of hydrocephalus, aberrant function of the SCO and vel cells has also been implicated in this disease.

Signal Transduction and the Regulation of SCO Secretion

The primary function of the SCO is to secrete high molecular weight glycoproteins that facilitate CSF flow and, in rodents, contribute to the formation of Reissner's fiber (RF), which extends along the length of the CSF tract to the ampulla caudalis (89). The major secreted glycoprotein and constituent of RF is SCO-spondin, a highly conserved protein containing

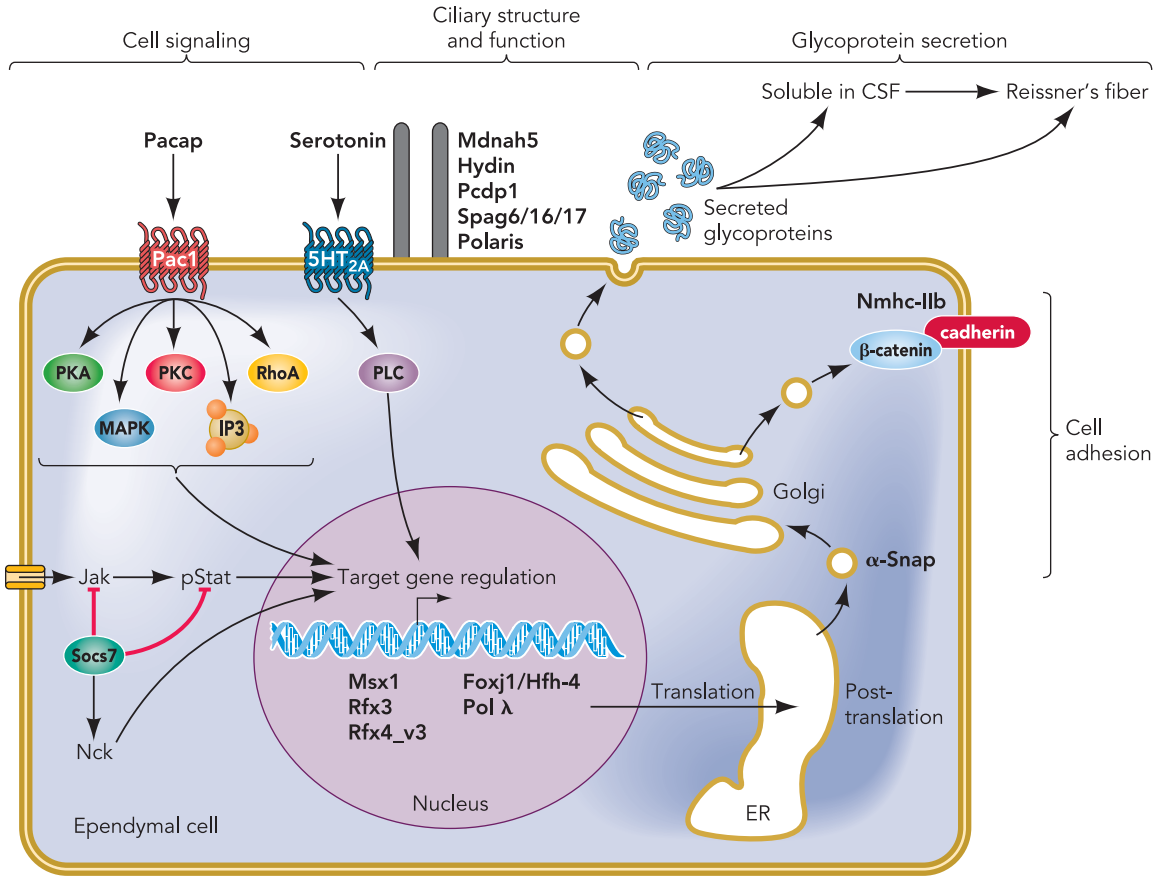

FIGURE 2. **Molecular pathways in ependymal cells implicated in congenital hydrocephalus**
Schematic representation of a SCO/vel ependymal cell highlighting the numerous molecular pathways underlying congenital hydrocephalus. Neuropeptides (Pacap, serotonin) induce cell signaling pathways that alter target gene regulation, presumably genes encoding secreted glycoproteins and proteins involved in ciliary function. The Socs7 protein is a regulator of the Jak/Stat signaling pathway. Ablation of several transcription factors (Msx1, Rfx3, Rfx4_v3) alters the terminal differentiation or cell fate of the ependymal cells. Numerous proteins (Mdnah5, Hydin, Pcdp1, Spag6, Polaris) and transcriptional regulators (Foxj1/Hfh-4, Pol λ) involved in the formation and function of cilia are implicated in hydrocephalus and are shown at the top of the diagram. The α-Snap protein is involved in regulating the transport of cell adhesion molecules (Nmhc-IIb, cadherin) to the apical cell surface and presumably also for proper glycoprotein secretion.

many protein-protein interaction domains that have fostered its numerous putative functions, including axonal pathfinding, promoting neuronal survival and neurite extension, and a detoxifying activity by removing monoamines from the CSF (67, 68). Regardless of its precise function, alterations in SCO secretions have been shown to precede diagnoses of hydrocephalus (99). Although transcription factors that promote terminal differentiation are important for regulating the expression of secreted proteins (e.g., Msx1) from the SCO, increasing evidence implicates signal transduction mechanisms in the processes regulating SCO secretion as a cause of hydrocephalus (FIGURE 2). The importance of signaling pathways downstream of G-protein-coupled receptors (GPCR) (73) in particular may modulate SCO glycoprotein secretion through the induction of transcriptional regulators, such as CREB, and perhaps also through the induction of intracellular calcium levels (10, 50, 74, 81, 94, 95). Recently developed hydrocephalic transgenic mouse models (Pac1, Ro1) seem to indicate that GPCR concentrations are rigidly controlled (50, 100).

The PACAP type I (Pac1) receptor is one example of a GPCR that contributes to hydrocephaly (50). Murine Pac1 is highly expressed in neural progenitor cells, and transgenic Pac1 was also found to be highly expressed in the differentiated SCO and ventricular ependyma (50, 106). Pituitary adenylate cyclase-activating polypeptide (PACAP) is the primary Pac1 ligand, and its interactions with Pac1 have been shown to activate or inhibit a variety of downstream signaling pathways, including PKA, PKC, MAPK, RhoA, and IP_3 (FIGURE 2) (66). Transgenic mice that overexpressed Pac1 developed communicating hydrocephalus with an enlarged aqueduct, which was associated with apoptosis-related SCO agenesis and shortened disorganized ventricular cilia (50). The mutant phenotype was correlated with an activation of both PKA and PKC signaling; however, the impact on SCO secretion was not assessed.

Neurotransmitting hormones are some of the most well characterized ligands of GPCRs, and the SCO is well innervated by serotonergic, GABAergic, dopaminergic, and noradrenergic fibers (42). Serotonin and GABA have also been previously characterized as regulators of SCO secretion; however, the molecular mechanisms have not been well explored (56, 70, 92). The most recent molecular studies concerning the effect of neurotransmitters on SCO secretion demonstrate a significant amount of serotonin and dopamine receptors on the apical surface of the mammalian SCO ependyma, implicating the CSF as the primary source of their respective ligands (87, 103). Although dopamine signaling did not have any significant effect on SCO secretion, serotonin signaling through the $5HT_{2A}$ receptor, which primarily stimulates the phospholipase C (PLC) pathway, was shown to inhibit the transcription of SCO-spondin. To date, defects in serotonin signaling have not been identified as a primary cause of hydrocephalus. However, a significant reduction in the rate of serotonin turnover has been observed in the CSF of human infants suffering from hydrocephalus (34), which may account for secondary defects in SCO secretion that could contribute to a worsening of the disease.

"Recent molecular evidence in humans indicates that the direction of cell adhesion molecules to the proper surface is vital."

Abnormal cytokine and growth factor signaling pathways have also been linked with hydrocephaly (reviewed in Ref. 112). One study has shown that suppressor of cytokine signaling 7 (*Socs7*) mutant mice develop late-onset communicating hydrocephalus, where the only observable physiological abnormality is a disorganized SCO (48). Abnormalities in SCO secretion and RF formation were not examined. SOCS proteins are traditionally considered to suppress cytokine signaling by binding to JAK receptors to prevent STAT transduction into the nucleus (51). Although this may be the role of Socs7 in SCO cells, the protein has also been implicated in several nontraditional transduction roles, including its binding to phosphorylated STATs (63), binding to other SOCS proteins (82), binding to the actin cytoskeleton through interactions with septins or vinexin (46, 49, 64), or contributing to the regulation of the actin cytoskeleton and cell cycle mechanisms by shuttling NCK to the nucleus (46, 49). At this time, the molecular significance of SOCS7 with respect to the SCO remains to be characterized.

Taken together, these studies highlight the possibility that constituents of the CSF feedback on the SCO to regulate glycoprotein production and/or secretion. Although disruptions in specific signaling pathways have not yet been proven to be a primary cause of hydrocephaly, it represents an exciting area for future studies that would provide an additional layer of complexity to our understanding of the causal mechanisms of congenital hydrocephalus and SCO function.

The Contribution of Ventricular Cilia to CSF Homeostasis

The ventricular ependyma shares complementary functions with the SCO in regulating CSF homeostasis and preventing the onset of hydrocephalus (81). Besides the requirement for SCO glycoproteins and RF to prevent stenosis of the Sylvian aqueduct, a unidirectional laminar flow of CSF generated by the ciliated ependyma is essential (41).

Hydrocephalus in humans arises in several ciliopathies, disorders that have been attributed to defects in cilia structure and function (4, 30, 40, 109). In the ventricular ependyma, the ciliary core, or axoneme, consists of an arrangement of a central pair of microtubules surrounded by nine peripheral microtubule doublets. Radial spokes project from the central pair and interact with the peripheral doublets, presumably to regulate interactions with dyneins, which are motor proteins that are responsible for generating ciliary beat (91).

Mouse axonemal dynein heavy chain (Mdnah5) was identified as a protein that is important for laminar CSF flow through the Sylvian aqueduct (41). *Mdnah5*-null mice have immotile cilia due to the absence of outer dynein arms in the axoneme (39). Its human counterpart, DNAH5, has been linked to outer dynein arm defects that lead to PCD, although only a small percentage of human patients carrying *DNAH5* mutations develop hydrocephalus (37, 75).

The molecular characterization of the hydrocephalus-3 (*hy3*) mouse, a commonly studied model of hydrocephalus, resulted in the identification of the *Hydin* gene (22). Hydin is a putative microtubule binding protein (83) required for the formation of a specific projection emanating from one of the central pair microtubules (23, 53, 54). Lechtreck et al. believe that Hydin is a dynein adaptor that is required to regulate the transition between the ciliary effective and recovery strokes (53, 54). This proposal is consistent with observations that the ependymal cilia of *hy3* mice have difficulty bending, leading to ciliary beats with reduced frequency and impaired synchronicity (53). At the same time, these cilia do not appear to have any structural defects other than the lack of this single central pair projection. The authors note that the phenotype is similar to that of PCD patients who suffer defects in the inner dynein arms or the radial spokes (21, 53).

Sperm-associated antigen 6 (Spag6) is another factor that associates with a specific central pair projection and, along with its interacting partners Spag16 and Spag17, is required for ciliary motility (93, 113–115). Like Hydin, *Spag6*$^{-/-}$ mutants suffer from hydrocephalus. The extent of the phenotype is made more severe when both *Spag6* and *Spag16* are knocked out, although *Spag16*$^{-/-}$ mice are not hydrocephalic (116). The ultrastructure of the ependymal cells in these animals appears normal, suggesting a molecular pathology that is similar to *hy3* mice. Moreover, *Spag6* has been described as a candidate gene for hydrocephalus in H-Tx rats, another commonly studied hydrocephalus model (43).

PCD protein 1 (Pcdp1) is another putative central pair-binding protein that, when ablated in mice, results in hydrocephalus (55). As with *hy3* and *Spag6*$^{-/-}$ mice, the tracheal cilia of the *Pcdp1*$^{-/-}$ mice have a reduced beat frequency but do not display any obvious ultrastructural axonemal defects. The ultrastructure and ciliary beat frequency of ependymal cilia were not reported, although Pcdp1 was identified throughout the cilia of human brain ependymal cells.

In the *Tg737*^{orpk} mouse (57), mutations in the intraflagellar transport protein (91) Polaris/Ift188 also led to hydrocephalus. Although ependymal cilia are shorter, disorganized, and beat asynchronously, the primary cause of hydrocephaly in these mice appears to be the regulation of intracellular and secretory mechanisms of the choroid plexus in response to the defects in the structure and function of its cilia (5, 6). IFT components appear to be well conserved and many await characterization, so it remains to be seen whether mutations in additional IFT factors also result in hydrocephalus.

Defects in the expression of transcriptional regulators that mediate ciliogenesis can also lead to hydrocephalus. For example, Foxj1/Hfh-4 is an important transcriptional activator of numerous genes required for the development of motile cilia and has been associated with left-right asymmetry developmental defects and associated hydrocephaly (13, 20, 108). Similarly, mice that lack DNA polymerase λ (Pol λ) also develop hydrocephalus (47). Although Pol λ is generally considered to be a DNA repair enzyme, it is required for the proper expression of the axonemal inner dynein arms whose dysfunction likely contributes to the hydrocephaly in these animals (33).

In this section, we have highlighted recent advances characterizing defects in ciliary structure and function that result in hydrocephalus. It is likely that additional proteins that interact with or comprise the cilia ultrastructure are potential candidates to be implicated in hydrocephalus in the near future.

Cell Adhesion Molecules and Hydrocephalus

The ependymal cells of the SCO possess tight junctions and zonulae adherens, which contribute to the formation of a blood-brain barrier between the vasculature and the ventricular cavities (89). Adding to the complexity of its functions is accumulating evidence that the SCO is able to act as a mechanosensor, altering the way it secretes glycoproteins in response to signals sent from circulating blood, as shown in hypertensive rats (65). In this regard, it is intriguing that hypertension was also observed in both *Pac1*-null and -overexpressing transgenic mice (50). Regardless, the presence of such a blood-brain barrier necessitates a functional complement of cell adhesion molecules.

Recent molecular evidence in humans indicates that the direction of cell adhesion molecules to the proper surface is vital. Mutations in the vesicular

transport proteins FILAMIN A and ARFGEF2 lead to periventricular heterotopia, which is associated with a reduction in cell adhesion and a loss of the neuroependyma, and is sometimes accompanied by hydrocephalus (28, 77, 98). In the hydrocephalus with hop gait (*hyh*) mouse, hydrocephalus is accompanied by a denudation of the ependymal cell layer (14, 79, 105). Ependymal denudation of the SCO has been identified in cases of human hydrocephaly (25).

A mutation in the soluble NSF attachment protein α (α-Snap), which directs secretory vesicles to the apical cell surface, was found to be responsible for the *hyh* phenotype (19, 36). α-Snap is known to direct cell adhesion molecules, such as E-cadherin and β-catenin, to the apical surface of neural progenitors (9, 19, 76). In vel cells, non-muscle myosin II-B heavy chain (Nmhc-IIb) forms a mesh-like structure with N-cadherin and β-catenin at the apical surface, thus it is possible that α-Snap is involved with the localization of one or more of these structural components (FIGURE 2) (61). Similar to the *hyh* phenotype, the loss of Nmhc-IIb results in a loss of integrity in the neuroepithelium, leading to hydrocephalus and defects in neuronal cell migration (61, 104). This phenotype can be somewhat rescued by replacing the expression of Nmhc-IIb with Nmhc-IIa (7).

Mouse-Human SCO Differences and the Relationship to the Human Condition

CNS patterning is a highly conserved process underpinned by fundamental molecular pathways and interactions in all vertebrates. Moreover, select classes of transcription factors such as the bHLH, homeobox, and paired box family are key regulators of CNS development in metazoans. Taken together, it suggests that mouse models represent a powerful system in which to understand the etiology of hydrocephaly in humans. Indeed, the presence of the SCO/vel in even the earliest of vertebrates suggests a high degree of conservation in the expression of factors that regulate the development and functionality of these tissues, and one might predict that most of the factors identified in mice (e.g. Rfx3, Rfx4_v3) would be prime candidates to cause human hydrocephaly. Unfortunately, studies that implicate the SCO-related developmental transcriptional regulators as a direct cause for human hydrocephaly have not been forthcoming as of yet.

Despite the similarities in SCO development and function, there are controversies that surface when drawing parallels between human and mouse that arise from SCO morphological differences. Unlike most other vertebrates, in which the SCO remains fully differentiated and active throughout adulthood, the human SCO reaches its functional peak of glycoprotein secretion during embryonic development (88). During later embryonic stages and postnatally, the SCO begins to regress to the point where, by late childhood, secretion is limited to only a few remaining islets. Additionally, the glycoproteins secreted by the human SCO do not aggregate into RF nor do they immunoreact to antibodies raised against RF-glycoproteins in other mammals, indicative of some differences in the secretory role of the human SCO vs. that of the mouse (88). Indeed a pessimist would argue that these interspecies differences supersede the benefits of studying hydrocephaly in models where the SCO is implicated. Although the species-specific roles of the SCO present challenges to the field, the adult vel still contributes to hydrocephalus in both species. In this regard, shared vel signaling pathways or factors involved in ciliary structure and function should allow for meaningful comparisons to be made; however, these comparisons are rare and tenuous at best. For example, the gene for the human PAC1 receptor is located at 7p15. Although a link could be made to communicating hydrocephalus, only a single patient with a duplication of this region has been described (69). The gene for its ligand, PACAP, is located at 18p11, and congenital hydrocephalus is one of the symptoms experienced by patients with tetrasomy 18p (102). Similarly, HYDIN, located at 16q22, is a candidate for one case of human hydrocephaly (16). A large-scale genetic screen has also recently revealed that mutations in a human-specific HYDIN paralog located at 1q21 may contribute to a number of behavioral and congenital brain disorders, although hydrocephalus was present in only a small number of these patients (15). Additional comparisons between human and mouse are summarized in a recent review of the genetics of human hydrocephaly (112).

Although we have highlighted a role for many factors in the etiology of hydrocephaly in the mouse, human studies identifying causative genes are lagging far behind. One reason for this delay may evolve from the general nature of hydrocephaly itself. It is a very heterogeneous disorder and without the availability of large families for genetic studies it is difficult to group patients together for successful linkage analyses. Another consideration is that many of the animal studies describe the ablation of specific genes that may be embryonic or early postnatal lethal in humans. Alternatively, viable human mutations in the gene may result in subtler phenotypes with little or no penetrance of hydrocephaly. On the other hand, the identification of human genes should be studied in mice to further characterize the similarities and differences between the two species in disease development. In this regard, L1-CAM, an X-linked cell adhesion molecule important for neurite outgrowth, is the best characterized determinant of congenital human hydrocephaly, and mouse models have been shown to accurately recapitulate the human phenotype (44, 72, 90, 107). Overall, a combination of animal and human studies remains the best approach for disease gene identification.

Concluding Remarks

Collectively, these studies demonstrate that defects in multiple aspects of SCO cell function are implicated in the development of congenital hydrocephalus. As such, the new frontier for SCO research is clearly toward a further understanding of the molecular mechanisms governing SCO development and function. The plethora of genetic mouse models available is phenomenal and should continue to be extremely valuable for researchers in this field and in the hunt for causes of human hydrocephaly.

Developmental studies will continue to elucidate the hierarchical transcription factor organization that dictates the stage-specific differentiation of these cells and underlies the critical points of functional regulation. Defining these pathways will present researchers with candidate disease genes and opportunities to augment differentiation of progenitors toward a SCO fate to generate cell culture models. Similarly, a complete understanding of the signaling mechanisms between the CSF and SCO/vel cells should identify ligands that could be administered to promote glycoprotein secretion and restore CSF homeostasis. Finally, the use of high throughput approaches will enhance the knowledge of the important protein-protein interactions. For example, proteomic approaches have been used in the initial characterization of the secreted glycoproteins from the SCO and, more generally, for delineating the ciliary proteome (78). Interestingly, this proteomic study identified more than 600 proteins, of which over 200 were conserved between humans and *Chlamydomonas*, including a surprising number of proteins involved in signal transduction mechanisms (78). All of these approaches will increase our knowledge of SCO function and help elucidate where similarities to human hydrocephaly exist, thereby facilitating the characterization of genetic causes of congenital hydrocephalus. ■

This work was funded by Canadian Institute of Health grants MOP-14112 and MOP-53224 to D. J. Picketts. M. A. M. Todd was funded by a National Science and Engineering Research Council PGS-M award.

References

1. Ait-Lounis A, Baas D, Barras E, Benadiba C, Charollais A, Nlend Nlend R, Liegeois D, Meda P, Durand B, Reith W. Novel function of the ciliogenic transcription factor RFX3 in development of the endocrine pancreas. *Diabetes* 56: 950–959, 2007.
2. Baas D, Meiniel A, Benadiba C, Bonnafe E, Meiniel O, Reith W, Durand B. A deficiency in RFX3 causes hydrocephalus associated with abnormal differentiation of ependymal cells. *Eur J Neurosci* 24: 1020–1030, 2006.
3. Bach A, Lallemand Y, Nicola MA, Ramos C, Mathis L, Maufras M, Robert B. Msx1 is required for dorsal diencephalon patterning. *Development* 130: 4025–4036, 2003.
4. Badano JL, Mitsuma N, Beales PL, Katsanis N. The ciliopathies: an emerging class of human genetic disorders. *Annu Rev Genomics Hum Genet* 7: 125–148, 2006.
5. Banizs B, Komlosi P, Bevensee MO, Schwiebert EM, Bell PD, Yoder BK. Altered pH_i regulation and $Na^+/HCO3^-$ transporter activity in choroid plexus of cilia-defective Tg737(orpk) mutant mouse. *Am J Physiol Cell Physiol* 292: C1409–C1416, 2007.
6. Banizs B, Pike MM, Millican CL, Ferguson WB, Komlosi P, Sheetz J, Bell PD, Schwiebert EM, Yoder BK. Dysfunctional cilia lead to altered ependyma and choroid plexus function, and result in the formation of hydrocephalus. *Development* 132: 5329–5339, 2005.
7. Bao J, Ma X, Liu C, Adelstein RS. Replacement of nonmuscle myosin II-B with II-A rescues brain but not cardiac defects in mice. *J Biol Chem* 282: 22102–22111, 2007.
8. Barak O, Lazzaro MA, Lane WS, Speicher DW, Picketts DJ, Shiekhattar R. Isolation of human NURF: a regulator of Engrailed gene expression. *EMBO J* 22: 6089–6100, 2003.
9. Batiz LF, Paez P, Jimenez AJ, Rodriguez S, Wagner C, Perez-Figares JM, Rodriguez EM. Heterogeneous expression of hydrocephalic phenotype in the hyh mice carrying a point mutation in alpha-SNAP. *Neurobiol Dis* 23: 152–168, 2006.
10. Bermudez-Silva FJ, Leon-Quinto T, Martin F, Soria B, Nadal A, Perez J, Fernandez-Llebrez P. Bovine subcommissural organ displays spontaneous and synchronous intracellular calcium oscillations. *Brain Res* 977: 90–96, 2003.
11. Blackshear PJ, Graves JP, Stumpo DJ, Cobos I, Rubenstein JL, Zeldin DC. Graded phenotypic response to partial and complete deficiency of a brain-specific transcript variant of the winged helix transcription factor RFX4. *Development* 130: 4539–4552, 2003.
12. Bonnafe E, Touka M, AitLounis A, Baas D, Barras E, Ucla C, Moreau A, Flamant F, Dubruille R, Couble P, Collignon J, Durand B, Reith W. The transcription factor RFX3 directs nodal cilium development and left-right asymmetry specification. *Mol Cell Biol* 24: 4417–4427, 2004.
13. Brody SL, Yan XH, Wuerffel MK, Song SK, Shapiro SD. Ciliogenesis and left-right axis defects in forkhead factor HFH-4-null mice. *Am J Respir Cell Mol Biol* 23: 45–51, 2000.
14. Bronson RT, Lane PW. Hydrocephalus with hop gait (hyh): a new mutation on chromosome 7 in the mouse. *Brain Res Dev* 54: 131–136, 1990.
15. Brunetti-Pierri N, Berg JS, Scaglia F, Belmont J, Bacino CA, Sahoo T, Lalani SR, Graham B, Lee B, Shinawi M, Shen J, Kang SH, Pursley A, Lotze T, Kennedy G, Lansky-Shafer S, Weaver C, Roeder ER, Grebe TA, Arnold GL, Hutchison T, Reimschisel T, Amato S, Geragthy MT, Innis JW, Obersztyn E, Nowakowska B, Rosengren SS, Bader PI, Grange DK, Naqvi S, Garnica AD, Bernes SM, Fong CT, Summers A, Walters WD, Lupski JR, Stankiewicz P, Cheung SW, Patel A. Recurrent reciprocal 1q21.1 deletions and duplications associated with microcephaly or macrocephaly and developmental and behavioral abnormalities. *Nat Genet* 40: 1466–1471, 2008.
16. Callen DF, Baker EG, Lane SA. Re-evaluation of GM2346 from a del(16)(q22) to t(4;16)(q35;q22.1). *Clin Genet* 38: 466–468, 1990.
17. Catron KM, Wang H, Hu G, Shen MM, Abate-Shen C. Comparison of MSX-1 and MSX-2 suggests a molecular basis for functional redundancy. *Mech Dev* 55: 185–199, 1996.
18. Catron KM, Zhang H, Marshall SC, Inostroza JA, Wilson JM, Abate C. Transcriptional repression by Msx-1 does not require homeodomain DNA-binding sites. *Mol Cell Biol* 15: 861–871, 1995.
19. Chae TH, Kim S, Marz KE, Hanson PI, Walsh CA. The hyh mutation uncovers roles for alpha Snap in apical protein localization and control of neural cell fate. *Nat Genet* 36: 264–270, 2004.
20. Chen J, Knowles HJ, Hebert JL, Hackett BP. Mutation of the mouse hepatocyte nuclear factor/forkhead homologue 4 gene results in an absence of cilia and random left-right asymmetry. *J Clin Invest* 102: 1077–1082, 1998.
21. Chilvers MA, Rutman A, O'Callaghan C. Ciliary beat pattern is associated with specific ultrastructural defects in primary ciliary dyskinesia. *J Allergy Clin Immunol* 112: 518–524, 2003.
22. Davy BE, Robinson ML. Congenital hydrocephalus in hy3 mice is caused by a frameshift mutation in Hydin, a large novel gene. *Hum Mol Genet* 12: 1163–1170, 2003.
23. Dawe HR, Shaw MK, Farr H, Gull K. The hydrocephalus inducing gene product, Hydin, positions axonemal central pair microtubules. *BMC Biol* 5: 33, 2007.

24. Dietrich P, Shanmugasundaram R, Shuyu E, Dragatsis I. Congenital hydrocephalus associated with abnormal subcommissural organ in mice lacking huntingtin in Wnt1 cell lineages. *Hum Mol Genet* 18: 142–150, 2009.

25. Dominguez-Pinos MD, Paez P, Jimenez AJ, Weil B, Arraez MA, Perez-Figares JM, Rodriguez EM. Ependymal denudation and alterations of the subventricular zone occur in human fetuses with a moderate communicating hydrocephalus. *J Neuropathol Exp Neurol* 64: 595–604, 2005.

26. Dubruille R, Laurencon A, Vandaele C, Shishido E, Coulon-Bublex M, Swoboda P, Couble P, Kernan M, Durand B. *Drosophila* regulatory factor X is necessary for ciliated sensory neuron differentiation. *Development* 129: 5487–5498, 2002.

27. Estivill-Torrus G, Vitalis T, Fernandez-Llebrez P, Price DJ. The transcription factor Pax6 is required for development of the diencephalic dorsal midline secretory radial glia that form the subcommissural organ. *Mech Dev* 109: 215–224, 2001.

28. Ferland RJ, Batiz LF, Neal J, Lian G, Bundock E, Lu J, Hsiao YC, Diamond R, Mei D, Banham AH, Brown PJ, Vanderburg CR, Joseph J, Hecht JL, Folkerth R, Guerrini R, Walsh CA, Rodriguez EM, Sheen VL. Disruption of neural progenitors along the ventricular and subventricular zones in periventricular heterotopia. *Hum Mol Genet* 18: 497–516, 2009.

29. Fernandez-Llebrez P, Grondona JM, Perez J, Lopez-Aranda MF, Estivill-Torrus G, Llebrez-Zayas PF, Soriano E, Ramos C, Lallemand Y, Bach A, Robert B. Msx1-deficient mice fail to form prosomere 1 derivatives, subcommissural organ, and posterior commissure and develop hydrocephalus. *J Neuropathol Exp Neurol* 63: 574–586, 2004.

30. Fliegauf M, Benzing T, Omran H. When cilia go bad: cilia defects and ciliopathies. *Nat Rev Mol Cell Biol* 8: 880–893, 2007.

31. Furuta Y, Piston DW, Hogan BL. Bone morphogenetic proteins (BMPs) as regulators of dorsal forebrain development. *Development* 124: 2203–2212, 1997.

32. Galarza M. Evidence of the subcommissural organ in humans and its association with hydrocephalus. *Neurosurg Rev* 25: 205–215, 2002.

33. Garcia-Diaz M, Bebenek K, Gao G, Pedersen LC, London RE, Kunkel TA. Structure-function studies of DNA polymerase lambda. *DNA Repair (Amst)* 4: 1358–1367, 2005.

34. Gopal SC, Sharma V, Chansuria JP, Gangopadhyaya AN, Singh TB. Serotonin and 5-hydroxy indole acetic acid in infantile hydrocephalus. *Pediatr Surg Int* 23: 571–574, 2007.

35. Haycraft CJ, Schafer JC, Zhang Q, Taulman PD, Yoder BK. Identification of CHE-13, a novel intraflagellar transport protein required for cilia formation. *Exp Cell Res* 284: 251–263, 2003.

36. Hong HK, Chakravarti A, Takahashi JS. The gene for soluble N-ethylmaleimide sensitive factor attachment protein alpha is mutated in hydrocephaly with hop gait (hyh) mice. *Proc Natl Acad Sci USA* 101: 1748–1753, 2004.

37. Hornef N, Olbrich H, Horvath J, Zariwala MA, Fliegauf M, Loges NT, Wildhaber J, Noone PG, Kennedy M, Antonarakis SE, Blouin JL, Bartoloni L, Nusslein T, Ahrens P, Griese M, Kuhl H, Sudbrak R, Knowles MR, Reinhardt R, Omran H. DNAH5 mutations are a common cause of primary ciliary dyskinesia with outer dynein arm defects. *Am J Respir Crit Care Med* 174: 120–126, 2006.

38. Houzelstein D, Cohen A, Buckingham ME, Robert B. Insertional mutation of the mouse Msx1 homeobox gene by an nlacZ reporter gene. *Mech Dev* 65: 123–133, 1997.

39. Ibanez-Tallon I, Gorokhova S, Heintz N. Loss of function of axonemal dynein Mdnah5 causes primary ciliary dyskinesia and hydrocephalus. *Hum Mol Genet* 11: 715–721, 2002.

40. Ibanez-Tallon I, Heintz N, Omran H. To beat or not to beat: roles of cilia in development and disease. *Hum Mol Genet* 12, *Spec No* 1: R27–R35, 2003.

41. Ibanez-Tallon I, Pagenstecher A, Fliegauf M, Olbrich H, Kispert A, Ketelsen UP, North A, Heintz N, Omran H. Dysfunction of axonemal dynein heavy chain Mdnah5 inhibits ependymal flow and reveals a novel mechanism for hydrocephalus formation. *Hum Mol Genet* 13: 2133–2141, 2004.

42. Jimenez AJ, Fernandez-Llebrez P, Perez-Figares JM. Neural input and neural control of the subcommissural organ. *Microsc Res Tech* 52: 520–533, 2001.

43. Jones HC, Yehia B, Chen GF, Carter BJ. Genetic analysis of inherited hydrocephalus in a rat model. *Exp Neurol* 190: 79–90, 2004.

44. Jouet M, Rosenthal A, MacFarlane J, Kenwrick S, Donnai D. A missense mutation confirms the L1 defect in X-linked hydrocephalus (HSAS). *Nat Genet* 4: 331, 1993.

45. Katan-Khaykovich Y, Shaul Y. RFX1, a single DNA-binding protein with a split dimerization domain, generates alternative complexes. *J Biol Chem* 273: 24504–24512, 1998.

46. Kinoshita M, Takeda S. Connecting the dots between septins and the DNA damage checkpoint. *Cell* 130: 777–779, 2007.

47. Kobayashi Y, Watanabe M, Okada Y, Sawa H, Takai H, Nakanishi M, Kawase Y, Suzuki H, Nagashima K, Ikeda K, Motoyama N. Hydrocephalus, situs inversus, chronic sinusitis, and male infertility in DNA polymerase lambda-deficient mice: possible implication for the pathogenesis of immotile cilia syndrome. *Mol Cell Biol* 22: 2769–2776, 2002.

48. Krebs DL, Metcalf D, Merson TD, Voss AK, Thomas T, Zhang JG, Rakar S, O'Bryan MK, Willson TA, Viney EM, Mielke LA, Nicola NA, Hilton DJ, Alexander WS. Development of hydrocephalus in mice lacking SOCS7. *Proc Natl Acad Sci USA* 101: 15446–15451, 2004.

49. Kremer BE, Adang LA, Macara IG. Septins regulate actin organization and cell-cycle arrest through nuclear accumulation of NCK mediated by SOCS7. *Cell* 130: 837–850, 2007.

50. Lang B, Song B, Davidson W, MacKenzie A, Smith N, McCaig CD, Harmar AJ, Shen S. Expression of the human PAC1 receptor leads to dose-dependent hydrocephalus-related abnormalities in mice. *J Clin Invest* 116: 1924–1934, 2006.

51. Larsen L, Ropke C. Suppressors of cytokine signalling: SOCS. *APMIS* 110: 833–844, 2002.

52. Laurencon A, Dubruille R, Efimenko E, Grenier G, Bissett R, Cortier E, Rolland V, Swoboda P, Durand B. Identification of novel regulatory factor X (RFX) target genes by comparative genomics in *Drosophila* species. *Genome Biol* 8: R195, 2007.

53. Lechtreck KF, Delmotte P, Robinson ML, Sanderson MJ, Witman GB. Mutations in Hydin impair ciliary motility in mice. *J Cell Biol* 180: 633–643, 2008.

54. Lechtreck KF, Witman GB. Chlamydomonas reinhardtii hydin is a central pair protein required for flagellar motility. *J Cell Biol* 176: 473–482, 2007.

55. Lee L, Campagna DR, Pinkus JL, Mulhern H, Wyatt TA, Sisson JH, Pavlik JA, Pinkus GS, Fleming MD. Primary ciliary dyskinesia in mice lacking the novel ciliary protein Pcdp1. *Mol Cell Biol* 28: 949–957, 2008.

56. Leger L, Degueurce A, Lundberg JJ, Pujol JF, Mollgard K. Origin and influence of the serotoninergic innervation of the subcommissural organ in the rat. *Neuroscience* 10: 411–423, 1983.

57. Lehman JM, Michaud EJ, Schoeb TR, Aydin-Son Y, Miller M, Yoder BK. The Oak Ridge Polycystic Kidney mouse: modeling ciliopathies of mice and men. *Dev Dyn* 237: 1960–1971, 2008.

58. Liem KF Jr, Tremml G, Jessell TM. A role for the roof plate and its resident TGFbeta-related proteins in neuronal patterning in the dorsal spinal cord. *Cell* 91: 127–138, 1997.

59. Liem KF Jr, Tremml G, Roelink H, Jessell TM. Dorsal differentiation of neural plate cells induced by BMP-mediated signals from epidermal ectoderm. *Cell* 82: 969–979, 1995.

60. Louvi A, Wassef M. Ectopic engrailed 1 expression in the dorsal midline causes cell death, abnormal differentiation of circumventricular organs and errors in axonal pathfinding. *Development* 127: 4061–4071, 2000.

61. Ma X, Bao J, Adelstein RS. Loss of cell adhesion causes hydrocephalus in nonmuscle myosin II-B-ablated and mutated mice. *Mol Biol Cell* 18: 2305–2312, 2007.

62. Makiyama Y, Shoji S, Mizusawa H. Hydrocephalus in the Otx2$^{+/-}$ mutant mouse. *Exp Neurol* 148: 215–221, 1997.

63. Martens N, Uzan G, Wery M, Hooghe R, Hooghe-Peters EL, Gertler A. Suppressor of cytokine signaling 7 inhibits prolactin, growth hormone, and leptin signaling by interacting with STAT5 or STAT3 and attenuating their nuclear translocation. *J Biol Chem* 280: 13817–13823, 2005.

64. Martens N, Wery M, Wang P, Braet F, Gertler A, Hooghe R, Vandenhaute J, Hooghe-Peters EL. The suppressor of cytokine signaling (SOCS)-7 interacts with the actin cytoskeleton through vinexin. *Exp Cell Res* 298: 239–248, 2004.

65. Martinez-Penay, Valenzuela I, Carmona-Calero EM, Perez-Gonzalez H, Ormazabal-Ramos C, Fernandez-Rodriguez P, Gonzalez-Marrero I, Castaneyra-Perdomo A, Ferres-Torres R. Alterations of the cerebrospinal fluid proteins and subcommissural organ secretion in the arterial hypertension and ventricular dilatation A study in SHR rats. *Histol Histopathol* 21: 179–185, 2006.

66. Masmoudi-Kouki O, Gandolfo P, Castel H, Leprince J, Fournier A, Dejda A, Vaudry H, Tonon MC. Role of PACAP and VIP in astroglial functions. *Peptides* 28: 1753–1760, 2007.

67. Meiniel O, Meiniel A. The complex multidomain organization of SCO-spondin protein is highly conserved in mammals. *Brain Res Rev* 53: 321–327, 2007.

68. Meiniel O, Meiniel R, Lalloue F, Didier R, Jauberteau MO, Meiniel A, Petit D. The lengthening of a giant protein: when, how, and why? *J Mol Evol* 66: 1–10, 2008.

69. Miller M, Kaufman G, Reed G, Bilenker R, Schinzel A. Familial, balanced insertional translocation of chromosome 7 leading to offspring with deletion and duplication of the inserted segment, 7p15 leads to 7p21. *Am J Med Genet* 4: 323–332, 1979.

70. Mollgard K, Lundberg JJ, Wiklund L, Lachenmayer L, Baumgarten HG. Morphologic consequences of serotonin neurotoxin administration: neuron-target cell interaction in the rat subcommissural organ. *Ann NY Acad Sci* 305: 262–288, 1978.

71. Morotomi-Yano K, Yano K, Saito H, Sun Z, Iwama A, Miki Y. Human regulatory factor X 4 (RFX4) is a testis-specific dimeric DNA-binding protein that cooperates with other human RFX members. *J Biol Chem* 277: 836–842, 2002.

72. Nagaraj K, Hortsch M. Phosphorylation of L1-type cell-adhesion molecules: ankyrins away! *Trends Biochem Sci* 31: 544–546, 2006.

73. Neves SR, Ram PT, Iyengar R. G protein pathways. *Science* 296: 1636–1639, 2002.

74. Nurnberger F, Schoniger S. Presence and functional significance of neuropeptide and neurotransmitter receptors in subcommissural organ cells. *Microsc Res Tech* 52: 534–540, 2001.

75. Olbrich H, Haffner K, Kispert A, Volkel A, Volz A, Sasmaz G, Reinhardt R, Hennig S, Lehrach H, Konietzko N, Zariwala M, Noone PG, Knowles M, Mitchison HM, Meeks M, Chung EM, Hildebrandt F, Sudbrak R, Omran H. Mutations in DNAH5 cause primary ciliary dyskinesia and randomization of left-right asymmetry. *Nat Genet* 30: 143–144, 2002.

76. Paez P, Batiz LF, Roales-Bujan R, Rodriguez-Perez LM, Rodriguez S, Jimenez AJ, Rodriguez EM, Perez-Figares JM. Patterned neuropathologic events occurring in hyh congenital hydrocephalic mutant mice. *J Neuropathol Exp Neurol* 66: 1082–1092, 2007.

77. Parrini E, Ramazzotti A, Dobyns WB, Mei D, Moro F, Veggiotti P, Marini C, Brilstra EH, Dalla Bernardina B, Goodwin L, Bodell A, Jones MC, Nangeroni M, Palmeri S, Said E, Sander JW, Striano P, Takahashi Y, Van Maldergem L, Leonardi G, Wright M, Walsh CA, Guerrini R. Periventricular heterotopia: phenotypic heterogeneity and correlation with Filamin A mutations. *Brain* 129: 1892–1906, 2006.

78. Pazour GJ, Agrin N, Leszyk J, Witman GB. Proteomic analysis of a eukaryotic cilium. *J Cell Biol* 170: 103–113, 2005.

79. Perez-Figares JM, Jimenez AJ, Perez-Martin M, Fernandez-Llebrez P, Cifuentes M, Riera P, Rodriguez S, Rodriguez EM. Spontaneous congenital hydrocephalus in the mutant mouse hyh. Changes in the ventricular system and the subcommissural organ. *J Neuropathol Exp Neurol* 57: 188–202, 1998.

80. Perez-Figares JM, Jimenez AJ, Rodriguez EM. Subcommissural organ, cerebrospinal fluid circulation, and hydrocephalus. *Microsc Res Tech* 52: 591–607, 2001.

81. Picketts DJ. Neuropeptide signaling and hydrocephalus: SCO with the flow. *J Clin Invest* 116: 1828–1832, 2006.

82. Piessevaux J, Lavens D, Montoye T, Wauman J, Catteeuw D, Vandekerckhove J, Belsham D, Peelman F, Tavernier J. Functional cross-modulation between SOCS proteins can stimulate cytokine signaling. *J Biol Chem* 281: 32953–32966, 2006.

83. Ponting CP. A novel domain suggests a ciliary function for ASPM, a brain size determining gene. *Bioinformatics* 22: 1031–1035, 2006.

84. Ramos C, Fernandez-Llebrez P, Bach A, Robert B, Soriano E. Msx1 disruption leads to diencephalon defects and hydrocephalus. *Dev Dyn* 230: 446–460, 2004.

85. Ramos C, Robert B. Msh/Msx gene family in neural development. *Trends Genet* 21: 624–632, 2005.

86. Reith W, Ucla C, Barras E, Gaud A, Durand B, Herrero-Sanchez C, Kobr M, Mach B. RFX1, a transactivator of hepatitis B virus enhancer I, belongs to a novel family of homodimeric and heterodimeric DNA-binding proteins. *Mol Cell Biol* 14: 1230–1244, 1994.

87. Richter HG, Tome MM, Yulis CR, Vio KJ, Jimenez AJ, Perez-Figares JM, Rodriguez EM. Transcription of SCO-spondin in the subcommissural organ: evidence for down-regulation mediated by serotonin. *Brain Res Mol Brain Res* 129: 151–162, 2004.

88. Rodriguez EM, Oksche A, Montecinos H. Human subcommissural organ, with particular emphasis on its secretory activity during the fetal life. *Microsc Res Tech* 52: 573–590, 2001.

89. Rodriguez EM, Rodriguez S, Hein S. The subcommissural organ. *Microsc Res Tech* 41: 98–123, 1998.

90. Rolf B, Kutsche M, Bartsch U. Severe hydrocephalus in L1-deficient mice. *Brain Res* 891: 247–252, 2001.

91. Rosenbaum JL, Witman GB. Intraflagellar transport. *Nat Rev Mol Cell Biol* 3: 813–825, 2002.

92. Saha SG, Jain MR, Subhedar N. Subcommissural organ-Reissner's fiber complex of the teleost Clarias batrachus responds to GABA treatment. *Brain Res* 852: 335–343, 2000.

93. Sapiro R, Kostetskii I, Olds-Clarke P, Gerton GL, Radice GL, Strauss IJ. Male infertility, impaired sperm motility, and hydrocephalus in mice deficient in sperm-associated antigen 6. *Mol Cell Biol* 22: 6298–6305, 2002.

94. Schoniger S, Kopp MD, Schomerus C, Maronde E, Dehghani F, Meiniel A, Rodriguez M, Korf HW, Nurnberger F. Effects of neuroactive substances on the activity of subcommissural organ cells in dispersed cell and explant cultures. *Cell Tissue Res* 307: 101–114, 2002.

95. Schoniger S, Maronde E, Kopp MD, Korf HW, Nurnberger F. Transcription factor CREB and its stimulus-dependent phosphorylation in cell and explant cultures of the bovine subcommissural organ. *Cell Tissue Res* 308: 131–142, 2002.

96. Semenza GL, Wang GL, Kundu R. DNA binding and transcriptional properties of wild-type and mutant forms of the homeodomain protein Msx2. *Biochem Biophys Res Commun* 209: 257–262, 1995.

97. Senti G, Swoboda P. Distinct isoforms of the RFX transcription factor DAF-19 regulate ciliogenesis and maintenance of synaptic activity. *Mol Biol Cell* 19: 5517–5528, 2008.

98. Sheen VL, Basel-Vanagaite L, Goodman JR, Scheffer IE, Bodell A, Ganesh VS, Ravenscroft R, Hill RS, Cherry TJ, Shugart YY, Barkovich J, Straussberg R, Walsh CA. Etiological heterogeneity of familial periventricular heterotopia and hydrocephalus. *Brain Dev* 26: 326–334, 2004.

99. Somera KC, Jones HC. Reduced subcommissural organ glycoprotein immunoreactivity precedes aqueduct closure and ventricular dilatation in H-Tx rat hydrocephalus. *Cell Tissue Res* 315: 361–373, 2004.

100. Sweger EJ, Casper KB, Scearce-Levie K, Conklin BR, McCarthy KD. Development of hydrocephalus in mice expressing the G(i)-coupled GPCR Ro1 RASSL receptor in astrocytes. *J Neurosci* 27: 2309–2317, 2007.

101. Swoboda P, Adler HT, Thomas JH. The RFX-type transcription factor DAF-19 regulates sensory neuron cilium formation in *C. elegans*. *Mol Cell* 5: 411–421, 2000.

102. Takeda K, Okamura T, Hasegawa T. Sibs with tetrasomy 18p born to a mother with trisomy 18p. *J Med Genet* 26: 195–197, 1989.

103. Tome M, Jimenez AJ, Richter H, Vio K, Bermudez-Silva FJ, Rodriguez EM, Perez-Figares JM. The subcommissural organ expresses D2, D3, D4, and D5 dopamine receptors. *Cell Tissue Res* 317: 65–77, 2004.

104. Tullio AN, Bridgman PC, Tresser NJ, Chan CC, Conti MA, Adelstein RS, Hara Y. Structural abnormalities develop in the brain after ablation of the gene encoding nonmuscle myosin II-B heavy chain. *J Comp Neurol* 433: 62–74, 2001.

105. Wagner C, Batiz LF, Rodriguez S, Jimenez AJ, Paez P, Tome M, Perez-Figares JM, Rodriguez EM. Cellular mechanisms involved in the stenosis and obliteration of the cerebral aqueduct of hyh mutant mice developing congenital hydrocephalus. *J Neuropathol Exp Neurol* 62: 1019–1040, 2003.

106. Waschek JA, Casillas RA, Nguyen TB, DiCicco-Bloom EM, Carpenter EM, Rodriguez WI. Neural tube expression of pituitary adenylate cyclase-activating peptide (PACAP) and receptor: potential role in patterning and neurogenesis. *Proc Natl Acad Sci USA* 95: 9602–9607, 1998.

107. Weller S, Gartner J. Genetic and clinical aspects of X-linked hydrocephalus (L1 disease): mutations in the L1CAM gene. *Hum Mutat* 18: 1–12, 2001.

108. Yu X, Ng CP, Habacher H, Roy S. Foxj1 transcription factors are master regulators of the motile ciliogenic program. *Nat Genet* 40: 1445–1453, 2008.

109. Zariwala MA, Knowles MR, Omran H. Genetic defects in ciliary structure and function. *Annu Rev Physiol* 69: 423–450, 2007.

110. Zhang D, Stumpo DJ, Graves JP, DeGraff LM, Grissom SF, Collins JB, Li L, Zeldin DC, Blackshear PJ. Identification of potential target genes for RFX4_v3, a transcription factor critical for brain development. *J Neurochem* 98: 860–875, 2006.

111. Zhang H, Catron KM, Abate-Shen C. A role for the Msx-1 homeodomain in transcriptional regulation: residues in the N-terminal arm mediate TATA binding protein interaction and transcriptional repression. *Proc Natl Acad Sci USA* 93: 1764–1769, 1996.

112. Zhang J, Williams MA, Rigamonti D. Genetics of human hydrocephalus. *J Neurol* 253: 1255–1266, 2006.

113. Zhang Z, Jones BH, Tang W, Moss SB, Wei Z, Ho C, Pollack M, Horowitz E, Bennett J, Baker ME, Strauss JF 3rd. Dissecting the axoneme interactome: the mammalian orthologue of *Chlamydomonas* PF6 interacts with sperm-associated antigen 6, the mammalian orthologue of *Chlamydomonas* PF16. *Mol Cell Proteomics* 4: 914–923, 2005.

114. Zhang Z, Kostetskii I, Moss SB, Jones BH, Ho C, Wang H, Kishida T, Gerton GL, Radice GL, Strauss JF 3rd. Haploinsufficiency for the murine orthologue of *Chlamydomonas* PF20 disrupts spermatogenesis. *Proc Natl Acad Sci USA* 101: 12946–12951, 2004.

115. Zhang Z, Kostetskii I, Tang W, Haig-Ladewig L, Sapiro R, Wei Z, Patel AM, Bennett J, Gerton GL, Moss SB, Radice GL, Strauss JF 3rd. Deficiency of SPAG16L causes male infertility associated with impaired sperm motility. *Biol Reprod* 74: 751–759, 2006.

116. Zhang Z, Tang W, Zhou R, Shen X, Wei Z, Patel AM, Povlishock JT, Bennett J, Strauss JF 3rd. Accelerated mortality from hydrocephalus and pneumonia in mice with a combined deficiency of SPAG6 and SPAG16L reveals a functional interrelationship between the two central apparatus proteins. *Cell Motil Cytoskeleton* 64: 360–376, 2007.

APPENDIX D

Snf2h-mediated chromatin organization and histone H1 dynamics govern cerebellar morphogenesis and neural maturation

Purpose

To understand the role and contribution of Snf2h/Smarca5 towards Purkinje and granular neuronal cell maturation during cerebellar development.

Submission Information

Submitted: 12 February 2014
Accepted: 15 May 2014
Published: 20 June 2014

Contribution of Co-Authors

Matthew A.M. Todd performed molecular cloning of the SNF2L/SMARCA1 and SNF2H/SMARCA5 pBrit-LoxP-NTAP and -CTAP tagged constructs.

Matias Alvarez-Saavedra designed, interpreted and executed all experiments. David J. Picketts supervised the project. Keqin Yan, Emile Hashem, Danton Ivanochko, and Michael S. Huh provided technical support. Pamela L. Lagali and Chelsea P. Corcoran helped establish the breeding colony and made some preliminary phenotypic observations with the Snf2h cKO-Nes mice. Yves De Repentigny and Rashmi Kothary performed and analysed the TEM experiments. Edupuganti V.S. Raghu Ram and Eran Meshorer performed and analysed FRAP experiments. Alan J. Mears, Erin Bassett, Nicholas Tokarew, and Valerie A. Wallace performed and analysed in situ hybridizations and microarrays. Doo Yang and Ilya Ioshikhes provided bioinformatics support. $Snf2h^{fl/fl}$ and $Snf2h^{+/-}$ mice were generated and provided by Tomas Stopka, Juraj Kokavec, Romit Majumder, and Arthur I. Skoultchi. The paper was written by Matias Alvarez-Saavedra and David J. Picketts.

nature COMMUNICATIONS

ARTICLE

Received 12 Feb 2014 | Accepted 15 May 2014 | Published 20 Jun 2014

DOI: 10.1038/ncomms5181 OPEN

Snf2h-mediated chromatin organization and histone H1 dynamics govern cerebellar morphogenesis and neural maturation

Matías Alvarez-Saavedra[1,2], Yves De Repentigny[1], Pamela S. Lagali[1], Edupuganti V.S. Raghu Ram[3], Keqin Yan[1], Emile Hashem[1,2], Danton Ivanochko[1,4], Michael S. Huh[1], Doo Yang[4,5], Alan J. Mears[6], Matthew A.M. Todd[1,4], Chelsea P. Corcoran[1], Erin A. Bassett[4], Nicholas J.A. Tokarew[4], Juraj Kokavec[7], Romit Majumder[8], Ilya Ioshikhes[4,5], Valerie A. Wallace[4,6], Rashmi Kothary[1,2], Eran Meshorer[3], Tomas Stopka[7], Arthur I. Skoultchi[8] & David J. Picketts[1,2,4]

Chromatin compaction mediates progenitor to post-mitotic cell transitions and modulates gene expression programs, yet the mechanisms are poorly defined. Snf2h and Snf2l are ATP-dependent chromatin remodelling proteins that assemble, reposition and space nucleosomes, and are robustly expressed in the brain. Here we show that mice conditionally inactivated for *Snf2h* in neural progenitors have reduced levels of histone H1 and H2A variants that compromise chromatin fluidity and transcriptional programs within the developing cerebellum. Disorganized chromatin limits Purkinje and granule neuron progenitor expansion, resulting in abnormal post-natal foliation, while deregulated transcriptional programs contribute to altered neural maturation, motor dysfunction and death. However, mice survive to young adulthood, in part from *Snf2l* compensation that restores *Engrailed-1* expression. Similarly, Purkinje-specific *Snf2h* ablation affects chromatin ultrastructure and dendritic arborization, but alters cognitive skills rather than motor control. Our studies reveal that *Snf2h* controls chromatin organization and histone H1 dynamics for the establishment of gene expression programs underlying cerebellar morphogenesis and neural maturation.

[1] Regenerative Medicine Program, Ottawa Hospital Research Institute, Ottawa, Ontario, Canada K1H 8L6. [2] Department of Cellular and Molecular Medicine, University of Ottawa, Ottawa, Ontario, Canada K1H 8M5. [3] Department of Genetics, The Alexander Silberman Institute of Life Sciences, The Hebrew University of Jerusalem, Jerusalem 91904, Israel. [4] Department of Biochemistry, Microbiology and Immunology, University of Ottawa, Ottawa, Ontario, Canada K1H 8M5. [5] Institute of Systems Biology, University of Ottawa, Ottawa, Ontario, Canada K1H 8M5. [6] Vision Program, Ottawa Hospital Research Institute, Ottawa, Ontario, Canada K1H 8L6. [7] Institute of Pathologic Physiology, First Faculty of Medicine, Charles University in Prague, Prague 12853, Czech Republic. [8] Department of Cell Biology, Albert Einstein College of Medicine, Bronx, New York 10461, USA . Correspondence and requests for materials should be addressed to D.J.P. (email: dpicketts@ohri.ca).

The importance of epigenetic regulation to brain development is recognized by the increasing number of developmental disorders caused by mutations in genes that encode proteins that modify or remodel chromatin structure[1]. Nonetheless, discerning precise mechanisms has proven challenging since these proteins impact all nuclear processes from transcription and replication to higher-order chromatin compaction. Genome-wide epigenetic profiling experiments have supported the hypothesis that neurogenesis is accompanied by the transition of a highly dynamic chromatin environment within progenitor cells to a more restrictive epigenetic landscape that dictates gene expression programs specific to each lineage[2,3]. Chromatin restriction involves the expansion of repressive histone marks such as H3K9Me3 and H3K27Me3, increased DNA methylation and a reduction in the distribution of the histone variant H2A.Z within gene bodies slated for silencing[4,5]. Concomitant with these histone and DNA modifications, chromatin compaction also requires regular nucleosome spacing and the inclusion of the linker histone H1[6,7].

The repositioning of nucleosomes is catalysed by evolutionarily conserved multiprotein chromatin remodelling complexes (CRCs) that include a SNF2-domain containing catalytic subunit related to the Swi2/Snf2 family[8]. One such class of ATP-dependent nucleosome remodellers is the ISWI family, first identified in yeast[9]. Mammals have two ISWI homologues *SNF2H* (*SNF2 homologue*; human *SMARCA5)* and *SNF2L* (*SNF2-like*; human *SMARCA1*) that are the orthologs of yeast *Isw1* and *Isw2* genes[10]. ISWI can assemble regularly spaced nucleosomal arrays *in vitro* alone, or within a diverse number of protein complexes many of which contain a BAZ-family transcription factor (TF)[11]. ISWI complexes regulate many nuclear processes including DNA replication and repair (ACF, CHRAC and WICH), transcriptional regulation (NURF, RSF and CERF), and nucleolar structure and function (NoRC)[11]. ISWI inactivation in *Drosophila* also highlighted a role in higher-order chromatin structure[12]. However, despite a good understanding of the *in vitro* biochemical properties of ISWI and its related complexes, their *in vivo* roles remain poorly characterized.

In the murine central nervous system (CNS), *Snf2h* and *Snf2l* display dynamic patterns of expression, where *Snf2h* expression peaks in neuronal progenitors, while *Snf2l* is expressed predominantly in terminally differentiated neurons[10]. For this reason, we postulated that Snf2h and Snf2l might regulate the transition from a progenitor to a differentiated neuron to restrict and compact chromatin while poising other genes for expression. In this regard, catalytically inactive *Snf2l* mice exhibit hypercellularity of cortical progenitors and delayed their differentiation, resulting in a larger brain[13]. However, *Snf2h* knockout (KO) mice die at the peri-implantation stage due to growth arrest of the trophoectoderm and inner cell mass, thereby preventing the study of Snf2h during brain development[14]. To overcome this problem we describe the generation of an *Snf2h*-targeted allele that facilitated its characterization throughout mouse brain development. Our studies reveal that *Snf2h* controls higher-order chromatin organization to mediate the establishment of gene expression programs underlying cerebellar morphogenesis and neural maturation.

Results

Snf2h and Snf2l are developmentally regulated in the cerebellum. The closely related mammalian ISWI genes, *Snf2h* and *Snf2l*, display complementary expression patterns that suggest they have distinct roles during tissue development[10]. Embryonic brain mRNA and protein expression analyses reveals that Snf2h is robustly expressed in the developing rhombic lip, similarly to the hindbrain patterning TFs Engrailed-1 (En1) and Engrailed-2 (En2), whereas Snf2l expression was not detected within the rhombic lip at embryonic day (E) 14.5 (Fig. 1a–e). During late embryonic development, we observed robust Snf2h expression in developing Purkinje cells (PCs; Fig. 1f), mature PCs (Fig. 1g,i) and in nearly all NeuroD1+ neural lineages (Fig. 1h and Supplementary Fig. 1a,b). In contrast, Snf2l expression was prominent only within PCs after P7 (Fig. 1i and Supplementary Fig. 1c). Immunoblots of hindbrain and cerebellar extracts demonstrated that Snf2h levels peaked during the period of granule neuron progenitor (GNP) proliferation (~E18 to P7), whereas Snf2l levels increased as a function of cerebellar maturity with peak expression after ~P10 (Fig. 1j,k). Interestingly, Snf2h downregulation after P7 coincides with En1 downregulation, whereas En2 expression is robust throughout cerebellar development (Fig. 1j,k). Expression of all proteins was maintained in adulthood, albeit at lower levels (Fig. 1j,k). We conclude that Snf2h is robustly expressed in hindbrain progenitors while Snf2h and Snf2l protein levels are dynamically modulated during post-natal development.

Generation and characterization of Snf2h cKO mice. To investigate the significance of ISWI expression changes within the cerebellum we proceeded to generate *Snf2h* conditional KO mice since *Snf2h* germline KO mice die at the peri-implantation stage[14]. We inserted loxP sites flanking exon 5, which encodes the evolutionarily conserved ATP-binding pocket critical for remodelling activity (Fig. 2a,b)[15]. $Snf2h^{-/fl}$ mice were bred with a Nestin-Cre driver line that demonstrated Cre expression in neural progenitors by ~E11 and displayed robust Cre activity in cerebellar progenitors during the early post-natal period (Supplementary Fig. 2)[16]. $Snf2h^{-/fl}$::Nestin-$Cre^{-/+}$ conditional KO mice (*Snf2h* cKO-Nes hereon) were born at normal Mendelian ratios, but had a significant reduction in body weight by P7 (Fig. 2c), and were approximately half the size of control littermates by P20 (Fig. 2d). Brains isolated from these animals were reduced in size with striking cerebellar hypoplasia by P40 (Fig. 2e). Immunoblots of P0 cerebellar extracts confirmed an ~90% reduction in Snf2h protein levels (Fig. 2f). Three different behavioural assays demonstrated that *Snf2h* cKO mice have severe motor defects (Fig. 2g). We observed ataxia-like symptoms that began at ~P10, became severe by ~P15 to P20 and clearly contributed to the premature death of *Snf2h* cKO animals by ~P25 to P40 (Fig. 2h and Supplementary Movies 1–5). Concomitantly, $Snf2h^{-/fl}$ mice bred onto our $Snf2l^{-/Y}$ line were then crossed with the Nestin-Cre driver line to generate animals deficient for both ISWI genes (Snf2h and Snf2l)[13]. However, these cDKO-Nes mice did not survive past birth (Fig. 2h).

To further elucidate the contribution of Snf2h to cerebellar function, we generated a second strain of *Snf2h* cKO mice using the PCP2-Cre driver line that becomes active specifically in post-mitotic PCs after P10 (ref. 17; Supplementary Fig. 3). *Snf2h* cKO-PCP2 and cDKO-PCP2 were both born at normal Mendelian ratios and survived into adulthood (Fig. 2h). As such, we assessed the performance of *Snf2h* cKO-PCP2 animals in a cohort of motor and cognitive behavioural assays. We observed an enhanced performance in the rotating rotarod (Fig. 2i), but no additional alterations in motor control or spatial learning (Supplementary Fig. 4). In the fear-conditioning assay, the mice are exposed to a novel cue (cue tone), followed by a foot-shock (context), and the 'fear' response is measured (conditional response)[18]. *Snf2h* cKO-PCP2 mice had a normal response to the cue tone, but a reduced response to the context, suggestive of impaired associative learning skills (Fig. 2j). The social interaction

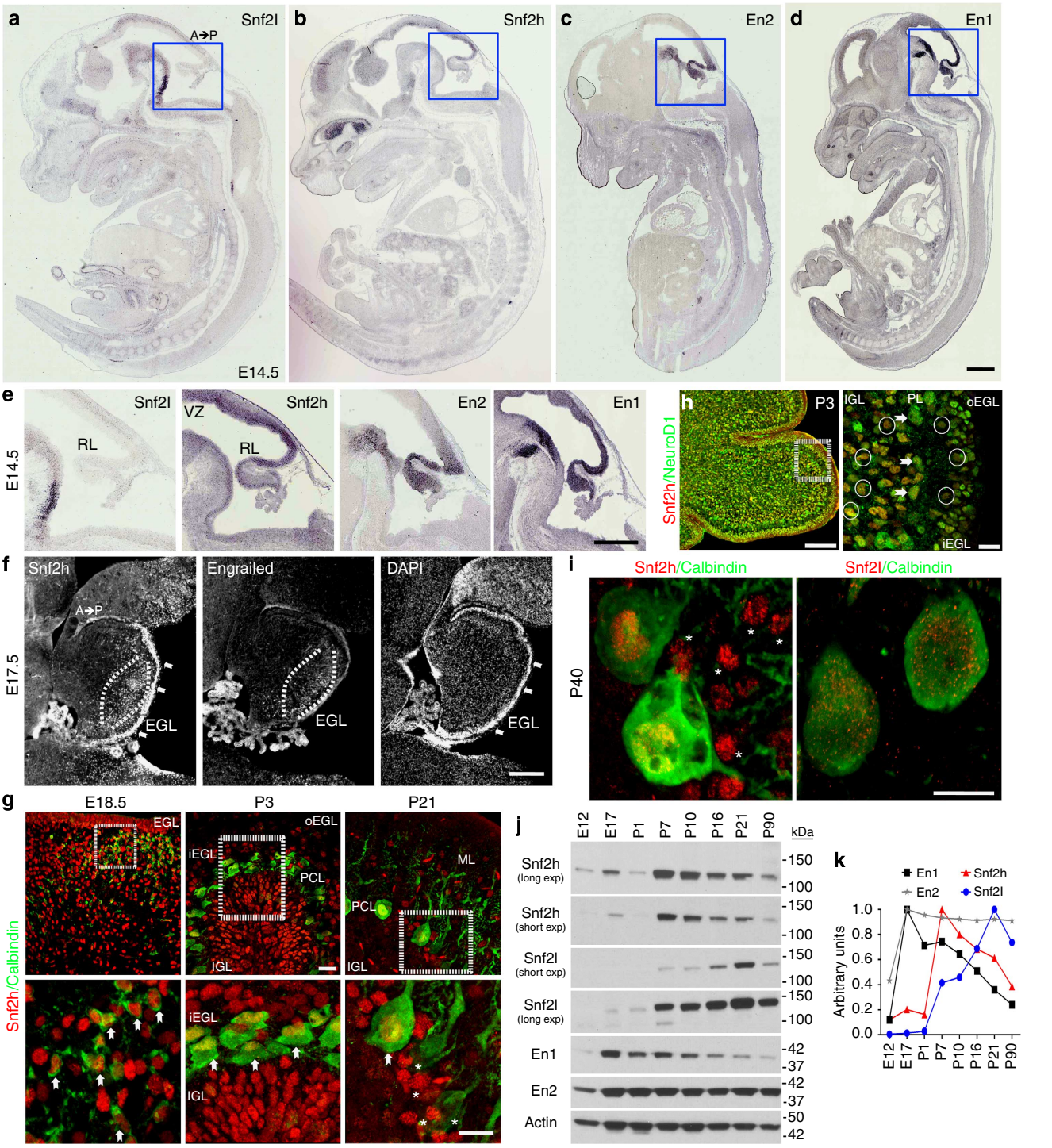

Figure 1 | Snf2h and Snf2l are dynamically regulated in the developing cerebellum. (**a**–**d**) *In situ* hybridization for Snf2l, Snf2h, En2 and En1 from wild-type (WT) embryonic (E) 14.5 sagittal sections adapted from Genepaint.org[70]. Scale bar, 500 μm. (**e**) Boxed areas from **a**–**d** highlight the robust expression of Snf2h, En2 and En1 within the developing rhombic lip, while Snf2l is not detectable. A, anterior; P, posterior. Scale bar, 200 μm. (**f**) E17.5 WT sagittal cerebellar sections serially immunolabelled with Snf2h and Pan-Engrailed (En) antibodies. Brackets highlight regions of robust Snf2h and Engrailed immunoreactivity (−ir). Arrows denote robust Snf2h-ir within the EGL. DAPI labels all nuclei. Scale bar, 200 μm. (**g**) Confocal Z-stacks through the WT cerebellar vermis co-labelled with Snf2h (red) and Calbindin (green), a marker of the PC lineage at the indicated ages. Boxed areas are enlarged at bottom. Arrows denote Snf2h+ PCs. Asterisks denote Snf2h+ interneurons at P21. EGL, external granule layer; IGL, internal granule layer; PCL, Purkinje cell layer; o, outer; i, inner. Scale bars, 20 μm (top panels); 10 μm (bottom panels). (**h**) Confocal Z-stacks through the WT cerebellar vermis at post-natal day 3 (P3) co-labelled with Snf2h (red) and NeuroD1 (green), a marker of differentiated neurons. Arrows denote NeuroD1+, Snf2h+ PCs, as distinguished by their nuclear size and laminar position. Circles denote NeuroD1+, Snf2h+ granule cells (GCs) within the iEGL and the IGL. Scale bar, 20 μm. (**i**) Confocal Z-stacks through the P40 WT cerebellar vermis co-labelled with calbindin (green) and Snf2h (red, left panel); or Snf2l (red, right panel). Asterisks denote Snf2h+ interneurons. Scale bar, 5 μm. At least three mice from each genotype were used for evaluation. (**j**) Snf2h, Snf2l, En1 and En2 immunoblots of WT cerebellar extracts, except for E12 and E17 where hindbrain extracts were used. Actin served as loading control. (**k**) Plot of relative Snf2h, Snf2l, En1 or En2 expression during cerebellar development. The peak expression for each protein was normalized to 1, $n=3$.

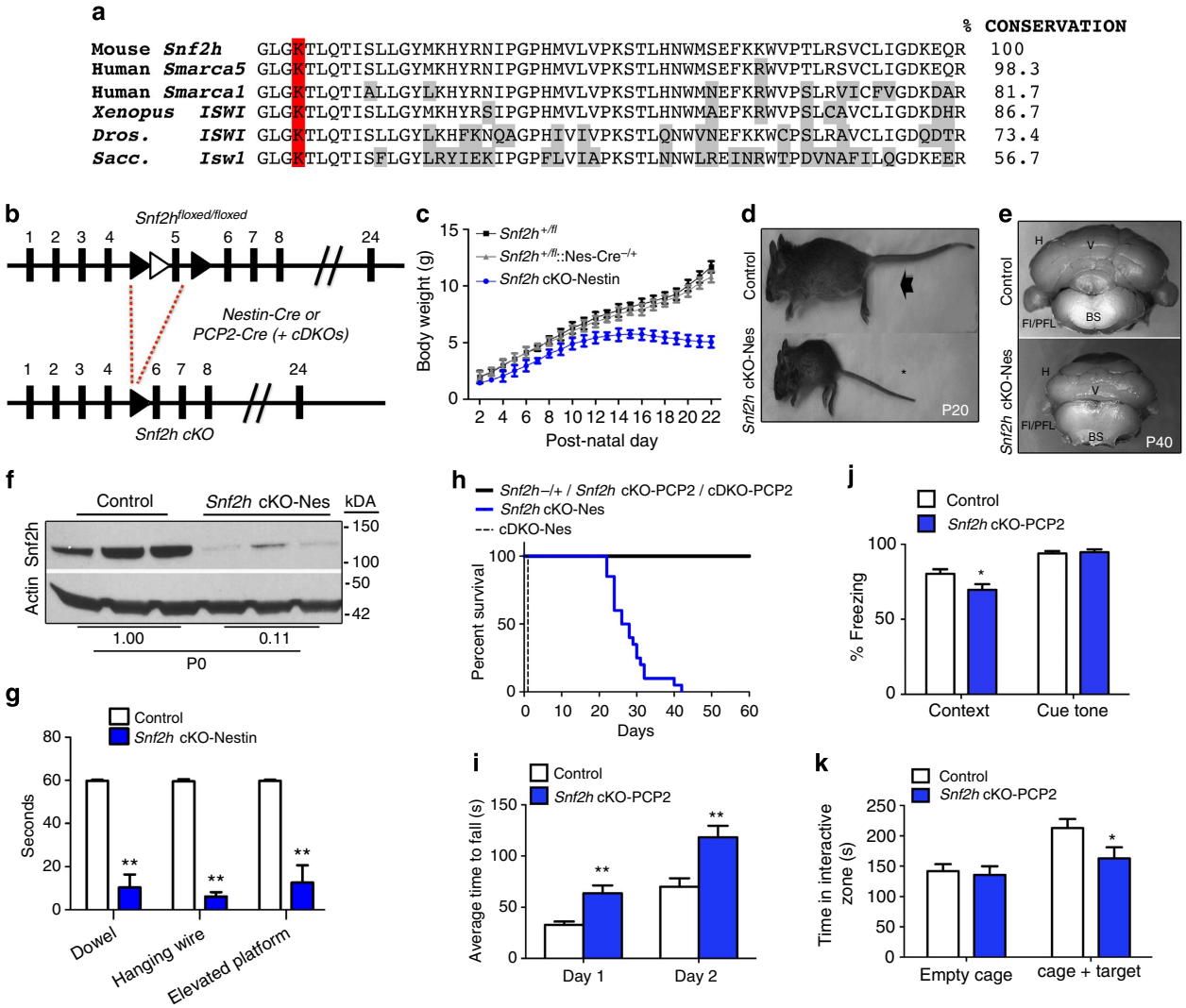

Figure 2 | Snf2h loss in cerebellar progenitors causes cerebellar ataxia or cognitive deficits when ablated in post-mitotic PCs. (**a**) Amino-acid conservation of *Snf2h* exon 5 across species. The lysine residue within this ATP-binding motif and essential for catalytic activity is highlighted in red. Divergent amino acids are boxed grey. *Xenopus*, *Xenopus laevis*; *Dros.*, *Drosophila melanogaster*; *Sacc.*, *Saccharomyces cerevisiae*. (**b**) Schematic of the targeting strategy (LoxP sites, black arrowheads; Frt sites = white arrowheads) used to ablate *Snf2h* expression using the Nestin-Cre or PCP2-Cre drivers. (**c**) Plot of body weights from *Snf2h* cKO-Nes and control mice from P2 to P22. $^{*}P<0.05$, one-way ANOVA, $n=5$–10. (**d**) Control (arrow) and *Snf2h* cKO-Nes (asterisk) littermates at P20. (**e**) Whole-mount images of *Snf2h* cKO-Nes and control cerebella at P40. (**f**) Snf2h immunoblot from *Snf2h* cKO-Nes and control cerebellar extracts at birth. Actin served as loading control. Values denote averaged densitometry, $n=4$. (**g**) Dowel, hanging wire and elevated platform tests reveal severe motor abnormalities in *Snf2h* cKO-Nes mice relative to control littermates at P20–P25. $^{**}P<0.01$, one-way ANOVA, $n=10$–14. (**h**) Kaplan–Meier survival curves of *Snf2h* cKO-Nes, cDKO-Nes and control littermates. *Snf2h* cKO-Nes mice were not viable under standard laboratory conditions after ~P30–P45, while cDKO-Nes mice did not survive past birth, $n=20$–30. (**i**) Rotarod test: *Snf2h* cKO-PCP2 exhibit enhanced ability to stay on the rotarod after five sessions of training relative to controls. $^{**}P<0.01$, one-way ANOVA, $n=10$–14. (**j**) Fear conditioning test: *Snf2h* cKO-PCP2 exhibit no differences in freezing response during training, but a decreased freezing response in context-dependent learning relative to controls. $^{*}P<0.05$, one-way ANOVA, $n=10$–14. (**k**) Social interaction test: *Snf2h* cKO-PCP2 exhibit reduced interaction time with a stranger mouse in a controlled social environment relative to control littermates. $^{*}P<0.05$, one-way ANOVA, $n=10$–14. Values are presented as the mean ± s.e.m.

assay measures the preference of mice to interact with a stranger mouse over an inanimate object. *Snf2h* cKO-PCP2 mice spent less time interacting with the stranger mouse than control littermates (Fig. 2k). We conclude that the loss of Snf2h in post-mitotic PCs does not result in motor deficits but rather in cognitive alterations.

Snf2h loss affects GNP and PC progenitor expansion. Since previous studies have highlighted a role for Snf2h-containing CRCs during DNA replication[19,20], we assessed whether the cerebellar hypoplasia in *Snf2h* cKO-Nes mice resulted from poor GNP or PC expansion. First, we examined the expression of proliferation markers in GNPs residing in the external granule layer (EGL) at E17.5 and E18.5. This analysis revealed that the proportions of cycling (Ki67 +), mitotic (phosphorylated histone H3 +, pH3 +) and S-phase (BrdU +) cells were specifically reduced in the EGL of *Snf2h* cKO-Nes embryos (Fig. 3a–c). The proliferation defects coincided with a dramatic increase in cell death, as shown by an increased number of TUNEL + cells at E17 and P0 relative to controls (Fig. 3c). Moreover, measurements of the EGL showed that it was significantly reduced in size at P7 (Fig. 3d). Reduced proliferation in the *Snf2h* mutant cerebellum is in stark contrast to *Snf2l* deficient animals

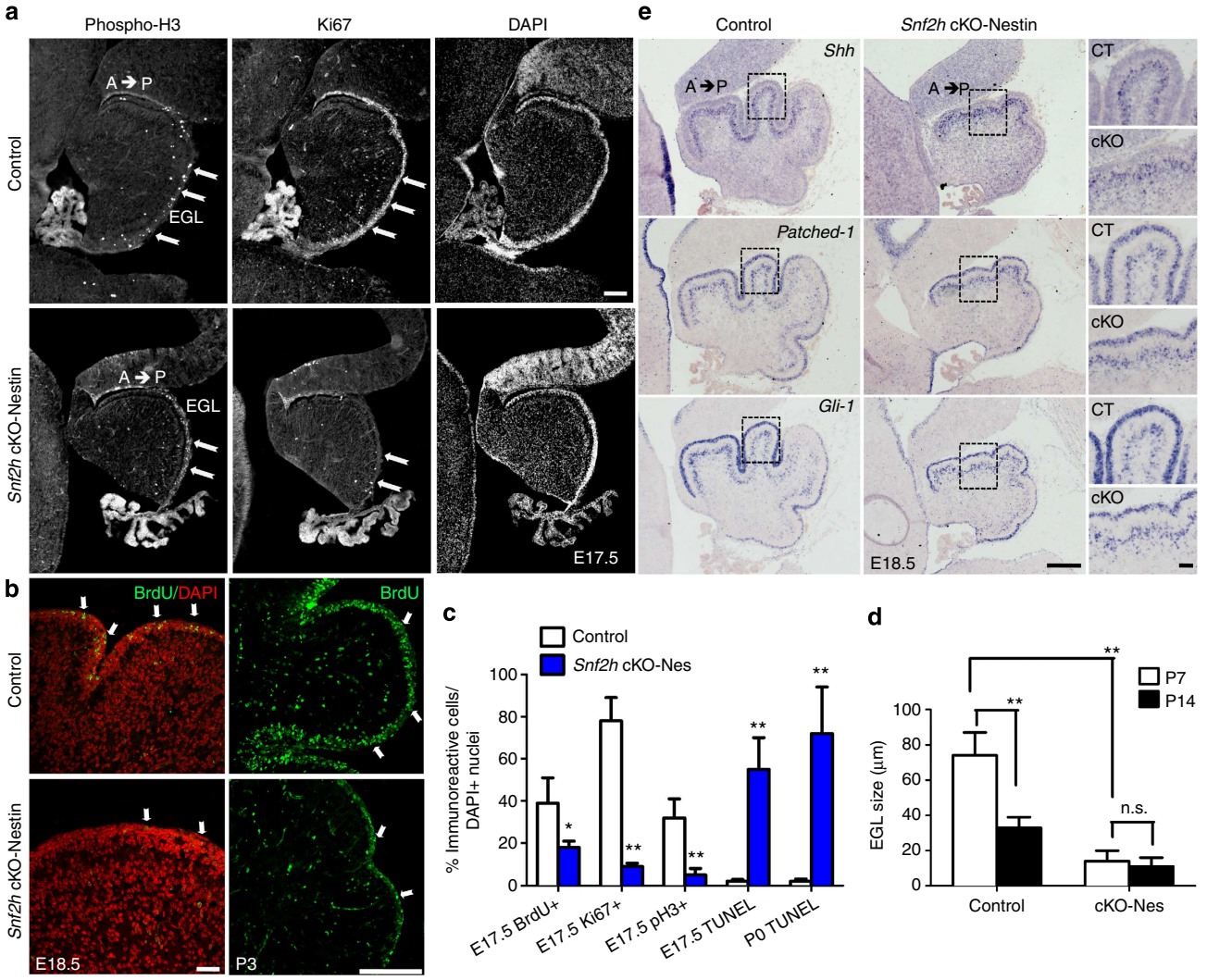

Figure 3 | Snf2h loss results in intrinsic GNP cell death without altering *Shh* signalling. (**a**) E17.5 sagittal cerebellar sections from *Snf2h* cKO-Nes and control littermates immunolabelled for phosphorylated Histone H3 (phospho-H3) or Ki67, and counterstained with the nuclear marker DAPI. Note a severe reduction of cells undergoing mitosis or S-phase throughout the mutant EGL (arrows). EGL, external granular layer. Scale bar, 100 μm. (**b**) Confocal Z-stacks through the E18.5 and P3 cerebellum from *Snf2h* cKO-Nes and control littermates immunolabelled for BrdU after a 90-min BrdU-pulse (arrows). Scale bars, 100 μm. (**c**) Quantification of BrdU+, Ki67+, phospho-H3+ or TUNEL+ cells throughout the mutant and control EGL at E17.5 and P0. $^{**}P<0.01$, Student's *t*-test, $n=4$. (**d**) EGL size at P7 and P14 in *Snf2h* cKO-Nes and control littermates. $^{**}P<0.01$, student's *t*-test. n.s., not significant, $n=4$. Values are presented as the mean ± s.e.m. for c,d. (**e**) *In situ* hybridization through the cerebellar vermis from E18.5 *Snf2h* cKO-Nes and control littermates for *Sonic Hedgehog* (*Shh*), its receptor *Patched-1*, and their downstream target *Gli-1*. Note the spatiotemporal expression gradients (anterior high, posterior low) observed in both genotypes. Scale bar, 200 μm. Boxed areas are shown in rightmost panels to highlight robust mRNA levels in both genotypes. Scale bar, 50 μm. At least three mice from each genotype were used for evaluation.

where we observed increased proliferation and delayed differentiation of cortical progenitors[13].

It is well established that the signalling factor *Sonic Hedgehog* (*Shh*) is secreted from PCs and plays a key role during GNP expansion and cerebellar foliation[21–23]. To assess whether poor GNP proliferation resulted from impaired Shh signalling, we examined the expression of *Shh* and its receptor, *Patched-1*, as well as the downstream effectors *Gli-1*, *CyclinD1* and *N-Myc* by *in situ* hybridization. Sagittal sections through the cerebellar vermis from E18.5 *Snf2h* cKO-Nes and control littermates showed that surviving PCs secrete *Shh* normally, and that all downstream targets are activated in surviving GNPs (Fig. 3e and Supplementary Fig. 5a).

To investigate PC progenitor proliferation, we birthdated cells by BrdU injection at E12.5 and harvested embryos at E17.5 for analysis[24]. *Snf2h* cKO-Nes embryos showed a significant reduction in the proportion of BrdU+, Calbindin+ PCs relative to controls (Fig. 4a,d). Additionally, BrdU-birthdating at E18.5 with analysis at P7 revealed that reduced GNP proliferation in *Snf2h* cKO-Nes mice resulted in a dramatic reduction in the number of BrdU+ GCs but not Calbindin+ PCs, residing within the internal granule layer (IGL), relative to controls (Fig. 4b). However, co-staining with Pax6 and NeuN demonstrated that the timing of neuronal differentiation was not affected (Fig. 4c). Moreover, a normal percentage of BrdU+, GFAP+ glial cells within the white matter suggested that the reduced cellular output was specific to neurons (Fig. 4d and Supplementary Fig. 5b).

Taken together, these results suggest that the extrinsic cues (that is, *Shh* pathway) for progenitor expansion are unaltered and that the poor GNP and PC expansion in *Snf2h* cKO-Nes mice results from a cell-intrinsic defect, most likely from known ISWI functions in transcriptional regulation and DNA replication.

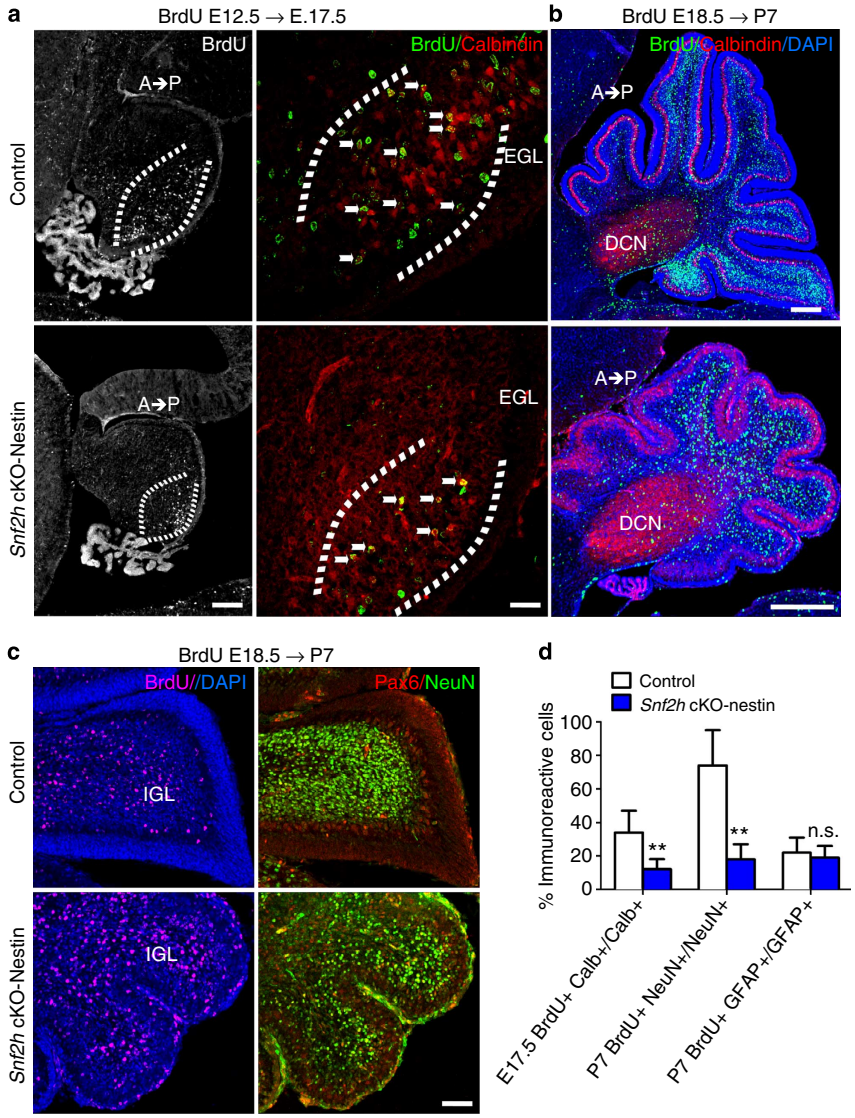

Figure 4 | Snf2h loss affects PC and GNP expansion resulting in cerebellar hypoplasia. (**a**) Confocal Z-stacks from *Snf2h* cKO-Nes and control littermates that were BrdU-birthdated at E12.5, a time of PC birth, and co-labelled for BrdU (green) and Calbindin (red) at E17.5 (brackets). Note the reduction of BrdU+, Clabindin+PCs in mutant embryos (arrows). Scale bar, 50 μm. (**b**) Confocal Z-stacks from *Snf2h* cKO-Nes and control littermates that were BrdU-birthdated at E18.5, a time of robust GNP expansion, and co-labelled for BrdU (green) and Calbindin (red) at P7. DAPI (blue) stains all nuclei. Note the spatiotemporal (anterior low, posterior high) distribution of BrdU+ GCs throughout the internal granule layer in control cerebella that is altered in mutant brains. DCN, deep cerebellar nuclei. Scale bar, 100 μm. (**c**) Confocal Z-stacks through the cerebellar vermis from *Snf2h* cKO-Nes and control littermates that were BrdU-birthdated at E18.5, and labelled for BrdU (magenta); or co-labelled for Pax6 (red) and NeuN (green) at P7. DAPI (blue) stains all nuclei. Scale bar, 50 μm. At least three mice from each genotype were used for evaluation. (**d**) Quantification of double-labelled BrdU+ and Calbindin+ PCs at E17.5 (E12.5 BrdU birthdating); double-labelled BrdU+ and NeuN+ GCs at P7 (E18.5 BrdU-birthdating); or double-labelled BrdU+ and GFAP+ glial cells from mutant and control mice at P7 (E18.5 BrdU-birthdating). $^{**}P<0.01$, Student's *t*-test. n.s., not significant, $n=3$. Values are presented as the mean ± s.e.m.

Snf2h and Snf2l co-modulate the *En1* locus. In *Drosophila*, ISWI binding is enriched at transcriptional start sites where it influences gene transcription by repositioning nucleosomes[25]. We reasoned that altered nucleosome spacing within key developmental genes might perturb their expression and contribute to the impaired cerebellar development in the *Snf2h* cKO-Nes mice. Array hybridization of RNA isolated from mutant and control cerebella identified 110 genes differentially expressed at P0 that increased to 2,916 transcripts at P10 ($P<0.01$, $n=3$ per genotype, statistics was carried out using WEBARRAY online tool (http://www.webarraydb.org/webarray/index.html), which utilizes linear model statistical analysis (modified *t*-test)). Gene ontology analysis using the DAVID online tool (http://david.abcc.ncifcrf.gov/) revealed significant enrichment ($P<0.05$) for downregulated genes associated with transcriptional regulation, cell adhesion and pattern specification (Fig. 5). We further filtered our P0 and P10 microarrays with publicly available RNA-Seq data from isolated adult PCs, GCs and Bergmann glia, to assign a specific cerebellar cell type to the gene expression changes observed, where possible (for example, GNP/GC expression: *En2*, *Pax6*, *Uncx* and *NeuroD1*; PC expression: *protocadherin-ß (Pcdh-ß)* isoforms; Supplementary Data 1)[26]. Validation of the microarray results by qRT–PCR confirmed that the expression of the TFs *Rfx3*, *Uncx*, *Cbp*, *Math1*, *Pax6*, *En2*, *En1*; the signalling

Accession	Symbol	Fold-change @ P0	Fold-change @ P10	Pattern specification	Chromatin	Apoptosis	Immune response	Transcriptional regulation	Ion transport	Metabolic process	Cell adhesion	Cell cycle	Cell morphogenesis	Signal transduciton	Development
AK021079	C030014C12Rik	–6.0	1.5												
NM_011727	Xir3b	–3.4	–3.6												
NR_002888	Smarca5-ps	–2.8	–3.5												
AK006697	1700044K19Rik	–2.7	–1.1												
NR_024325	9130024F11Rik	–2.5	–1.4												
NM_198652	Hjurp	–2.5	1.3		■							■			
NM_053142	Pcdhb17	–2.5	–2.1								■				
NM_010136	Eomes	–2.4	–3.3				■	■		■			■		■
NM_010378	H2-Aa	–2.4	1.7				■								■
NM_053141	Pcdhb16	–2.3	–2.9								■				
NM_146709	Olfr411	–2.2	1.0											■	
NM_011726	Xlr3a	–2.2	–2.9												
NM_145522	Rabepk	–2.2	–1.3												
NM_010894	Neurod1	–2.2	–1.4	■				■		■					■
NM_011369	Shcbp1	–2.2	–1.2												
AK011598	2610028L16Rik	–2.1	1.1												
NM_053131	Pcdhb6	–2.1	–2.0								■				
NM_053147	Pcdhb22	–2.0	–1.8								■				
AK020613	9530057J20Rik	–2.0	1.1												
AK052185	D330004O07Rik	–2.0	–1.0												
NM_053140	Pcdhb15	–2.0	–3.3								■				
AK016895	4933424L07Rik	–2.0	1.4												
NM_177780	Dock5	–2.0	1.3												
NR_045760	0610031O16Rik	–1.9	–1.1												
NM_001199113	Slc29a1	–1.9	–2.3												
NM_023064	Tbata	–1.9	–6.4												■
NM_009188	Sin3b	–1.9	1.0					■		■		■			■
NM_053124	Smarca5	–1.9	–2.4		■			■		■					
NM_007673	Cdx2	–1.9	–1.3	■				■		■					■
NM_182993	Slc17a7	–1.9	–2.1					■	■						
NM_011265	Rfx3	–1.9	1.4	■				■		■					
NM_027472	5730455P16Rik	–1.9	1.1												
AK018252	6330575P09Rik	–1.9	–1.4												
NM_134052	Adi1	–1.8	1.2							■					
NM_010916	Nhlh1	–1.8	–5.8					■							
NM_011602	Tln1	–1.8	1.2								■				
AK013461	2900001G08Rik	–1.8	1.4												
NM_027049	1700008O03Rik	–1.8	1.2												
NM_175013	Pgm5	–1.8	1.0								■	■			
NM_178767	Agmo	–1.8	1.0								■				
NM_013627	Pax6	–1.8	–3.6	■				■			■		■		■
NM_020577	As3mt	–1.8	–1.5								■				
NM_001001321	Slc35d2	–1.8	1.5												
NM_146025	Samd14	–1.7	–1.2												
AK019118	2410057H14Rik	–1.7	1.4												
NR_033325	Gm5089	–1.7	1.0												
NM_001109747	Cenpw	–1.7	–1.0									■			
NM_026985	1810033B17Rik	–1.7	1.0												
NM_175653	Hist1h3c	–1.7	–1.2		■										
NM_010203	Fgf5	–1.7	–1.2												
NM_011451	Sphk1	–1.7	1.7		■						■				
NM_008185	Gstt1	–1.7	–1.7								■				
NM_008318	Ibsp	–1.7	1.6								■				■
NM_053132	Pcdhb7	–1.7	–1.8								■				
NM_178017	Hmgxb4	–1.7	1.0												
NM_178650	Tbc1d10c	–1.6	–1.3												■
NM_153565	Pcsk9	–1.6	–1.2		■						■				
NM_145226	Oas3	–1.6	–1.4			■									
NM_010449	Hoxa1	–1.6	1.2	■				■		■			■		■
NM_001146342	Rnls	–1.6	1.2												
AK009626	2310034P14Rik	–1.6	–1.4												
NM_175252	Zfp934	–1.6	1.1												
NM_145073	Hist1h3g	–1.6	–1.7		■										
NM_013702	Uncx	–1.5	–4.4	■				■		■	■				■
NM_033560	Vps37a	–1.5	1.1												
NM_007500	Atoh1	–1.2	–3.7			■		■		■			■		■
NM_010134	En2	–1.1	–2.8					■		■					■
NM_010133	En1	1.0	1.5	■				■		■					■

Figure 5 | List of downregulated genes at P0 and corresponding gene expression changes at P10 from *Snf2h* cKO-Nes cerebella. Cyan highlights TFs and yellow highlights cell adhesion molecules. Note that ~110 genes were deregulated at P0, while ~2,900 genes were deregulated by P10. Three microarrays per genotype were averaged from wild-type and mutant P0 and P10 cerebellar extracts. Underlined values denote $P<0.05$. Statistics was carried out using WEBARRAY online tool (http://www.webarraydb.org/webarray/index.html) that utilizes linear model statistical analysis (modified *t*-test).

factor *Bmp4* and the cell adhesion molecules *Pcdh-ß6* and *Pcdh-ß17* were all significantly downregulated (~1.5–2.5-fold) in mutant cerebella at birth (Fig. 6a; Supplementary Table 1). Moreover, we observed a ~2.6-fold downregulation of *Snf2h*, while *Snf2l* levels were unperturbed in mutant cerebella at this time point (Fig. 6a). While most genes analysed remained downregulated at P10, we observed an unexpected increase in *En1* (~1.9-fold), *Bmp4* (~2.1-fold) and *Snf2l* (~1.7-fold) mRNA levels (Fig. 6a), the latter suggesting that Snf2l may be compensating for Snf2h loss in the activation of some targets. In this regard, P10 immunoblots demonstrated that Snf2l protein levels were increased by ~2.3-fold, whereas Snf2h protein levels were decreased by ~2-fold (Fig. 6b). Snf2l immunolabelling at P7 revealed comparable expression levels throughout the PC layer (Fig. 6c). We next investigated whether Snf2l could be responsible for the upregulation of genes at P10 that were reduced at P0, focusing our attention on *En1*.

The *En1* and *En2* homeobox genes are essential for cerebellar patterning and foliation[27]. During early post-natal development they adopt distinct expression patterns with En1 and En2 expressed in PCs and GCs, respectively[28]. Since Snf2l expression is limited to PCs (Fig. 1i and Supplementary Fig. 1c), we reasoned that upregulation of En1 but not En2 might occur from Snf2l compensation. P7 sections through the cerebellar vermis were labelled with pan-Engrailed (Engrailed) antibodies, counterstained with DAPI and quantified for Engrailed immunoreactivity (-ir) within PCs (identified by their large nuclear size, >10 µm) from a minimum of 50 cells per genotype. We found that *Snf2h* cKO-Nes and control PC nuclei showed no significant differences in Engrailed-ir (Fig. 6d). However, the PCs of *Snf2h* cKO-PCP2 mice showed a significant reduction in Engrailed-ir, suggesting that Snf2l compensation is temporally regulated (Fig. 6e).

Given that Snf2l compensates for embryonic Snf2h loss, we next investigated whether reducing *Snf2l* levels would increase the severity of the phenotype. Indeed, removal of one copy of *Snf2l* on the *Snf2h* cKO-Nes background (*Snf2l*$^{-/+}$::*Snf2h* cKO-Nes) resulted in a more severe ataxic phenotype and death by ~P25 (Fig. 6f and Supplementary Movie 6). As discussed earlier, the cDKO-Nes mice had the most severe phenotype, resulting in death at birth (Fig. 6f), which is comparable to the neonatal lethality of *En1* KO mice[29]. Microarray and immunostaining suggested that the Snf2l compensation begins between P0 and P7. Using immunoblots we were able to demonstrate *En1* compensation as early as P5 with *En2* expression reduced by ~60% (Fig. 6g). Similar results were observed at P20, suggesting

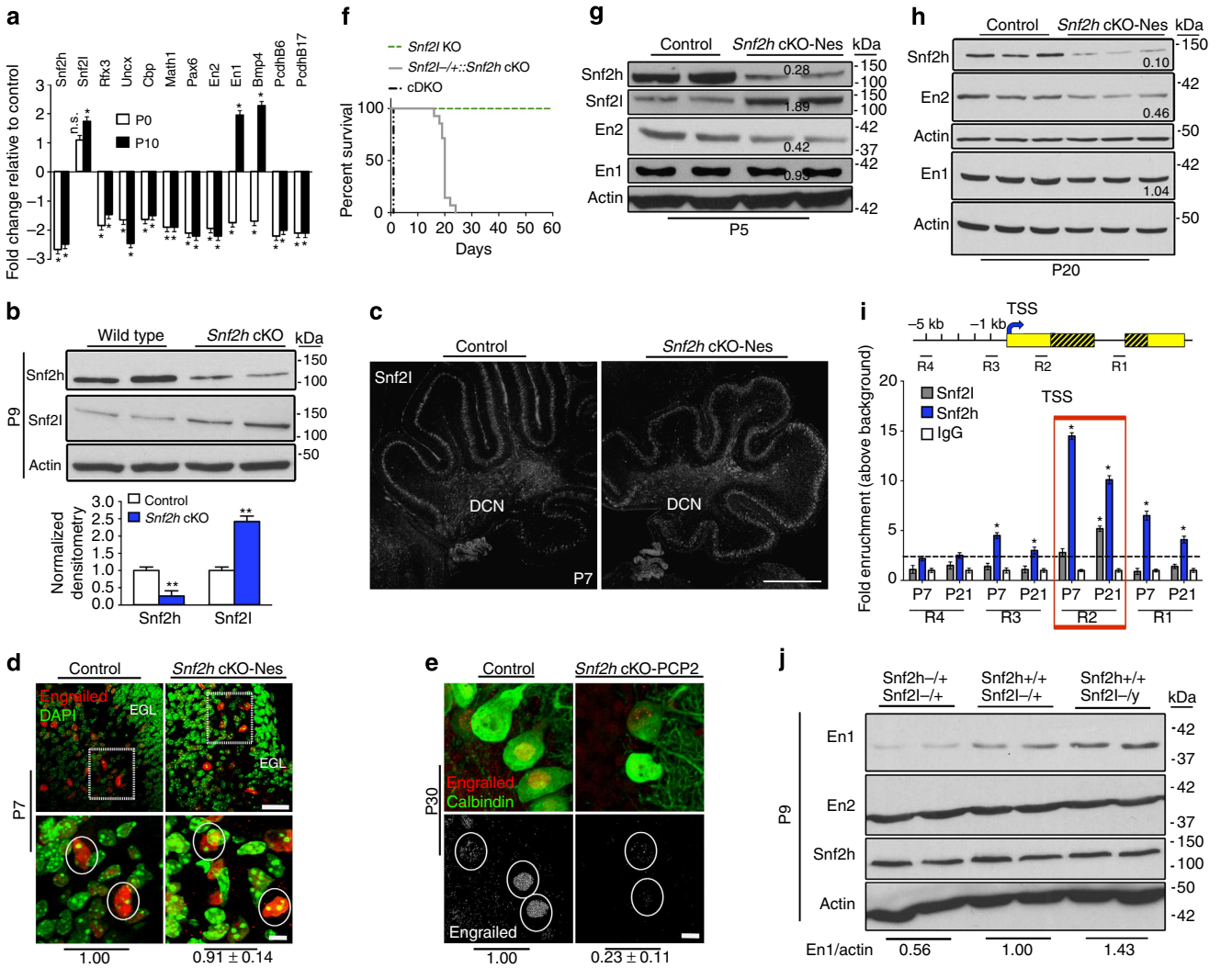

Figure 6 | Snf2h and Snf2l co-modulate the *En1* locus. (**a**) RT-qPCR analysis of selected genes from *Snf2h* cKO-Nes and control cerebella at P0 and P10. $^*P<0.05$, Student's *t*-test. n.s., not significant, $n=6$ from one of two independent experiments. (**b**) Immunoblots for Snf2h and Snf2l from *Snf2h* cKO-Nes and control cerebellar extracts at P9. Graph below depicts quantification for Snf2h and Snf2l, normalized to actin. $^{**}P<0.01$, Student's *t*-test, $n=3$. Values are presented as the mean ± s.e.m. (**c**,**d**) Confocal Z-stacks of P7 cerebellum from *Snf2h* cKO-Nes and controls immunolabelled for (**c**) Snf2l. DCN, deep cerebellar nuclei. Scale bar, 200 μm; or (**d**) Pan-Engrailed (red) and counterstained with DAPI (green). Boxed areas are enlarged at bottom and denote similar En immunoreactivity in cells from both genotypes. Scale bars, 50 μm (top); 10 μm (bottom). (**e**) Confocal Z-stacks of P30 cerebellum from *Snf2h* cKO-PCP2 and controls immunolabelled with Pan-Engrailed (red) and Calbindin (green). Engrailed images in bottom panel are pseudocolored (silver) for contrast. Scale bar, 5 μm. Values (**d**,**e**) denote Engrailed immunopixels normalized to WT within cells with a nuclear size $>10\ \mu m^2$ (circles). At least 50 PCs from three independent mice were quantified per genotype. (**f**) Kaplan–Meier curves of *Snf2l* KO, *Snf2l* −/+::*Snf2h* cKO-Nes and cDKO-Nes mice. Note that one *Snf2l* allele in a *Snf2h*-null background rescues the lethality of cDKO-Nes mice up to ~P25 ($n=25$). (**g**,**h**) Immunoblots for Snf2l, Snf2h, En2 and En1 from *Snf2h* cKO-Nes and control cerebellar extracts at P5 (**g**) and P20 (**h**). Actin served as loading control. Values denote averaged densitometry ($n=4$). (**i**) Top: schematic diagram of the mouse *En1* locus indicating primer set locations. Yellow boxes, 5′ and 3′ untranslated regions (UTRs); striped yellow boxes, coding region; black line = non-coding region; TSS, transcription start site (arrow); kb, kilobases away from the TSS (+1). Bottom: ChIP-qPCR from WT cerebellar extracts for the *En1* locus reveals Snf2h enrichment throughout the gene (R3, R2 and R1) at P7 and P21. Snf2l enrichment occurs only in the 5′-UTR (R2) at P21. $^*P<0.05$, Student's *t*-test, $n=4$ from one of three independent experiments. Values are presented as the mean ± s.e.m. (**j**) Immunoblots for Snf2h, En2 and En1 from $Snf2h^{+/+}$::$Snf2l^{-/+}$ (WT); $Snf2h^{-/+}$::$Snf2l^{-/+}$ (Snf2h heterozygote); or $Snf2h^{+/+}$::$Snf2l^{-/y}$ (Snf2l KO) cerebellar extracts at P9. Values denote averaged densitometry relative to WT levels ($n=4$).

that both ISWI proteins mediate *En1* regulation, but *En2* regulation is specific to Snf2h (Fig. 6h). Furthermore, P5 immunoblots show reduced En1 levels in the $Snf2l^{-/+}$::*Snf2h* cKO-Nes animals compared with *Snf2h* cKO-Nes mice, thus providing additional support for a *Snf2l*-dependent *En1* compensation in *Snf2h* cKO-Nes mice (Supplementary Fig. 6a).

To determine the interactions at the *En1* gene *in vivo*, we performed chromatin immunoprecipitation (ChIP) followed by quantitative PCR (ChIP–qPCR) assays for Snf2h and Snf2l with wild-type cerebellar extracts at P7, when Snf2h levels are at their peak; and at P21, when Snf2l levels reach their maximal level. *En1* occupancy was analysed by qPCR with primer pairs corresponding to the intragenic region (R1), the 5′-UTR (R2), the proximal promoter (R3) and an upstream region (R4) (Fig. 6i). Snf2h binding showed the greatest enrichment at R2 at both time points with maximal binding observed at P7 (Fig. 6i). At P21, we also observed significant binding of Snf2l at R2 (Fig. 6i), suggesting that the ISWI proteins co-regulate *En1* transcription and that increased *Snf2l* expression provides functional compensation in *Snf2h* cKO-Nes mice. In contrast, only Snf2h was enriched at the

En2 promoter (Supplementary Fig. 6b), providing further support for *Snf2h*-specific regulation of *En2*.

As a last step to understand the endogenous function of Snf2h and Snf2l during normal cerebellar development, we assessed En1 and En2 expression levels upon deletion of one *Snf2h* allele ($Snf2h^{+/+}$ versus $Snf2h^{-/+}$) or upon complete ablation of *Snf2l* ($Snf2l^{-/y}$ versus $Snf2l^{-/+}$). $Snf2h^{-/+}$ cerebella had a ~40% reduction of En1 total protein levels, while En2 and Snf2h protein levels were unaffected (Fig. 6j). Conversely, Snf2l deletion ($Snf2l^{-/y}$; Snf2l is X-linked) resulted in a ~40% upregulation of En1 protein levels, while En2 and Snf2h protein levels remained unchanged (Fig. 6j).

Collectively, our results suggest that when both Snf2h and Snf2l are present the endogenous role of Snf2l is to function as a repressor of *En1* transcription, as En1 protein levels are increased in *Snf2l* KO cerebella at P9. However, when Snf2h is ablated embryonically (*Snf2h* cKO-Nes model) we observed an upregulation of Snf2l that functionally compensates to restore En1 expression and early PC functions (probably by substitution within Snf2h complexes). However, this novel gain-of-function effect by Snf2l is temporally regulated since it does not rescue En1 expression when Snf2h is ablated at P10 (Snf2h cKO-PCP2 model). Moreover, Snf2l restoration of *En1* expression within the *Snf2h* cKO-Nes mice is insufficient to rescue the progressive ataxic phenotype.

Snf2h loss alters PC maturation. The post-natal survival and progressive phenotype of *Snf2h* cKO-Nes mice allowed us to investigate the cell-intrinsic defects present in surviving post-mitotic neurons. For this analysis we chose the P7 cerebellum, a time when PC dendritic arbors extend towards the molecular layer for formation of parallel fibre circuits, while GCs migrate to the internal granule layer for establishment of mossy fibre circuitry[24]. We validated the loss of Snf2h in nearly all surviving Calbindin+ PCs (Fig. 7a), which were present in multiple PC layers compared with control PCs that were present in uniform developing rows (Fig. 7b). The growth of the molecular layer, which rapidly occurs between P7 and P14, was significantly reduced in size in the mutant animals (Fig. 7d). Indeed, a dramatic reduction of the PC apical dendritic arbor is observed with Golgi–Cox staining at P20, which is further aggravated in cDKO-Nes mice (Fig. 7c,f). In addition, we also observed a progressive and dose-dependent increase in the total number of PC pyknotic nuclei as assessed by toluidine blue staining (Fig. 7e).

The poor dendritic arborization and progressive death of PCs could be a consequence of the reduced number of cerebellar neurons that synapse onto the PC rather than an intrinsic defect in arborization. To investigate whether Snf2h is necessary for dendritic arborization and PC survival we further characterized the *Snf2h* cKO-PCP2 model, in which Snf2h loss is specific to PCs beginning at ~P10 (ref. 17). In this model, there is normal GNP proliferation resulting in a normally sized cerebellum and proper activation of post-mitotic markers in GCs and PCs, including *Pax6*, *Patched-1* and *Gli-1* (Supplementary Fig. 7a,c). However, we observed a significant reduction of the PC apical dendritic arbor by P30 (Fig. 7g,h). Moreover, *Snf2h* cKO-PCP2 mice also display an ISWI dose-dependent increase in the total number of pyknotic PCs between P50 and P300 (Supplementary Fig. 7b). Similar results from both Snf2h cKO mouse strains allow us to conclude that Snf2h plays a cell-autonomous role in post-mitotic PC maturation and survival.

Snf2h governs chromatin organization and histone H1 dynamics. We reasoned that the progressive PC loss might result from altered chromatin architecture that impacts gene expression and compromises cell function. Indeed, studies in yeast and *Drosophila* have demonstrated multiple roles for ISWI complexes in chromatin compaction by repositioning nucleosomes to mediate linker DNA length and by facilitating histone H1 deposition[12,30,31]. To assess chromatin organization, we examined nuclear ultrastructure of cerebellar neurons by transmission electron microscopy (TEM). TEM images of E18.5 *Snf2h* cKO-Nes mice revealed that GNPs and PCs display numerous densely stained clumps within the euchromatin, a dispersed nucleolar region, chromatin loops and structures indicative of nuclear invaginations or micronuclei that collectively indicate that the chromatin structure is highly disorganized (Fig. 8a). Moreover, we observed that the altered chromatin organization is augmented in cDKO-Nes mice at E18.5 (Fig. 8a, rightmost panel) and is progressive, both temporally and in a Snf2l-dose-dependent manner (Fig. 8b–e). Indeed, many pyknotic nuclei and cell 'ghosts' were clearly visible in *Snf2h* cKO-Nes mice by P21 (Fig. 8c). Collectively, these experiments demonstrate a progressive disorganization of the chromatin structure that correlates with the progressive death of GNPs and PCs, and the ataxic phenotype.

To confirm the cell-autonomous nature of the chromatin disorganization, we once again made use of *Snf2h* cKO-PCP2 mice. Sections from P50 mice were examined for chromatin ultrastructure changes by TEM. Similar to *Snf2h* cKO-Nes mice, we observed chromatin disorganization and loss of nuclear and nucleolar ultrastructure in P50 sections processed for TEM from *Snf2h* cKO-PCP2 but not from WT littermates (Fig. 8f).

The temporal increase in densely stained clumps and disorganized nucleolar structures likely contribute to the dramatic increase in deregulated gene expression we observed between P0 and P10. To address this we investigated whether any global perturbations in histone modifications occur during this time. Indeed, P9 immunoblots of acid-extracted histones from *Snf2h* cKO-Nes and control mice identified a significant decrease in histone marks for active transcription including H3K4Me3 and H3K18Ac, and for transcriptional elongation (H3K36Me2), but not for the repressive mark H3K9Me3 (Fig. 9a). We additionally found that the histone variants H2A.Z and macro-H2A, which mark regions of active or repressed chromatin, respectively, were normal at P2 but were markedly reduced in mutant cerebella by P9 (Fig. 9b). These results suggested that altered gene expression likely arises from a defect in establishing specific chromatin domains.

Studies in *Drosophila* have shown that *ISWI* ablation leads to global chromatin decompaction and a reduction in histone H1 (refs 12,31). As such, we analysed core histone proteins by immunoblot from *Snf2h* cKO-Nes mice and control cerebella at P2 and P9. At P2, all core histones were present at levels equivalent to wild-type mice (Fig. 9c). In contrast, we observed a severe reduction in histone H1 but not the other core histones by P9 (Fig. 9c,d). Interestingly, we noted that the H2A C-terminal antibody showed reduced detection of H2A at P9 but the N-terminal antibody showed normal levels, as did its dimer partner H2B (Fig. 9c,d). While this suggests that the epitope recognized by the C-terminal H2A antibody might be masked, modified or proteolytically cleaved, it remains unclear why we are observing this differential effect.

Recent studies have demonstrated that the C-terminal tail of histone H2A is required for histone H1 loading onto DNA and is also necessary for Snf2h-dependent nucleosome translocation[32]. Moreover, the reduced levels of H1 and the possibility that the H2A tail is modified or clipped in *Snf2h* cKO-Nes mice suggested that Snf2h regulates histone H1 dynamics. To decipher an *in vivo* role for Snf2h in H1 chromatin dynamics, we performed fluorescence recovery after photobleaching (FRAP) experiments

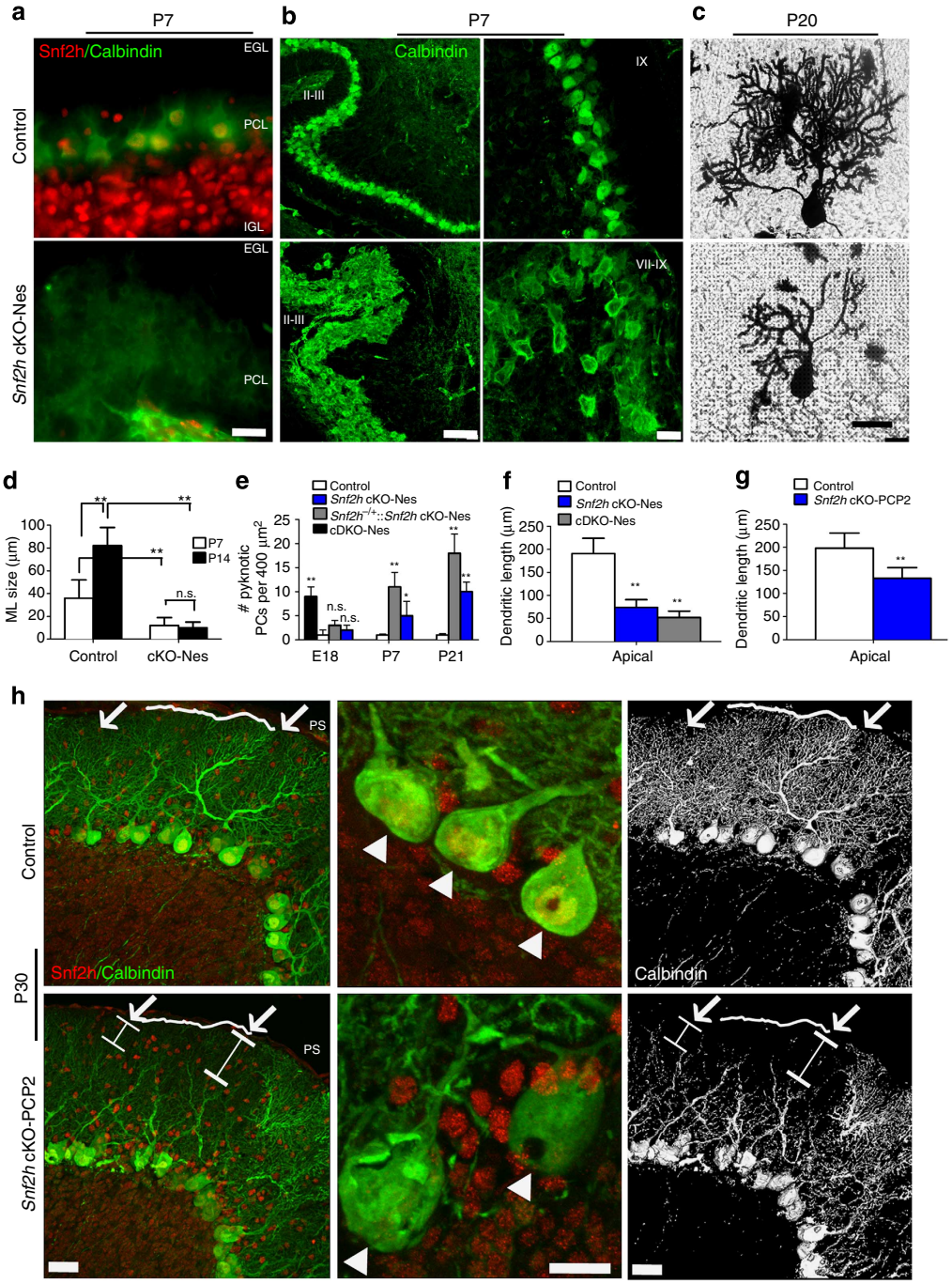

Figure 7 | Snf2h loss alters PC maturation. (**a**) Snf2h (red) and Calbindin (green) co-labelling through the cerebellum from *Snf2h* cKO-Nes and control littermates at P7. Note the absence of Snf2h expression in mutant PCs. Scale bar, 20 μm. (**b**) Confocal Z-stacks through the cerebellar vermis from *Snf2h* cKO-Nes and control littermates at P7 immunolabelled for Calbindin (green). Roman numerals denote the corresponding lobules of the mammalian cerebellum. Scale bars, 100 μm (left panels); 20 μm (right panels). (**c**) Light microscopy Z-stacks of PCs through the cerebellar vermis stained with the Golgi–Cox method from *Snf2h* cKO-Nes mice and control littermates at P20. Scale bar, 10 μm. (**d**) Molecular layer size at P7 and P14 in *Snf2h* cKO-Nes and control littermates. (**e**) Quantification of pyknotic PC nuclei using toluidine blue reveals an ISWI-dependent modulation of PC survival in *Snf2h* cKO-Nes, *Snf2l*$^{-/+}$::*Snf2h* cKO-Nes and cDKO-Nes mice. (**f**,**g**) PC apical arbor dendritic length measurements from the indicated genotypes at P20 or P30, respectively. For panels (**d**–**g**) $^{**}P<0.01$, Student's *t*-test, n.s., not significant, $n=6$. Values are presented as the mean ± s.e.m. (**h**) Left panels: confocal Z-stacks through the cerebellum from P30 *Snf2h* cKO-PCP2 mice and control littermates co-immunolabelled for Snf2h (red) and calbindin (green). Arrows and bars denote mutant PC arbors that do not reach the pial surface (ps) (bars, arrows). Middle panels: higher magnification images of PCs (arrowheads) denote Snf2h+ staining in control but not mutant PCs. Right panels: pseudocolored Calbindin-ir (silver) denotes the atrophied dendritic arbor in mutant PCs (bars, arrows). Scale bar, 20 μm (left and rightmost panels); 10 μm (middle panels). For **a**–**c** and **h**, at least three mice from each genotype were used for evaluation.

using GFP-H1e-tagged constructs transfected into Neuro2A cells before Snf2h knockdown (KD)[33,34]. To avoid any non-specific effects of cell death upon acute Snf2h ablation, FRAP experiments were performed at the 48-h time point. The cell nucleus in both siScrambled (siScr) control and siSnf2h-treated cells appeared normal in size and shape at the time of the experiments (Fig. 9f).

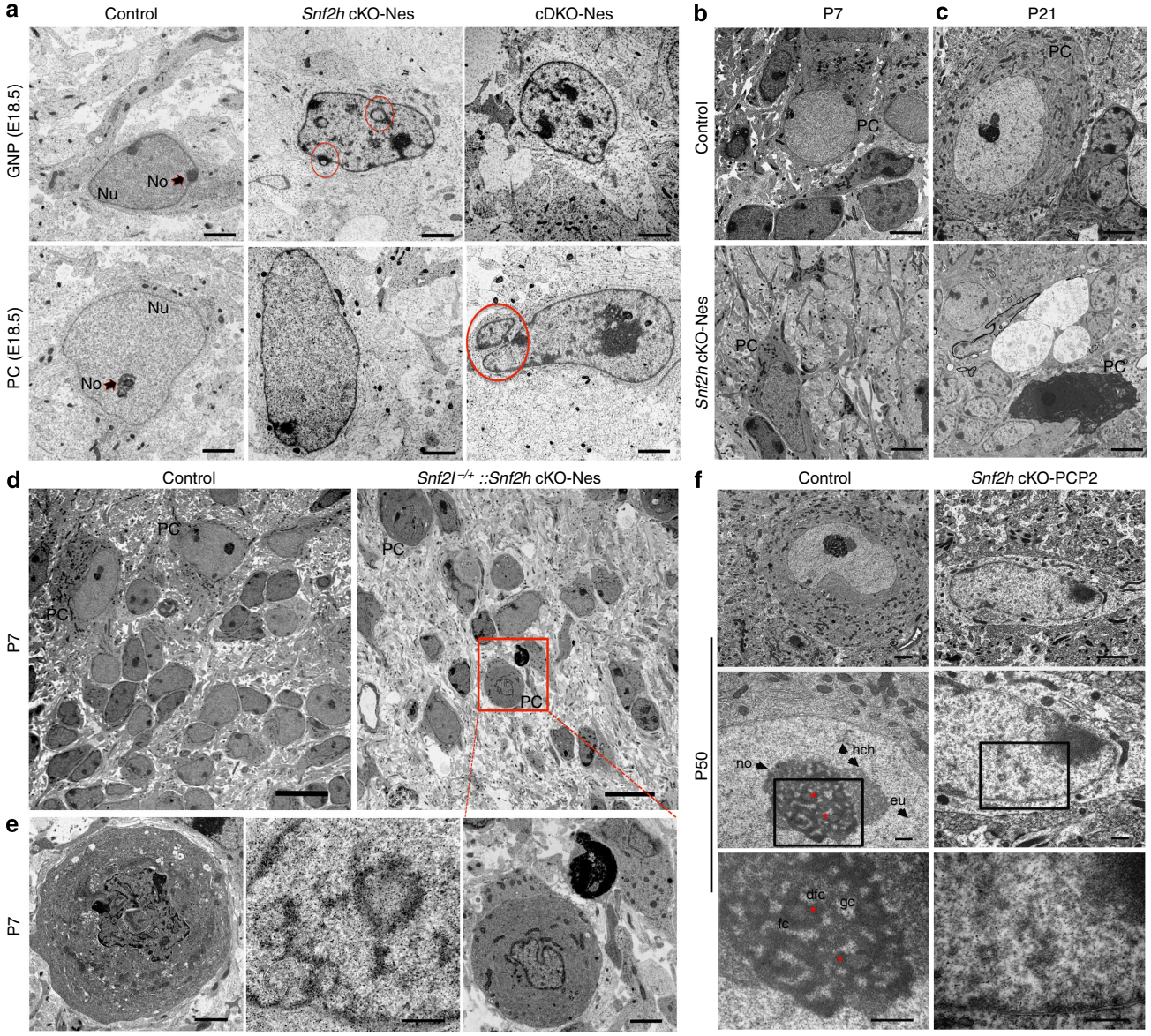

Figure 8 | Snf2h is necessary for proper chromatin folding. (**a**) Transmission electron microscopy (TEM) of GNPs and PCs through the cerebellar vermis from *Snf2h* cKO-Nes, cDKO-Nes mice and control mice at E18.5. Red circles denote nuclear invaginations. GNP, granule neuron progenitor; PC, Purkinje cell; Nu, nucleus; No, nucleolus. Scale bars, 2 μm. (**b**,**c**) TEM from *Snf2h* cKO-Nes and control mice through the cerebellum at P7 and P21. Note the abnormal morphology of mutant PCs and 'cell ghosts' in mutant cerebella. PC, Purkinje cell. Scale bars, 2 μm. (**d**,**e**) TEM through the cerebellar vermis from control and *Snf2l* −/+ ::*Snf2h* cKO-Nes mice at P7, revealing the aggravation of chromatin ultrastructure abnormalities within PCs upon additional removal of one *Snf2l* copy. Boxed area is enlarged in bottom rightmost panel. Scale bars, 10 μm (top panels); 2 μm (bottom panels). (**f**) TEM from P50 *Snf2h* cKO-PCP2 mice and control littermates through the cerebellar vermis. Higher magnification images are provided in descending panels. Note the loss of nucleolar, heterochromatin and euchromatin ultrastructure and increased electron density, evidenced as 'chromatin clumps' within mutant PC nuclei. Stars denote nucleolar dense fibrillar centers (dfc). gc, granular centre; fc, fibrillar centre; no, nucleolus; eu, euchromatin; hch, heterochromatin. Scale bars, 2 μm (top panels); 500 nm (middle and bottom panels). At least three mice from each genotype were used for evaluation.

siSnf2h-treated cells displayed an increased 'bleached depth' that suggests that the pool of unbound H1 is increased in the mutant samples. In addition to an increase in the unbound fraction, there was also a subtle change in H1 dynamics as we observed an ~10% reduction in histone H1e-GFP mobility and an ~20% increase in the half-maximal recovery time (t-half) compared with siScr controls (Fig. 9e–g and Supplementary Movies 7 and 8). To demonstrate that the observed effect was specific to Snf2h, we restored the mobility of GFP-H1e by co-transfecting hSNF2H (addback hSNF2H) that is unaffected by the siRNA treatment (Fig. 9e,g and Supplementary Movie 9). Conversely, Snf2l KD did not alter GFP-H1e dynamics (Supplementary Fig. 8c). However, exogenous expression of hSNF2L was also able to rescue GFP-H1e dynamics following Snf2h KD (addback hSNF2L), which is indicative of the functional compensation we have observed in *Snf2h* cKO-Nes mice (Fig. 9e,g and Supplementary Movie 10). These studies suggest that Snf2h participates in the loading of histone H1 onto chromatin.

We next investigated whether acute KD of *Snf2h* by siRNA treatment in Neuro2A cells could recapitulate the chromatin changes we observed in the *Snf2h* cKO mice. We observed a significant KD of Snf2h by 48 h and >90% loss by 96 h (Fig. 9h). We next analysed the cells for changes in nuclear morphology after DAPI staining. We observed a subtle reduction in the

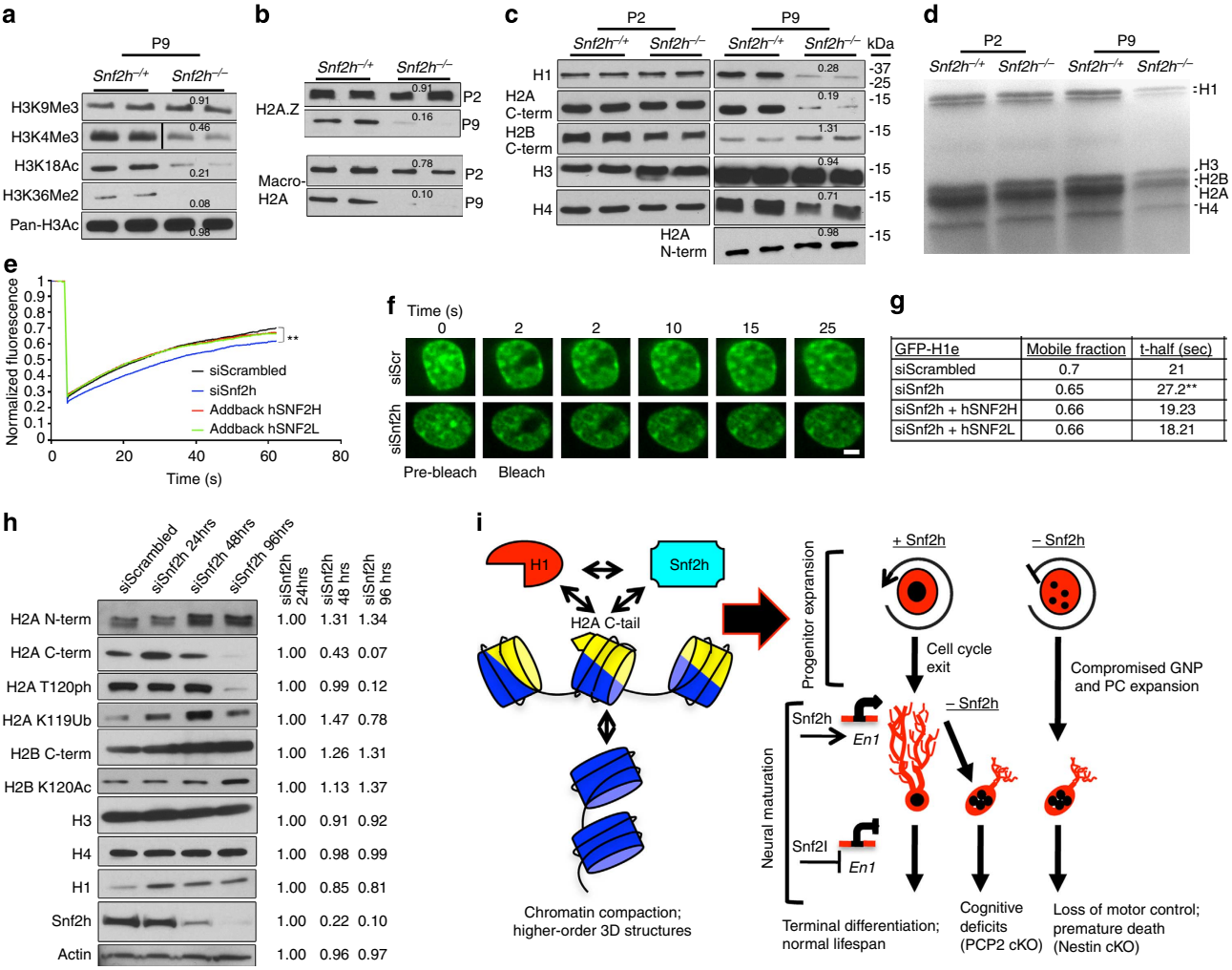

GFP-H1e	Mobile fraction	t-half (sec)
siScrambled	0.7	21
siSnf2h	0.65	27.2**
siSnf2h + hSNF2H	0.66	19.23
siSnf2h + hSNF2L	0.66	18.21

Figure 9 | Snf2h mediates chromatin transitions through linker histone H1 dynamics. (**a,b**) Immunoblots of acid-extracted cerebellar histones from *Snf2h* cKO-Nes (*Snf2h*$^{-/-}$) and control littermates (*Snf2h*$^{-/+}$) for (**a**) histone H3 post-translational modifications at P9; or (**b**) histone variants H2A.Z and macro-H2A at P2 and P9. Values denote average densitometry relative to control samples ($n=4$). (**c**) Immunoblots of core histones from P2 and P9 cerebellar extracts from *Snf2h* cKO-Nes and control littermates. Values denote average densitometry relative to control samples ($n=4$). (**d**) Colloidal blue staining of isolated P2 and P9 histones from *Snf2h* cKO-Nes and control littermates to examine stoichiometry. (**e**) Mean normalized GFP-H1e FRAP curves of siScrambled (siScr); siSnf2h; siSnf2h + addback human (h) SNF2H; or siSnf2h + addback hSNF2L from transiently transfected mouse Neuro2A cells 48 h after treatment. A significant difference between recovery curves of siScrambled and siSnf2h is indicated. $^{**}P=0.008$, $n=20$, Student's *t*-test. Error bars were omitted for clarity. (**f**) FRAP images of GFP-H1e from siScr (top) or siSnf2h (bottom) Neuro2A treated cells at the indicated times. Scale bar, 1 μm. (**g**) Mobile fractions and t-half values for GFP-H1e FRAP experiments. $^{**}P=0.008$, $n=20$, Student's *t*-test. (**h**) Histone immunoblots of Neuro2A cells treated with siScr or siSnf2h for the indicated times. Snf2h KD is observed by 48 h. Actin served as loading control. Values denote average densitometry relative to siSnf2h 24 h treatment. ($n=4$). (**i**) Proposed model of Snf2h-dependent chromatin organization. Left, Snf2h interacts with the C-terminal tail of H2A to mediate histone H1 deposition and promote higher-order chromatin compaction and terminal differentiation[32]. Right-top, Snf2h is required for normal progression through the cell cycle[35,37]. *Snf2h* cKO-Nes mice have compromised expansion of the GNP and PC progenitor pools resulting in cerebellar atrophy. Right-bottom, after cell cycle exit, Snf2h- and Snf2l-dependent chromatin remodelling drives the establishment and maintenance of gene expression profiles. The co-regulation at the *En1* locus is depicted as an example and this regulation promotes neural maturation. The embryonic removal of Snf2h (Nestin model) results in cerebellar hypoplasia and reduced dendritic arborization of PCs, causing severe ataxia and premature death. Similarly, Snf2h ablation in PCs (PCP2 model) also affects PC arborization, but conversely results in cognitive deficits rather than motor alterations.

number of DAPI dense foci at 48 h and this preceded activation of phosphorylated Caspase-3, which was only detectable at 96 h after siSnf2h KD (Supplementary Fig. 8a,b). Despite significant Snf2h KD we only observed a modest ~20% decrease in histone H1 by 96 h after siSnf2h treatment (Fig. 9h). The core histones H3 and H4 showed no change, although we observed an unexplained increase in H2A and H2B protein levels. Similar to our results with the P9 cerebellar extracts, we observed a dramatic loss of H2A signal using the C-terminal H2A antibody (Fig. 9h). In addition, we also observed reduced signal with two H2A C-terminal tail modifications, namely phosphorylation of T120 and ubiquitination at K119 (Fig. 9h). While suggestive of a H2A C-terminal tail modification upon Snf2h loss, we were unable to identify the nature of such a change. Nonetheless, our studies indicate that an integral relationship between Snf2h, H1 and H2A is critical for chromatin folding and gene expression during cerebellar development (Fig. 9i).

Discussion

Ablation of Snf2h results in the loss of functional ACF/CHRAC, WICH and NoRC remodelling complexes that collectively have a

major impact on the dynamics and organization of chromatin. Indeed, altered chromatin dynamics impaired cerebellar progenitor expansion, the transcription of key cerebellar patterning genes and the morphological maturation of PCs. As a result, *Snf2h* cKO-Nes mice developed cerebellar ataxia that resulted in their premature death, while *Snf2h* cKO-PCP2 had a normal lifespan, but displayed cognitive deficits and progressive PC death.

A key feature of the developing post-natal cerebellum is the massive expansion of GNPs, a critical event in cerebellar foliation[24]. We demonstrate that the reduced cerebellar size in *Snf2h* cKO-Nes mice results from a combination of poor GNP and PC proliferation, without altering *Shh* signalling. Several studies have implicated ACF/CHRAC and WICH complexes in the replication of heterochromatin[19,20]. The WICH complex acts behind the replication fork to re-establish the local chromatin environment while the ACF/CHRAC complex is recruited as part of the DNA damage checkpoint response to collapsed replication forks[35]. Indeed, defective replication of heterochromatin is known to result in DNA damage, mitotic catastrophe and cell death, which can have a significant effect on cell number during the proliferative phase of tissue growth[36,37]. This would be consistent with our findings of increased TUNEL staining in *Snf2h* cKO-Nes mice at the onset of GNP expansion. Similarly, RNAi depletion in HeLa or U2OS cells results in increased apoptosis 24 h after SNF2H or ACF1 protein expression was strongly reduced[37,38]. Nonetheless, several alternative explanations exist that could account for the decreased growth of the cerebellum. Reduction of histone H1 may be sufficient to induce cell cycle arrest, as found with H3 ablation studies in yeast[39]. Similarly, reduced expression of *Engrailed* and/or other GNP or PC-specific TFs may impair growth, particularly since mouse models null for *Pax6*, *Math1*, *NeuroD1*, *En2* or *En1* result in cerebellar hypoplasia[40–43]. Regardless, our experiments demonstrate a requirement for Snf2h in the proliferation of GNPs and PCs and the subsequent foliation of the cerebellum during the post-natal period.

Purkinje neurons are critical for cerebellar function and we demonstrate that Snf2h is important for the maturation and function of this cell type. We show that dendritic arborization was compromised using two different Cre-driver lines (Nestin-Cre and PCP2-Cre) to ablate Snf2h. In the *Snf2h* cKO-Nes model, the poor arborization resulted in severe motor deficits that we attribute to the combined loss of both PCs and GCs. Conversely, the *Snf2h* cKO-PCP2 model presented with cognitive abnormalities reminiscent of the Purkinje-specific *Tsc1* mouse strain with autistic-like features[44]. Indeed, dendritic defects and aberrant synaptic plasticity are common phenotypes for mouse strains inactivated for chromatin remodelling proteins[45,46]. Recent evidence shows that epigenetic regulation of synaptic plasticity extends beyond development, since electrophysiological deficits can be rescued by re-introduction of the missing CRC subunit in post-mitotic neurons[47]. Similar studies are required to dissect the individual roles of *Snf2h*-associated subunits to PC synaptic physiology and cognitive functions. In this regard, we are currently exploring whether environmental enrichment or *in vivo* re-introduction of Snf2h can rescue the motor dysfunction in *Snf2h* cKO-Nes mice.

We surmise that the dendritic defects arise from aberrant transcription of target genes, particularly given the rampant increase in deregulated genes between birth and P10 (110 genes at P0 versus ~2,900 genes at P10). High-throughput ChIP-Sequencing studies from *Drosophila* and mouse cell lines indicate that ISWI and Snf2h interact at genes ~300 bp downstream of the transcriptional start site where it localizes nucleosomes into positions that stabilize a transcriptional (active or repressed) state[25,48]. Indeed, we observed enrichment for both Snf2h and Snf2l in a similar position at the *En1* locus. The specific positioning of nucleosomes by Snf2h may also facilitate the loading of H2A.Z in progenitors, which acts to 'poise' genes for expression upon differentiation[4]. An inability to position nucleosomes around the promoter or exchange H2A for H2A.Z or macro-H2A may account for the poor regulation we observed for many genes by P10. It is also possible that Snf2h and Snf2l impart exquisite transcriptional control on developmentally important genes, as suggested by the function of known targets[13,49,50]. For example, *Foxg1* levels determine whether a progenitor undergoes self-renewal or differentiation[51] and *Snf2l* mutant mice had increased *Foxg1* expression that enhanced progenitor proliferation and increased brain size[13]. Similarly, the interaction of both Snf2h and Snf2l at the *En1* gene (co-modulation) may regulate its expression levels and/or recruitment to target loci to control PC maturation, as has been observed for the TF Olig2 and the chromatin remodeller Brg1 during oligodendrocyte differentiation[52]. We propose that Snf2h poises and/or triggers the *En1* locus for activation, while Snf2l is turned on during late cerebellar development to tightly modulate (i.e. repress) *En1* levels in the mature PC. Certainly, the interaction at co-modulated target genes may facilitate rapid and dynamic changes in gene expression induced by extrinsic signals.

Genome wide epigenetic profiling experiments have supported the hypothesis that neurogenesis is accompanied by the transition of a highly dynamic chromatin environment within progenitor cells to a more restrictive epigenetic landscape that dictates gene expression programmes specific to each lineage[2,3]. Chromatin condensation is dependent on nucleosome repeat length and the incorporation of the linker histone H1 (ref. 6,7). *In vitro* studies have shown that ISWI protein complexes assemble and evenly space nucleosomes on a chromatin template[11], while loss of ISWI function in *Drosophila* results in reduced histone H1 levels and the decondensation of the X chromosome[12,30,31]. Other studies have noted a requirement for NoRC in the formation of perinucleolar heterochromatin structures[53]. In this regard, we observed a wide range of chromatin changes in *Snf2h* cKO mice both by TEM and immunoblot including patches of condensed euchromatin, loss of histone H1, altered levels of specific histone marks and histone variants, and disorganized nucleolar structures that collectively indicate that chromatin organization is abnormal. As discussed above, aberrant heterochromatin formation during replication could lead to mitotic catastrophe and cell death of the GNPs, thereby accounting for the cerebellar hypoplasia we observed. In addition, aberrant nucleosome spacing and maintenance of nucleosome-free regions could disrupt gene expression programs that could result in the maturation defects we observed and the progressive cell death, perhaps initiated in a cell with an inability to respond to an external signal. While we favour the idea that Snf2h loss promotes changes in chromatin structure directly, resulting in an inability to function and subsequent death, we cannot rule out that the chromatin disorganization we observed in Snf2h-null cells is indirect and representative of cells that were in the early stages of programmed cell death. Future studies will aim to distinguish between these possibilities.

Higher-order chromatin packaging is dependent on histone H1 as embryos lacking three histone H1 subtypes (H1c, H1d and H1e) die by mid-gestation with a broad range of defects[54]. Histone H1 has been shown to play a key role in silencing gene expression by tethering Su(var)3–9 to heterochromatin[55]. Unlike core histones, which display very slow kinetics with residence time in the range of hours, linker histones are highly mobile, and more recently were shown to have metastable states with partially bound molecules[56,57]. Indeed, H1 dynamics reflects cell plasticity and chromatin compaction in general[33]. This may explain the

modest ~10% reduction in H1e-GFP mobility observed upon Snf2h depletion in Neuro2A cells. Whereas this mobility was restored upon hSNF2H or hSNF2L overexpression, these measurements may only reflect the unbound H1 pool. Nonetheless, our evidence suggests that Snf2h loss results in abnormal higher-order chromatin packaging that disrupts genome organization and chromatin fluidity.

Recent studies have demonstrated that the C-terminal tail of histone H2A is required for histone H1 loading and for Snf2h-dependent nucleosome translocation[32]. Indeed, the altered H1 levels and abnormal H2A post-translational processing in *Snf2h* cKO-Nes mice is suggestive of a functional relationship between Snf2h, histone H1 and H2A. We propose that an interaction between H2A and Snf2h may alter the accessibility of the H2A C-tail for loading histone H1 onto chromatin to facilitate chromatin packaging. In this regard, biochemical studies have shown that removal of the H2A C-tail increased the mobility of nucleosomes *in vitro*[32,58]. Such a mechanism for increasing the mobility of the nucleosome may be a compensatory response in the *Snf2h* cKO mice to facilitate nucleosome spacing and chromatin compaction, a function normally provided by Snf2h-dependent chromatin remodelling. In addition, Snf2h interactions with the H2A tail could promote H2A/H2B dimer removal and subsequent H2A variant exchange to activate and/or repress gene activity. Within progenitor cells these functions could mark genes for expression (H2A.Z loading) or repression (macro-H2A loading) upon differentiation, while establishing the restrictive chromatin landscape (through histone H1 loading) that accompanies the transition from progenitor expansion to terminal differentiation[59,60]. While exciting, such mechanisms remain speculative and the exact relationship between Snf2h loss and H2A C-tail post-translational processing remains to be deciphered with more biochemical studies. Indeed, delineating the epigenetic regulation of neuronal development is crucial to our understanding of intellectual-disability disorders caused by mutations in epigenetic modifying enzymes. As a whole, our findings highlight the complexity and functional diversity of Snf2h-containing CRCs during brain development, and their roles in controlling chromatin organization as cells modulate their chromatin environment from a 'largely open' progenitor state to the 'highly restricted' state of a fully differentiated neuron during cerebellar morphogenesis and neural maturation (Fig. 9i)[60].

Methods

Generation of Snf2h$^{fl/fl}$ mice. *Snf2h$^{exon5fl/exon5fl}$* (*Snf2h$^{fl/fl}$*) mice were generated through homologous recombination in WW6 ES cells as described[14]. Briefly, a 6.0-kb fragment of the Snf2h gene containing exons 4–8, into which loxP sites were inserted 5′ and 3′ of exon 5, was cloned into the pEasyFlirt vector (a gift of Dr M.P. Lisanti, University of Manchester, UK). This vector has a neomycin resistance gene flanked by Frt sites, which was removed in mice generated from correctly targeted ES cells by breeding to *Flp1* recombinase mice[61]. *Snf2h$^{fl/fl}$* mice were viable, fertile and did not exhibit any gross behavioural abnormalities. Cre-mediated deletion of *Snf2h* exon 5 was tested by breeding to ZP3-Cre mice[62] for which embryos homozygous for a deleted exon 5 died *in utero* due to abnormal progenitor expansion, as previously described[14].

Mouse breeding. *Snf2h$^{fl/fl}$* mice were backcrossed for six generations to a C57Cl/6 background and bred with a C57Bl/6 Nestin-Cre$^{-/+}$ driver line[16] that also carried a *Snf2h* null allele[14], thereby generating *Snf2h* cKO-Nes mice (*Snf2h$^{-/fl}$*::Nes-Cre$^{-/+}$). We also bred *Snf2h$^{fl/fl}$* mice to the PCP2-Cre driver line[17] that lived normally into adulthood and showed no gross behavioural abnormalities. For *Snf2l* ablation, we used the previously characterized Ex6Del line[13] for breeding, thus generating *Snf2l-/y*::*Snf2h* cKO (cDKO-Nes) and *Snf2l−/y*::*Snf2h* cKO-PCP2 (cDKO-PCP2), as well as *Snf2l−/+*::*Snf2h* cKO-Nes and *Snf2l−+*::*Snf2h* cKO-PCP2 compound heterozygotes. For embryo staging, embryonic day 0.5 (E0.5) was defined as noon on the day of vaginal plug detection. Animals were kept in an animal house under specific pathogen-free conditions in a 12/12 light:dark cycle with water and food *ad libitum*. The University of Ottawa Animal Care and Use Committee approved all experiments. C57Bl/6 and FVBN/J wild type mice were purchased from Charles River (Montreal, QC, Canada). PCP2-Cre mice were obtained from The Jackson Laboratory (Stock no. 004146; Bar Harbor, ME, USA).

Behavioural analysis. All behavioural tests were completed in the Behavior Core Facility at the University of Ottawa using standardized protocols. Animals were habituated to the testing room at least ~1 h before testing. Behavioural assays were performed irrespective of sex for *Snf2h* cKO-Nes mice and tested between P20-P25. For *Snf2h* cKO-PCP2 mice, female and male mice were assessed independently at 4–6 months of age, for which we did not observe sex-specific differences in behaviour and pooled the data. For behavioural assays, one-way ANOVA was used for at least 10 mice per genotype. The values are presented as the mean ± s.e.m.

Suspended wire test. Mice were suspended by their forepaws on a 2 mm wire, and the amount of time they remained on the wire was recorded.

Dowel test. Mice were placed in the centre of a horizontal pole (1 cm diameter) and the time mice remained on the pole was recorded. If mice walked across and off the dowel, they were placed back onto the dowel. Trials lasted for a maximum of 2 min.

Elevated platform. Mice were placed in the centre of a 15-cm^2 round elevated platform 50 cm above the ground and the time mice remained on the platform was recorded. Student's *t*-test was used for statistical significance.

Rotarod. Mice were trained and tested on the accelerated rotarod (rod diameter 3 cm) for 300 s for five times before measurements (IITC, Woodland Hills, CA, USA). Starting speed was set at 4 r.p.m. and maximum speed at 40 r.p.m. The latency to fall from the rotarod was recorded. If animals were able to stay on the rod for 300 s, the latency to fall recorded was 300 s. The animals received four trials per day, with a trial interval of 30 min, for 2 consecutive days.

Pole test. Mice were placed head-upward on the top of a rough surfaced vertical pole (8 mm diameter × 55 cm tall) and the time for descending recorded. The time required for the mouse to turn downward after placing and the total time on the pole until the mouse reaches the bottom is recorded. Mice were trained for 2 days before test. Five trials were averaged on day 3.

Open field. Animals were placed in the centre of a 45 × 45 × 45-cm chamber equipped with photobeams (Accuscan) to record activity during a 10-min test period.

Elevated plus maze. Animals were habituated to the test room for at least 2 days before test. Animals were placed in the centre of a maze consisting of two arms (each arm 5 cm wide × 60 cm long) enclosed by ~15-cm-high walls, and two open arms (each arm 25 × 7.5 cm, with a raised 0.5 cm lip at edges) elevated 1 metre above ground and with equidistant arms from the centre of the platform. The amount of time the animals spent in the open or closed arms, the total number of entries and the total distance travelled were recorded for 10 min using video detection software (Ethovision, Wageningen, Netherlands).

Social interactions. A control mouse is placed in the corner of an open field box (under dim red light) that measures 45 cm long on each side × 45 cm high and containing a 5.5 × 9.6 cm wire mesh rectangular cage. The mouse is given 5 min to explore the arena and then removed. A few seconds later, a test mouse (or social target) of the same strain, age and gender is placed inside the rectangular wire mesh cage and the control mouse placed back in the arena. The time the social target interacts with the control mouse in 5 min trials is recorded using Ethovision 7 XT automatic tracking software. Total distance travelled, time spent in two corners across the wire mesh cage and velocity is also recorded.

Fear conditioning. On the first day (training), the animal is placed in the fear-conditioning apparatus for a total of 6 min. After the first 2 min in the apparatus a tone is played for 30 s ending with a 2-s shock. One minute following the shock, the tone is played again for 30 s ending with a 2-s foot shock. For the remaining 2 min there is no tone or shock. The freezing behaviour of the animal is recorded throughout the 6 min. This is the training in which the mouse receives two exposures to the tone followed by the shock and this occurs in a novel context, which is the conditioning box. On the second day, contextual conditioned fear testing begins. This measures the fear associated with being in the same environment where the shock was delivered (done ~24 h after training). The mouse is placed in the same apparatus with all the same lighting and room conditionings for 6 min and freezing behaviour is recorded.

BrdU-birthdating. Timed-pregnant females were injected intraperitoneally with 100 µg per g body weight of 5-bromo-2′-deoxyuridine (BrdU; Sigma) and pups killed at indicated times. For BrdU-pulse labelling, timed-pregnant females were injected with BrdU and killed 90 min later. For BrdU immunodetection, sections were incubated in 2 N HCl for 10 min at 37 °C, rinsed in 0.1 M sodium borate

(pH 8.3), blocked and incubated overnight at 4 °C with rat monoclonal anti-BrdU antibody 1:300 (Abcam no. 6326). The average number of immunopositive cells was determined from five separate fields under ×40 magnification in confocal Z-stacks (or cubic bins) of 18×10^3 μm^3.

TUNEL assay. Sections were examined for DNA fragmentation with the TUNEL *in situ* cell death detection kit (Roche Applied Science, ON, Canada) according to the manufacturer's instructions. The average number of TUNEL-positive cells was determined from five separate fields under ×40 magnification in cubic bins.

Golgi–Cox staining. Golgi staining was completed using FD Rapid GolgiStain Kit (FD NeuroTechnologies). Briefly, P20 mice were intracardially perfused with 4% paraformaldehyde (PFA) in 0.1 M PBS and stained according to the manufacturer's instructions. Tissues were sectioned at 60–100 μm and mounted on gelatin-coated slides.

Immunofluorescent histochemistry. For embryonic tissue, 16–20 μm sections were used. For post-natal brains, 40–50 μm free-floating sections were used. Sections were washed four times in PBST (PBS with 0.1% Triton X-100), blocked (1 h, room temperature (RT)) in 10% horse serum/PBST, and incubated (overnight, 4 °C) in primary antibodies. The following primary antibodies were used from Abcam: rabbit anti-Snf2h (1:500, no. 72499); rabbit anti-Snf2l (1:100, no. 37003); mouse anti-NeuroD1 (1:500, no. 60704); rat anti-BrdU (1:300; no. 6326) and rabbit anti-Engrailed (1:500; no. 32817). Mouse anti-calbindin (1:200, Sigma C9848); rabbit anti-calbindin (1:300, Sigma C2724); rabbit anti-GFP (1:1,000, Molecular Probes); mouse anti-BrdU (1:100, DAKO); rabbit anti-phospho histone H3 (pH3; 1:200; Millipore no. 06-570); rabbit anti-Pax6 (1:200; Covance no. PRB-278P); mouse anti-NeuN (1:200, Millipore no. MAB377) and rabbit anti-pan-Engrailed (gift of Dr Alexandra Joyner, Memorial Sloan-Kettering Cancer Center, NY, USA). The following day, sections were washed five times in PBST and incubated (2 h, RT) with DyLight^{488}, DyLight^{594} or DyLight^{649}-conjugated mouse pre-adsorbed secondary antibodies (1:1,000, Jackson Immunoresearch, PA, USA) against the IgG domains of the primary antibodies. All sections were counterstained with the nuclear marker DAPI (Invitrogen). Sections were mounted on slides with Dako Fluorescence Mounting Medium (Dako Canada, ON, Canada).

X-Gal staining. Staged embryos were quickly dissected and rinsed in 0.1 M PBS (pH 7.4) and fixed in 4% PFA for 30 min. Embryos were then rinsed three times with 0.1 M PBS supplemented with 0.01% Triton X-100 and incubated for ~1 h in the dark with staining solution (2 mM $MgCl_2$, 0.02% NP-40, 5 mM potassium ferricyanide, 5 mM potassium ferrocyanide and 0.01% sodium deoxycholate in 0.1 M PBS, pH 7.4). Staining solution was rinsed off three times with 0.1 M PBS and embryos post-fixed for 30 min in 4% PFA.

***In situ* hybridization.** *In situ* hybridization was performed from E18.5 or P0 14–16 μm sections through the cerebellar vermis using digoxigenin (DIG)-labelled antisense RNA riboprobes prepared by *in vitro* transcription from linearized plasmids containing complete or partial cDNA sequences of the following mouse genes: *Shh*, *Gli1*, *Mycn*, *Ptch1*, *Ccnd1* and *Pax6*. Labelling of RNA probes with DIG-UTP was performed according to the manufacturer's recommendations. Briefly, 1 μg of linearized template was transcribed in a total volume of 20 μl using T7 or T3 polymerase (Roche) and DIG-UTP (Roche) for 1 hour at 37 °C. The reaction products were precipitated, resuspended in 100 μl of 10 mM EDTA and stored at −20 °C. DIG-labelled RNA probes were diluted in hybridization buffer (50% formamide, 10% dextran sulphate, 1 mg ml^{-1} yeast RNA, 1× Denhardt's and 1× salt) and denatured for 10 min at 70 °C. Sections were hybridized overnight at 65 °C in a humidified box. The slides were washed twice in 50% formamide, 1× SSC, 0.1% Tween 20 at 65 °C for 30 min followed by two washes in MABT (100 mM maleic acid, 150 mM NaCl, pH 7.5, 0.1% Tween-20) for 30 min at RT. Sections were blocked for 1 h at RT in MABT containing 20% sheep serum (Sigma) and 2% blocking reagent (Roche). The blocking solution was then replaced with blocking solution containing a 1:1,500 dilution of alkaline-phosphatase-conjugated Fab fragments of sheep anti-DIG antibodies (Roche) and the slides were incubated overnight at 4 °C in a humidified box. Slides were washed five times in MABT for 20 min at RT, twice in staining buffer (100 mM NaCl, 50 mM $MgCl_2$, 100 mM Tris pH 9.5 and 0.1% Tween-20) and incubated for 1–5 h in staining buffer containing 10% polyvinyl alcohol, 4.5 μl ml^{-1} NBT and 3.5 μl ml^{-1} BCIP (Roche) in the dark at RT. Slides were washed several times in 1× PBS and mounted in 50:50 glycerol:PBS.

Western blotting. Cerebellar or hindbrain (for E12 and E17 time points only) extracts were quickly dissected from individual pups and snap-frozen in dry ice. Cerebella were then homogenized in ice-cold RIPA buffer supplemented with protease inhibitor cocktail (Sigma) and incubated for 20 min on ice with gentle mixing. After pre-clearing by centrifugation (15 min at 17,000 *g*), proteins were quantified by the Bradford method. Protein samples were resolved on sodium dodecyl sulphate polyacrylamide gels under denaturing conditions or using Bis-Tris 4–12% and Tris-Acetate 3–8% gradient gels (NuPage, Invitrogen) and blotted onto PVDF membranes (Immobilon-P; Millipore, MA, USA) by wet transfer for 1–2 h at 90 V. Membranes were blocked (45 min, RT) with 5% skim milk in TBST (Tris-buffered saline containing 0.05% Triton X-100), and incubated (4 °C, overnight) with the following antibodies: rabbit anti-Snf2h (1:4,000; Abcam no. 72499); sheep anti-Snf2l (1:2,000)[63]; mouse monoclonal anti-Snf2l 1:1,000 (Alvarez-Saavedra and Picketts, unpublished); mouse anti-ß-actin (1:30,000, Sigma); rabbit anti-Engrailed-1 (1:2,000, Millipore) or mouse anti-Engrailed 4G11 (1:20, Developmental Studies Hybridoma Bank). Membranes were incubated (1 h, RT) with ImmunoPure HRP-conjugated goat anti-rabbit or goat anti-mouse IgG (H + L) secondary antibodies (1:50,000; Pierce, Rockford, IL, USA). Membranes were washed 5 × 5 min in TBST after antibody incubations, and the signal was detected using the Pierce Supersignal West Fempto chemiluminescence substrate (Pierce). Western blots were quantified using ImageJ software (rsbweb.nih.gov/ij/). At least four individual lanes from multiple litters were used for quantification. All original western blots are shown in Supplementary Fig. 9.

Chromatin immunoprecipitation. Cerebella was isolated from C57Bl/6 wild-type mice and cell pellets resuspended in 50 mM HEPES-KOH, pH 7.5, 140 mM NaCl, 1 mM EDTA, 1% Triton X-100, 0.1% sodium deoxycholate, 0.1% SDS and protease inhibitor cocktail and incubated on ice for ~30 min. Cells were then sonicated for 100 cycles (30 s pulse, 30 s rest intervals) to an average size of ~500–800 bp using a 4 °C sonicator (Bioruptor UCD-200, Diagenode, Inc., Sparta, NJ, USA). After sonication, cell debris was pelleted by centrifuging 2 min, 4 °C at 8,000 *g*. Supernatant was collected and a 20 μl input sample was analysed on a 2% agarose gel to verify chromatin size. Additionally, 100 μl of recovered chromatin was used for DNA quantification and as qPCR positive control (Input). GammaBind Plus Sepharose Beads (GE Healthcare, Piscataway, NJ, USA; Cat. No. 17-0886-01) were blocked with BSA (100 ng μl^{-1} beads; New England Biolabs, Ipswich, MA, USA) and salmon sperm DNA (100 ng μl^{-1} beads; Invitrogen) for 30 min at RT. Beads were washed three times with RIPA buffer (50 mM Tris–Cl, pH 8, 150 mM NaCl, 2 mM EDTA, pH 8, 1% NP-40, 0.5% sodium deoxycholate, 0.1% SDS with protease inhibitor cocktail) and resuspended in two volumes of RIPA. Pre-clearing of recovered chromatin was performed by incubating with 100 μl of blocked GammaBind Plus Sepharose Bead slurry for 30 min at 4 °C. Beads were centrifuged for 2 min, 4 °C at 8,000 *g*, and pre-cleared chromatin was recovered and further diluted 1:10 in RIPA for IP. IP was performed overnight at 4 °C by incubating ~50 μg of pre-cleared chromatin with 2 μg of the following rabbit antibodies from Abcam: anti-Snf2h; anti-Snf2l; anti-histone H3; or rabbit IgG (Jackson Immunoresearch). We also used anti-H3K9Ac; and anti-H3K9Me3 as internal controls. Immune complexes were captured with 120 μl of blocked GammaBind Plus Sepharose Bead slurry for 2 h at 4 °C. Beads were then collected by centrifuging for 2 min at 8,000 *g*. Beads were washed three times with 20 mM Tris–Cl, pH 8, 150 mM NaCl, 0.1% SDS, 1% Triton X-100 and 2 mM EDTA, pH 8, and once with 20 mM Tris–Cl, pH 8, 500 mM NaCl, 0.1% SDS, 1% Triton X-100 and 2 mM EDTA (pH 8). DNA was eluted with 150 μl of elution buffer (1% SDS, 100 mM $NaHCO_3$) for 15 min at RT. Eluted DNA was further diluted in two volumes of elution buffer and incubated overnight at 65 °C with 100 μg of proteinsase K (Invitrogen) for crosslink reversal. The DNA was phenol–chloroform-extracted and resuspended in 100 μl of TE, pH 8 (10 mM Tris–Cl, pH 8, 1 mM EDTA, pH 8). In all, 1 μl (1/100th) of DNA was used per reaction for quantitative PCR analysis. Triplicate or quadruplicate samples were ran per reaction and three independent ChIP experiments were carried out per time point. Primers are listed in Supplementary Table 1.

Quantitative real-time PCR. For qPCR analysis of ChIP DNA, PCRs were carried out using the SYBR Green Advantage qPCR premix (Clontech) and run under the following conditions: one cycle at 95 °C for 1 min, 45 cycles at 95 °C for 10 s, 60 °C for 10 s and 72 °C for 20 s. All primers were analysed by melt curve analysis and agarose gel electrophoresis after qPCR amplification. Primers are listed in Supplementary Table 1. The ΔΔCt method was used to compare fold-change. L32 was used as internal control. Triplicate or quadruplicate samples were ran per reaction and a minimum of three mice were analysed per genotype. Student's *t*-test was used for statistical significance.

Reverse transcription. Cerebella were quickly dissected from mutant and control littermates and RNA was isolated using Trizol (Invitrogen) according to the manufacturer's instructions. Glycogen (Ambion) was used as carrier. One microgram of total RNA was reverse-transcribed using random primers and SuperScriptIII (Invitrogen). cDNA was further diluted 1:20 and 1 μl was used per qPCR (described above). RNA integrity is shown in Supplementary Fig. 9

Microarrays. Gene expression profiling was performed on RNA isolated from dissected cerebella tissue of P0 or P10 *Snf2h* cKO-Nes and wild-type control mice. RNA samples were labelled with Cy5 or Cy3 using 3DNA Array 900 kits (Genisphere, Hatfield, PA, USA) following the manufacturer's instructions. *Snf2h* cKO-Nes and control samples were then cohybridized to MEEBO 38.5K arrays (Microarrays Inc., Huntsville, AL, Canada). A total of four replicates were performed for P0 and three for P10 and in both cases the labelling dyes were flipped

for at least one replicate to counter dye bias. Probe-specific signals were quantified using the ScanArray express (Perkin Elmer, Waltham, MA). On the resulting raw background subtracted signals intra-array normalization (correcting for Cy5/Cy3 bias) was performed with global loess, inter-array normalization with the quantile method and statistical analysis via the WEBARRAY online tool (http://www.webarraydb.org/webarray/index.html). M ($\log_2$ ratio of *Snf2h* cKO/control signal) and A values ($\log_2$ average signal strength) were then determined for all probes. A probe (gene) was scored as differentially expressed on an array if it demonstrated a *P*-value <0.01, and had sufficient detectable signals across all replicates (A value ($\log_2$) >7).

Microarray filtering. Cell-type-specific gene expression from P0 and P10 *Snf2h* cKO-Nes cerebellar arrays was determined by comparing the differentially expressed genes with the cell-type-specific gene expression lists from publicly available RNA-Seq data from adult cerebellar PCs, GCs and BG[26]. The unique gene identifiers of the differentially expressed genes from our arrays and from the RNA-Seq datasets were converted to MGI-approved gene symbols. This conversion ensures that genes presented with synonyms are not missed during the comparisons. The MGI symbols from the differentially expressed genes in our arrays were compared with each cell-type-specific gene list and reported as differentially expressed genes from *Snf2h* cKO-Nes cerebella in the corresponding cell types.

Image acquisition and processing. Tissue sections were examined and images captured using a Zeiss 510 laser scanning confocal microscope with UV (405 nm), argon (488 nm), helium/neon (546 nm) and helium/neon (633 nm) lasers. All images were acquired as 10–30 µm Z-stacks (in 1–2 µm intervals) and analysed as projections using the LSM 510 Image Browser software (Zeiss, Oberkochen, Germany). Epifluorescent and light microscopy images were acquired with a Zeiss Axiovert Observer Z1 epifluorescent/light microscope equipped with an AxioCam cooled-color camera (Zeiss). Images were exported to Adobe Photoshop CS5 (Adobe Systems Inc., San Jose, CA, USA) and further processed for contrast when necessary.

Acid-based histone extraction. Histones were acid-extracted from P2 and P9 *Snf2h* cKO and control cerebella or from Neuro2A cells after siRNA treatment. Briefly, cerebellar tissue was quickly dissected and separated from the inferior and superior colliculi and brain stem and snap-frozen on dry ice. Then, tissue was homogenized in TEB + buffer (0.1 M PBS, 0.5% Triton X-100, 5 mM sodium butyrate, 0.02% NaN3 complemented with protease inhibitors cocktail (Sigma)), lysed on ice for 20 min and centrifuged for 10 min at 2,000 r.p.m. at 4 °C. Then, the supernatant was discarded and the pellet resuspended in 0.2 N HCl at a cell density of 4×10^7 cells per ml overnight with stirring at 4 °C. Samples were then centrifuged for 10 min at 2,000 r.p.m. at 4 °C and supernatant containing free histones collected and quantified for western blotting. The following antibodies were used from Active Motif: anti-histone H1 1:4,000 (no. 61201); anti-H2A acidic patch N-terminal 1:4,000 (no. 39111); anti-H2A C-terminal (no. 39591); anti-H2A T120ph 1:2,000 (no. 61195); anti-H2B 1:4,000 (no. 39125); anti-H2B K120Ac 1:4,000 (no. 39119); anti-macro-H2A1 1:1,000 (no. 39593). From Abcam: anti-H3 1:30,000 (no. 1791); anti-H4 1:5,000 (no. 10158); anti-H2AZ 1:5,000 (no. 4174); anti-H3K4Me3 1:10,000 (no. 8580); anti-H3K9Me3 1:5,000 (no. 8898) and anti-H3K18Ac 1:5,000 (no. 1191). From Millipore: anti-H3K36Me2 1:1,000 (no. 07-274); anti-pan-H3Ac 1:5000 (no. 382158) and anti-H2A K119Ub1 1:2000 (no. 8240; Cell Signaling). In all, 3–5 µg of total histones were loaded onto 15% SDS–PAGE linear gels and immunoblotted as described above. All original western blots are shown in Supplementary Fig. 9. Colloidal Blue Staining Kit (Invitrogen) was used to assess histone stoichiometry in 18% SDS–PAGE linear gels as indicated by the manufacturer.

Vector construction. Human SNF2L cDNA comprising the entire open reading frame (+exon1/−exon13/+NLS) was amplified from a pcDNA3 expression plasmid[64] in a two-step process. The 5′ end of SNF2L cDNA was amplified with SNF2L-EcoRI-Fwd (5′-TAAGGAATTCATGGAGCA-3′) and SNF2L-XhoI-Rev-internal (5′-ACCTCTCGAGCTATGT-3′) primers, followed by purification of the PCR products, restriction digest by EcoRI and XhoI, and directional subcloning into the pBRIT-LoxP-NTAP and pBRIT-LoxP-CTAP retroviral plasmid vectors, which have been previously described[65]. The remaining 3′ sequence of SNF2L was then subcloned non-directionally following amplification with SNF2L-XhoI-Fwd-internal (5′-ATAGCTCGAGAGGTAG-3′) and SNF2L-XhoI-Rev (5′-ATGCTCGAGGGATTTCACCTTCTTG-3′) primers and a restriction digest with XhoI. Similarly, SNF2H cDNA comprising the entire open reading frame was cloned into the pCI-neo expression vector (Promega Corp. Madison, WI, USA) then amplified with the SNF2H-BamHI-Fwd (5′-AAAAGGATCCATGTCGTCC GCGGCCGAGCC-3′) and SNF2H-XhoI-Rev (5′-AAAACTCGAGTAGTTTCAGC TTCTTTTTTCTTCC-3′) primers and directionally subcloned into the pBRIT-LoxP-NTAP and pBRIT-LoxP-CTAP vectors, following restriction digest with BamHI and XhoI. All clones were verified by sequencing at McGill University and Génome Québec Innovation Centre (Montreal, QC, Canada).

siRNA knockdown on Neuro2A cells. Neuro2A cells were freshly obtained from ATCC (Manassas, VA, USA) and grown in DMEM medium containing 10% FBS, L-glutamine and no antibiotics. Briefly, cells were grown to a confluency of ~80% and transfected using Lipofectamine 2000 (Invitrogen) with 75 nM siSnf2h (Thermo Scientific, Ottawa, ON, Canada; siGENOME, mouse *Smarca5*, D-041484-03); 75 nM siScrambled (siGENOME non-targeting siRNA no. 1, D-001210-01-05); or 75 nM siSnf2l (OriGene Technologies, Inc, Rockville, MD, USA; *Smarca1* (mouse) no. SR421862B). Total proteins or acid-extracted histones were collected as described above and analysed by immunoblotting.

Fluorescence recovery after photobleaching. Neuro2A cells were grown in DMEM medium containing 10% FBS, L-glutamine and 1 × penicillin/streptomycin. H1e-GFP plasmid has been previously described[34]. FRAP experiments were conducted essentially as described[33]. Cells were grown in eight-well µ-slides (ibidi LLC, Martinsried, Germany) and transfected with H1e-GFP plasmid together with 75 nM of each of the siRNAs using Lipofectamine 2000 (Invitrogen). For hSNF2H and hSNF2L 'addback' studies, pBRIT-FLAG-hSNF2H or pBRIT-FLAG-hSNF2L was added to the transfection mix. Photobleaching studies were performed using a Revolution spinning disk (CSUX, Yokogawa, Japan) and an EMCCD high-speed imaging system (Andor Technology, Belfast, UK) equipped with a FRAPPA module (Andor Technology) and with solid-state lasers mounted on an Olympus IX81 fully automated microscope. During the entire imaging process, cells were maintained under controlled CO_2, temperature and humidity using an environmental chamber (Life Imaging Services, Basel, Switzerland). Bleaching was performed with a × 60 oil objective (NA = 1.4). Images were captured every 250 ms using an EMCCD iXon + camera (Andor, UK). Typically 240 post-bleach images were collected. Data from more than 20 cells were collected per experiment. All FRAP experiments were performed at least three times and plots for one representative experiment are shown. Data processing was performed using the easyFRAP program[66], based on the double normalization method[67]. Curve fitting was performed using MATLAB's non-linear least-squares function. The method to calculate fully normalized recovery curves has been described previously[68]. This method was used to estimate the mobile protein fraction and t-half of protein. Two-tailed Student's *t*-test was used to compare the significance of differences between FRAP curves[69].

Transmission electron microscopy. Cerebella (E18.5, P7 and P21) were collected under a stereomicroscope, cut into sections of 1–2 mm thickness through the cerebellar vermis region and fixed for at least 4 h to overnight in Karnovsky's fixative (4% PFA, 2% glutaraldehyde and 0.1 M cacodylate in phosphate-buffered saline, pH 7.4) at 4 °C. These specimens were subsequently washed twice in 0.1 M cacodylate buffer for 1 h and once overnight at RT. Sections were then post-fixed with 1% osmium tetroxide in 0.1 M cacodylate buffer for 1 h at 4 °C, and washed twice for 5 min in water. The specimens were dehydrated twice for 20 min for each step in a graded series of ethanol from water through 30–50–70–85–95% ethanol and twice for 30 min in 100% ethanol (molecular sieves were used to dehydrate ethanol), followed by twice for 15 min in 50% ethanol/50% acetone and twice for 15 min in 100% acetone. Sections were infiltrated in 30% spurr/acetone for 15 h (overnight) then in 50% spurr/acetone for 6 h and in fresh 100% spurr resin overnight. Spurr was changed twice a day for 3 days at RT. All infiltration steps were carried out on a rotator. Sections were then embedded in fresh liquid spurr epoxy resin and polymerized overnight at 70 °C. Ultrathin sections (80 nm) from the cerebellar vermis were collected onto 200-mesh copper grids and allowed to dry overnight before staining. Grids were stained with 2% aqueous uranyl acetate and with Reynold's lead citrate. Sections were observed under a transmission electron microscope (Hitachi 7100). All ultrastructural analyses were based on at least three mice per genotype of the same age for each group examined.

Toluidine blue staining. Semithin sections of 0.5 µm were stained with 1% toluidine blue and 2% borate in distilled water. Histological samples were scanned with a MIRAX MIDI automated scanning light microscope (Zeiss) and images processed with Zeiss MIRAX Viewer software (Zeiss).

Statistics. Group statistical analysis was performed via two-tailed Student's *t*-test or one-way ANOVA, where indicated. $P<0.05$ was accepted as statistically significant. At least three mice per genotype were used for evaluation. Values are presented as the mean ± s.e.m.

References

1. Lasalle, J. M., Powell, W. T. & Yasui, D. H. Epigenetic layers and players underlying neurodevelopment. *Trends Neurosci.* **36,** 460–470 (2013).
2. Xie, W. *et al.* Epigenomic analysis of multilineage differentiation of human embryonic stem cells. *Cell* **153,** 1134–1148 (2013).
3. Hawkins, R. D. *et al.* Distinct epigenomic landscapes of pluripotent and lineage-committed human cells. *Cell Stem cell* **6,** 479–491 (2010).
4. Creyghton, M. P. *et al.* H2AZ is enriched at polycomb complex target genes in ES cells and is necessary for lineage commitment. *Cell* **135,** 649–661 (2008).

5. Hattori, N., Niwa, T., Kimura, K., Helin, K. & Ushijima, T. Visualization of multivalent histone modification in a single cell reveals highly concerted epigenetic changes on differentiation of embryonic stem cells. *Nucleic Acids. Res.* **41,** 7231–7239 (2013).
6. Robinson, P. J. *et al.* 30 nm chromatin fibre decompaction requires both H4-K16 acetylation and linker histone eviction. *J. Mol. Biol.* **381,** 816–825 (2008).
7. Routh, A., Sandin, S. & Rhodes, D. Nucleosome repeat length and linker histone stoichiometry determine chromatin fiber structure. *Proc. Natl Acad. Sci. USA* **105,** 8872–8877 (2008).
8. Hauk, G. & Bowman, G. D. Structural insights into regulation and action of SWI2/SNF2 ATPases. *Curr. Opin. Struct. Biol.* **21,** 719–727 (2011).
9. Elfring, L. K., Deuring, R., McCallum, C. M., Peterson, C. L. & Tamkun, J. W. Identification and characterization of Drosophila relatives of the yeast transcriptional activator SNF2/SWI2. *Mol. Cell Biol.* **14,** 2225–2234 (1994).
10. Lazzaro, M. A. & Picketts, D. J. Cloning and characterization of the murine Imitation Switch (ISWI) genes: differential expression patterns suggest distinct developmental roles for Snf2h and Snf2l. *J. Neurochem.* **77,** 1145–1156 (2001).
11. Erdel, F. & Rippe, K. Chromatin remodelling in mammalian cells by ISWI-type complexes—where, when and why? *FEBS J.* **278,** 3608–3618 (2011).
12. Deuring, R. *et al.* The ISWI chromatin-remodeling protein is required for gene expression and the maintenance of higher order chromatin structure *in vivo*. *Mol. Cell* **5,** 355–365 (2000).
13. Yip, D. J. *et al.* Snf2l regulates Foxg1-dependent progenitor cell expansion in the developing brain. *Dev. Cell* **22,** 871–878 (2012).
14. Stopka, T. & Skoultchi, A. I. The ISWI ATPase Snf2h is required for early mouse development. *Proc. Natl Acad. Sci. USA* **100,** 14097–14102 (2003).
15. Corona, D. F. *et al.* ISWI is an ATP-dependent nucleosome remodeling factor. *Mol. Cell* **3,** 239–245 (1999).
16. Berube, N. G. *et al.* The chromatin-remodeling protein ATRX is critical for neuronal survival during corticogenesis. *J. Clin. Invest.* **115,** 258–267 (2005).
17. Barski, J. J., Dethleffsen, K. & Meyer, M. Cre recombinase expression in cerebellar Purkinje cells. *Genesis* **28,** 93–98 (2000).
18. Maren, S. Neurobiology of Pavlovian fear conditioning. *Annu. Rev. Neurosci.* **24,** 897–931 (2001).
19. Poot, R. A. *et al.* HuCHRAC, a human ISWI chromatin remodelling complex contains hACF1 and two novel histone-fold proteins. *EMBO J.* **19,** 3377–3387 (2000).
20. Bozhenok, L., Wade, P. A. & Varga-Weisz, P. WSTF-ISWI chromatin remodeling complex targets heterochromatic replication foci. *EMBO J.* **21,** 2231–2241 (2002).
21. Wallace, V. A. Purkinje-cell-derived Sonic hedgehog regulates granule neuron precursor cell proliferation in the developing mouse cerebellum. *Curr. Biol.* **9,** 445–448 (1999).
22. Wechsler-Reya, R. J. & Scott, M. P. Control of neuronal precursor proliferation in the cerebellum by Sonic Hedgehog. *Neuron* **22,** 103–114 (1999).
23. Dahmane, N. & Ruiz i Altaba, A. Sonic hedgehog regulates the growth and patterning of the cerebellum. *Development* **126,** 3089–3100 (1999).
24. Sillitoe, R. V. & Joyner, A. L. Morphology, molecular codes, and circuitry produce the three-dimensional complexity of the cerebellum. *Annu. Rev. Cell Dev. Biol.* **23,** 549–577 (2007).
25. Sala, A. *et al.* Genome-wide characterization of chromatin binding and nucleosome spacing activity of the nucleosome remodelling ATPase ISWI. *EMBO J.* **30,** 1766–1777 (2011).
26. Mellen, M., Ayata, P., Dewell, S., Kriaucionis, S. & Heintz, N. MeCP2 binds to 5hmC enriched within active genes and accessible chromatin in the nervous system. *Cell* **151,** 1417–1430 (2012).
27. Sillitoe, R. V., Vogel, M. W. & Joyner, A. L. Engrailed homeobox genes regulate establishment of the cerebellar afferent circuit map. *J. Neurosci.* **30,** 10015–10024 (2010).
28. Wilson, S. L., Kalinovsky, A., Orvis, G. D. & Joyner, A. L. Spatially restricted and developmentally dynamic expression of engrailed genes in multiple cerebellar cell types. *Cerebellum* **10,** 356–372 (2011).
29. Wurst, W., Auerbach, A. B. & Joyner, A. L. Multiple developmental defects in Engrailed-1 mutant mice: an early mid-hindbrain deletion and patterning defects in forelimbs and sternum. *Development* **120,** 2065–2075 (1994).
30. Corona, D. F. *et al.* ISWI regulates higher-order chromatin structure and histone H1 assembly *in vivo*. *PLoS Biol.* **5,** e232 (2007).
31. Siriaco, G., Deuring, R., Chioda, M., Becker, P. B. & Tamkun, J. W. Drosophila ISWI regulates the association of histone H1 with interphase chromosomes *in vivo*. *Genetics* **182,** 661–669 (2009).
32. Vogler, C. *et al.* Histone H2A C-terminus regulates chromatin dynamics, remodeling, and histone H1 binding. *PLoS Genet.* **6,** e1001234 (2010).
33. Melcer, S. *et al.* Histone modifications and lamin A regulate chromatin protein dynamics in early embryonic stem cell differentiation. *Nat. Commun.* **3,** 910 (2012).
34. Gerlitz, G. *et al.* Migration cues induce chromatin alterations. *Traffic* **8,** 1521–1529 (2007).
35. Collins, N. *et al.* An ACF1-ISWI chromatin-remodeling complex is required for DNA replication through heterochromatin. *Nat. Genet.* **32,** 627–632 (2002).
36. Huh, M. S. *et al.* Compromised genomic integrity impedes muscle growth after Atrx inactivation. *J. Clin. Invest.* **122,** 4412–4423 (2012).
37. Sanchez-Molina, S. *et al.* Role for hACF1 in the G2/M damage checkpoint. *Nucleic Acids Res.* **39,** 8445–8456 (2011).
38. Eckey, M. *et al.* Nucleosome remodeler SNF2L suppresses cell proliferation and migration and attenuates Wnt signaling. *Mol. Cell Biol.* **32,** 2359–2371 (2012).
39. Gossett, A. J. & Lieb, J. D. *In vivo* effects of histone H3 depletion on nucleosome occupancy and position in *Saccharomyces cerevisiae*. *PLoS Genet.* **8,** e1002771 (2012).
40. Cho, J. H. & Tsai, M. J. Preferential posterior cerebellum defect in BETA2/NeuroD1 knockout mice is the result of differential expression of BETA2/NeuroD1 along anterior-posterior axis. *Dev. Biol.* **290,** 125–138 (2006).
41. Ben-Arie, N. *et al.* Math1 is essential for genesis of cerebellar granule neurons. *Nature* **390,** 169–172 (1997).
42. Engelkamp, D., Rashbass, P., Seawright, A. & van Heyningen, V. Role of Pax6 in development of the cerebellar system. *Development* **126,** 3585–3596 (1999).
43. Joyner, A. L., Herrup, K., Auerbach, B. A., Davis, C. A. & Rossant, J. Subtle cerebellar phenotype in mice homozygous for a targeted deletion of the En-2 homeobox. *Science* **251,** 1239–1243 (1991).
44. Tsai, P. T. *et al.* Autistic-like behaviour and cerebellar dysfunction in Purkinje cell Tsc1 mutant mice. *Nature* **488,** 647–651 (2012).
45. Nogami, T. *et al.* Reduced expression of the ATRX gene, a chromatin-remodeling factor, causes hippocampal dysfunction in mice. *Hippocampus* **21,** 678–687 (2011).
46. Shioda, N. *et al.* Aberrant calcium/calmodulin-dependent protein kinase II (CaMKII) activity is associated with abnormal dendritic spine morphology in the ATRX mutant mouse brain. *J. Neurosci.* **31,** 346–358 (2011).
47. Vogel-Ciernia, A. *et al.* The neuron-specific chromatin regulatory subunit BAF53b is necessary for synaptic plasticity and memory. *Nat. Neurosci.* **16,** 552–561 (2013).
48. Morris, S. A. *et al.* Overlapping chromatin-remodeling systems collaborate genome wide at dynamic chromatin transitions. *Nat. Struct. Mol. Biol.* **21,** 73–81 (2014).
49. Dirscherl, S. S., Henry, J. J. & Krebs, J. E. Neural and eye-specific defects associated with loss of the imitation switch (ISWI) chromatin remodeler in *Xenopus laevis*. *Mech. Dev.* **122,** 1157–1170 (2005).
50. Landry, J. *et al.* Essential role of chromatin remodeling protein Bptf in early mouse embryos and embryonic stem cells. *PLoS Genet.* **4,** e1000241 (2008).
51. Siegenthaler, J. A., Tremper-Wells, B. A. & Miller, M. W. Foxg1 haploinsufficiency reduces the population of cortical intermediate progenitor cells: effect of increased p21 expression. *Cereb. Cortex* **18,** 1865–1875 (2008).
52. Yu, Y. *et al.* Olig2 targets chromatin remodelers to enhancers to initiate oligodendrocyte differentiation. *Cell* **152,** 248–261 (2013).
53. Postepska-Igielska, A. *et al.* The chromatin remodelling complex NoRC safeguards genome stability by heterochromatin formation at telomeres and centromeres. *EMBO Rep.* **14,** 704–710 (2013).
54. Fan, Y. *et al.* H1 linker histones are essential for mouse development and affect nucleosome spacing *in vivo*. *Mol. Cell Biol.* **23,** 4559–4572 (2003).
55. Lu, X. *et al.* Drosophila H1 regulates the genetic activity of heterochromatin by recruitment of Su(var)3-9. *Science* **340,** 78–81 (2013).
56. Misteli, T., Gunjan, A., Hock, R., Bustin, M. & Brown, D. T. Dynamic binding of histone H1 to chromatin in living cells. *Nature* **408,** 877–881 (2000).
57. Stasevich, T. J., Mueller, F., Brown, D. T. & McNally, J. G. Dissecting the binding mechanism of the linker histone in live cells: an integrated FRAP analysis. *EMBO J.* **29,** 1225–1234 (2010).
58. Higashi, T. *et al.* Histone H2A mobility is regulated by its tails and acetylation of core histone tails. *Biochem. Biophys. Res. Commun.* **357,** 627–632 (2007).
59. Meshorer, E. *et al.* Hyperdynamic plasticity of chromatin proteins in pluripotent embryonic stem cells. *Dev. Cell* **10,** 105–116 (2006).
60. Efroni, S. *et al.* Global transcription in pluripotent embryonic stem cells. *Cell stem cell* **2,** 437–447 (2008).
61. Raymond, C. S. & Soriano, P. ROSA26Flpo deleter mice promote efficient inversion of conditional gene traps *in vivo*. *Genesis* **48,** 603–606 (2010).
62. Lewandoski, M., Wassarman, K. M. & Martin, G. R. Zp3-cre, a transgenic mouse line for the activation or inactivation of loxP-flanked target genes specifically in the female germ line. *Curr. Biol.* **7,** 148–151 (1997).
63. Barak, O. *et al.* Isolation of human NURF: a regulator of Engrailed gene expression. *EMBO. J.* **22,** 6089–6100 (2003).
64. Lazzaro, M. A. *et al.* Characterization of novel isoforms and evaluation of SNF2L/SMARCA1 as a candidate gene for X-linked mental retardation in 12 families linked to Xq25-26. *BMC Med. Genet.* **9,** 11 (2008).
65. Todd, M. A. & Picketts, D. J. PHF6 interacts with the nucleosome remodeling and deacetylation (NuRD) complex. *J. Proteome Res.* **11,** 4326–4337 (2012).
66. Rapsomaniki, M. A. *et al.* easyFRAP: an interactive, easy-to-use tool for qualitative and quantitative analysis of FRAP data. *Bioinformatics* **28,** 1800–1801 (2012).

67. Phair, R. D., Gorski, S. A. & Misteli, T. Measurement of dynamic protein binding to chromatin *in vivo*, using photobleaching microscopy. *Methods Enzymol.* **375,** 393–414 (2004).
68. Ellenberg, J. *et al.* Nuclear membrane dynamics and reassembly in living cells: targeting of an inner nuclear membrane protein in interphase and mitosis. *J. Cell Biol.* **138,** 1193–1206 (1997).
69. Nissim-Rafinia, M. & Meshorer, E. Photobleaching assays (FRAP & FLIP) to measure chromatin protein dynamics in living embryonic stem cells. *J. Vis. Exp.* **52,** 2696 (2011).
70. Visel, A., Thaller, C. & Eichele, G. GenePaint.org: an atlas of gene expression patterns in the mouse embryo. *Nucleic Acids Res.* **32,** D552–D556 (2004).

Acknowledgements

We are grateful to Dr Diane Lagace and Mirela Hasu at the University of Ottawa Behavioral Core for assistance with behavioural experiments and expert discussions. We thank Dr Alexandra Joyner for pan-Engrailed antibodies. M.A.-S. thanks D.J.P. for funding and Dr Peter Becker for expert discussions. This work was funded by operating grants GACR P305/12/1033 and UNCE 20421 to T.S.; NIH grant R01 CA079057 to A.I.S.; and CIHR grants MOP97764 and MOP84412 to D.J.P.

Author contributions

M.A.-S. designed, interpreted and executed all experiments. D.J.P. supervised the project. K.Y., E.H., D.I., M.S.H. and M.A.T. provided technical support. P.S.L. and C.P.C. helped establish the breeding colony and made some preliminary phenotypic observations with the Snf2h cKO-Nes mice. Y.D.R. and R.K. performed and analysed TEM experiments. E.V.R.R. and E.M. performed and analysed FRAP experiments. A.J.M., E.B., N.T. and V.A.W. performed and analysed *in situ* hybridizations and microarrays. D.Y. and I.I. provided bioinformatics support. $Snf2h^{fl/fl}$ and $Snf2h^{-/+}$ mice were generated and provided by T.S., J.K., R.M. and A.I.S. M.A.-S. and D.J.P. wrote the paper.

Additional information

Accession codes: All raw and processed microarray data have been deposited into Gene Expression Omnibus under the accession number GSE42371.

Supplementary Information accompanies this paper at http://www.nature.com/naturecommunications

Competing financial interests: The authors declare no competing financial interests.

Reprints and permission information is available online at http://npg.nature.com/reprintsandpermissions/

How to cite this article: Alvarez-Saavedra, M. *et al.* Snf2h-mediated chromatin organization and histone H1 dynamics govern cerebellar morphogenesis and neural maturation. *Nat. Commun.* 5:4181 doi: 10.1038/ncomms5181 (2014).

APPENDIX E

Reproduction Authorizations

Permission to reproduce manuscript in Chapter 2:

Reprinted with permission from "**Pediatric Blood & Cancer, Chao M.M., Todd M.A., Kontny U., Neas K., Sullivan M.J., Hunter A.G., Picketts D.J., and Kratz C.P., T-cell acute lymphoblastic leukemia in association with Börjeson-Forssman-Lehmann syndrome due to a mutation in PHF6, 2010, Volume 55 (4), pp 722-724**." Copyright © 2010 Wiley-Liss, Inc.

Dear Matthew Todd,

Thank you for your request.

Permission is granted for you to use the material requested for your thesis/dissertation subject to the usual acknowledgements (author, title of material, title of book/journal, ourselves as publisher) and on the understanding that you will reapply for permission if you wish to distribute or publish your thesis/dissertation commercially.

You should also duplicate the copyright notice that appears in the Wiley publication in your use of the Material. Permission is granted solely for use in conjunction with the thesis, and the material may not be posted online separately.

Any third party material is expressly excluded from this permission. If any material appears within the article with credit to another source, authorisation from that source must be obtained.

Kind Regards

Emma Willcox
Permissions Coordinator

WILEY

Permission to reproduce manuscript in Chapter 3:

Reprinted with permission from "**Journal of Proteome Research, Todd M.A.M. and Picketts D.J., PHF6 Interacts with the Nucleosome Remodeling and Deacetylation (NuRD) Complex, 2012, Volume 11 (8), pp 4326–4337**." Copyright (2012), American Chemical Society.

PERMISSION/LICENSE IS GRANTED FOR YOUR ORDER AT NO CHARGE

This type of permission/license, instead of the standard Terms & Conditions, is sent to you because no fee is being charged for your order. Please note the following:

- Permission is granted for your request in both print and electronic formats, and translations.
- If figures and/or tables were requested, they may be adapted or used in part.
- Please print this page for your records and send a copy of it to your publisher/graduate school.
- Appropriate credit for the requested material should be given as follows: "Reprinted (adapted) with permission from (COMPLETE REFERENCE CITATION). Copyright (YEAR) American Chemical Society." Insert appropriate information in place of the capitalized words.
- One-time permission is granted only for the use specified in your request. No additional uses are granted (such as derivative works or other editions). For any other uses, please submit a new request.

BACK CLOSE WINDOW

Permission to reproduce manuscript in Appendix B:

Reprinting of the Open Access article "**BMC Medical Genetics, Lazzaro M.A., Todd M.A.M., Lavigne P., Vallee D., De Maria A., and Picketts D.J., Characterization of novel isoforms and evaluation of SNF2L/SMARCA1 as a candidate gene for X-linked mental retardation in 12 families linked to Xq25-26, 2008, Volume 9: 11**" is in accordance with the terms and conditions of its Creative Commons license.

BMC Medical Genetics 2008, **9**:11 doi:10.1186/1471-2350-9-11

The electronic version of this article is the complete one and can be found online at:
http://www.biomedcentral.com/1471-2350/9/11

Received: 1 November 2007
Accepted: 26 February 2008
Published: 26 February 2008

Permission to reproduce manuscript in Appendix C:

Reprinted from "**Physiology, Huh, M.S., Todd M.A.M., and Picketts D.J., SCO-ping out the mechanisms underlying the etiology of hydrocephalus, 2009, Volume 24, pp 117-126**," in accordance with the copyright (2009) permission policies of The American Physiological Society.

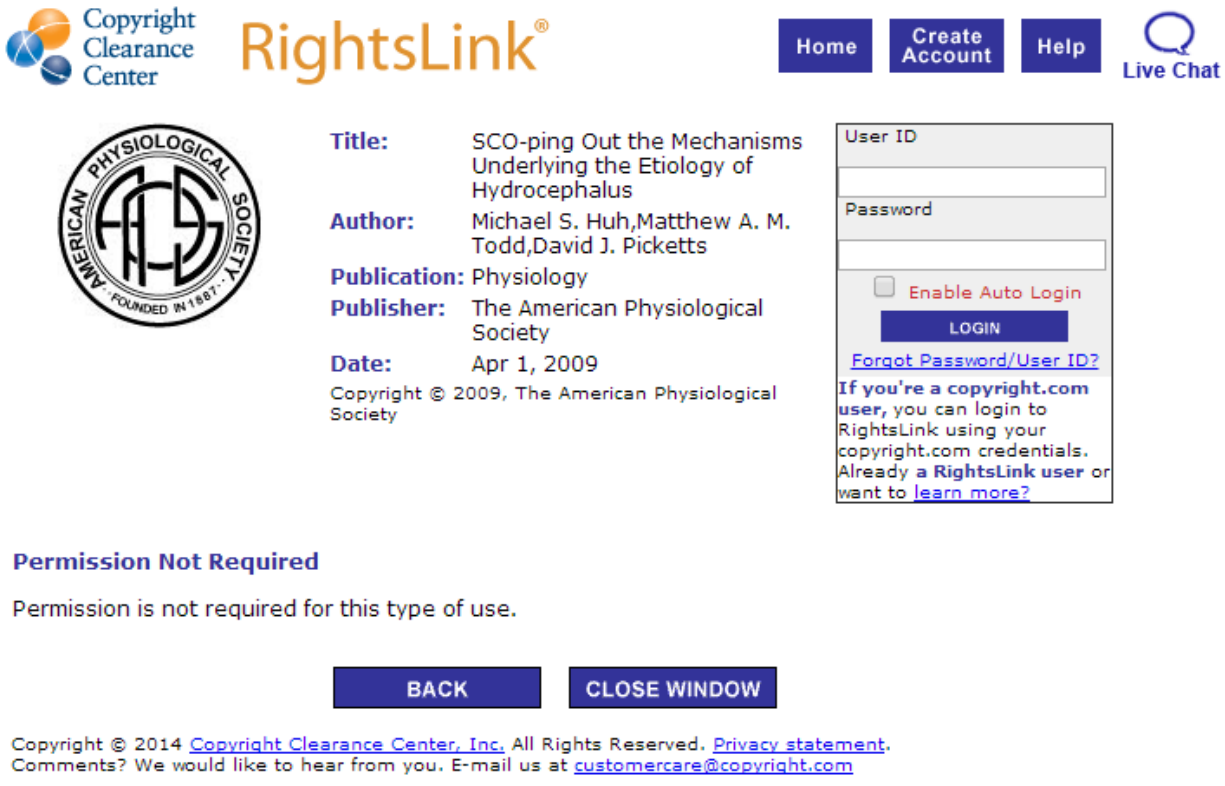

Permission to reproduce manuscript in Appendix D:

Reprinting of the Open Access article "**Nature Communications, Alvarez-Saavedra M., De Repentigny Y., Lagali P.S., Raghu Ram E.V., Yan K., Hashem E., Ivanochko D., Huh M.S., Yang D., Mears A.J., Todd M.A.M., Corcoran C.P., Bassett E.A., Tokarew N.J., Kokavec J., Majumder R., Ioshikhes I., Wallace V.A., Kothary R., Meshorer E., Stopka T., Skoultchi A.I., and Picketts D.J., Snf2h-mediated chromatin organization and histone H1 dynamics govern cerebellar morphogenesis and neural maturation, 2014, Volume 5: 4181**" is in accordance with the terms and conditions of its Creative Commons license.

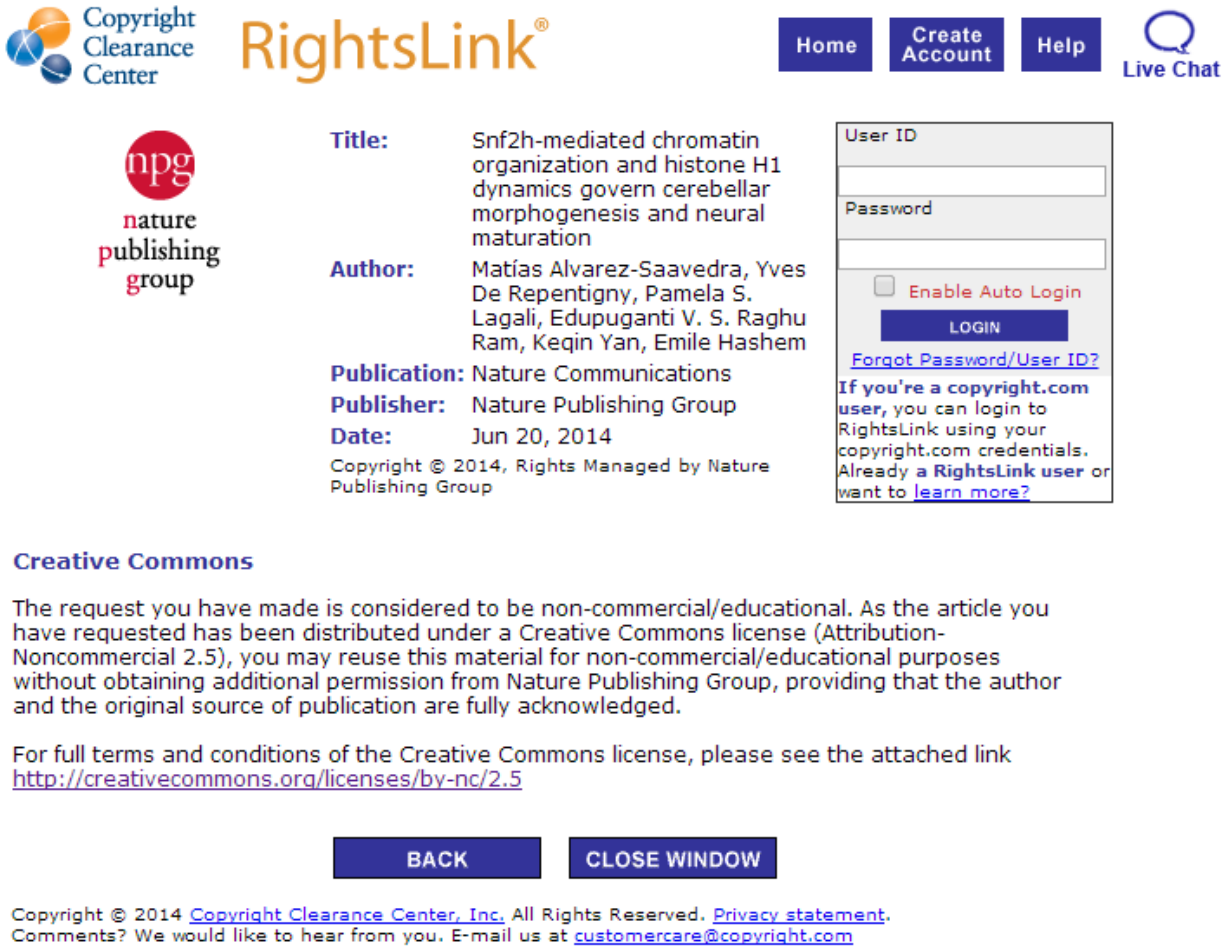

Copyright Clearance Center RightsLink®

Home | Create Account | Help | Live Chat

nature publishing group

Title: Snf2h-mediated chromatin organization and histone H1 dynamics govern cerebellar morphogenesis and neural maturation

Author: Matías Alvarez-Saavedra, Yves De Repentigny, Pamela S. Lagali, Edupuganti V. S. Raghu Ram, Keqin Yan, Emile Hashem

Publication: Nature Communications

Publisher: Nature Publishing Group

Date: Jun 20, 2014

Copyright © 2014, Rights Managed by Nature Publishing Group

User ID

Password

Enable Auto Login

LOGIN

Forgot Password/User ID?

If you're a copyright.com user, you can login to RightsLink using your copyright.com credentials. Already a **RightsLink user** or want to learn more?

Creative Commons

The request you have made is considered to be non-commercial/educational. As the article you have requested has been distributed under a Creative Commons license (Attribution-Noncommercial 2.5), you may reuse this material for non-commercial/educational purposes without obtaining additional permission from Nature Publishing Group, providing that the author and the original source of publication are fully acknowledged.

For full terms and conditions of the Creative Commons license, please see the attached link http://creativecommons.org/licenses/by-nc/2.5

BACK | CLOSE WINDOW

Copyright © 2014 Copyright Clearance Center, Inc. All Rights Reserved. Privacy statement.
Comments? We would like to hear from you. E-mail us at customercare@copyright.com

APPENDIX F

Curriculum Vitae

EDUCATION

2007- 2014 **PhD Thesis (transfer from MSc), Biochemistry with specialization in Human Molecular Genetics, University of Ottawa ON, Canada**
Thesis topic: Investigating the cellular role of PHF6, a gene implicated in intellectual disability and T-cell leukemia.
Supervisor: Dr. David Picketts, Professor
Funded by: NSERC Canada Postgraduate Scholarship, Ontario Graduate Scholarship, and an admission scholarship

2002-2007 **BSc, Biopharmaceutical Science with specialization in Genomics, University of Ottawa, Ottawa, ON, Canada**

ADDITIONAL RESEARCH AND WORK EXPERIENCE

2008-2014 **Teaching assistant/lab demonstrator, University of Ottawa**
Courses: Introduction to Biochemistry, Molecular Biology lab
Supervisors: Dr. Vas Mezl, Dr. Gabriel Guillet, Dr. Luc Poitras

2006 **Co-op Student, Research and Development, Sanofi Pasteur Canada Ltd, Toronto ON, Canada**
Research project: Designing a capillary isoelectric focusing method to analyze vaccine components.
Supervisor: Dr. Marina Kirkitadze, Senior Scientist

2005 **Co-op Student, Medicinal Chemistry department, Merck Frosst Canada Ltd, Kirkland QC, Canada**
Research project: Designing high throughput HPLC-MS/MS screens for the analysis of cytochrome P450-related drug-drug interactions.
Co-supervisors: Dr. Qingping Wang and Jean-Francois Levesque
Funded by: NSERC Undergraduate Student Research Award

2005 **Co-op Student, Analytical Chemistry department, MethylGene Inc, Montreal QC, Canada**
Research project: Developing an in-house HPLC-MS/MS method for analyzing drug inhibition with cytochrome P450 enzymes.
Supervisor: Dr. Xuejun Peng

2004 **Undergraduate Research Student**, Chemistry department, University of Ottawa and the Biologics and Genetic Therapies Directorate, Health Canada, Ottawa ON, Canada
Research project: Developing a novel method for detecting histidine residues by MALDI-TOF
Co-supervisors: Dr. Harvey Kaplan and Dr. Terry Cyr
Funded by: NSERC Undergraduate Student Research Award

AWARDS

2011-12	Ontario Graduate Scholarship
2011-12	University of Ottawa Admission Scholarship
2011	Institute of Human Development, Child and Youth Health Travel Research Award
2007-09	NSERC Canada Graduate Scholarship
2007-09	University of Ottawa Excellence Award
2002-07	University of Ottawa Undergraduate Admission Scholarship
2002-07	University of Ottawa Dean's Honour List
2005	NSERC Undergraduate Student Research Award
2004	NSERC Undergraduate Student Research Award
2002	Lena MacNeil Scholarship (declined)

PUBLICATIONS

Todd MAM, Huh MS, Picketts DJ. 2014. RNA tethers PHF6 to the nucleolus to mediate rDNA transcript levels. [manuscript submitted to *J. Med. Genet.*]

Alvarez-Saavedra M, De Repentigny Y, Lagali PS, Raghu Ram EV, Yan K, Hashem E, Ivanochko D, Huh MS, Yang D, Mears AJ, **Todd MAM**, et al. 2014. Snf2h-mediated chromatin organization and histone H1 dynamics govern cerebellar morphogenesis and neural maturation. *Nat. Commun*. **5**: 4181.

Todd MAM, Picketts DJ. 2012. PHF6 Interacts with the Nucleosome Remodeling and Deacetylation (NuRD) Complex. *J Proteome Research*. **11**: 4326–4337.

Chao MM, **Todd MA**, Kontny U, Neas K, Sullivan MJ, Hunter AG, Picketts DJ, Kratz CP. 2010. T-cell acute lymphoblastic leukemia in association with Börjeson-Forssman-Lehmann syndrome due to a mutation in PHF6. *Pediatr Blood Cancer*. **55**: 722-724.

Huh MS, **Todd MAM**, Picketts DJ. 2009. SCO-ping out the mechanisms underlying the etiology of hydrocephalus. *Physiology*. **24**: 117-126.

Lazzaro MA, **Todd MAM**, Lavigne P, Vallee D, De Maria A, Picketts DJ. 2008. Characterization of novel isoforms and evaluation of SNF2L/SMARCA1 as a candidate gene for X-linked mental retardation in 12 families linked to Xq25-26. *BMC Med Genet*. **9**: 11.

ABSTRACTS AND PRESENTATIONS

Todd MAM and Picketts DJ. "Towards a functional understanding of PHF6, a nucleolar zinc finger protein mutated in Börjeson-Forssman-Lehmann syndrome and T-cell acute lymphoblastic leukemia." Poster presented at the Miami 2011 Winter Symposium: Epigenetics in development and disease. Miami, FL. February 6-9, 2011. Poster.

Kirkitadze M, Hu J, **Todd M**, and Cates G. "Application of Capillary Isoelectrofocusing for protein analysis." Poster presented at the 11th Symposium on the Interface of Regulatory and Analytical Sciences for Biotechnology Health Products. Washington, DC. January 29, 2007. Poster.